

Dissertation
submitted to the
Combined Faculty of Mathematics, Engineering and Natural Sciences
of Heidelberg University, Germany
for the degree of
Doctor of Natural Sciences

Put forward by

Robert Ott

born in: *Weißenhorn*

Oral examination: *June 28, 2022*

Quantum simulations with ultra-cold atoms out of equilibrium

Referees:

Prof. Dr. Jürgen Berges
apl. Prof. Dr. Jörg Evers

Zusammenfassung

Quantensimulationen mit ultra-kalten Atomen außerhalb des Gleichgewichts

Der rasche technologische Fortschritt ultrakalter Quantengasexperimente führte zu starken Bemühungen Quantensimulatoren zur Lösung grundlegender Fragestellungen der modernen Physik zu entwickeln. Die weitreichenden Anwendungen beinhalten verschiedenste Forschungsgebiete - von der Hochenergiephysik und Kernphysik, über die Kosmologie, bis hin zur Festkörperphysik und Chemie. Speziell die Beschreibung von evolvierenden Quantenfeldern, die vielen Forschungsaktivitäten zugrunde liegt, ist dabei häufig nicht mit klassischen Computern zu bewältigen. Diese Dissertation beschäftigt sich mit solchen Quantensimulationen im Zusammenhang der komplexen Nichtgleichgewichtsdynamik ultrakalter Quantengase, sowie deren Verwendung zur Beschreibung von Eichtheorien. Zunächst präsentieren wir einen skalierbaren Vorschlag zur Implementierung einer eindimensionalen Gittereichtheorie in einem groß-skaligen Bose-Hubbard Quantensimulator. Die experimentelle Realisierung des Vorschlags erlaubt uns die Thermalisierungsdynamik der Eichtheorie zu untersuchen. Zweitens, wird ein skalierbarer Vorschlag zur Quantensimulation von Eichfelddynamik in zwei Raumdimensionen ausgearbeitet. Ein Baustein des Vorschlags wird mit Hilfe eines Quantengasexperiments untersucht, wobei das Vielteilchenproblem durch die Untersuchung der Fluktuationsdaten charakterisiert wird. Zuletzt widmen wir uns der Echtzeitdynamik von Quantenfeldern über eine zeit-lokale effektive Wirkung. Wir leiten kinetische Gleichungen für nicht-perturbative Bosefelder ab und etablieren eine Verbindung von effektiven Beschreibungen mit Beobachtungsgrößen, die mit gegenwärtiger Technologie verfügbar sind.

Abstract

Quantum simulations with ultra-cold atoms out of equilibrium

Recent technological advances in ultra-cold atom experiments have triggered strong efforts to develop quantum simulators for solving fundamental questions in modern physics. Far-reaching applications range from quantum chemistry and condensed matter physics to high-energy physics, nuclear physics and cosmology, where the evolution of underlying quantum fields is often difficult to compute with classical simulations. This dissertation contributes to the field of quantum simulations for the complex out-of-equilibrium dynamics of gauge fields and the ultra-cold quantum gases realized in current experiments and their applications to gauge theories. First, we present a scalable scheme to engineer a one-dimensional lattice gauge theory using ultra-cold atoms in a large-scale Bose-Hubbard quantum simulator, which is demonstrated in an experiment. The implementation allows us to furthermore investigate the thermalization dynamics of the gauge theory. Secondly, a scalable cold-atom quantum simulator for gauge-field dynamics in two spatial dimensions is proposed. We investigate an experimental building block of the proposal, where the many-body problem is characterized using the fluctuations in the data. Finally, we present an equal-time approach to the real-time dynamics of quantum fields through the non-equilibrium effective action. Focusing on non-perturbative Bose fields, we derive kinetic equations to establish a link between effective theories and observables accessible with current technology.

Acknowledgments

First of all, I thank Jürgen Berges for supervising me on my journey over the past years and for providing such an active and open research environment. I have learned a lot from our projects, the countless discussions and your precious advice.

Secondly, I want to express my gratitude towards Philipp Hauke for his great ideas on our projects and for inviting me to Trento.

Furthermore, I am indebted to Bing Yang and Fred Jendrzejewski for the great collaborations and their help with everything related to ultra-cold atom experiments.

My gratitude extends to the great people involved in the collaborations, which I had the opportunity to be part of during these years. Here, I want to especially thank Torsten Zache for our endless discussions.

A special notice of Jürgen's research group is in order, including all the past and present members, which created an exciting, welcoming and enjoyable atmosphere.

Moreover, I was very lucky to represent the young researchers of the IsoQuant together with Eleonora Lippi and Bruno Faigle-Cedzich. I am much indebted to Tina Kuka for her help and the great ideas, as well as to the administrations of IsoQuant and ITP in general.

At last, I would like to thank the people who have supported me during the past years, especially my family, my friends and Alina. I am grateful for the help during the completion of this dissertation, including the valuable comments on the manuscript from Daniel, Gregor, Linda, Martin, Niklas, Torsten and Valentin.

List of publications

Parts of the content of this dissertation have been published in the following articles:

- B. Yang, H. Sun, R. Ott, H.-Y. Wang, T. V. Zache, J. C. Halimeh, Z.-S. Yuan, P. Hauke, and J.-W. Pan, “Observation of gauge invariance in a 71-site bose–hubbard quantum simulator”, *Nature* **587**, 392–396 (2020)
- J. C. Halimeh, R. Ott, I. P. McCulloch, B. Yang, and P. Hauke, “Robustness of gauge-invariant dynamics against defects in ultracold-atom gauge theories”, *Physical Review Research* **2**, 033361 (2020)
- R. Ott, T. V. Zache, F. Jendrzejewski, and J. Berges, “Scalable cold-atom quantum simulator for two-dimensional qed”, *Physical Review Letters* **127**, 130504 (2021)
- Z.-Y. Zhou, G.-X. Su, J. C. Halimeh, R. Ott, H. Sun, P. Hauke, B. Yang, Z.-S. Yuan, J. Berges, and J.-W. Pan, “Thermalization dynamics of a gauge theory on a quantum simulator”, arXiv preprint arXiv:2107.13563 (2021) (under review in *Science*)
- N. Mueller, T. V. Zache, and R. Ott, “Thermalization of gauge theories from their entanglement spectrum”, arXiv preprint arXiv:2107.11416 (2021) (under review in *Physical Review Letters*)
- R. Ott, T. V. Zache, and J. Berges, “Equal-time approach to real-time dynamics of quantum fields”, arXiv preprint arXiv:2204.06463 (2022)
- A. Hegde, R. Ott, A. Xia, V. Kasper, J. Berges, and F. Jendrzejewski, “Non-equilibrium dynamics of fluctuations in an ultra-cold atomic mixture”, arXiv preprint arXiv:2204.06456 (2022)

The following article, which has been completed during my doctoral studies and which contains the main results of my master’s thesis, is not part of this dissertation:

- R. Ott, T. V. Zache, N. Mueller, and J. Berges, “Non-cancellation of the parity anomaly in the strong-field regime of qed $_{2+1}$ ”, *Physics Letters B*, 135459 (2020)

Wherever content of these articles has been used for this thesis, it is clearly stated at the beginning of each chapter, where I also summarize my contributions to the collaborative publications.

Contents

Zusammenfassung	i
Abstract	iii
Acknowledgments	v
List of publications	vii
1 Introduction	1
1.1 Motivation	1
1.2 Outline	4
1.3 Main concepts	7
2 Large-scale quantum simulation of a U(1) gauge theory in 1D	19
2.1 Overview	20
2.2 Model and implementation with ultra-cold atoms	20
2.3 Experimental set-up	24
2.4 Gauge-invariance and quantum phase transition	25
2.5 Thermalization dynamics	35
2.6 Summary	42
2.A Perturbation Theory	43
2.B Correlation length	45
2.C Numerics	46
2.D Thermal states	47
3 Quantum simulation and gauge field dynamics in 2D	51
3.1 Overview	52
3.2 Scalable cold-atom quantum simulator	52
3.3 Charge confinement	57
3.4 Experimental realization of a unit plaquette	61
3.5 Non-equilibrium entanglement spectrum of a gauge theory	69
3.6 Summary	75
3.A Detailed derivation of cold-atom Hamiltonian	76
3.B Flux fields and potential	80
3.C Details on the theoretical modelling of the experiment	89

4	Equal-time approach to quantum field dynamics	103
4.1	Motivation and Overview	103
4.2	Correlations in a Bose gas	105
4.3	Equal-time 1PI effective action	107
4.4	Perturbative expansion	112
4.5	Non-perturbative large- N expansion	117
4.6	Measurement protocol	125
4.7	Summary	129
4.A	Derivation of flow equation	130
4.B	Diagrammatic rules and examples	135
4.C	Details on the non-perturbative Boltzmann equation	141
5	Conclusion	147
5.1	Summary	147
5.2	Outlook	148
	List of figures	151
	List of abbreviations	153
	Bibliography	155

Chapter 1

Introduction

1.1 Motivation

Gauge fields mediate the fundamental forces in the Standard Model of particle physics and hence describe the interactions among elementary particles such as electrons or quarks [9–11]. For example, the positively charged nuclei attract electrons to form atoms through the electromagnetic force described by quantum electrodynamics (QED), and are held together by the strong force exhibited by the gluon fields of quantum chromodynamics (QCD). Typically, detailed theoretical investigations into the workings of these forces require costly numerical simulations, which challenge the largest computing facilities across the globe.

A typical problem in high-energy physics concerns the time evolution of gauge fields during and after the collisions of heavy nuclei. For instance, such experiments are currently conducted at the large-hadron collider at CERN [12], where lead nuclei are first accelerated to velocities close to the speed of light, and subsequently collided. At high energies the remnants of the collision are believed to form a plasma of deconfined quarks and gluons [13]. This plasma constitutes the hottest known phase of matter and its investigation promises insights into properties of the early universe shortly after the Big Bang. The theoretical description of the collision and the ensuing dynamics toward the thermal plasma is challenging and to date there is no first-principle method to describe the phenomenon with classical computing techniques [14].

In this context, the possibility of applying quantum technology to such dynamical quantum phenomena has recently triggered strong international research efforts, where current platforms termed *quantum simulators* are often based on ultra-cold atoms [15], trapped ions [16] and superconducting circuits [17]. Such quantum simulators can be used to investigate a wealth of quantum systems for regimes where classical computations fail as a consequence of complexity [18]: While microscopic interactions of constituents are known in many cases, the theoretical description of emergent phenomena for large systems requires extensive computing resources [19, 20]. Besides the thermalization dynamics of gauge fields, the difficulty of describing complex systems affects major research directions today, for example investigations of strongly-correlated phases for condensed matter systems, or the description of large molecules in chemistry.

Quantum simulators make use of their many constituents' quantum nature as a resource for computations, where microscopic interactions in these systems may be tuned precisely to realize a variety of many-body target theories. For instance, ultra-cold atoms may be used to represent atomic nuclei and electrons in a simulation of large molecules [21], or even quarks and gluons of the collided nuclei [22]. Here, target scenarios may drastically differ in size and energy from corresponding scales of the simulating platform. While heavy-ion collisions happen within femtoseconds, the same phenomena might take place in ultra-cold quantum gases on the order of milliseconds or even seconds. Quantum simulators exploit that physical systems can be described in dimensionless ratios of relevant energy or distance scales, and the freedom of choosing the absolute energy scale allows us to study high-energy physics at ultra-cold temperatures. The change of scales subsequently enables the extraction detailed observables in space and time, such as correlation functions [23, 24] or measures of entanglement [25, 26], to investigate the complex quantum dynamics in ways which are impossible to access in collider experiments.

However, quantum simulators face the problem of implementing the extensive set of local constraints in time and space implied by gauge symmetry. Such constraints tie the evolution of matter particles to the corresponding gauge fields and embody the nature of these forces and their emergent properties. Examples are the transversal polarization of photons, the long-ranged Coulomb law, or the absence of single quarks due to their confinement in hadrons [9, 27].

In recent years, an extensive set of techniques to quantum simulate gauge theories has been developed [28, 29], and current theoretical [30–50] and experimental [51–60] efforts are devoted to developing, testing, and applying protocols for different platforms. Despite great success in these developments, many challenges remain to be overcome [61, 62]. The central motivation of this thesis is based on a selection of these challenges summarized as follows:

(i) **Scalability:**

To establish quantum simulators of gauge theories with synthetic quantum matter, strategies to realize the local constraints between microscopic constituents must be applicable in the limit of large systems. The many degrees of freedom [63] are an important prerequisite to reaching the quantum field limit for realistic applications. One possibility to achieve this is to exploit symmetry properties of the underlying architecture [30, 52, 64].

(ii) **Dimensionality:**

Nature exhibits three spatial dimensions, but, so far, most experimental realizations of synthetic gauge theories are based on implementation schemes for the simpler case of a one-dimensional universe. Despite being an important proof-of-principle step, one-dimensional setups must be extended to higher dimensions for many applications in high-energy physics [65]. A major obstacle toward this goal concerns the realization of four-body terms for magnetic

field interactions, which are not present in one dimension, and which typically require precise control over higher-order interactions.

(iii) **Characterization:**

Characterizing quantum simulators with experimental measurements is a non-trivial task. How can we access the underlying state of the system with efficiently obtainable observables? Can such observables be used to benchmark the quantum simulator model-independently or even learn new approximation schemes for efficient descriptions? These questions especially affect the quantum field limit where classical simulations of the quantum simulator often become unfeasible.

In general, the quest of realizing quantum simulators for realistic applications is demanding. Achieving progress along the items (i)-(iii) will pave the road to artificial equilibrium and non-equilibrium gauge fields for applications in high-energy physics, or condensed matter. This thesis addresses quantum simulation in the context of high-energy phenomena such as confinement [27], phase transitions [66], thermalization dynamics [67], instabilities [68] or turbulence [69], where we demonstrate the current capabilities of quantum simulators or propose new protocols for experiments.

1.2 Outline

This dissertation contributes to the field of quantum simulations for applications to quantum field theories such as lattice gauge theories. We describe the engineering of gauge symmetries at the microscopic level and highlight their importance for the resulting system evolution. In the following, we discuss quantum simulations of gauge theories first in one spatial dimension and secondly for two-dimensional setups. Third, we describe the real-time dynamics of scalar quantum fields within an equal-time framework, which is well-suited to address current quantum simulation experiments.

The thesis is organized into the following chapters:

In the remainder of *Chapter 1*, we introduce the underlying concepts relevant for the contents of this thesis. We cover quantum field theory and gauge theories, and discuss a Hamiltonian formulation of the gauge fields and their finite dimensional representations for applications in quantum simulation. We furthermore introduce Bose gases and how they are used in optical potentials.

In *Chapter 2: "Large-scale quantum simulation of a $U(1)$ gauge theory in one dimension (1D)"*, we devise a scalable scheme to realize a synthetic $U(1)$ lattice gauge theory coupling gauge fields and matter. Our scheme is realized with ultra-cold bosonic atoms in a one-dimensional optical lattice with up to 71 sites. It implements the gauge symmetry by penalizing unwanted tunneling processes of the atoms with a staggered external potential. To demonstrate the feasibility of our approach, the synthetic gauge theory is investigated experimentally. We explore two different equilibrium phases by driving the system across a quantum phase transition in a quasi-static evolution. To validate our results, we experimentally quantify gauge invariance in the system during the evolution.

Subsequently, the quantum simulator is applied to investigate the non-equilibrium dynamics of the gauge theory. We observe that late-time steady states of the evolution agree with predictions from a gauge-invariant thermal ensemble. The thermalization dynamics is characterized by an effective loss of information during the unitary dynamics, where initial states with equal energy evolve toward the same steady-state values. To probe the importance of gauge symmetry in the complex dynamics, we also perform quantum simulations with loosened symmetry constraints which relax toward different ensembles.

In *Chapter 3: "Quantum simulation and gauge field dynamics in two dimensions (2D)"*, we propose a scalable scheme to engineer $U(1)$ gauge fields with ultra-cold atoms in two spatial dimensions. Our proposal employs spin-changing collisions of the atoms to engineer the required four-body interaction terms. Applying our scheme

to the gauge fields of compact QED, we discuss how charge confinement could be observed in a quantum simulator.

We subsequently investigate the non-equilibrium dynamics of gauge fields within an experimental realization of our scheme for the simpler case of a single plaquette. The spin-changing collisions are realized with a mixture of ultra-cold sodium (^{23}Na) and lithium (^7Li) atoms. We characterize the dynamics in terms of three non-equilibrium regimes: a long-lived metastable state, an instability regime with growth of fluctuations, and a regime that exhibits signatures of fast relaxation toward thermal equilibrium. The various types of dynamics are identified and related to effective potentials through theoretical modelling of experimentally measured fluctuations in the system.

The non-equilibrium dynamics of two-dimensional gauge fields is furthermore studied for a \mathbb{Z}_2 lattice gauge theory by computing entanglement spectra. The spectra reveal different stages of the dynamics such as level repulsion, self-similar dynamics and the approach to equilibrium at late times.

In *Chapter 4: “Quantum field dynamics from the equal-time effective action”*, we consider the non-equilibrium dynamics of an ultra-cold Bose gas. Using an equal-time formulation of quantum field theory, we derive an exact evolution equation for a time-local effective action of the non-relativistic fields. This allows us to formulate corresponding evolution equations coupling equal-time correlations and vertices, which we solve in two approximations resulting in effective late-time kinetic equations: A perturbative expansion for weakly interacting, dilute gases and an expansion in the number of field components to describe the non-perturbative dynamics of over-occupied Bose fields. We furthermore present an experimental strategy to extract the correlations of underlying Bose fields.

The results of these main chapters are summarized and discussed in *Chapter 5: “Conclusion”*, followed by an outlook on future extensions and applications of the presented work.

1.3 Main concepts

In this section we give an introduction to the main concepts relevant for the contents of this thesis - references to more detailed literature are presented. We start by introducing the concept of quantum fields in general, before specifying gauge theories. For practical applications, gauge theories are often considered in finite dimensional representations, where their configuration space is truncated in a controlled manner to match experimental resources. We give the two representations used in this thesis before ending this chapter by explaining quantum gases and optical lattices.

1.3.1 Quantum field theory

Quantum field theory (QFT) [9] is the modern tool to address many-body quantum systems, as realized in nature from the highest known energy scales down to the very coldest conditions explored so far. Quantum field theoretical methods have become powerful tools to investigate the laws of elementary particles and fundamental forces in the Standard Model of particle physics, as well as the complex interplay of non-relativistic matter in condensed matter systems or ultra-cold atoms and molecules. The description of many-body systems in terms of field theory is ubiquitous, and also extends to classical complex systems.

QFT is usually formulated in terms of path integrals acting as generating functionals for correlations of fields at different positions and times

$$Z[J] = \int \mathcal{D}\phi e^{iS[\phi]+iJ\cdot\phi}. \quad (1.1)$$

The *scalar field* $\phi(x)$ represents a real number at every point in space and time, where $J(x)$ is an external source field, and \cdot implies an integral over all spacetime coordinates. The path integral sums over all possible field configurations, which are weighted with a complex phase factor carrying the microscopic action of the theory. This complex weight factor induces interferences between different evolution histories of the system and eventually determines the propagation of particles or, more generally, information in a field theory. The path integral highlights the statistical nature of QFT, i.e., it predicts expectation values, or *correlation functions* of fields

$$\langle \mathcal{T}\phi(x_1)\dots\phi(x_n) \rangle = \int \mathcal{D}\phi \phi(x_1)\dots\phi(x_n) e^{iS[\phi]+iJ\cdot\phi}, \quad (1.2)$$

which typically involve an field ordering prescription, here the time ordering \mathcal{T} . The microscopic action of a QFT is motivated by fundamental constraints such as locality and symmetries, for example Lorentz invariance. Motivated by this reasoning, we consider the action of a relativistic, free, real scalar field theory in 3+1 spacetime

dimensions with Minkowski metric $\eta_{\mu\nu} = \text{diag}(1, -1, -1, -1)$,

$$S_0[\phi] = \int_x \left(\frac{1}{2} \eta_{\mu\nu} (\partial^\mu \phi) (\partial^\nu \phi) - \frac{m^2}{2} \phi^2 \right), \quad (1.3)$$

where we integrate over all four-vectors $x = x^\mu = (t, \mathbf{x})^\mu$ with spacetime index $\mu = 0, 1, 2, 3$, and we abbreviated $\int_x = \int d^4x$. Coupled by the partial derivatives ∂^μ , the field represents a set of harmonic oscillators which evolve in freely propagating waves. In this case, the path integral is exactly solvable in terms of Gaussian integrals. In general, this is not the case once interactions are introduced, i.e.,

$$S[\phi] = S_0[\phi] + \lambda_4 \int_x \phi^4 + \lambda_6 \int_x \phi^6 + \dots, \quad (1.4)$$

where interaction strengths are quantified by the couplings λ_i . This classical action is associated with a corresponding microscopic or ultra-violet (UV) cutoff scale Λ . For typical energies Λ it describes the physics of the fields through the variational principle $\delta S = 0$. However, in practice we are interested in the properties of quantum fields at macroscopic or infra-red (IR) scales k . The path integral systematically includes quantum fluctuations into correlation functions when moving from UV to IR, where the scale-dependent fluctuations enter corresponding coupling constants of effective actions Γ_k

$$e^{i\Gamma_k[\Phi] + iJ \cdot \Phi} = \int \mathcal{D}\phi_k e^{iS[\phi] + iJ \cdot \phi}, \quad (1.5)$$

where $\Phi(J) = \int \mathcal{D}\phi_k \phi \exp(iS[\phi] + iJ \cdot \phi)$ is the field expectation value and $\mathcal{D}\phi_k$ takes into account field fluctuations with spatial size $< k^{-1}$. The scale-dependent couplings of Γ_k run from UV (where $\Gamma_{k=\Lambda} = S$) to IR scales, and the IR physics at typical energies k becomes accessible through the variational principle $\delta\Gamma_k = 0$.

The power of QFT is rooted in the classification of interactions in terms of *relevant and irrelevant operators*. At any scale k , all interaction terms in accordance with the *symmetries* of the theory are generated through quantum fluctuations¹. Relevant operators are those which we need to take into account in the running of observable quantities, while the effects of irrelevant operators wash out toward the IR. To identify the relevant operators of a theory, it is often sufficient to consider a naive power-counting in terms of mass or energy dimensions of coupling constants. While λ_4 is a dimensionless number, $\lambda_{i>4}$ carry units of energy (and higher powers thereof) and are irrelevant in 3+1 spacetime dimensions. In this case, we may set $\lambda_{i>4} = 0$, and also discard terms with higher powers of derivatives without loss of generality.

In general, the introduction of microscopic interactions with different symmetry properties may change the entire process of the outlined running of observables, which poses a major challenge for quantum simulation: To reach the desired IR

¹In the present case, we consider interaction terms symmetric under $\phi \rightarrow -\phi$.

physics of target theories a meticulous control of the microscopic symmetry properties is of utmost importance, which, for large-scale systems involves an extensive number of degrees of freedom, and efficient mechanisms to protect the symmetries are required.

While scalar field theories are the prototypes of QFTs, and their non-relativistic counterparts are often naturally implemented in ultra-cold quantum gases, quantum simulations of gauge theories require more complex fields. In the next section, we consider fermionic fields, which constitute the fundamental building blocks of matter, and how they interact via gauge fields resulting from a local U(1) symmetry of the fermions.

1.3.2 Gauge theory

Continuum gauge theory

U(1) symmetry is an invariance of the action² under local transformations of the fermionic matter fields with the abelian group U(1)

$$\psi(x) \mapsto \psi'(x) = e^{i\alpha(x)}\psi(x), \quad (1.6)$$

where ψ is a four component Dirac spinor, see e.g. Ref. [11] for details. Here, we distinguish a *global* symmetry with $\alpha = \text{const.}$ from a *local* or *gauge* symmetry for space and time dependent phases $\alpha(x)$. Global continuous symmetries lead to classical conservation laws³ via Noether's theorem. Examples are electric charge conservation in QED or particle number conservation in non-relativistic low-energy effective field theories. In contrast, gauge symmetries introduce entirely new structures to the theory. The necessity to introduce covariant derivatives in order to "compare" fields with different transformation behavior at different spacetime points yields a new dynamical degree of freedom

$$\partial^\mu \rightarrow D^\mu = \partial^\mu + iA^\mu, \quad (1.7)$$

where A^μ is the four component *gauge field* equipped with the transformation behavior $A^\mu(x) \mapsto A^\mu(x) - \partial^\mu \alpha(x)$. The continuum action of QED is given by

$$S[\psi^\dagger \psi, A] = \int_x \left(-\frac{1}{4e^2} F^{\mu\nu} F_{\mu\nu} + \psi^\dagger \gamma^0 (i\gamma^\mu D_\mu - m) \psi \right). \quad (1.8)$$

where we included the gauge-invariant QED field strength tensor $F^{\mu\nu} = \partial^\mu A^\nu - \partial^\nu A^\mu$ as a relevant extension of the fermion action which respects the underlying symmetries. The field strength term allows for the propagation of gauge fields which mediate interactions between the elementary fermion particles with interaction

²and the path integral measure

³In cases where the path integral measure is not invariant under the symmetry group this conservation law is broken by quantum fluctuations. This is called a quantum anomaly [70].

strength e , and we also introduced the gamma matrices γ^μ as a representation of the Clifford algebra $\gamma^\mu\gamma^\nu + \gamma^\nu\gamma^\mu = 2\eta^{\mu\nu}$ [11]. The concept of gauge theories may be generalized to more complex symmetry groups, such as *non-abelian* gauge groups, e.g., $SU(3)$ in the case of QCD, or even to the symmetry groups realized in the Standard Model of particle physics.

Complex calculations beyond the analytically accessible regimes (e.g. perturbation theory) require numerical computing techniques to solve the path integral. In this context, lattice field theory [10, 11, 71] has been developed to map a field theory of infinitely many degrees of freedom onto a finite lattice which may be addressed with classical computers. In quantum simulation, we make similar use of lattice representations to represent field theories with finite experimental resources in the laboratory.

Lattice gauge theory

In order to formulate quantum field theories on lattices, the continuous spacetime is replaced with a discrete set of points on which matter fields reside. The lattice provides cutoffs to both IR and UV scales - by definition the lattice spacing is the smallest possible separation between two points and the extent of the lattice is the largest accessible scale. This allows the controlled investigation of field theories with a finite number of degrees of freedom, where *continuum* and *thermodynamic* limits are reached by demonstrating the independence of results with respect to the details of the cutoffs.

To formulate the action on a lattice⁴, derivatives of fields are replaced by finite differences

$$\partial_\mu\psi(x) \rightarrow \frac{\psi(x + a\mathbf{e}_\mu) - \psi(x)}{a}, \quad (1.9)$$

where $a \sim 1/\Lambda$ is the lattice spacing and \mathbf{e}_μ is a lattice unit vector in direction μ . There are various choices of discretizing quantum fields on the lattice - typically they differ by irrelevant terms and agree for small lattice spacings. Specifically, for fermions there are subtleties associated with their discretization termed the *fermion doubling* problem: The naive discretization procedure outlined above leads to an enhancement in the number of fermionic degrees of freedom, rather than describing a single flavor of fermions in the continuum limit ($a \rightarrow 0$) [72]. There exist several procedures to circumvent this issue, typical choices being staggered fermions [73], as employed in Chapter 2, or Wilson fermions [71]. To illustrate the emergence of gauge fields on the lattice, we outline a *naive* discretization of lattice fermions here, which reads for free fermions

$$S_F[\psi^\dagger, \psi] = \frac{1}{2a} \sum_x \left(\psi^\dagger(x) \gamma^0 \gamma^\mu \psi(x + a\mathbf{e}_\mu) + c.c. \right) - m \sum_x \psi^\dagger(x) \gamma^0 \psi(x), \quad (1.10)$$

⁴For the remainder of this section we consider a four-dimensional Euclidean hyper-cubic spacetime lattice.

where *c.c.* abbreviates complex conjugation. To “compare” the fermion fields at two neighboring lattice points we introduce the *Wilson line* or *gauge link variable* $U_\mu(x)$, rather than a covariant derivative as in the continuum field case considered above. With the transformation behavior

$$U_\mu(x) \mapsto U'_\mu(x) = e^{i\alpha(x)} U_\mu(x) e^{-i\alpha(x+a\mathbf{e}_\mu)}, \quad (1.11)$$

the phase of the gauge link changes by the discrete expression $-a\hat{\partial}_\mu\alpha(x) \equiv \alpha(x) - \alpha(x + \mathbf{e}_\mu)$. The following replacement renders products of fermion fields on neighboring sites gauge-invariant:

$$\psi^\dagger(x)\psi(x + a\mathbf{e}^\mu) \rightarrow \psi^\dagger(x)U_\mu(x)\psi(x + a\mathbf{e}_\mu). \quad (1.12)$$

Comparison with the definition of gauge fields in continuum suggests the identification

$$U_\mu(x) = e^{iaA_\mu(x)}. \quad (1.13)$$

The gauge links are promoted to dynamical degrees of freedom through the gauge field action

$$S_{\text{gf}}[U] = \frac{1}{2e^2} \sum_{x,\mu\nu} (1 - \text{Re}(U_{\mu\nu}(x))), \quad (1.14)$$

where we defined the plaquette operator $U_{\mu\nu}(x) = U_\mu(x)U_\nu(x+a\mathbf{e}_\mu)U_\mu^\dagger(x+a\mathbf{e}_\nu)U_\nu^\dagger(x)$. It is a product of four gauge links closing in a square (or “plaquette”), which represents a closed Wilson loop. Using Eq. (1.13), the gauge field action yields the field strength term of the continuum action (1.8) in the limit of small lattice spacings

$$S_{\text{gf}}[U] \xrightarrow{a \rightarrow 0} -\frac{1}{4e^2} F_{\mu\nu} F_{\mu\nu}. \quad (1.15)$$

Hamiltonian formulation of gauge theories

To quantize the gauge theory outlined in the previous section, one can evaluate a path integral analogous to Eq. (1.1) with the action of the lattice gauge theory $S[\psi^\dagger, \psi, U] = S_{\text{gf}}[U] + S_{\text{F}}[\psi^\dagger, \psi, U]$. Throughout this thesis, we quantize the theory canonically using a Hamiltonian formulation instead. This turns out to be beneficial for their implementation in quantum simulation experiments, where typical tools and methods are often described with Hamiltonians. The Hamiltonian of the lattice gauge theory will generate the continuous time evolution for discretized gauge fields and fermions on a spatial lattice.

To obtain the Hamiltonian of the lattice gauge theory from the action one may apply the transfer matrix approach [74]. Choosing temporal-axial gauge, we use the gauge-invariance of the action to eliminate the A_0 degree of freedom, i.e., to set $U_0(x) = 1$ everywhere. By considering the change of matrix elements from one

infinitesimal time slice to the other, one finds the Kogut-Susskind Hamiltonian [75]

$$\begin{aligned} \hat{H} = & \frac{e^2}{2} \sum_{\mathbf{x},i} \hat{E}_{\mathbf{x},i}^2 - \frac{1}{2e^2 a_s^2} \sum_{\mathbf{x},ij} \left(\hat{U}_{\mathbf{x},ij} + h.c. \right) \\ & + \frac{1}{2a} \sum_{\mathbf{x},i} \left(\hat{\psi}_{\mathbf{x}}^\dagger \gamma^0 \gamma^i \hat{U}_{\mathbf{x},i} \hat{\psi}_{\mathbf{x}+\mathbf{e}_i} + h.c. \right) + m \sum_{\mathbf{x}} \hat{\psi}_{\mathbf{x}}^\dagger \gamma^0 \hat{\psi}_{\mathbf{x}}, \end{aligned} \quad (1.16)$$

where \mathbf{x} is a three dimensional index labeling the sites of the spatial lattice with spacing a_s and $h.c.$ abbreviates hermitian conjugation. $\hat{\psi}_{\mathbf{x}}^{(\dagger)}$, $\hat{U}_{\mathbf{x},i}^{(\dagger)}$, and $\hat{E}_{\mathbf{x},i}$ are quantum field operators with commutation relations

$$\{\hat{\psi}_{\mathbf{x}}, \hat{\psi}_{\mathbf{y}}^\dagger\} = \delta_{\mathbf{x}\mathbf{y}} \delta_{ij}, \quad (1.17a)$$

$$[\hat{E}_{\mathbf{x},i}, \hat{U}_{\mathbf{y},j}] = \hat{U}_{\mathbf{x},i} \delta_{\mathbf{x}\mathbf{y}} \delta_{ij}, \quad (1.17b)$$

$$[\hat{U}_{\mathbf{x},i}^\dagger, \hat{U}_{\mathbf{y},j}] = 0, \quad (1.17c)$$

where $[A, B] = AB - BA$ is the commutator and $\{A, B\} = AB + BA$ the anti-commutator, and i, j represent vector indices for gauge fields, but also the indices of spinor components which we suppressed in our notation. We defined a spatial plaquette operator $\hat{U}_{\mathbf{x},ij}$ in analogy to the plaquettes in the previous section. Although we used the gauge symmetry to eliminate the temporally oriented gauge links, there is a residual symmetry under time-independent choices of α . Such ‘‘spatial’’ gauge transformations are generated by the so-called Gauss operators

$$\hat{G}_{\mathbf{x}} = \sum_i (\hat{E}_{\mathbf{x},i} - \hat{E}_{\mathbf{x}-\mathbf{e}_i,i}) - e \hat{Q}_{\mathbf{x}}, \quad (1.18)$$

with charge operator⁵ $\hat{Q}_{\mathbf{x}} = \hat{\psi}_{\mathbf{x}}^\dagger \hat{\psi}_{\mathbf{x}}$, and they are given by

$$\hat{O} \mapsto \hat{O}' = e^{i\alpha_{\mathbf{x}} \hat{G}_{\mathbf{x}}} \hat{O} e^{-i\alpha_{\mathbf{x}} \hat{G}_{\mathbf{x}}}, \quad (1.19)$$

for field operators \hat{O} . Invariance under these transformations can be expressed as $[\hat{O}, \hat{G}_{\mathbf{x}}] = 0$, which is fulfilled by the Hamiltonian (1.16) as well as all physical observables [76]. Quantum states which are part of the physical subspace need to be invariant under such transformations, too, and thus require fulfilment of the condition $\hat{G}_{\mathbf{x}} |\psi_{\text{phys}}\rangle = 0$ for all \mathbf{x} co-ordinates⁶. This is the quantum analog of *Gauss law*, which is also known in classical electrodynamics.

1.3.3 Finite dimensional representations

To represent gauge theories with synthetic quantum systems, where one typically only has control over a finite number of degrees of freedom, we resort to finite

⁵Its explicit form depends on the fermion discretization and is different for e.g. staggered fermions.

⁶In the presence of classical external charges $Q_{\mathbf{x}}$ they acquire a global phase, i.e., $\hat{G}_{\mathbf{x}} |\psi_{\text{phys}}\rangle = Q_{\mathbf{x}}$.

dimensional representations of the gauge fields. In this section, we briefly introduce two representations - one in terms of spin variables (quantum link models), and a second where gauge link operators are represented by rescaled bosonic creation/annihilation operators. Both will be used to represent gauge theories in one- and two-dimensional settings in later chapters.

The operator algebra introduced in Eq. (1.17) spans an infinite dimensional Hilbert space on each link. This can be understood from the fact that gauge link operators \hat{U}/\hat{U}^\dagger act as raising/lowering operators on electric field eigenstates with $\hat{E}|E\rangle = E|E\rangle$ (illustrated here for a single gauge link). Using the commutation relations (1.17), one finds

$$\hat{E}(\hat{U}|E\rangle) = \hat{U}(\hat{E} + 1)|E\rangle = (E + 1)(\hat{U}|E\rangle) \rightarrow |E + 1\rangle = \hat{U}|E\rangle. \quad (1.20)$$

As a consequence, the gauge link operators indeed generate an infinite set of (orthonormal) basis states, such that the single-site Hilbert space is given by

$$\mathcal{H} = \text{span}\{|E\rangle | E \in \mathbf{Z}\}, \quad (1.21)$$

where \mathbf{Z} denotes the set of integer numbers.

Quantum link model (QLM)

To reduce the size of the Hilbert space, we approximate the algebra of the QED gauge fields with an algebra of spin S . Here, S is a free parameter which controls the truncation of the Hilbert space dimension and the infinite-dimensional gauge field algebra is recovered in the limit $S \rightarrow \infty$. However, it is important to note that gauge symmetry is manifest at any value of S , yet, the physics may in general be different from the phenomena known from QED.

To formulate a QLM we employ the replacements

$$\hat{E} \rightarrow \hat{S}^z, \quad (1.22a)$$

$$\hat{U} \rightarrow \frac{\hat{S}^+}{\sqrt{S(S+1)}}, \quad (1.22b)$$

$$\hat{U}^\dagger \rightarrow \frac{\hat{S}^-}{\sqrt{S(S+1)}}, \quad (1.22c)$$

where $\hat{S}^\pm = \hat{S}^x \pm i\hat{S}^y$, and the spin operators fulfill commutation relations $[\hat{S}^i, \hat{S}^j] = \epsilon_{ijk}\hat{S}^k$, with $i, j, k \in \{x, y, z\}$ and ϵ being the anti-symmetric Levi-Civita tensor. The

commutation relations of the gauge fields are thus replaced by

$$\left[\hat{S}^z, \frac{\hat{S}^\pm}{\sqrt{S(S+1)}} \right] = \pm \frac{\hat{S}^\pm}{\sqrt{S(S+1)}} \quad (1.23a)$$

$$\left[\frac{\hat{S}^-}{\sqrt{S(S+1)}}, \frac{\hat{S}^+}{\sqrt{S(S+1)}} \right] = \frac{2\hat{S}^z}{S(S+1)}. \quad (1.23b)$$

The first relation (1.23a) ensures gauge-invariance under gauge transformations generated by the QLM Gauss operators

$$\hat{G}_{\mathbf{x}} = \sum_i (\hat{S}_{\mathbf{x}}^z - \hat{S}_{\mathbf{x}-\mathbf{e}_i}^z) - \hat{Q}_{\mathbf{x}}. \quad (1.24)$$

The second relation (1.23b), however, differs from the corresponding relation in QED (see Eq. (1.17)) - while gauge link operators are unitary in QED, corresponding operators in QLMs are not. In general, this discrepancy leads to observable differences between both theories, however, for bounded fluctuations of \hat{S}^z one expects convergence to QED for $S \rightarrow \infty$, as for instance shown in Refs. [77, 78] for dynamical phenomena and Ref. [79] for equilibrium properties.

QLMs may in turn be expressed with bosonic operators using the Schwinger boson representation, i.e., for a set of two bosonic modes $\hat{a}^{(\dagger)}$ and $\hat{b}^{(\dagger)}$ one has the identities

$$\hat{S}^x = \frac{\hat{a}^\dagger \hat{b} + \hat{b}^\dagger \hat{a}}{2}, \quad (1.25a)$$

$$\hat{S}^y = \frac{\hat{a}^\dagger \hat{b} - \hat{b}^\dagger \hat{a}}{2i}, \quad (1.25b)$$

$$\hat{S}^z = \frac{\hat{a}^\dagger \hat{a} - \hat{b}^\dagger \hat{b}}{2} \quad (1.25c)$$

where $[\hat{a}, \hat{a}^\dagger] = [\hat{b}, \hat{b}^\dagger] = 1$. Here, the parameter S is given by the combined atom number $\hat{a}^\dagger \hat{a} + \hat{b}^\dagger \hat{b} = 2S$, with physical states being in corresponding atom number eigenstates.

The representation of gauge fields in terms of QLMs will be employed for the case of $S = 1/2$ in Chapter 2.

Bosonic representation

In this section we turn to a different strategy of representing gauge fields, see also previous works [31, 34, 80]. For each link, we use a single bosonic mode with

creation and annihilation operators \hat{a}^\dagger and \hat{a} , and replace gauge field operators with

$$\hat{U} \rightarrow \frac{\hat{a}^\dagger}{\sqrt{\bar{n}}}, \quad (1.26a)$$

$$\hat{U}^\dagger \rightarrow \frac{\hat{a}}{\sqrt{\bar{n}}}, \quad (1.26b)$$

$$\hat{E} \rightarrow \hat{a}^\dagger \hat{a} - \bar{n}. \quad (1.26c)$$

This mapping of operators is in spirit similar to a Holstein-Primakoff transformation to represent a spin algebra with a single bosonic mode. The identification of link operators with bosonic creation and annihilation operators will enable the construction of spatial plaquette operators with the existing scattering interactions of Bose gases in Chapter 3. In this case, the present mapping yields an advantage over the Schwinger boson representation of QLMs, where plaquette operators would require eight-body interactions of the underlying bosons.

The commutation relations are given by

$$\left[\hat{a}^\dagger \hat{a} - \bar{n}, \frac{\hat{a}^\dagger}{\sqrt{\bar{n}}} \right] = \frac{\hat{a}^\dagger}{\sqrt{\bar{n}}}, \quad (1.27a)$$

$$\left[\frac{\hat{a}}{\sqrt{\bar{n}}}, \frac{\hat{a}^\dagger}{\sqrt{\bar{n}}} \right] = \frac{1}{\bar{n}}, \quad (1.27b)$$

where we used the bosonic commutation relation $[\hat{a}, \hat{a}^\dagger] = 1$. Similar to the previously discussed QLMs, the first commutation relation, and thus the transformation behavior of operators under gauge transformations generated by Gauss operators

$$\hat{G}_{\mathbf{x}} = \sum_i (\hat{n}_{\mathbf{x}} - \hat{n}_{\mathbf{x}-\mathbf{e}_i}) - \hat{Q}_{\mathbf{x}}, \quad (1.28)$$

is preserved. However, the second relation is again altered compared to the QED case, due to the creation and annihilation operators not being unitary. For small number fluctuations around a background number \bar{n} , the approach to QED is approximated in a number-phase representation of the operators

$$\frac{\hat{a}}{\sqrt{\bar{n}}} = \frac{\sqrt{\hat{n}} e^{i\hat{\phi}}}{\sqrt{\bar{n}}} \rightarrow e^{i\hat{\phi}} = \hat{U}^\dagger, \quad (1.29a)$$

$$\frac{\hat{a}^\dagger}{\sqrt{\bar{n}}} = \frac{\sqrt{\hat{n}} e^{-i\hat{\phi}}}{\sqrt{\bar{n}}} \rightarrow e^{-i\hat{\phi}} = \hat{U}, \quad (1.29b)$$

where $[\hat{n}, \hat{\phi}] = -i$. In Chapter 3 we explore the relation of such a representation with QED for equilibrium and non-equilibrium aspects of the gauge fields.

1.3.4 Ultra-cold atoms and quantum simulation

In recent years, quantum simulation has become a powerful tool to investigate fundamental questions for quantum systems. This involves phenomena both in and

out of thermal equilibrium, and examples range from equilibrium quantum phase transitions [66] to the complex dynamics of large-scale quantum systems [81, 82]. Examples include the thermalization process of isolated quantum systems [67, 83], quantum many-body scars [55, 84–86], many-body localization [87], or universal dynamics [88–90].

A strong motivation for quantum simulation experiments is the numerical sign problem [19]. It prevents the efficient simulation of certain classes of problems in quantum field theory, such as real-time dynamics, or equilibrium properties of systems including fermions with a non-zero chemical potential [19]. In both cases, the problem originates from strongly oscillating factors inside the path integral, see Eq. (1.1). Quantum simulators offer the promising prospect of circumventing the sign problem to yield a “quantum advantage” over classical computing techniques [91]. The idea is to realize a resource system with microscopic interactions described by $\hat{H}_{\text{resource}}$ to simulate a target system \hat{H}_{target} . We hence require

$$\hat{H}_{\text{resource}} \hat{=} \hat{H}_{\text{target}}, \quad (1.30)$$

where $\hat{=}$ refers to the equivalence in terms of relevant operators, i.e., for macroscopic scales. One typically distinguishes *analog* quantum simulation schemes from *digital* simulations or *quantum computations*. Both schemes are illustrated in Fig. 1.1.

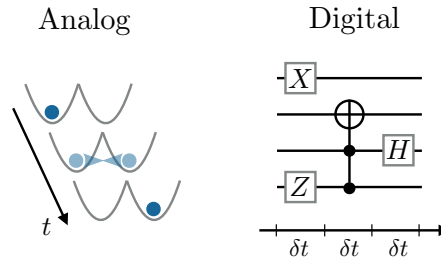


FIGURE 1.1: Analog vs. digital quantum simulations: A prominent difference between analog and digital quantum simulation concerns *time*: Analog simulators realize a continuous time evolution of quantum systems. Conversely, digital quantum computations use a stroboscopic, discrete sequence of individual operations.

Quantum simulation of large systems described by QFT require very precise control over the synthetic quantum systems in question. They need to be sufficiently cold as well as isolated from the environment to observe the many-body quantum dynamics. It is important to thoroughly realize the symmetries of the target theory and closely monitor their potential violations, since even small relevant microscopic perturbations might dominate the system’s large-scale behavior. The central idea for high-energy physics applications is then to find efficient mappings between high-energy target theories, such as gauge theories, and synthetic quantum systems in the laboratory to realize the associated constraints implied by gauge symmetry.

Ultra-cold atoms as a quantum field theory

We introduce the quantum field theory description of ultra-cold atoms at the example of a *Bose gas*. We consider the Hamiltonian

$$\hat{H} = \int_{\mathbf{x}} \left[\hat{\psi}_{\mathbf{x}}^{\dagger} \left(-\frac{\nabla^2}{2m} - \mu + V(\mathbf{x}) \right) \hat{\psi}_{\mathbf{x}} + g \hat{\psi}_{\mathbf{x}}^{\dagger} \hat{\psi}_{\mathbf{x}}^{\dagger} \hat{\psi}_{\mathbf{x}} \hat{\psi}_{\mathbf{x}} \right], \quad (1.31)$$

with atomic mass m , chemical potential μ , potential $V(\mathbf{x})$ and interaction strength g . Here, $\hat{\psi}_{\mathbf{x}}$ represents a bosonic field operator, at spatial position \mathbf{x} , which fulfills canonical commutation relations $[\hat{\psi}_{\mathbf{x}}, \hat{\psi}_{\mathbf{y}}^{\dagger}] = \delta_{\mathbf{x}\mathbf{y}}$. The quantum fields $\hat{\psi}^{\dagger}$ ($\hat{\psi}$) are the creation (annihilation) operators of atomic field excitations, where the total number of atoms is set by the operator $\hat{N}_{\text{tot.}} = \int_{\mathbf{x}} \hat{\psi}_{\mathbf{x}}^{\dagger} \hat{\psi}_{\mathbf{x}}$. $V(\mathbf{x})$ is the spatial potential seen by the individual atoms. For instance, this could be an optical potential created by detuned laser beams, or the gravitational potential.

The Bose gas is an example of a low-energy effective theory⁷ - while in principle there is additional structure underlying the composition of atoms, their long-distance properties are well-described by this scalar non-relativistic field theory. At leading order, the resulting contact interaction is given by a four-vertex with coupling constant g - the *s-wave scattering constant*. Microscopically, the scattering constant quantifies the rate of two-particle scattering events, which may individually be computed by solving Schrödinger's equation for single atoms scattering off an inter-atomic potential in the long-distance limit. It is given by $g = 4\pi a_{s\text{-wave}}/m$, where $a_{s\text{-wave}}$ is the scattering length which depends on the details of the inter-atomic potential. We will frequently consider such Bose gases throughout this thesis. In Chapter 4 we compute the dynamics of Bose gases and their generalization to more field components or *species* with an equal-time formulation of the effective action. Furthermore, we consider Bose gases in Chapters 2 and 3 to construct and investigate cold-atom gauge theories. To realize the discrete spatial structure of lattice gauge theories, the Bose gases will be trapped in periodic *optical lattices*, which we explain next.

Optical lattice

An elegant way of realizing the aforementioned lattice field theories in quantum simulations is by loading ultra-cold atoms into optical lattices [92]. The idea is to trap the atoms in the evenly spaced potential minima, where they realize the local lattice degrees of freedom of the target theory.

To realize an optical lattice, one uses standing light waves to create a sinusoidal single-particle potential $V(\mathbf{x})$. In the tight-binding limit, the atoms will localize at the minima of the optical potential to form the lattice degrees of freedom. We may

⁷Actually, the previously considered theories, QED and $\lambda\phi^4$, are low-energy effective theories as well, since they have a Landau pole and are therefore not renormalizable.

expand the field operator as

$$\hat{\psi}_{\mathbf{x}} = \sum_{\mathbf{n}} w_{\mathbf{n}}(\mathbf{x}) \hat{b}_{\mathbf{n}}, \quad (1.32)$$

where $w_{\mathbf{n}}(\mathbf{x})$ are *Wannier functions* localized around the minima at positions $\mathbf{x}_0 = \mathbf{n}a_s$, and we restrict ourselves to the lowest band. For the example of a one-dimensional lattice, we consider the potential

$$V(\mathbf{x}) = V_0 \sin^2(k_L z) e^{-\alpha_{\perp}(x^2+y^2)}. \quad (1.33)$$

Here, $k_L = 2\pi/\lambda$ is the wave vector of the standing lattice wave with wavelength λ , as for instance created by two counter-propagating laser beams. The perpendicular confinement of the atoms in the xy -plane α_{\perp} and the lattice depth V_0 are set by beam waist and intensity. For deep lattices, the atoms experience an approximately harmonic potential resulting in Wannier functions with approximate Gaussian envelope⁸. Atoms on different sites are coupled by quantum tunneling whenever wave functions transmit the potential barriers of the lattice lasers. The overlap reduces exponentially with distance and lattice depth such that we only consider tunneling between nearest neighbors.

Denoting the position index of the one-dimensional lattice's minima by n , we obtain the effective *Hubbard* Hamiltonian

$$\hat{H} = \sum_n \left(J(\hat{b}_n^{\dagger} \hat{b}_{n+1} + h.c.) - \tilde{\mu} \hat{b}_n^{\dagger} \hat{b}_n + \frac{U}{2} \hat{b}_n^{\dagger} \hat{b}_n^{\dagger} \hat{b}_n \hat{b}_n \right), \quad (1.34)$$

with tunneling rate J , lattice chemical potential $\tilde{\mu}$ and on-site energy U . The interaction constants emerge from the underlying microscopic couplings (see Eq. (1.31)) in combination with overlap integrals of wave functions

$$J \approx \int_{\mathbf{x}} w_n^*(x) \Phi^*(y) \Phi^*(z) \left(-\frac{\nabla^2}{2m} - \mu + V(\mathbf{x}) \right) w_{n+1}(x) \Phi(y) \Phi(z), \quad (1.35a)$$

$$\tilde{\mu} \approx \int_{\mathbf{x}} w_n^*(x) \Phi^*(y) \Phi^*(z) \left(-\frac{\nabla^2}{2m} - \mu + V(\mathbf{x}) \right) w_n(x) \Phi(y) \Phi(z), \quad (1.35b)$$

$$U \approx g \int_{\mathbf{x}} |w_n(x) \Phi(y) \Phi(z)|^4, \quad (1.35c)$$

where we separated the wave functions for the different spatial directions as $\Psi(\mathbf{x}) = w_n(x) \Phi(y) \Phi(z)$. As we show for two examples in the upcoming chapters, such optical lattices can be used to realize lattice gauge theories with ultra-cold Bose gases.

⁸The details of the spatial shape of the wave function are important when calculating overlaps.

Chapter 2

Large-scale quantum simulation of a U(1) gauge theory in 1D

Parts of this chapter have previously been published in the following articles:

- B. Yang, H. Sun, R. Ott, H.-Y. Wang, T. V. Zache, J. C. Halimeh, Z.-S. Yuan, P. Hauke, and J.-W. Pan, “Observation of gauge invariance in a 71-site bose–hubbard quantum simulator”, *Nature* **587**, 392–396 (2020), see [1].

In collaboration with the co-authors, I developed the theoretical framework, performed numerical calculations and compared them with experimental data. Furthermore, I significantly contributed to the presentation of the results in the main text and figures.

- Z.-Y. Zhou, G.-X. Su, J. C. Halimeh, R. Ott, H. Sun, P. Hauke, B. Yang, Z.-S. Yuan, J. Berges, and J.-W. Pan, “Thermalization dynamics of a gauge theory on a quantum simulator”, arXiv preprint arXiv:2107.13563 (2021), see [4], submitted to *Science*.

In collaboration with the co-authors, I developed the theoretical framework, performed numerical calculations and compared them with experimental data. Furthermore, I significantly contributed to the presentation of the results in the main text and figures.

- J. C. Halimeh, R. Ott, I. P. McCulloch, B. Yang, and P. Hauke, “Robustness of gauge-invariant dynamics against defects in ultracold-atom gauge theories”, *Physical Review Research* **2**, 033361 (2020), see [2].

I contributed to the development of the theoretical concept, the interpretation of numerical results, and their presentation in main text and figures.

Large parts of the text as well as figures are taken from these publications, where the experimental results presented in this chapter have been obtained by the group of Zhen-Sheng Yuan and Jian-Wei Pan. Specifically, Section 2.2 and 2.3 are based on Refs. [1, 4], Sections 2.4.1-2.4.2 on Ref. [1], Section 2.4.3 on Ref. [2], and Section 2.5 is taken from Ref. [4]. Section 2.6 summarizes the contents of this chapter and relies on all references [1, 2, 4]. These references also apply to the corresponding appendices.

2.1 Overview

Recent years have seen great progress in the engineering of gauge-invariant synthetic quantum systems, where successful realizations are based on ultra-cold atoms [52–54], trapped ions [48, 51, 56] or superconducting qubits [57]. As outlined in the previous Chapter 1, crucial challenges toward realistic applications in high-energy physics include the development of faithful strategies to realize the many constraints imposed by the local symmetry. The scaling-up of these strategies in macroscopic quantum systems poses a major challenge for current setups.

In this chapter, we demonstrate the realization of a lattice gauge theory in a large-scale quantum simulator through a scalable implementation scheme based on ultra-cold neutral atoms in optical lattices. It employs the local potentials from a spatial super-structure of the lattice to enforce the relevant gauge constraints. We subsequently probe the gauge theory experimentally for system sizes of up to 71 sites, where we focus on two complementary scenarios: The near-equilibrium evolution across a quantum phase transition, and the non-equilibrium thermalization dynamics starting from highly excited initial states. Our results demonstrate the controlled operation of the quantum simulator, even in the strongly correlated regime close to a phase transition as well as during the complex far-from-equilibrium dynamics of the gauge theory.

2.2 Model and implementation with ultra-cold atoms

In this section, we present the scalable scheme to implement the symmetry constraint in detail. Our proposal for the quantum simulator builds on defect-free arrays of ultra-cold atoms in an optical lattice. The constraints are realized by a combination of a suitable alternation of the lattice structure (“super-lattice”) and repulsive interactions between the atoms, which allows us to suppress unwanted processes. The resulting effective theory describes a lattice gauge theory coupling charged matter with spin-1/2 quantum-link gauge fields.

2.2.1 $U(1)$ lattice gauge theory

Our target theory is a $U(1)$ lattice gauge theory on a 1D spatial lattice, described by the Hamiltonian

$$\hat{H} = \sum_{\ell} \left[\frac{\kappa}{2} \left(\hat{\psi}_{\ell} \hat{S}_{\ell, \ell+1}^{+} \hat{\psi}_{\ell+1} - h.c. \right) + m \hat{\psi}_{\ell}^{\dagger} \hat{\psi}_{\ell} \right]. \quad (2.1)$$

It is motivated by the QED Hamiltonian (see Chapter 1) in one spatial dimension, often referred to as the *Schwinger model* [93]. The theory describes the gauge-invariant interaction of relativistic fermionic quantum fields on sites ℓ and gauge fields on links $\ell, \ell+1$ in-between, reflecting the typical alternating structure of lattice gauge theories. In this discrete “quantum link” representation [94], gauge fields are represented by

spin-1/2 operators on the links connecting neighboring lattice sites, where electric fields and link operators are identified as $\hat{E}_{\ell,\ell+1} \rightarrow (-1)^{\ell+1} \hat{S}_{\ell,\ell+1}^z$ and $\hat{U}_{\ell,\ell+1} \rightarrow \hat{S}_{\ell,\ell+1}^+$ for ℓ even, and conversely $\hat{U}_{\ell,\ell+1} \rightarrow \hat{S}_{\ell,\ell+1}^-$ for ℓ odd. For spin-1/2, the electric fields are restricted to two eigenvalues, such that the usual electric field energy \hat{E}^2 is a constant which can be dropped from the Hamiltonian.

The fermionic matter is represented by the field operator $\hat{\psi}_\ell$, where we employ the staggered fermion formulation to discretize the relativistic Dirac spinors [73]. The central idea is to distribute its two components on even and odd sub-lattices which are then associated with even and odd indices ℓ . Excitations of the field represent either particles with positive charge (even sites) or anti-particles with negative charge (odd sites), as summarized in the alternating charge operator $\hat{Q}_\ell = (-1)^\ell \hat{\psi}_\ell^\dagger \hat{\psi}_\ell$ and shown in Fig. 2.1. We furthermore employ a particle-hole transformation to express the Hamiltonian in a ‘‘charge basis’’. Here, excitations of the fermion fields on matter sites relate to the presence of electric charges as illustrated in Fig. 2.2. To this end, we have replaced

$$\hat{\psi}_{2l}^\dagger \hat{\psi}_{2l} \rightarrow 1 - \hat{\psi}_{2l}^\dagger \hat{\psi}_{2l}, \quad (2.2a)$$

$$\hat{\psi}_{2l} \rightarrow \hat{\psi}_{2l}^\dagger, \quad (2.2b)$$

$$\hat{S}_{2l,2l+1}^z \rightarrow (-1) \hat{S}_{2l,2l+1}^z, \quad (2.2c)$$

$$\hat{S}_{2l,2l+1}^\pm \rightarrow \hat{S}_{2l,2l+1}^\mp, \quad (2.2d)$$

for even and odd sites, respectively. This maps the QLM Hamiltonian $\hat{H} = \sum_l [\frac{\kappa}{2} (\hat{\psi}_l^\dagger \hat{S}_{l,l+1}^+ \hat{\psi}_{l+1} + h.c.) + m(-1)^l \hat{\psi}_l^\dagger \hat{\psi}_l]$ onto Eq. (2.1).

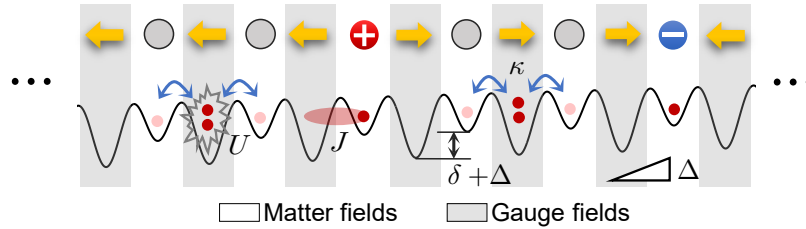


FIGURE 2.1: Quantum simulator for the gauge theory: Matter and gauge fields are represented by occupations of bosonic atoms in an optical superlattice. Here, charges are illustrated as red (positive) and blue (negative) circles and electric flux is shown as yellow arrows. On matter sites, the presence of an atom (red dot) signals a corresponding charge in the gauge theory. Figure taken from [4].

Using these transformations, the U(1) gauge transformations are generated by the Gauss operators

$$\hat{G}_\ell = \hat{S}_{\ell,\ell+1}^z + \hat{S}_{\ell-1,\ell}^z + \hat{\psi}_\ell^\dagger \hat{\psi}_\ell. \quad (2.3)$$

Gauss law requires the operators \hat{G}_ℓ to be conserved quantities for each matter site ℓ , which yields an extensive set of constraints for the quantum state $|\psi\rangle$. Specifically, we consider the subspace where $\hat{G}_\ell |\psi\rangle = 0, \forall \ell$. Ensuring adherence to this local

conservation law is the main experimental challenge, as it intrinsically constrains matter and electric fields across three neighboring lattice wells, see Fig. 2.2. Besides these *local* conservation laws, the system furthermore carries a *global* $U(1)$ symmetry which entails global charge conservation. Hence, starting from charge-neutral initial states, the system will remain neutral throughout the gauge-invariant evolution, i.e., $\sum_\ell \hat{Q}_\ell |\psi(t)\rangle = 0$.

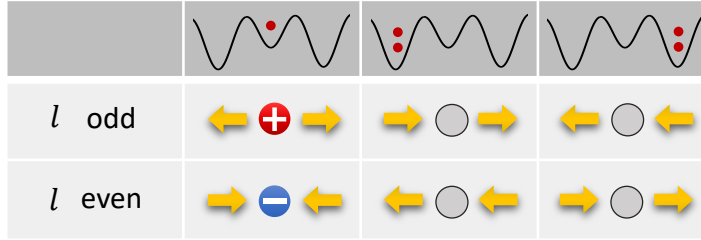


FIGURE 2.2: Gauss law: The figure shows locally gauge-invariant states fulfilling Gauss law and illustrates the state-correspondences between original gauge theory and quantum simulator. Figure taken from a revised version of [4].

2.2.2 Realization with ultra-cold atoms

To realize this gauge theory with quantum technology, we first map the Hamiltonian (2.1) to ultra-cold bosons in a 1D optical super-lattice as sketched in Fig. 2.1. Microscopically, the atoms' dynamics is governed by the Bose–Hubbard Hamiltonian (BHM)

$$\hat{H}_{\text{BHM}} = \sum_j \left[-J(\hat{b}_j^\dagger \hat{b}_{j+1} + h.c.) + \frac{U}{2} \hat{n}_j(\hat{n}_j - 1) + \varepsilon_j \hat{n}_j \right], \quad (2.4)$$

where $\hat{b}_j^\dagger, \hat{b}_j$ are atomic creation and annihilation operators, $\hat{n}_j = \hat{b}_j^\dagger \hat{b}_j$ is the atom number operator, J represents the rate of tunneling across neighboring lattice wells, and $h.c.$ denotes hermitian conjugation. The single particle energies $\varepsilon_j = (-1)^j \delta/2 + j\Delta$ contain the staggering potential δ , as formed by the super-lattice structure, and a linear tilt $\Delta = 57\text{Hz}$ from the gravitational potential, which we use to suppress unwanted tunneling processes across two or more lattice sites. The characteristic super-lattice structure allows us to represent both matter and gauge field degrees of freedom by suitable site occupations of atoms. Choosing $\delta \gg J$ and an approximately resonant on-site repulsion potential $U \sim 2\delta$, we restrict the system to the number states $|0\rangle, |2\rangle$ on odd wells (gauge links) and $|0\rangle, |1\rangle$ on even wells (matter sites). As a consequence, our system is effectively constrained to an (excited) sub-manifold of the global Hilbert space, where the gauge symmetry is realized.

Within this manifold, the dynamics is described by the effective Hamiltonian

$$\hat{H}_{\text{eff}} = \sum_{j \in e} \left[\frac{\kappa}{2\sqrt{2}} (\hat{b}_j^\dagger \hat{b}_{j+1}^2 \hat{b}_{j+2}^\dagger + h.c.) + m \hat{b}_j^\dagger \hat{b}_j \right], \quad (2.5)$$

to order $\mathcal{O}(J^2/U)$, where $j \in e$ runs over even lattice wells. At this order, a pair of atoms on neighboring sites has mass $2m = 2\delta - U$, which is set by the energy balance of the gauge-invariant basis states. The corresponding gauge-invariant interaction process is realized with strength

$$\kappa = 2\sqrt{2}J^2 \left[\frac{\delta}{\delta^2 - \Delta^2} + \frac{U - \delta}{(U - \delta)^2 - \Delta^2} \right]. \quad (2.6)$$

Close to resonance, i.e., $U \approx 2\delta$, and using $\Delta \ll \delta, U$, we have $\kappa \approx 8\sqrt{2}J^2/U$. To obtain the effective bosonic Hamiltonian, we used an approximate Schrieffer-Wolff transformation to second order in the tunneling coupling, as outlined in the appendix 2.A. One approximately block-diagonalizes the Hamiltonian by use of a unitary transformation $\hat{U} = \exp(i\hat{T})$, with a hermitian generator $\hat{T} = \mathcal{O}(J/U)$. While this transformation generates the effective Hamiltonian up to corrections of order $\mathcal{O}(J^3/U^2)$, it also transforms the initial states and observables. This second aspect, which is expected to influence the interpretation of our measurements at order $\mathcal{O}(J^2/U^2)$, is not considered in this thesis - gauge invariance is considered with respect to the bare Gauss operators. A technique to improve measurements in such perturbative realizations of many-body systems has recently been proposed in Ref. [95].

To identify the effective Hamiltonian (2.5) with the original gauge theory we replace the operators on odd wells (gauge links) as

$$\hat{b}_{j \in o}^2 \rightarrow \sqrt{2} \hat{S}_{\ell, \ell+1}^-, \quad (2.7a)$$

$$\hat{n}_{j \in o} \rightarrow 2\hat{S}_{\ell, \ell+1}^z + 1. \quad (2.7b)$$

Additionally, using a Jordan–Wigner transformation, we map the boson operators on even lattice wells, $2\ell = j \in e$, to the fermion field operators $\hat{\psi}_\ell$ fulfilling the anti-commutator relations $\{\hat{\psi}_\ell^\dagger, \hat{\psi}_{\ell'}\} = \delta_{\ell\ell'}$,

$$\hat{b}_{j \in e}^{(\dagger)} \rightarrow (-1)^l e^{(-i\pi \sum_{\ell' < \ell} \hat{\psi}_{\ell'}^\dagger \hat{\psi}_{\ell'})} \hat{\psi}_\ell^{(\dagger)}, \quad (2.8a)$$

$$\hat{n}_{j \in e} \rightarrow \hat{\psi}_\ell^\dagger \hat{\psi}_\ell, \quad (2.8b)$$

which implies the replacement $\hat{b}_{2\ell}(\hat{b}_{2\ell+1}^\dagger)^2 \hat{b}_{2\ell+2} \rightarrow \sqrt{2} \hat{\psi}_\ell \hat{S}_{\ell, \ell+1}^+ \hat{\psi}_{\ell+1}$ in the Hamiltonian and for the considered subspace of the global Hilbert space. These mappings yield the Hamiltonian of the lattice gauge theory, Eq. (2.1).

2.3 Experimental set-up

In the experiment, we consider a system of approximately 10^5 ultra-cold rubidium atoms (^{87}Rb) [96]. Using laser light, the atoms are confined to a pancake-shaped cloud aligned with the two-dimensional x - y plane. Here, transversal degrees of freedom are effectively frozen by a steep potential along the perpendicular z -axis, such that the system is quasi two-dimensional. Additional laser beams create an optical lattice in the x - y plane to form a Mott insulator with near-unity filling (99.2%), across approximately 10,000 lattice sites, see Fig. 2.3a. To quantum simulate the one-dimensional gauge theory the system is split into an array of one-dimensional chains, such that an average over several realizations can be taken in a single experimental cycle. For the evaluation of observables we choose a region of interest of 36 chains with a length of 71 lattice wells each.

A second laser beam creates the optical super-lattice which allows us to differentiate between alternating deep and shallow lattice wells. This structure is the basis for our implementation scheme - it reflects the characteristic structure of lattice gauge theories, where we distinguish between matter sites and gauge links. The optical potential along the one-dimensional lattice is given by

$$V(x) = V_1 \cos^2(k_s x) + V_2 \cos^2\left(\frac{k_s x}{2} + \phi\right), \quad (2.9)$$

where $V_{1/2}$ are the lattice depths, $k_s = 2\pi/\lambda_s$ is the wave-number of the “short” lattice laser with wavelength $\lambda_s = 767\text{nm}$, and ϕ is a relative phase. Two configurations of the lattice phase are used: at $\phi = \pi/4$, one has symmetric tunneling rates of atoms in both directions, at $\phi = 0$ the atoms are isolated into double wells for state preparation and read-out. The starting point for both following experiments is the staggered initial state where odd lattice wells are empty. To achieve this, the corresponding atoms are removed by first transforming them to another hyperfine state and subsequently exciting them from the lattice using resonant laser light, see Fig. 2.3b. The remaining atoms on the even sites of the 1D chains correspond to an overall charge neutral configuration in the target gauge theory. They form its ground state, Eq. (2.1), at $m \rightarrow -\infty$ in the $\hat{G}_\ell |\psi\rangle = 0$ sub-sector.

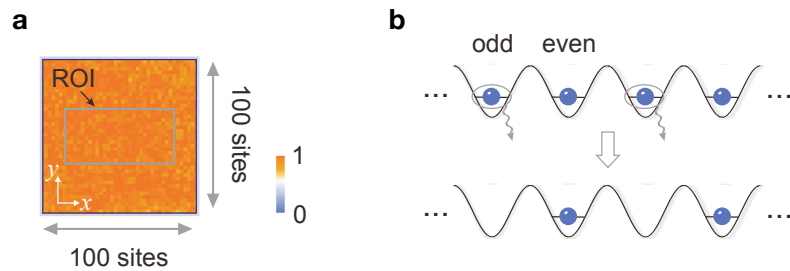


FIGURE 2.3: Initial state preparation: (a) The experiment starts with a near-unity filling Mott insulator. (b) The staggered initial state is prepared by removing the atoms on odd wells corresponding to gauge links. Figure adapted from [1].

2.4 Gauge-invariance and quantum phase transition

In this section, we explore gauge-invariance in the Bose-Hubbard quantum simulator, which we apply to study a near-equilibrium evolution of the gauge theory by adiabatically “ramping” the system couplings. We consider our cold-atom gauge theory in two different phases: one phase where matter sites are filled with excitations of charge pairs, and a second phase where the charges become energetically costly and annihilate. The two phases are separated by a quantum critical point (QCP), where the system exhibits a second-order phase transition. At a quantum critical point energy gaps close and the system is subject to strong fluctuations. It is thus especially interesting to study the gauge symmetry at this point. By tuning the mass m , we drive the system across this quantum phase transition from the “charge-dominated” phase to a second, “vacuum” phase, which is characterized by the spontaneous breaking of charge and parity (C/P) symmetries [93, 97].

2.4.1 Many-body dynamics across a phase transition

We start the evolution in the initial staggered state, i.e., the instantaneous ground state for $m \rightarrow -\infty$, see Fig. 2.4a. In this scenario, the system prefers a full occupation of matter sites, corresponding to a mean density of $\langle \hat{n}_{\text{matter}} \rangle = \sum_{j \in m} \langle \hat{n}_j \rangle / L_m = 1$, where L_m is the number of even “matter site” lattice wells ($j \in m$). To initiate the quasi-static evolution of the many-body system, we slowly adjust the system parameters to reach the vacuum phase corresponding to the gauge-invariant ground state at $m \rightarrow \infty$. If controlled precisely, the system approximately follows the instantaneous ground state of the model during its evolution, which allows us to access the phase transition. For the successful quantum simulation, we expect the annihilation of the charged matter occupations on even lattice wells and the emergence of ordered domains with electric field pointing either to the left, or to the right. The domains are a consequence of the spontaneous breaking of \mathbb{Z}_2 symmetries in the many-body system: While the QLM Hamiltonian Eq. (2.1) is invariant under both parity transformation (P) and charge conjugation (C) of field operators [97], the

ground state for large and positive values of m does not necessarily respect these symmetries. An example of such a domain is illustrated in Fig. 2.4b for both gauge theory and quantum simulator.

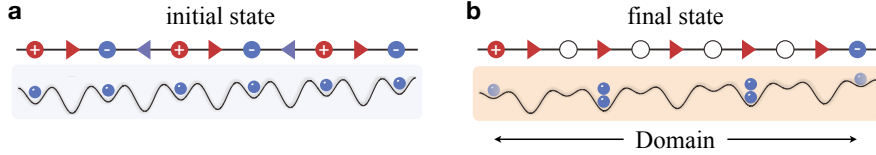


FIGURE 2.4: Schematic ground states: Starting from the staggered initial state in the charge-dominated phase (a), we expect the formation of ordered domains of homogeneous electric field configurations (b). Figure adapted from [1].

In the experiment, the evolution is initiated by tuning the super-lattice structure to slowly adjust the Hubbard parameters. Their time-dependent values are shown in Fig. 2.5(a): While the staggering strength is kept at a fixed value $\delta = 0.73(1)\text{Hz}$, the onsite interaction strength U is changed to dynamically tune the mass parameter $m = \delta - U/2$ from negative to positive values. Simultaneously, we increase the interaction strength κ in the first half of the 120ms evolution time and reduce it back to the initial value again afterwards. The details of this process have been chosen to minimize both non-adiabatic excitations, as well as undesired heating effects for long evolution times in the experiment. Throughout the experiment, we keep a linear tilt of 57Hz to suppress tunneling across two or more lattice wells.

The resulting dynamics is displayed in Fig. 2.5. It shows the system's evolution from the initial state in the charge-dominated phase toward the final vacuum state, where atoms on matter sites have combined to form doublons on the neighboring lattice wells associated with gauge links. Here, the mean matter density $\langle \hat{n}_{\text{matter}} \rangle$ acts as an order parameter to detect the transition. As the data shows, approximately 80(3)% of the atoms leave the even lattice wells during the 120ms evolution time, while simultaneously, we observe an increase of atom numbers on the neighboring gauge links. Extracting the detailed single-site counting statistics during the evolution [1] reveals that the atoms on gauge links appear in pairs (or doublons) rather than single atoms, which indicates the successful suppression of direct tunneling and the emergence of dynamics as described by the effective theory, see panel a. The dynamics results in the formation of 39(2)% such double occupancies. Due to the finite speed of the ramp, as well as experimental imperfections, the transition is, however, not complete - the system is excited from the target ground state and approximately 22(5)% of the atoms remain on even sites. In panel b we compare the experimental data with numerical simulations of gauge theory and experiment, where our real-time calculations of the unitary dynamics are based on exact diagonalization and the time-adaptive density matrix renormalization group (t -DMRG). The curves are generally in good agreement with the experimental data, but predict a slightly higher amount of formed doublons.

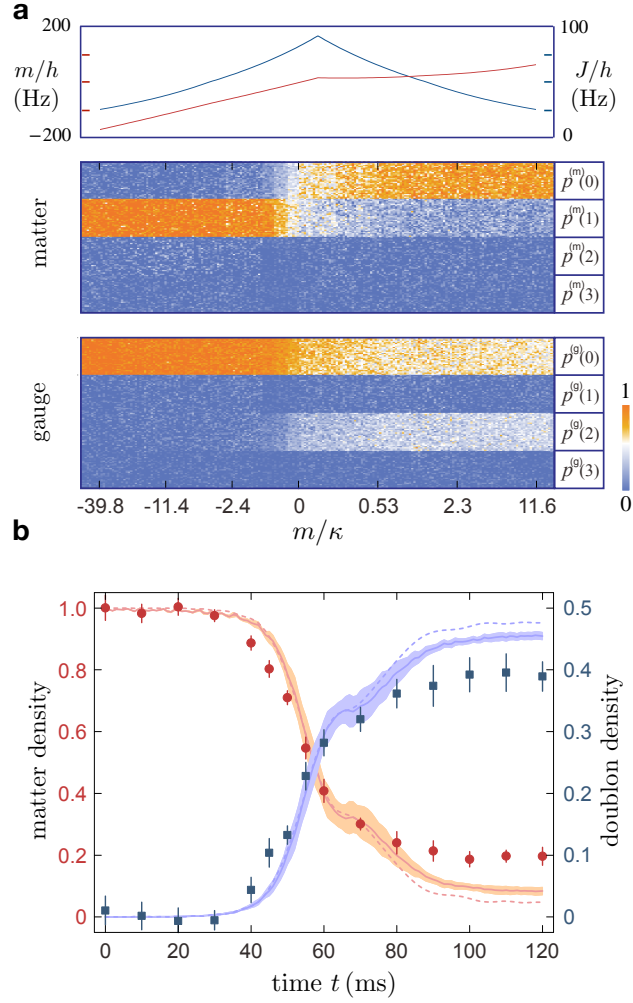


FIGURE 2.5: Time-resolved transition: (a) (Top) The system is driven with time-dependent parameters $m = \delta - U/2$ and J . *In-situ* occupation probabilities indicate the transition of single atoms from matter sites (middle panel) into gauge links (bottom panel), where they form doublons. (b) The integrated signal is compared to theoretical predictions from the time-adaptive density matrix renormalization group (t -DMRG, solid), including sampling over noisy experimental parameters. The dashed lines represent real-time calculations of the lattice gauge theory with exact diagonalization, see appendix 2.C for details. Error bars and shaded regions represent standard deviations throughout this section. “Doublon density” is defined as $p^{(g)}(2)$ averaged over all gauge links, “matter density” is given by $\langle \hat{n}_{\text{matter}} \rangle$. Figure adapted from [1].

The final state of the system may be characterized in terms of the ordered domains in the symmetry broken state. Assuming their separation with domain walls, as given here by the 22(5)% remaining atoms on the matter sites (see Fig. 2.4b), the averages size of ordered domains can be estimated as 9(2) lattice wells. To experimentally confirm the formation of domains we measure the density correlations $C(i, j) = \langle \hat{n}_i \hat{n}_j \rangle$ among the lattice wells in the final state [98–100]. As illustrated in Fig. 2.4b, the correlation functions within domains are expected to show a characteristic separation of the atoms by four lattice wells. The correlation functions may be extracted directly in momentum space by a time-of-flight measurement,

where one lets the atoms expand for a duration of 8ms. Peaks in the resulting signal indicate the formation of corresponding patterns. For instance, a bosonic Mott state with unity filling [99] corresponds to a pair of peaks at momentum positions $\pm 2\hbar k_s$, where $k_s = 2\pi/\lambda_s$ is the wave vector of the short lattice laser, with $\lambda_s/2$ being the smallest separation of neighboring atoms. As shown in Fig. 2.6, the measurements of the expanded cloud exhibit such a peak structure. To demonstrate the formation of domains, we compare the correlation signal of the final state to a corresponding measurement of the initial state. Initially, the correlation function shows peaks at positions $\pm 2\hbar k_s$ and $\pm \hbar k_s$. The second set of peaks indicate the “staggered” initial state, where the atoms are separated by two lattice sites, see Fig. 2.4a. Since the fidelity for the creation of the staggered initial states is high (99.2%), the peak widths are mainly determined by the finite spatial resolution of the absorption imaging. In the final state, we discover additional peaks at momenta $\pm \hbar k_s/2$ and $\pm 3\hbar k_s/2$. The peaks at the smallest momenta $\pm \hbar k_s/2$ indicate states with average separation of atoms by four lattice sites, which we interpret as evidence for the formation of ordered domains. To estimate the size of the domains from these measurements,

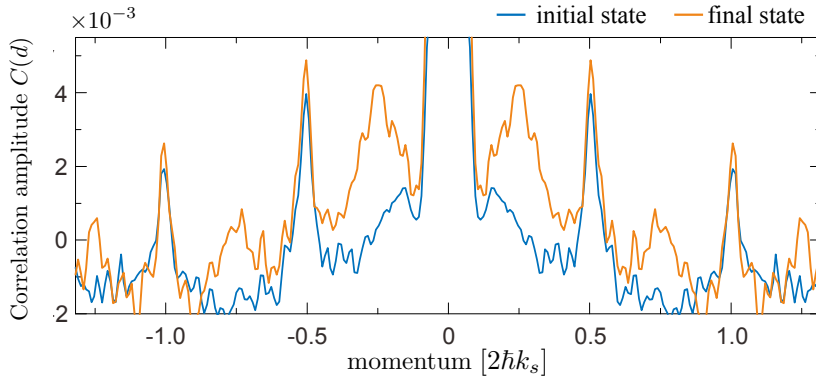


FIGURE 2.6: Density correlation: We show the correlation signals of initial and final state of the quasi-static evolution (after subtracting background). During the evolution, additional peaks at momenta $\pm 0.5\hbar k_s$ appear, indicating the emergence of domains. The data sets for initial and final state have been averaged over 523 and 1729 images, respectively. Adapted from [1].

we extract the average correlation length ξ of the final state. Specifically, we assume an ordered correlation signal which we augment by an exponential decay as $C(i, j) \propto \exp(-|i - j|/\xi)$, and estimate the width of the corresponding peak signal as follows [99, 101]. We consider the normalized connected density correlation function

$$C(d) = \frac{\int dx \langle \hat{n}(x - d/2) \hat{n}(x + d/2) \rangle}{\int dx \langle \hat{n}(x - d/2) \rangle \langle \hat{n}(x + d/2) \rangle} - 1, \quad (2.10)$$

where $\hat{n}(x)$ is the density operator at position x of the expanded cloud, and the subtraction by one removes the disconnected density correlations from the signal.

Assuming, the system is in a superposition of “domain states” we may write [101]

$$C(d) \propto \sum_{i,j} e^{im_{\text{Rb}} \frac{d}{\hbar t} (x_i - x_j)} C(i, j), \quad (2.11)$$

where m_{Rb} is the mass of the rubidium atoms, and the momenta of the atoms enter as $k_d = m_{\text{Rb}} d / \hbar t$ after the free expansion with duration $t = 8\text{ms}$, see section 2.B in this chapter’s appendix. We compare the data with a numerical evaluation of Eq. (2.11) for a system with 100 lattice wells after subtracting the finite optical resolution of the imaging technique. We obtain a correlation length of $\xi = 4.4_{-1.0}^{+2.0}$ for the final state, which exceeds the size of the gauge-invariant unit cells, and confirms the formation of ordered domains in the symmetry broken state.

2.4.2 Quantifying gauge invariance

Having established the system’s transition to ordered domains in the previous section, we quantify the local violation of Gauss law next. As sketched in Fig. 2.2, Gauss law restricts the local configurations of the atoms to three number states

$$|\psi_{1,j}\rangle = |0_{j-1}1_j0_{j+1}\rangle \quad , \quad |\psi_{2,j}\rangle = |0_{j-1}0_j2_{j+1}\rangle \quad , \quad |\psi_{3,j}\rangle = |2_{j-1}0_j0_{j+1}\rangle, \quad (2.12)$$

where the indices are centered around matter sites with j even. To access their population in the system, it is necessary to access correlated information of atom numbers of neighboring sites, unlike the approach in Fig. 2.5b, which does not give access to such quantities. We use the tunability of the super-lattice structure to isolate pairs of neighboring sites into double wells, where their occupation states may be distinguished by their oscillation frequencies. For instance, we make use of the fact that the rate of tunneling processes $|1_j0_{j+1}\rangle \rightarrow |0_j1_{j+1}\rangle$ is much higher than the frequency of super-exchange $|2_j0_{j+1}\rangle \rightarrow |0_j2_{j+1}\rangle$.

The amplitudes of the corresponding oscillation signal yield the probabilities $p_{|n_j n_{j+1}\rangle}$ and $p_{|n_{j-1} n_j\rangle}$ of finding the respective local configurations, averaged over the entire one-dimensional chain. For large systems close to the gauge-invariant limit, we may write

$$p_{|n_{j-1}1_j n_{j+1}\rangle} = p_{|1_j0_{j+1}\rangle} + p_{|0_{j-1}1_j\rangle} - p_{|0_{j-1}1_j0_{j+1}\rangle} + \text{rest}, \quad (2.13)$$

from which we may compute a lower bound for the desired probability as $p_{|0_{j-1}1_j0_{j+1}\rangle} \geq p_{|1_j0_{j+1}\rangle} + p_{|0_{j-1}1_j\rangle} - p_{|n_{j-1}1_j n_{j+1}\rangle}$ through the identification $p_{|n_{j-1}1_j n_{j+1}\rangle} = p_j^{(m)}(1)$. Similar reasoning yields a corresponding bound for the remaining occupation states $|0_{j-1}0_j2_{j+1}\rangle$ and $|2_{j-1}0_j0_{j+1}\rangle$ [1]. From these measurements, one can extract an average degree of gauge violation. To this end, we define the violation measure

$$\epsilon(t) = 1 - \langle \psi(t) | \hat{P}_\ell | \psi(t) \rangle, \quad (2.14)$$

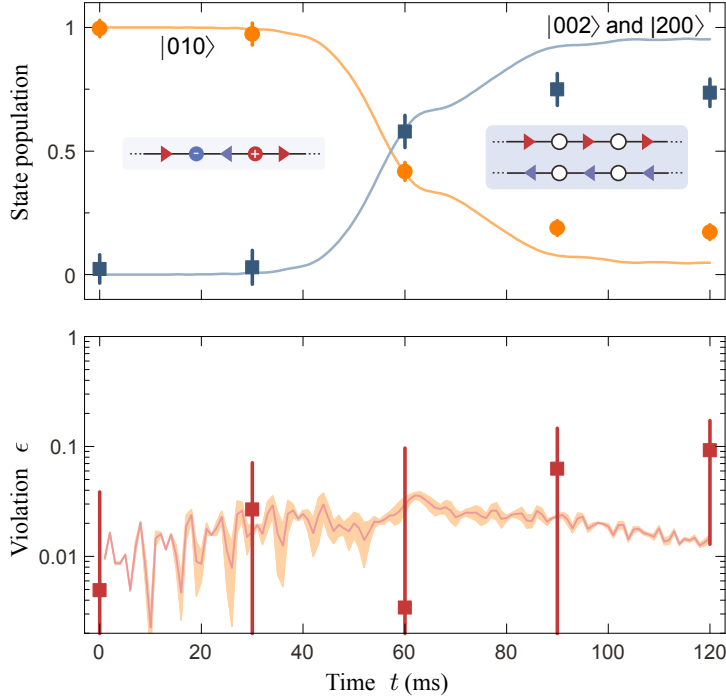


FIGURE 2.7: Local gauge invariance: (Top) During the evolution the average population of “matter states” ($|010\rangle$) reduces and the system occupies the “matter vacuum” states ($|002\rangle$ and $|200\rangle$), see insets. Solid lines are obtained from exact diagonalization of the gauge theory with 26 matter sites and periodic boundary conditions. (Bottom) The gauge violation defined by ϵ is monitored during the evolution. Experimental bounds (see main text) are in quantitative agreement with ϵ extracted from t -DMRG calculations for the isolated Bose–Hubbard system (red curve). Figure taken from [1].

where \hat{P}_ℓ projects the system state $|\psi(t)\rangle$ onto the locally gauge-invariant configurations centered around matter site ℓ as outlined above, and our measured quantities provide an upper bound for the violation measure ϵ . In Fig. 2.7, we give the experimentally obtained upper bound during the 120ms ramp evolution, and compare it to numerical real-time calculations of ϵ , finding overall good agreement. Throughout the experiment, our measure remains on the order of 10%, from which we conclude a high-level of gauge invariance for our quantum simulator.

2.4.3 Violations and imperfect state preparation

While the violation measure ϵ remains small throughout the many-body evolution, the indefinite suppression of unwanted processes is challenging. To identify the relevant violation processes, we numerically investigate the various non-gauge invariant quantum states remaining at the end of the ramp evolution next. We furthermore investigate the role of defects in the initial state preparation, finding that gauge-invariance remains approximately intact for certain classes of initial state defects where they remain localized during the ramp evolution. Others, however, spread through the system, accompanied with growth of average gauge-symmetry violation.

In the experiment, the initial Mott insulator is prepared with an approximate probability of 99.2%. The atoms are prepared via a so-called staggered-immersion cooling technique [96], where atoms are cooled by transferring entropy to constituents of the system which are subsequently removed. During this process errors may occur, which in most cases result in occupation states $|0\rangle$ or $|2\rangle$ locally, rather than the unity-filling Mott insulator state, which is the basis of the experiment. The probability for such defects can be estimated as approximately 0.4(1)% each [2]. Given the large system of 71 sites the probability of finding at least one defect is thus approximately given by $1 - (0.992)^{71} \approx 57\%$ ¹. To investigate the dynamics, we show calculations via t -DMRG for a system size of 32 lattice wells. We simulate the dynamics of the underlying Bose-Hubbard Hamiltonian (2.4) with couplings as employed in the ramp procedure, see Fig. 2.5a.

First, we consider the “clean” case without defects. Here, we expect the dominant violation processes to originate from the insufficient suppression of the direct, first-order tunneling in the effective realization of the gauge theory, and the expected violation processes are sketched for a smaller system in Fig. 2.8.

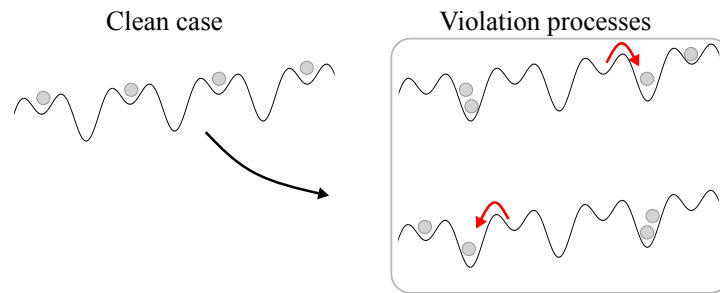


FIGURE 2.8: “Clean case” without defects: Dominant violations of gauge-symmetry are expected to originate from direct tunneling. Adapted from [2].

Secondly, we consider defects on matter sites, where we distinguish between a matter hole (occupation state $|0\rangle$, MH) and a matter impurity (occupation state $|2\rangle$, MI). These states are highly detuned when isolated and are therefore expected to remain localized. In that case the dynamics of the one-dimensional chain is approximately frozen at the defect position and it splits into two smaller subsystems. At last, we consider the case of a gauge link impurity (GI), i.e., a single-atom occupation of a gauge link. Here, we expect further violation processes from remaining higher-order processes, as shown in Fig. 2.9, where we focus on the lowest order processes which are approximately resonant.

The time evolution of the violation is shown in Fig. 2.10 for the different cases: “clean” initial state, MH and MI, as well as the GI. Here, we consider the violation

¹Note that the system is not “cut off” at the borders, i.e., no sharp boundary exists and processes outside of the ROI might still influence the dynamics. This aspect is neglected throughout this thesis.

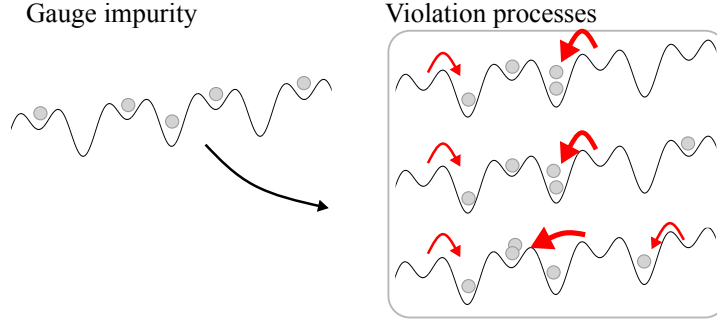


FIGURE 2.9: “Gauge impurity” defect: We sketch the higher-order processes which are expected to contribute dominantly to the spectrum of final states. Adapted from [2].

measure

$$\tilde{\epsilon}(t) = \sum_{j \in e} \frac{\epsilon_j(t) - \epsilon_j(0)}{L}, \quad (2.15)$$

where L counts the number of matter sites and $\epsilon_j(t) = 1 - \langle \psi(t) | \hat{P}_j | \psi(t) \rangle^2$ with \hat{P}_j projecting onto locally gauge-invariant states, see Fig. 2.2. While gauge symmetry is rather robust for the cases of “clean” initial state and matter defects, the gauge impurity indeed leads to enhanced violation during the second half of the evolution. We furthermore list the distribution of final state populations in Fig. 2.11, where the discussed processes can be identified. Specifically, the figure shows that the dominant final states which do not fulfill Gauss law are those sketched in Fig. 2.8 and Fig. 2.9. The analysis confirms the appearance of states from the expected underlying processes.

Specifically, the identification of gauge impurities as problematic error source helps to improve the experimental sequence, where the initial state preparation can be further developed to avoid such imperfections. For the clean case, the violation was dominated by individual direct tunneling processes, where $p^{(m)}(1)$ can already serve as an efficient measure to detect such processes. We exploit these findings to extract gauge-violation during the dynamics more efficiently compared to ϵ in the next section, where we apply the Bose-Hubbard simulator to investigate the complex thermalization dynamics of the gauge theory.

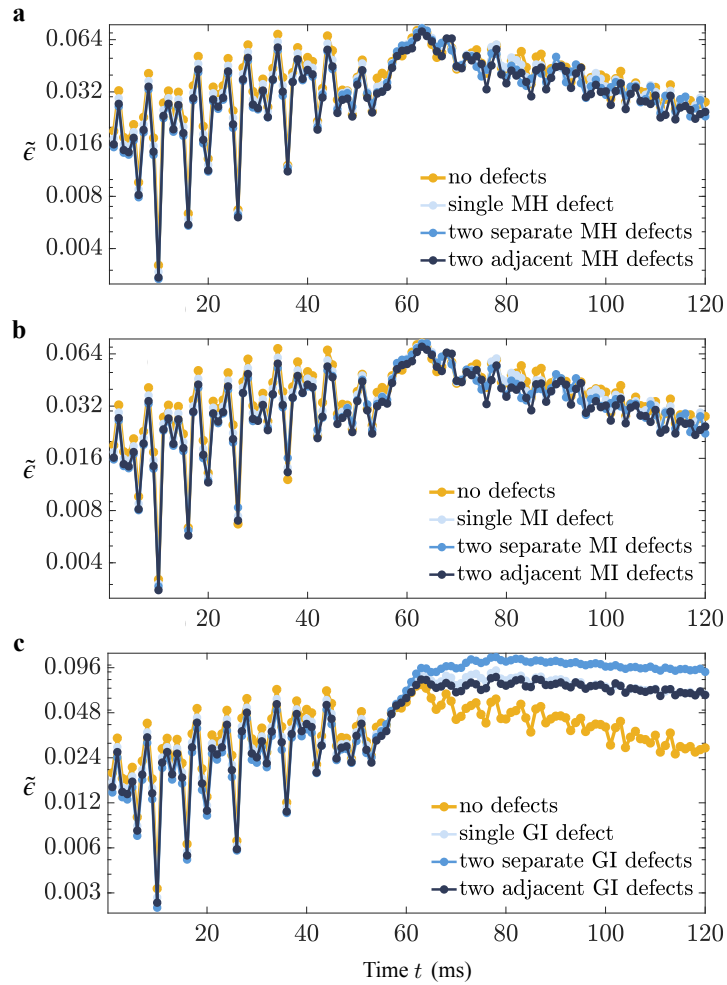


FIGURE 2.10: Effect of initial state defects: The build-up of gauge violation during the dynamics is shown in comparison with the “clean” case for various defect types: (a) matter hole (MH), (b) matter impurity (MI) and (c) the gauge link impurity (GI). Adapted from [2].

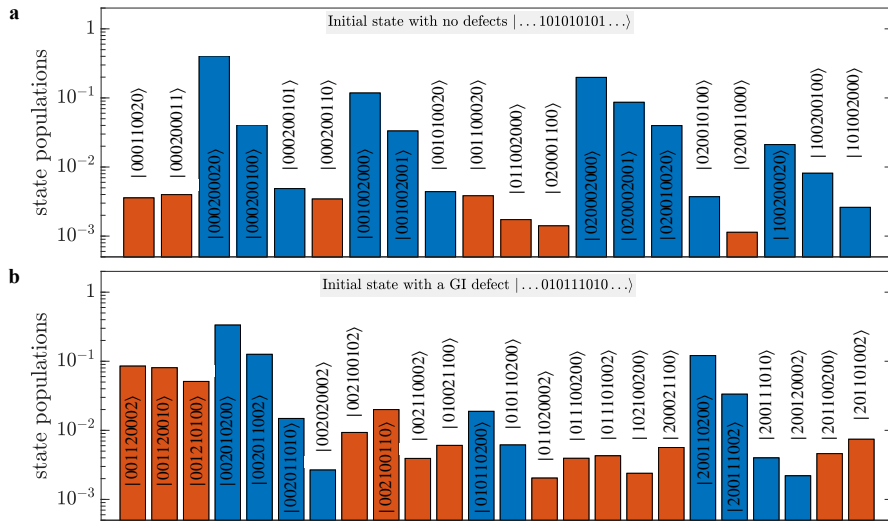


FIGURE 2.11: Final state distribution after the ramp: We show the population of states according to their configuration at the central nine wells around the center of the chain for the “clean” case (**a**) and the gauge link impurity (GI, **b**). Here, we focus on populations above a threshold of 10^{-3} (top) and 2×10^{-3} (bottom), respectively. States which lead to an increase in $\tilde{\epsilon}$ are shown in orange. Adapted from [2].

2.5 Thermalization dynamics

Having demonstrated the controlled operation of the quantum simulator near equilibrium, we turn to its many-body dynamics far from equilibrium next. Establishing the emergence of complex dynamical phenomena such as thermalization in gauge theories from first principles is an outstanding challenge in physics. While much progress on emergent phenomena has been achieved for simpler systems [67, 83], the direct connection of far-from-equilibrium behavior at early evolution times with thermalization at late times remains an outstanding task for gauge theories.

In this section, we perform quantum simulations of the far-from-equilibrium dynamics of the U(1) symmetric gauge theory and demonstrate the approach to thermal equilibrium. Exploiting the full experimental tunability of the super-lattice structure, we explore the influence of the gauge-symmetry constraints on the evolution and establish the thermalization dynamics of the U(1) gauge theory. Starting from gauge-invariant initial states far from equilibrium, we observe emergent many-body oscillations through the dynamical annihilation and creation of fermion pairs. We demonstrate an effective loss of information about the system's initial state by starting from different initial conditions with the same conserved quantities and observing relaxation toward a common steady state at longer times. The thermalization dynamics is illustrated in Fig. 2.12.

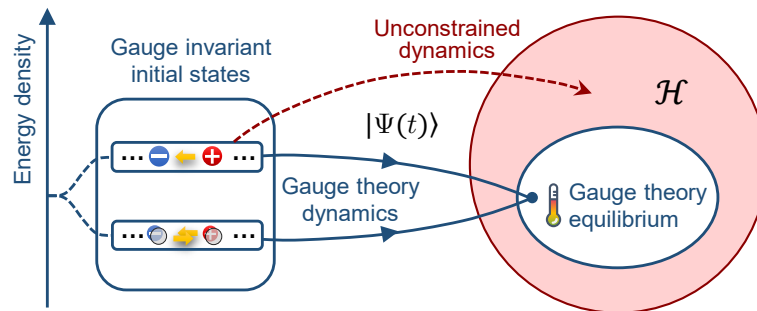


FIGURE 2.12: Schematic non-equilibrium evolution toward steady states: Under the constrained (gauge) condition, we find that different initial states with the same energy density evolve to a common thermal state of the gauge theory. Conversely, the system relaxes to different states at late times when gauge constraints are relaxed. Figure adapted from [4].

2.5.1 Non-equilibrium dynamics

After the preparation of the initial staggered state (see Section 2.3), the atoms are isolated in deep lattice wells ($J, \kappa \approx 0$). To initiate the non-equilibrium evolution of the atoms, the Hubbard parameters are tuned to realize the desired values of κ and m from a broad range. Subsequently, the system undergoes coherent many-body oscillations, and the resulting atom numbers on even (matter sites) and odd (gauge

links) lattice wells are extracted via site-selective addressing and absorption imaging techniques [1, 4]. Each data point is measured by averaging over 6 realizations of the experiment, where the one-dimensional gauge theory is realized in multiple chains simultaneously. In-situ data of the experimental non-equilibrium evolution up to times $t \leq 150$ ms is shown in Fig. 2.13 for $\kappa = 14.5$ Hz and $m = 0$.

For a broad range of model parameters, we observe relaxation to a steady state already after a few oscillations. The oscillation frequency is mildly affected by the inhomogeneous Gaussian profile of the optical trap toward the edges of our region of interest ($\Delta U \sim 10$ Hz). Overall, the system retains a high degree of homogeneity throughout the tractable evolution times, as demonstrated in Fig. 2.13.

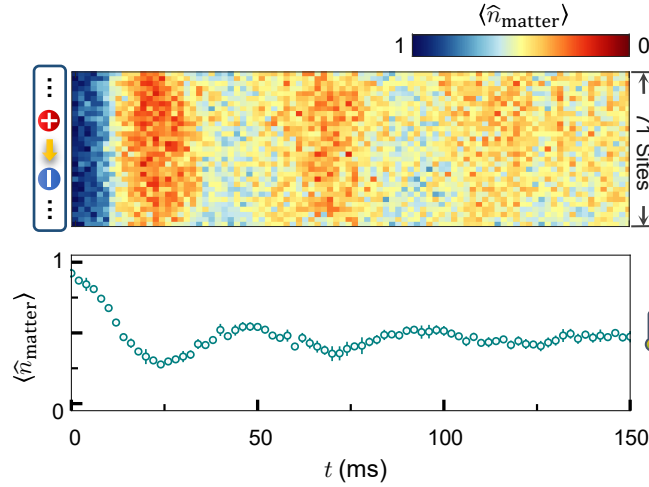


FIGURE 2.13: Non-equilibrium evolution of the matter density: (Top) Starting from initially unity-filled matter sites $\langle \hat{n}_{\text{matter}} \rangle = 1$ (see inset), we observe the evolution of in-situ matter densities for “violent” quenches ($m/\kappa = 0$). (Bottom) The non-equilibrium evolution of the mean matter density relaxes toward a steady state at late times. The signal is averaged over the 36 matter sites of the one-dimensional super-lattice and error bars denote standard deviations. Adapted from [4].

2.5.2 Approach to gauge theory

In Fig. 2.14, we show the system evolution for the most “violent” quench to $m/\kappa = 0$, corresponding to $U \approx 2\delta$. The real-time dynamics at various microscopic Bose-Hubbard parameters, which all map to the same m/κ but with different strengths of the gauge constraint (cases 1-3), is compared to theoretical estimates. Panel a shows the result for the ideal gauge field dynamics obtained through exact diagonalization of the Hamiltonian Eq. (2.1) for a smaller system with 18 matter sites. Conversely, panels b-d give the experimental results for the observable along with numerical estimates based on the time-dependent density matrix renormalization group (t -DMRG) [102] for a Bose-Hubbard chain of 32 sites. In the gauge-theory regime (case 1), we fit the evolution with a damped sine function to extract the characteristic

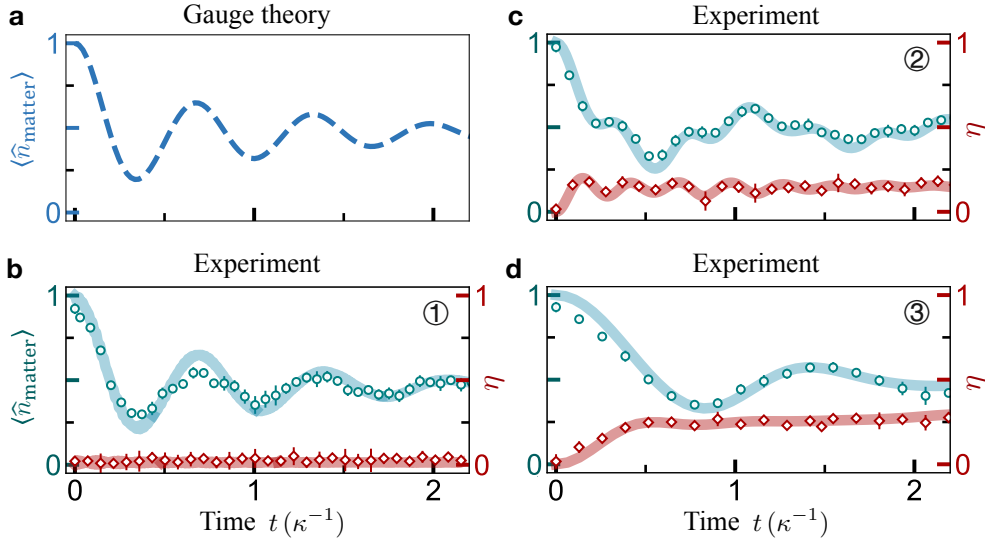


FIGURE 2.14: Controlled approach to gauge-theory dynamics: The experiment approximates the ideal gauge-theory dynamics (a) well for case 1 ($U, \delta \gg J$, b), while cases 2 and 3 fail (c and d). The time-dependent gauge violation η (see main text for definition) decreases from case 3 to case 1 and remains bounded throughout the tractable evolution dynamics. Solid curves are numerical t -DMRG results. Adapted from [4].

damping time scales $\gamma^{-1} = 63 \pm 9\text{ms}$ (experiment) and $64.4 \pm 0.4\text{ms}$ (t -DMRG), where earliest times can be sensitive to small differences in initial conditions.

The different levels of constrained dynamics are realized by tuning the Bose–Hubbard parameters from $\delta/J = 1$ (case 3) to $\delta/J = 16$ (case 1). This is reflected in the gauge violation η , which tends to zero in the gauge-theory regime. It is defined as the odd atom number expectation value on gauge links, i.e.,

$$\eta = \sum_{j \in g} \langle \hat{n}_j \bmod 2 \rangle / L_g, \quad (2.16)$$

where L_g is the number of odd (gauge link) lattice wells. This violation measure is extracted by removing pairs of atoms in the same well with a photo-association laser, and selectively addressing the gauge links for imaging, where site occupations ≥ 3 are neglected, see also Fig. 2.5. We use η as a measure to validate our quantum simulation of the gauge theory. In Fig. 2.15 we give the time averaged $\bar{\eta}$ for the considered evolution times, finding a controlled decrease from large violations in case 3 to $\bar{\eta} \approx 0$ in case 1. While the violation measure η is different from the previously considered ϵ and it gives less detailed insight into possible gauge violations, it can be measured more efficiently and is therefore in practice well-suited to validate the present non-equilibrium scenario.

To characterize the dynamics as a function of the staggering δ/J and onsite potential U/J , which are used to enforce the gauge constraint, we extract the oscillation frequency of the matter density by fitting the data with damped sine functions. In Fig. 2.15, our results show a fast approach to the gauge theory upon increasing δ/J

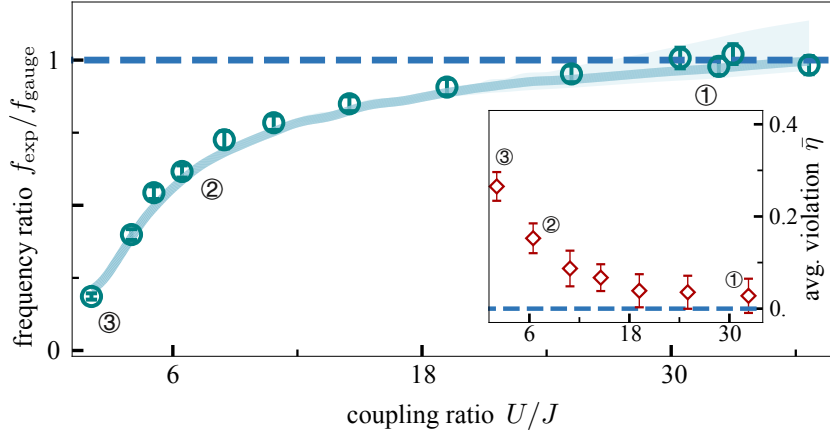


FIGURE 2.15: Controlled approach to gauge-theory dynamics: The frequencies of many-body oscillations (f_{exp}) show a fast approach to the gauge theory (f_{gauge}) for increasing onsite potential $U \approx 2\delta$. Data points are given as the smaller frequencies of dual-frequency damped sine fits of the early-time dynamics. (Inset) The time-averaged gauge violation $\bar{\eta}$ falls off toward zero for the strongly constrained system with $U/J \gg 1$. Adapted from [4].

and U/J simultaneously, thus quantifying the apparent success of realizing the gauge field dynamics observed in Fig. 2.14.

2.5.3 Thermalization and importance of Gauss law

We further investigate the role of the gauge constraints in the relaxation dynamics of the gauge theory by considering quenches to non-zero values of the mass m . This amounts to regions away from the resonance characterized by $U = 2\delta$, where the annihilation of fermion pairs is strongest. For $m = -0.8\kappa$, the resulting time evolution is displayed in Fig. 2.16 with both weakly ($\delta/J \sim 2$) and strongly constrained ($\delta/J \sim 11$) dynamics. Here and in the following, we focus on a region of interest of 50 chains each with an extent of 50 sites, which limits the influence of the inhomogeneous trap profile. We compare the strongly constrained dynamics with the thermal prediction of the gauge theory, finding good agreement within experimental precision at late times. In contrast, the unconstrained system evolves to a very different state, characterized by a thermal ensemble of the Bose–Hubbard system away from the gauge-theory regime.

The thermal predictions are obtained from the numerical evaluation of corresponding canonical ensembles with partition sums

$$Z_{\text{gauge}} = \text{Tr} \left(\hat{P}_G e^{-\beta \hat{H}} \right), \quad (2.17a)$$

$$Z_{\text{BHM}} = \text{Tr} \left(e^{-\beta \hat{H}_{\text{BHM}}} \right). \quad (2.17b)$$

For the gauge theory, the trace is restricted to physical states, where \hat{H} refers to the Hamiltonian Eq. (2.1), and \hat{P}_G denotes the projector onto the gauge-invariant subspace characterized by $\hat{G}_\ell |\psi\rangle = 0$, for all matter sites ℓ . We extract the respective

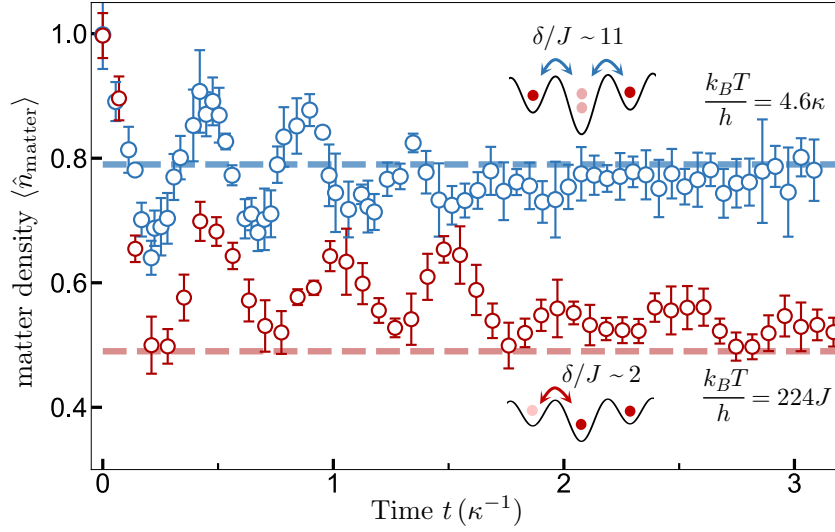


FIGURE 2.16: Thermalization dynamics with and without gauge-symmetry constraint: We investigate the real-time evolution of two data sets toward late-time steady states for constrained (blue) and unconstrained (red) dynamics. Dashed lines show exact-diagonalization predictions from canonical thermal ensembles for the gauge theory (blue) and the Bose–Hubbard model (red) with the same energy density. Insets show relevant processes with (top) and without (bottom) gauge-symmetry constraint. Figure taken from [4].

temperatures as shown in Fig. 2.16 by setting the (conserved) energy density of the ensembles equal to that of the pure initial state, i.e., $-\partial_\beta \log(Z_{\text{gauge/BHM}}) \equiv \langle \psi_0 | \hat{H}_{\text{gauge/BHM}} | \psi_0 \rangle$.

2.5.4 Effective loss of information

As a next step, we investigate the role of the initial state in the thermalization dynamics of the gauge theory. If the system approaches thermal equilibrium, its late-time behavior is entirely characterized by conserved quantities. As shown in the previous section 2.4, the tunability of Hubbard parameters allows us to access a broad range of gauge-symmetric initial states with an adiabatic ramp, ranging from the fully filled state ($\langle \hat{n}_{\text{matter}} \rangle = 1$) to states where a large fraction of fermion pairs have annihilated ($\langle \hat{n}_{\text{matter}} \rangle \approx 0.21$), see Fig. 2.17a. For the quench dynamics, we compare initial states with the same mean energy density with respect to the quench Hamiltonian, see Fig. 2.17b. To achieve this, we numerically follow the experimental sequence outlined in the previous section 2.4 and determine suitable ramp times as outlined in panel c for two sets of couplings, $m/\kappa = -0.8$ and $m/\kappa = 0$. For $m/\kappa = 0$, the initial states with the same mean energy density are prepared with the ramp times $\tau = 1.2\text{ms}$ and $\tau = 20\text{ms}$, corresponding to $\langle \hat{n}_{\text{matter}} \rangle = 1$ and $\langle \hat{n}_{\text{matter}} \rangle \approx 0.21$ respectively. For $m/\kappa = -0.8$, the ramp times are $\tau = 0\text{ms}$ and $\tau = 6.8\text{ms}$, corresponding to initial states with $\langle \hat{n}_{\text{matter}} \rangle = 1$ and $\langle \hat{n}_{\text{matter}} \rangle \approx 0.71$.

The ensuing dynamics is characterized by transient many-body oscillations, where the different initial states relax to a common steady state at long times,

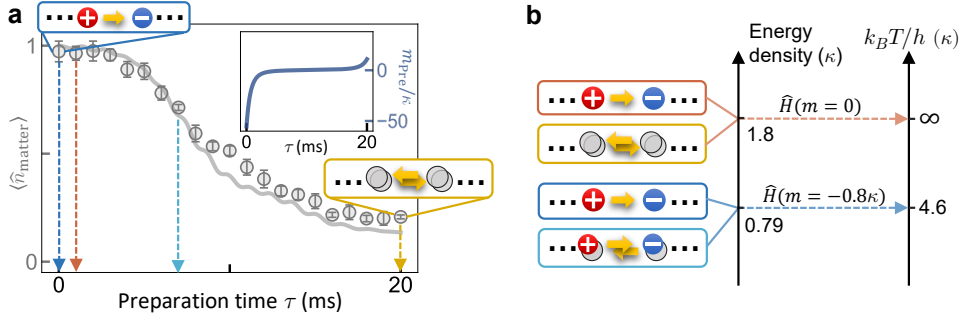


FIGURE 2.17: Initial state preparation and schematics of thermalization: (a) We prepare various initial states ranging from the “charge-dominated” state ($\langle \hat{n}_{\text{matter}} \rangle = 1$, blue box left) to the “vacuum” state ($\langle \hat{n}_{\text{matter}} \rangle \approx 0.21$, yellow box right) using the adiabatic ramp discussed in section 2.4. The prepared mass parameter m_{Pre}/κ as a function of the ramp time τ is shown in the inset. (b) For two sets of quench parameters ($m = 0$ and $m = -0.8\kappa$) we choose two initial states with equal energy density each. The thermalization dynamics is expected to evolve toward steady states in agreement with canonical thermal ensembles with corresponding temperatures. Energy densities are given with respect to the ground state of the evolution Hamiltonian. Adapted from [4].

see Fig. 2.17c and d. During the evolution, the information about initially different matter densities is seen to be effectively lost in the quantum many-body system. We again find the long-time steady states to be well-described by gauge-invariant thermal ensembles with the same conserved charges as the initial state. We observe this thermalization dynamics for different values of couplings in the gauge theory. Specifically for $m = 0$ our initial states are distributed symmetrically around the center of the energy spectrum, see appendix 2.D. In this case one observes a fast effective loss of initial-state memory, and the experiment relaxes to the steady-state value of the infinite-temperature state, see Fig. 2.17b.

In general, the emergence of effectively irreversible behavior, such as thermalization from the underlying reversible time evolution, concerns only typical thermodynamic quantities and initial conditions that do not violate essential ingredients for a thermodynamic description such as clustering properties [103]. Despite the non-integrability of the $U(1)$ QLM [79, 85, 104], certain fine-tuned quenches give rise to weak ergodicity breaking due to the presence of special eigenstates in the spectrum of the quench Hamiltonian [85, 104]. This could manifest in persistent oscillations around the thermal-ensemble prediction [55]. Currently, the level of control in our experiment limits us from probing such possible behavior in part due to an inherent residual inhomogeneity across the lattice. Thus, in our experiment we observe equilibration close to the thermal ensembles for the performed quenches and considered observable.

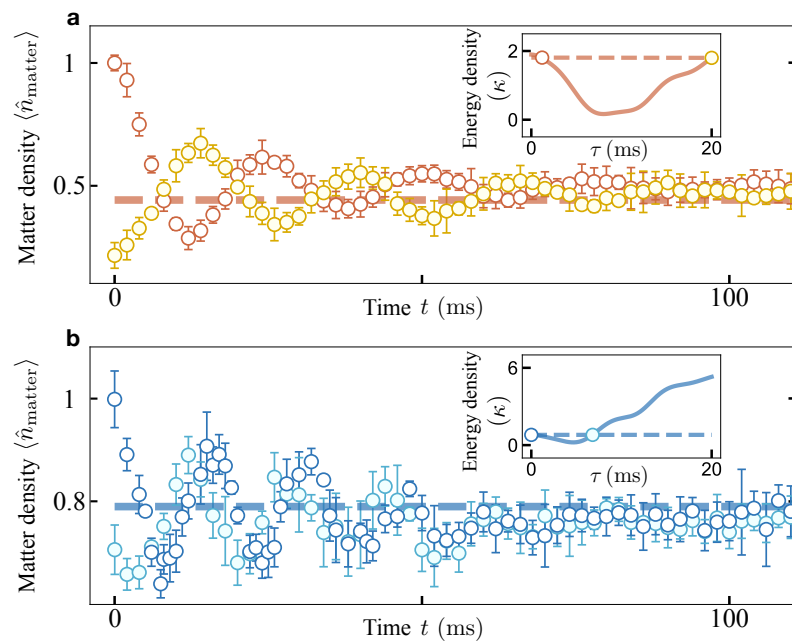


FIGURE 2.18: Effective loss of initial-state information: We show the thermalization dynamics for the chosen quench parameters and initial states (see Fig. 2.17). Experimental data is compared to predictions from corresponding gauge theory thermal ensembles (dashed lines) at temperatures $k_B T = \infty$ for $m/\kappa = 0$ (a) and $k_B T = 4.6\kappa$ for $m/\kappa = -0.8$ (b). Insets show the changing energy density during state preparation (with respect to instantaneous ground states), circles mark the chosen initial states. Figure adapted from [4].

2.6 Summary

We have demonstrated the controlled operation of a highly-tunable platform for quantum simulations of a lattice gauge theory. Specifically, we have shown that gauge symmetry remains intact to a good degree - even when the system is driven across a quantum critical point or operated far away from thermal equilibrium. Furthermore, initial-state defects have been identified as a source of errors and their influence on the observed near-equilibrium dynamics was characterized.

Subsequently, the quantum simulator was applied to explore the non-equilibrium dynamics of the gauge theory. We established the thermalization dynamics by comparing the late-time evolution of our quantum simulator to corresponding gauge-invariant thermal ensembles. To highlight the importance of gauge symmetry, we contrasted the relaxation dynamics with quantum simulations lacking the symmetry constraints. Finally, universality of thermalization was demonstrated by showing that late-time steady states of the evolution agree for different initial states with same energy.

2.A Perturbation Theory

To construct the effective Hamiltonian (2.1), we employ a Schrieffer-Wolff transformation to second order [105, 106]. In this section, we demonstrate the emergence of the effective Hamiltonian for a unit cell (see Fig. 2.19) and discuss its generalization to the larger systems considered in the main text. We follow Ref. [105].

For the simple case illustrated in Fig. 2.19 the Hamiltonian is given by

$$\hat{H} = J(\hat{b}_0^\dagger \hat{b}_1 + \hat{b}_1^\dagger \hat{b}_2 + h.c.) + \sum_j \left(j\Delta + \delta \frac{1 + (-1)^j}{2} \right) \hat{b}_j^\dagger \hat{b}_j + \frac{U}{2} \sum_j \hat{b}_j^\dagger \hat{b}_j^\dagger \hat{b}_j \hat{b}_j, \quad (2.18)$$

where lattice wells are labeled from the left as $j = 0, 1, 2$. We may write the four-state Hamiltonian (with fixed atom number $n = 2$) in matrix notation

$$\hat{H} = \begin{pmatrix} 2\delta + 2\Delta & J & J & 0 \\ J & \delta + \Delta & 0 & \sqrt{2}J \\ J & 0 & \delta + 3\Delta & \sqrt{2}J \\ 0 & \sqrt{2}J & \sqrt{2}J & U + 2\Delta \end{pmatrix}, \quad (2.19)$$

where the basis vectors are given by the four occupation states $|1\rangle = |101\rangle$, $|2\rangle = |110\rangle$, $|3\rangle = |011\rangle$, and $|4\rangle = |020\rangle$. The Hamiltonian can be split into a diagonal part $\hat{H}_0 = \text{diag}(2\delta + 2\Delta, \delta + \Delta, \delta + 3\Delta, U + 2\Delta)$, and a remaining off-diagonal interaction Hamiltonian $J\hat{V}$, such that $\hat{H} = \hat{H}_0 + J\hat{V}$. We consider the regime, where the dominant scales are given by δ , and U , i.e., where $J, \Delta \ll \delta, U$.

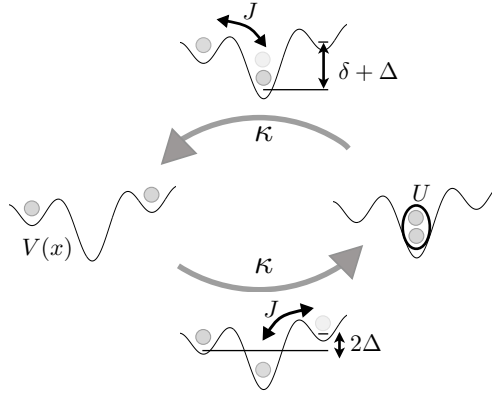


FIGURE 2.19: Perturbation theory of effective interactions: Shown are the different unit cell configurations for two atoms. The effective theory couples the gauge-invariant states (left and right) through intermediate states (top and bottom) with rate κ . The system potential $V(x)$ is tuned such to yield parameters for direct tunneling J , staggering δ , onsite interaction U , and linear tilt Δ .

To derive an effective Hamiltonian in this regime, we use a unitary transformation $\hat{U} = \exp(i\hat{T})$ with hermitian generator \hat{T} . The transformed Hamiltonian

reads

$$\hat{H}_{\text{eff}} = \hat{U} \hat{H} \hat{U}^\dagger. \quad (2.20)$$

For \hat{U} being close to unity, we may expand

$$\hat{T} = \alpha \hat{T}_0 + \frac{\alpha^2}{2} \hat{T}_1 + \mathcal{O}(\alpha^3), \quad (2.21)$$

where α is a small parameter. We subsequently get

$$\hat{\hat{H}} \approx \hat{H} + [i\hat{T}, \hat{H}] + \frac{1}{2} [i\hat{T}, [i\hat{T}, \hat{H}]] + \dots, \quad (2.22)$$

approximated to given order in α . At order $\mathcal{O}(\alpha)$ we choose the generator to eliminate the interaction Hamiltonian i.e.,

$$J\hat{V} + \alpha[i\hat{T}_0, \hat{H}_0] = 0. \quad (2.23)$$

Multiplying the resulting equation with the above basis states one obtains

$$J \langle i | \hat{V} | j \rangle + i\alpha \langle i | \hat{T}_0 | j \rangle (E_j - E_i) = 0, \quad (2.24)$$

which implies the matrix elements

$$\alpha \langle i | \hat{T}_0 | j \rangle = \frac{iJ \langle i | \hat{V} | j \rangle}{E_i - E_j}. \quad (2.25)$$

Here, the right-hand side involves factors on the order J/δ , and J/U , which can be identified with the perturbative expansion parameter α . At second order ($\mathcal{O}(\alpha^2)$), the effective Hamiltonian couples the states $|\psi_1\rangle = (1 \ 0 \ 0 \ 0) = |1\rangle$, and $|\psi_2\rangle = (0 \ 0 \ 0 \ 1) = |4\rangle$, which for $U \approx 2\delta$ are (approximately) energetically resonant. The coupling matrix element is given by

$$\frac{\kappa}{2} \equiv \langle \psi_1 | \hat{H}_{\text{eff}} | \psi_2 \rangle = \frac{1}{2} \alpha J \langle \psi_1 | [i\hat{T}_0, \hat{V}] | \psi_2 \rangle + \mathcal{O}(\alpha^3). \quad (2.26)$$

Furthermore, we get

$$\begin{aligned} \langle \psi_1 | i\hat{T}_0 \hat{V} | \psi_2 \rangle &= \sum_k \langle \psi_1 | i\hat{T}_0 (|k\rangle \langle k|) \hat{V} | \psi_2 \rangle \\ &= \langle \psi_1 | i\hat{T}_0 (|2\rangle \langle 2| + |3\rangle \langle 3|) \hat{V} | \psi_2 \rangle \\ &= \langle \psi_1 | i\hat{T}_0 | 2 \rangle \langle 2 | \hat{V} | \psi_2 \rangle + \langle \psi_1 | i\hat{T}_0 | 3 \rangle \langle 3 | \hat{V} | \psi_2 \rangle, \end{aligned} \quad (2.27)$$

such that

$$\begin{aligned} \frac{\kappa}{2} &= \frac{\alpha J}{2} \langle \psi_1 | i\hat{T}_0 | 2 \rangle \langle 2 | \hat{V} | \psi_2 \rangle + \frac{\alpha J}{2} \langle \psi_1 | i\hat{T}_0 | 3 \rangle \langle 3 | \hat{V} | \psi_2 \rangle \\ &\quad - \frac{\alpha J}{2} \langle \psi_1 | \hat{V} | 2 \rangle \langle 2 | i\hat{T}_0 | \psi_2 \rangle - \frac{\alpha J}{2} \langle \psi_1 | \hat{V} | 3 \rangle \langle 3 | i\hat{T}_0 | \psi_2 \rangle \\ &= \frac{\sqrt{2}}{2} \left(-\frac{J^2}{\delta + \Delta} - \frac{J^2}{\delta - \Delta} + \frac{J^2}{\delta - U - \Delta} + \frac{J^2}{\delta - U + \Delta} \right), \end{aligned} \quad (2.28)$$

which corresponds to Eq. (2.6) in the main chapter. Analogously, the states $|\psi_1\rangle$ and $|\psi_2\rangle$ get renormalized energies

$$\Delta E_1 \equiv \langle \psi_1 | \hat{H}_{\text{eff}} | \psi_1 \rangle \quad (2.29a)$$

$$\Delta E_2 \equiv \langle \psi_2 | \hat{H}_{\text{eff}} | \psi_2 \rangle. \quad (2.29b)$$

The difference $\Delta E_1 - \Delta E_2$, however, enters only at higher orders and will be neglected. The present analysis generalizes to extended systems, where no further resonant processes appear at this order.

In this analysis, the linear tilt has been used to avoid second-order processes of the kind $|001\rangle \rightarrow |100\rangle$, as illustrated in Fig. 2.20. Such configurations did not appear in the above unit cell, but are relevant in the extended many-body system. Corresponding unwanted tunneling processes are indefinitely suppressed for $\Delta \gg J^2/U$. While this condition cannot always be upheld in the experiment, we nevertheless observe good levels of gauge invariance, see also section 2.4.3.

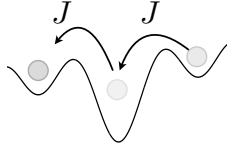


FIGURE 2.20: Suppression of second-order tunneling with a tilt: The tilt turns initial and final configurations off-resonant. Ideally, the tilt is much larger than the corresponding second-order tunneling strength, i.e., $\Delta \gg J^2/U$.

2.B Correlation length

In this section we give further details on the extraction of density correlations of the atoms and the corresponding correlation length ξ of the final state. We consider the expression

$$C(k) \propto \sum_{i,j} e^{2\pi k(i-j)} C(i,j), \quad (2.30)$$

where $k = k_d a$ is a dimensionless momentum variable, where a is the spacing between atoms. In the final state, we assume the lattice correlations

$$C(i, j) = \langle \hat{n}_i \hat{n}_j \rangle = \langle \hat{n}_i \hat{n}_j \rangle^c - \langle \hat{n}_i \rangle \langle \hat{n}_j \rangle, \quad (2.31)$$

where $\langle \cdot \rangle^c$ indicates connected correlations. We furthermore assume an exponential decay of connected correlations

$$\langle \hat{n}_i \hat{n}_j \rangle^c \propto \text{Re}(i^{|i-j|}) e^{-\frac{|i-j|}{\xi}}. \quad (2.32)$$

To compare to the experiment, we compute expression Eq. (2.30) for 100 lattice wells. Motivated by the Fourier transform for infinite systems and long correlation lengths

$$\int ds e^{\frac{i\lambda_s k_d s}{8}} e^{-\frac{|s|}{\xi}} \propto \frac{1}{k_d^2 + (\lambda_s \xi / 8)^2}, \quad (2.33)$$

we fit the resulting curve with Lorentzian functions for different values of ξ . Results are compared to the peak width of the data, where the optical resolution (width of neighboring peak) is subtracted (quadratically), see Fig. 2.21.

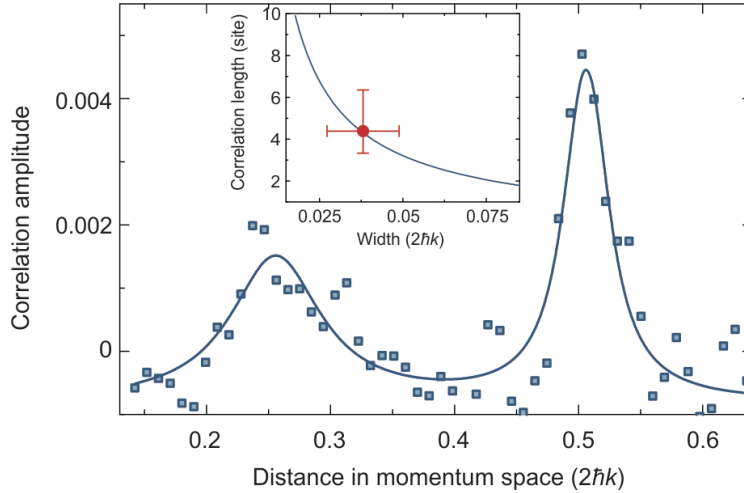


FIGURE 2.21: Extraction of the correlation length: The final state correlation length is extracted through the peak widths of the density correlation signal. The solid lines are Lorentzian fits to the data after subtracting background. (Inset) The peak width is compared to the correlation signal of a domain state with length 100 sites and exponentially decaying density correlation. Figure taken from [1].

2.C Numerics

To benchmark the experiment, we perform numerical simulations involving both the QLM as the “ideal” theory evolution as well as numerical t -DMRG simulations of the experimental system (Hubbard Hamiltonian). We compare the evolution for systems with different total numbers of lattice wells L , observing convergence

around $L = 40$ -50. The curves have been obtained by numerically computing the evolution with time-dependent parameters shown in Fig. 2.5, and the numerical calculation of the bosonic system excludes local atom populations $n > 2$, which are suppressed, see Fig. 2.5. To account for experimental imperfections, t -DMRG simulations of the experiment furthermore include a small homogeneity of the laser intensity resulting in a quadratic profile of the onsite potential which shifts by $\Delta U \approx 10\text{Hz}$ towards the edges of the 71-site region of interest. The results of the numerical analysis are shown in Fig. 2.22. Furthermore, in Fig. 2.5 of the main chapter, the t -DMRG simulations include an additional average over several runs with Gaussian fluctuations of the staggering potential with standard deviation $\sigma_\delta = 4.5\text{Hz}$.

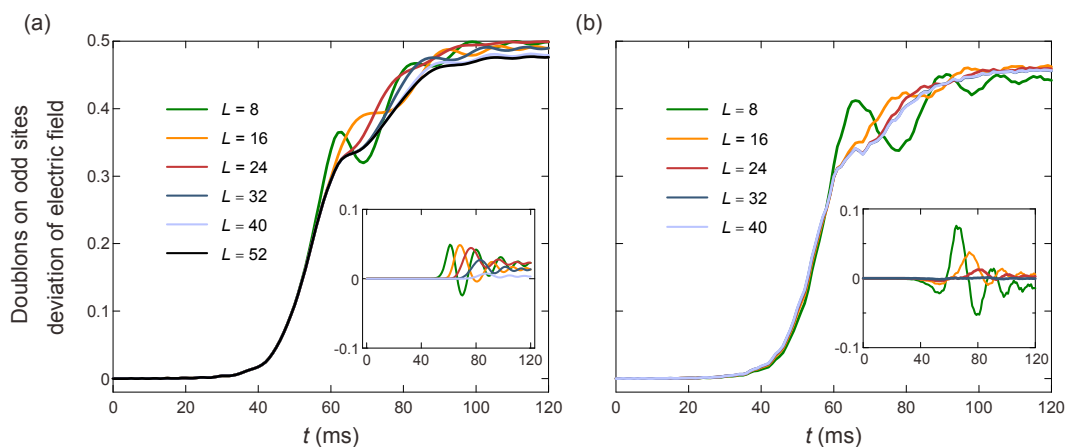


FIGURE 2.22: System size dependence: We compute the quasi-static evolution across the quantum critical point by comparing numerical simulations for different system sizes (number of optical lattice wells). We consider the gauge theory (a) using exact diagonalization and the Hubbard Hamiltonian (b) for t -DMRG simulations. The insets show the absolute difference with respect to the respective largest system size. Taken from [1].

To achieve the large system sizes for the ideal gauge theory with exact diagonalization [107], we explicitly make use of the gauge symmetry to remove un-physical states. To achieve even larger system sizes, a complete elimination of un-physical states can be obtained by considering the PXP model [55, 79, 104] which can be mapped to the $S = 1/2$ quantum link model. For instance, numerical simulations for chains of corresponding length $L = 64$ have been conducted in Ref. [85].

2.D Thermal states

In the main chapter we consider various quenches evolving the system from different initial states towards steady states at long times. In this section we give additional details on the thermal equilibrium states at infinite temperature.

Infinite-temperature state

We consider the fully filled initial state with $\langle \hat{n}_{\text{matter}} \rangle = 1$ in the gauge theory, which corresponds to $|\psi_0\rangle = |\dots 10101\dots\rangle$. For the evolution with mass parameter $m/\kappa = 0$, we have

$$E_0 = \langle \psi_0 | \hat{H} | \psi_0 \rangle = 0, \quad (2.34)$$

for the “ideal” gauge theory with Hamiltonian given by Eq. (2.1). The operator

$$\hat{V} = \prod_{\ell} \hat{S}_{\ell, \ell+1}^z \quad (2.35)$$

anti-commutes with the Hamiltonian, $\{\hat{V}, \hat{H}\} = 0$, such that for any eigenstate $|e\rangle$ with $\hat{H}|e\rangle = E|e\rangle$ there is an associated state $|\tilde{e}\rangle = \hat{V}|e\rangle$ with eigenvalue $\hat{H}|\tilde{e}\rangle = -E|\tilde{e}\rangle$. Hence, the spectrum is symmetric around $E_0 = 0$. Since $|\psi_0\rangle$ is an eigenstate of \hat{V} with eigenvalue ± 1 it is symmetrically distributed in the spectrum which is in conflict with a thermal state except for $T = \infty$.

System size dependence of matter density

In the case of the most extreme quench from $m/\kappa = -\infty$ to $m/\kappa = 0$, we consider the thermalization dynamics towards a steady state with infinite temperature. In this section, we employ the method outlined in Ref. [79] to compute the matter density in the infinite temperature state and for the case of periodic boundary conditions.

The configuration of gauge fields ($|\uparrow\rangle$ and $|\downarrow\rangle$) on neighboring links may be labeled using 2×2 matrices

$$\begin{pmatrix} |\uparrow\uparrow\rangle & |\downarrow\uparrow\rangle \\ |\downarrow\downarrow\rangle & |\uparrow\downarrow\rangle \end{pmatrix} \rightarrow \begin{pmatrix} 1 & 0 \\ 1 & 1 \end{pmatrix} \equiv C \quad (\text{even}), \quad (2.36)$$

$$\begin{pmatrix} |\uparrow\uparrow\rangle & |\downarrow\uparrow\rangle \\ |\downarrow\downarrow\rangle & |\uparrow\downarrow\rangle \end{pmatrix} \rightarrow \begin{pmatrix} 1 & 1 \\ 0 & 1 \end{pmatrix} \equiv C^T \quad (\text{odd}), \quad (2.37)$$

where states labeled with ones are allowed by Gauss law, while zeros indicate the opposite. Due to the staggered fermions, the matrices alternate between even and odd matter sites. Here, the off-diagonal terms indicate the presence of a charged pair, where the electric field eigenvalue changes from one gauge link to its neighboring link. To compute the pair density, we use the following matrix as an observable to project onto “pair” states

$$\hat{p} = \begin{pmatrix} 0 & 1 \\ 1 & 2 \end{pmatrix}, \quad (2.38)$$

i.e., the entries count the number of pairs on two neighboring matter sites for any configuration of the “external” gauge fields. The thermal expectation value in the

infinite temperature state ($\beta = 0$) for a system of $N = L/2$ matter sites is then given by

$$\begin{aligned}
\frac{1}{2}\langle \hat{n}_\ell + \hat{n}_{\ell+1} \rangle &= \text{Tr} \left[e^{-\beta \hat{H}} (\hat{n}_\ell + \hat{n}_{\ell+1}) \right] \\
&= \text{Tr} [\hat{n}_\ell + \hat{n}_{\ell+1}] \\
&= \text{tr} \left[(CC^T)^{(N-2)/2} \hat{p} \right] \\
&= \text{tr} \left[\begin{pmatrix} \left(\frac{3+\sqrt{5}}{2}\right)^{\frac{N-2}{2}} & 0 \\ 0 & \left(\frac{3-\sqrt{5}}{2}\right)^{\frac{N-2}{2}} \end{pmatrix} \hat{p} \right] \tag{2.39}
\end{aligned}$$

where “Tr” is the trace over a basis of the large Hilbert space and “tr” represents a trace over the two-dimensional matrix space. We evaluated the expression in the eigenbasis of the matrix CC^T , with accordingly transformed operator \hat{p} . The results for various N can be obtained for very large system sizes, where the final value is approached to precision $\sim 10^{-14}$ for system sizes of about ~ 35 matter sites. We show the results in Fig. 2.23. For $N = 2$ matter sites, the Hilbert space is three dimensional; it consists of one “pair” state and two “vacuum” states and the particle density is $\langle \hat{n}_{\text{matter}} \rangle = 1/3$. The shown extrapolated value for infinite systems is in good agreement with the experimental data within errors, see Fig. 2.18.

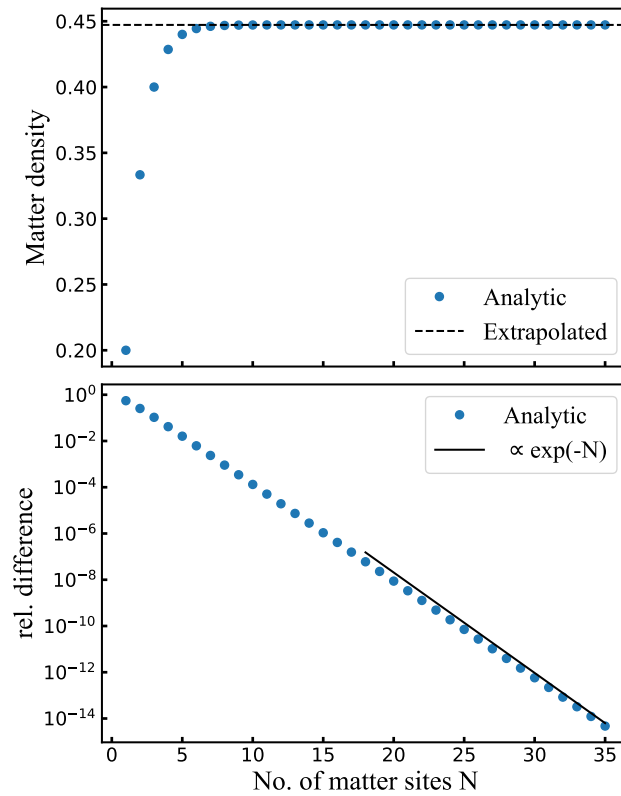


FIGURE 2.23: System size dependence of matter density for infinite temperature state: The matter density $\langle \hat{n}_{\text{matter}} \rangle$ for $\beta = 0$ and periodic boundary conditions monotonically increases with the number of matter sites N (top). The relative error $(\langle \hat{n}_{\text{matter}} \rangle - \langle \hat{n}_{\text{matter}}(N = 40) \rangle) / \langle \hat{n}_{\text{matter}} \rangle$ decreases approximately exponentially (bottom).

Chapter 3

Quantum simulation and gauge field dynamics in 2D

Parts of this chapter have previously been published in the following articles:

- R. Ott, T. V. Zache, F. Jendrzejewski, and J. Berges, “Scalable cold-atom quantum simulator for two-dimensional qed”, *Physical Review Letters* **127**, 130504 (2021), see [3].

I developed the theory, performed analytical and numerical calculations, and presented the results in text and figures in collaboration with the co-authors.

- A. Hegde, R. Ott, A. Xia, V. Kasper, J. Berges, and F. Jendrzejewski, “Non-equilibrium dynamics of fluctuations in an ultra-cold atomic mixture”, arXiv preprint arXiv:2204.06456 (2022), see [7].

I developed the theory, performed numerical and analytical calculations as well as their comparison to experimental data, and presented the results in text and figures in collaboration with the co-authors.

- N. Mueller, T. V. Zache, and R. Ott, “Thermalization of gauge theories from their entanglement spectrum”, arXiv preprint arXiv:2107.11416 (2021), see [5], under review in *Physical Review Letters*.

N. Mueller, T. V. Zache, and R. Ott, “Quantum thermalization of gauge theories: chaos, turbulence and universality”, arXiv preprint arXiv:2111.01155 (2021), see [108].

I contributed to the interpretation and presentation of the results, as well as the data generation.

Text and figures are largely taken from these publications, where the experimental results shown in Section 3.4 were obtained by the group of Fred Jendrzejewski and have partly been published in Ref. [52]. Specifically, Sections 3.2 and 3.3 are taken from Ref. [3], Section 3.4 from Ref. [7], and Section 3.5 builds on Refs. [5, 108]. The experimental results of Section 3.4 have partly also been included in the doctoral theses of A. Mil [109] and T. V. Zache [110]. These references also apply to the corresponding appendices.

3.1 Overview

In this chapter, we consider lattice gauge theories in two spatial dimensions, thus going beyond the one-dimensional system considered in the previous chapter. While gauge symmetry heavily constrains the dynamics of gauge fields in a single spatial dimension, two-dimensional setups allow for the complex interplay of gauge fields in ground state physics or non-equilibrium dynamics, even without the inclusion of fermions. In this chapter, we consider two different approaches:

First, we propose a new scheme to quantum simulate $U(1)$ gauge fields in two spatial dimensions. To achieve this, we employ a two-species mixture of ultra-cold spinor Bose gases trapped in an optical lattice. Our scheme is applicable in both equilibrium, and out-of-equilibrium scenarios. In equilibrium, we discuss the emergence of charge confinement at zero temperature in the quantum simulator. Subsequently, we apply the proposal to an experimental implementation of an ultra-cold atomic mixture. We investigate the non-linear evolution of the atoms, where we focus on the dynamics of fluctuations.

Secondly, we explore the thermalization dynamics of a \mathbb{Z}_2 gauge theory, by studying its entanglement structure. The entanglement spectrum reveals different stages of the complex evolution from early-time level repulsion to self-similar dynamics and relaxation at later times.

3.2 Scalable cold-atom quantum simulator

As also demonstrated in Chapter 2, much progress has been achieved for quantum simulations of gauge theories in one spatial dimension, and first experimental realizations of small systems in two dimensions have been shown [111–113]. However, scalable experimental implementations of two- and higher-dimensional setups are still elusive. Here the main challenge is the efficient construction of gauge invariant plaquette terms of the lattice field theory, corresponding to magnetic field interactions. So far, proposals to engineer the magnetic field interactions using atoms in optical lattices rely mainly on perturbative constructions [31, 32, 37, 80, 114, 115]. Other approaches, using Rydberg atoms in optical tweezers [50], two-dimensional arrays of superconducting qubits [35, 116], Floquet engineering in optical lattices [117], or universal quantum computers [41, 42, 46], currently focus on gauge theories with small local Hilbert spaces, which are typically unable to describe important far-from-equilibrium phenomena with large fluctuations of electromagnetic fields.

Here, we propose a new scheme to quantum simulate the gauge fields of compact QED in two spatial dimensions using a two-species mixture of ultra-cold spinor Bose gases trapped in an optical lattice. We represent electric fields by site occupations on a lattice [31, 34, 80] and the electric field energy results from on-site interactions. The engineering of gauge invariant plaquette terms is based on hetero-nuclear atomic collisions similar to those successfully demonstrated in the recent experiment of

Ref. [52]. Neighboring unit plaquettes are connected by forming superpositions of the atomic clouds. This can be realized via resonant microwave dressing or laser-assisted tunneling. We exploit that our cold-atom system approaches QED by putting Bose-Einstein condensates (BECs) with large numbers of atoms on the lattice [30, 64, 118], rather than single atoms [31]. The high tunability of the proposed approach gives access to a wide range of coupling strengths, including regimes of QED in which perturbative treatments are poorly controlled.

3.2.1 Gauge field theory

In the Hamiltonian formulation of compact QED we introduce electric fields and gauge links as outlined in Chapter 1. Presently they are positioned at links between sites $\mathbf{n} = (n_x, n_y)$ of a two-dimensional spatial lattice, as sketched in Fig. 3.1a. On a link at site \mathbf{n} , and pointing in direction i , the field operators act on electric field eigenstates as $\hat{E}_{\mathbf{n},i} |j\rangle_{\mathbf{n},i} = j |j\rangle_{\mathbf{n},i}$ and $\hat{U}_{\mathbf{n},i} |j\rangle_{\mathbf{n},i} = |j+1\rangle_{\mathbf{n},i}$, with $j \in \mathbb{Z}$ [119]. The conserved Gauss operators take the form $\hat{G}_{\mathbf{n}} = \sum_{i=x,y} (\hat{E}_{\mathbf{n},i} - \hat{E}_{\mathbf{n}-\hat{i},i}) - Q_{\mathbf{n}}/e$, where \hat{i} is the unit vector in direction i . Here, we consider the pure gauge fields of compact QED, such that $Q_{\mathbf{n}}$ represent classical static charges. In temporal-axial gauge, the Hamiltonian reads in two dimensions

$$\hat{H}_{\text{QED}} = \frac{e^2}{2} \sum_{\mathbf{n}} (\hat{E}_{\mathbf{n},x}^2 + \hat{E}_{\mathbf{n},y}^2) - \frac{1}{2a_s^2 e^2} \sum_{\mathbf{n}} \left(\hat{U}_{\mathbf{n},x} \hat{U}_{\mathbf{n}+\hat{x},y} \hat{U}_{\mathbf{n}+\hat{y},x}^\dagger \hat{U}_{\mathbf{n},y}^\dagger + \text{h.c.} \right), \quad (3.1)$$

with spatial lattice spacing a_s . The central result of this section is a scheme to implement both the electric field energy (first term in (3.1)) as well as the magnetic field energy (plaquette operators in second term) with sizable strength. Electric field operators have been made dimensionless by rescaling with appropriate powers of a_s , and we define a dimensionless coupling parameter as $g^2 = e^2 a_s$.

3.2.2 Cold-atom implementation

We propose to realize a quantum simulator for Hamiltonian (3.1) using an atomic mixture of two spinor Bose gases [120] in a two-dimensional optical lattice, see Fig. 3.1a. For the mapping we associate the gauge links of the original formulation with bosonic annihilation/creation operators, and electric fields with respective number operators. More precisely, within each well labeled \mathbf{n} according to its lower-left corner, we focus on two spin states for both species A and B : $|0\rangle_{\mathbf{n},A/B}$ and $|1\rangle_{\mathbf{n},A/B}$. We then couple neighboring wells through laser-assisted tunneling with appropriately chosen frequencies, which yield the superposition states $|+\rangle_{\mathbf{n},x} = (|0\rangle_{\mathbf{n}-\hat{y},B} + |1\rangle_{\mathbf{n},B})/\sqrt{2}$ and $|+\rangle_{\mathbf{n},y} = (|0\rangle_{\mathbf{n}-\hat{x},A} + |1\rangle_{\mathbf{n},A})/\sqrt{2}$, see Fig. 3.1a. Here, we use a tilted optical lattice to ensure the corresponding detuning of single particle energy levels, see also the appendix 3.A for details on our implementation scheme. The superposition states $|+\rangle_{\mathbf{n},i}$ are the ones which are identified with the gauge link degrees of freedom of link (\mathbf{n}, i) of the original lattice gauge theory formulation,

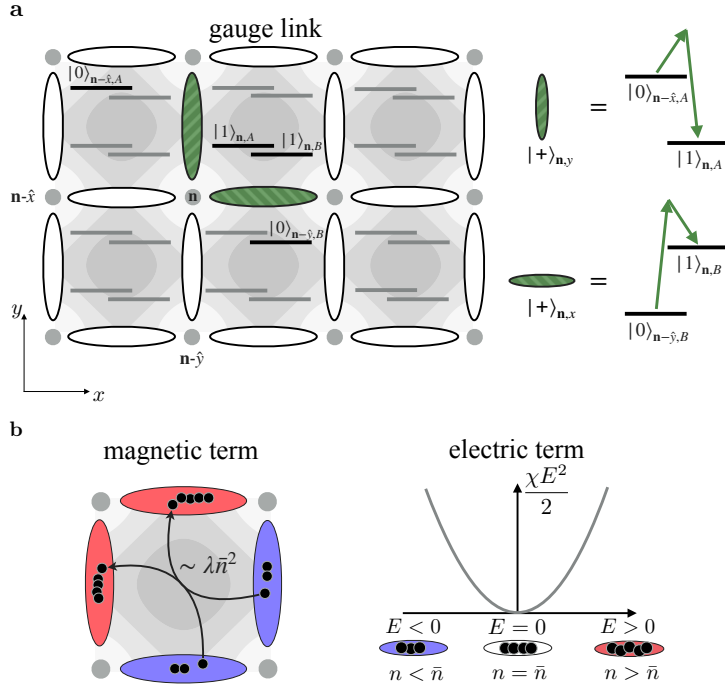


FIGURE 3.1: Proposed implementation:(a) Sketch of the implementation scheme. Atomic clouds are trapped in the minima of the optical lattice at the center of the plaquettes (dark gray shaded regions). The gauge field degrees of freedom (ellipses) are formed by creating superpositions of the four hyperfine levels in each well with neighboring clouds along the x - or y -axis, respectively. (b) Magnetic plaquette interactions of four neighboring links are formed by atomic scatterings within the minima of the optical lattice (left). The electric field energy is given by homo-nuclear density interactions forming an on-site potential (right). The electric field strength is represented by the atom number on each link relative to a background number \bar{n} . Taken from [3].

and the associated creation (annihilation) operator we denote by $\hat{b}_{n,i}^\dagger$ ($\hat{b}_{n,i}$). Hence, the wells of the optical lattice are centered in the associated plaquettes of the lattice gauge theory. The appropriate gauge field dynamics arises then from the on-site homo- and hetero-nuclear contact interactions between the atoms within each well. This construction constitutes the crucial ingredient for our proposed implementation: it allows gauge fields on links to interact with two neighboring plaquettes, thus realizing the gauge-invariant plaquette interaction for magnetic fields via atomic collisions of sizable strength.

The construction yields the cold-atom Hamiltonian

$$\begin{aligned} \hat{H}_{CA} = & \frac{\chi}{2} \sum_{\mathbf{n}} \sum_{i=x,y} \hat{b}_{n,i}^\dagger \hat{b}_{n,i}^\dagger \hat{b}_{n,i} \hat{b}_{n,i} - \lambda \sum_{\mathbf{n}} \left(\hat{b}_{n,x}^\dagger \hat{b}_{n+\hat{x},y}^\dagger \hat{b}_{n+\hat{y},x} \hat{b}_{n,y} + \text{h.c.} \right) \\ & + \frac{\delta}{2} \sum_{\mathbf{n}} \left(\hat{b}_{n,y}^\dagger \hat{b}_{n,y} + \hat{b}_{n+\hat{x},y}^\dagger \hat{b}_{n+\hat{x},y} \right) \times \left(\hat{b}_{n,x}^\dagger \hat{b}_{n,x} + \hat{b}_{n+\hat{y},x}^\dagger \hat{b}_{n+\hat{y},x} \right), \end{aligned} \quad (3.2)$$

as detailed in appendix 3.A. Here, the first term in the first line encodes intra-species density interactions corresponding to the electric field energy, see Fig. 3.1b. The

inter-species collisions in the second term describe the desired magnetic plaquette interaction. There are also additional gauge-invariant interaction terms, described by the terms in the second line, which represent inter-species density interactions. Direct tunneling is considered to be sufficiently suppressed through an external gradient such that associated processes can be neglected and do not appear in Eq. (3.2). Since we are dealing with a lattice field theory, we furthermore exploited that processes of order $\mathcal{O}(a_s)$ vanish in the continuum limit $a_s \rightarrow 0$. We also considered an equal strength of homo-nuclear density interactions in both species. All coupling constants are assumed to be positive $\chi, \lambda, \delta > 0$, which depends, in general, on the choice of species. The sign of λ can always be chosen by appropriate initialization of the condensate phases, see section 3.A.

To explain the relation of our cold-atom Hamiltonian with the Hamiltonian (3.1), we employ a number-phase representation of the bosons, where $\hat{b}_{\mathbf{n},i}^\dagger = \sqrt{\hat{n}_{\mathbf{n},i}} \exp(i\hat{\phi}_{\mathbf{n},i})$ with commutation relations $[\hat{n}_{\mathbf{m},j}, \exp(i\hat{\phi}_{\mathbf{n},i})] = \exp(i\hat{\phi}_{\mathbf{n},i}) \delta_{\mathbf{nm}} \delta_{ij}$. We expand the Hamiltonian (3.2) around a large background atom number $\bar{n} \gg 1$ and find

$$\hat{H}_{\text{CA}} = \hat{H}_{\text{QED}} + \mathcal{O}\left(\frac{\hat{n} - \bar{n}}{\bar{n}}\right) + \frac{\delta}{2} \sum_{\mathbf{n}} (\hat{\mathcal{E}}_{\mathbf{n},y} + \hat{\mathcal{E}}_{\mathbf{n}+\hat{x},y}) (\hat{\mathcal{E}}_{\mathbf{n},x} + \hat{\mathcal{E}}_{\mathbf{n}+\hat{y},x}), \quad (3.3)$$

where we dropped irrelevant constants. To identify the leading cold atom contribution with compact QED, we represent the atomic electric field operators as deviations of the boson number occupation from the background, $\hat{\mathcal{E}}_{\mathbf{n},i} = \hat{n}_{\mathbf{n},i} - \bar{n}$, and the corresponding gauge links by the approximately unitary operators, $\hat{\mathcal{U}}_{\mathbf{n},i} = \hat{b}_{\mathbf{n},i}^\dagger / \sqrt{\bar{n}} = \exp(i\hat{\phi}_{\mathbf{n},i}) + \mathcal{O}(\hat{\mathcal{E}}_{\mathbf{n},i}/\bar{n})$ [31, 34, 80]. This identification fulfills the commutation relations of compact QED with the exception of $[\hat{\mathcal{U}}_{\mathbf{n},i}^\dagger, \hat{\mathcal{U}}_{\mathbf{m},j}] = 1/\bar{n} \rightarrow 0$, which becomes accurate in the limit of large background atom numbers $\bar{n} \gg 1$, see also the explanations in Chapter 1.

While all terms in the effective cold-atom Hamiltonian (3.2) are gauge-invariant, the interaction $\sim \delta$ does not lead to a Lorentz scalar in the continuum limit. Thus, for a given lattice size, one has to limit the strength δ with respect to the electric field energy. Experimentally this may be efficiently achieved by reducing the inter-species overlap with respect to the homo-nuclear one, for instance through an off-resonant laser beam creating a species-dependent dipole force or by the gravitational potential. The overall time scale of the experiment is of the order 100 Hz as will be demonstrated in the experimental setup of Section 3.4. In the limit of negligible δ we then identify the atomic QED coupling constants as $e^2 = \chi$, $a_s^2 = 1/(4\chi\lambda\bar{n}^2)$, which yields the dimensionless coupling $g^2 = \sqrt{\chi/4\lambda\bar{n}^2}$. By appropriate choice of parameters one can in principle tune g^2 across a wide range of values reaching both the strong and the weak coupling regime. However, one needs to ensure convergence of physical observables with respect to further increases of \bar{n} while keeping the dimensionless gauge coupling fixed by, e.g., decreasing λ . Experimentally this can be achieved by reducing the ratio of inter-species to homo-nuclear overlaps in a similar way as for δ . Varying total atom numbers will mainly translate to fluctuations in

\bar{n} and hence in a_s^2 and g^2 . This can be closely monitored during the experiment to estimate and control resulting errors.

Having introduced our implementation scheme, we apply it to the phenomenon of charge confinement next. In our setup, confinement will be directly detectable as a finite change in occupation number on the links that connect two static charges, even for increasing distance $D \rightarrow \infty$ between the charges. As an illustration, we discuss the emergence of confinement in compact QED in the weak coupling regime, using a variational ansatz for the ground state wave function [121]. We explain that confinement will be robustly observable for the proposed cold-atom implementation against experimental imperfections due to finite boson numbers and unwanted inter-species density interactions $\sim \delta$ of the atoms.

3.3 Charge confinement

Gauge field dynamics in two or more spatial dimensions can give access to one of the most intriguing phenomena: confinement. The most prominent example is the confinement of quarks into colorless hadrons, forming the basis for nuclear matter in quantum chromodynamics [11]. Here, we apply our implementation scheme for two-dimensional gauge fields to confinement of electric charges in compact quantum electrodynamics [122]. Its description can be a difficult problem for classical computational techniques and quantum simulators promise important progress in our abilities to address equilibrium as well as dynamical properties out of equilibrium from first principles.

In compact QED, charge confinement manifests itself as a string of electric flux connecting two static sources of opposite electric charge. While for $g^2 \rightarrow \infty$, the flux string carries unit electric field strength along the shortest path between the charges, it is delocalized by fluctuations due to magnetic interactions or finite temperature. However, in two spatial dimensions and for small temperatures, a finite flux string persists at arbitrarily weak coupling ($g^2 \rightarrow 0$). The energy of this string increases linearly with the separation D of the charges, which are thus confined [121–123].

As an illustration of our approach, we characterize confinement in the weak coupling regime employing the variational technique of Ref. [121], which makes use of a dual description of the gauge fields as outlined in more detail in the appendix 3.B. Choosing a gauge-invariant superposition of quadratic trial wave functionals, one minimizes the Hamiltonian energy density under the Gauss constraint of two external charges with separation D . For large separation D , this procedure yields the energy $\langle \hat{H}_{\text{QED}} \rangle \sim \sigma D$, where $\sigma = (\pi^2 - 4)\mu^2/2\pi^3$ is the string tension¹ and

$$\mu^2 a_s^2 = 4\pi^2 \exp\left(-\frac{1}{(2g)^2} \int_{-\pi}^{\pi} d^2k \frac{1}{\sqrt{4 - 2\cos(k_x) - 2\cos(k_y)}}\right), \quad (3.4)$$

is a characteristic infrared scale, generated by self-interactions of the gauge fields, and setting the length scale of confinement $D_C = e^2/\mu^2$ [121].

3.3.1 Confinement in the cold-atom quantum simulator

We now turn to the cold-atom implementation of compact QED, (3.2) and (3.3), which includes the two main imperfections of a finite boson number and the interspecies density interactions. In the following, we account for both of them using a perturbative analysis around the variational ground state wave functional in the limit $\bar{n} \rightarrow \infty$ and $\delta/\chi \rightarrow 0$ for small couplings g^2 to compute atom numbers $\langle \hat{n}_{\mathbf{n},i} \rangle$ and the ground state energy $\langle \hat{H}_{\text{CA}} \rangle$.

Since the perturbations enter the ground state only in second order, the leading result for the atom number gives the same electric field as in compact QED, $\langle \hat{\mathcal{E}}_{\mathbf{n},i} \rangle =$

¹We have a factor 2 difference compared to Ref. [121], see also the appendix 3.B.

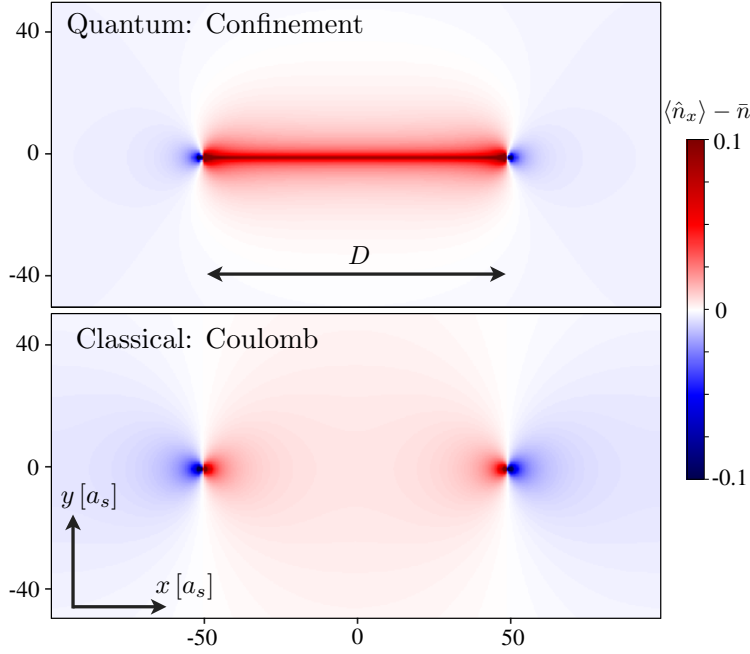


FIGURE 3.2: Flux string: (Top) The relative atom number on the x -links, $\langle \hat{n}_{\mathbf{n},x} \rangle - \bar{n}$, exhibits a confining string (top) between two opposite external charges in the quantum theory. Here, the distance is $D = 100a_s$ with $g^2 = 1$ and $\mu^2/e^2 \approx 0.071/a_s$. (Bottom) The corresponding classical Coulomb case is shown by switching off quantum fluctuations ($g^2 \rightarrow 0$). Taken from [3].

$\langle \hat{n}_{\mathbf{n},i} \rangle - \bar{n} = \langle \hat{E}_{\mathbf{n},i} \rangle$. For the atom number on x -links in the center of the string we find $\langle \hat{n}_x \rangle \approx \bar{n} - \mu^2 a_s / (\pi e^2) \log(\mu^2 a_s / (\pi e^2))$, for y -links we get $\langle \hat{n}_y \rangle \approx \bar{n}$ in the limit of infinite volume and charge separation, see also the derivations outlined in Section 3.B. For finite lattices, which are relevant experimentally, we show the result in Fig. 3.2 where one observes that the atoms form a confining flux tube between two external charges at $\mathbf{n}_+ = (-D/(2a_s), 0)$ and $\mathbf{n}_- = (D/(2a_s), 0)$. The result is obtained on a 200×200 square lattice with periodic boundary conditions, where the detailed expressions which we evaluate numerically are presented in the appendix 3.B. While our theoretical estimates are strictly valid only in the $g^2 \ll 1$ region, confinement is expected to persist for all values of the gauge coupling. For the illustration of Fig. 3.2 we have evaluated our theoretical results at $g^2 = 1$, i.e., extrapolating beyond the well-established weak coupling regime. The validity of such a procedure could be tested in a future quantum simulation experiment at intermediate to strong couplings [124].

The result for the energy expectation $\langle \hat{H} \rangle$ of the ground state is shown in Fig. 3.3. Results are obtained on a 4000×4000 lattice for $g^2 = 1$, corresponding to $\mu^2/e^2 = 1/D_C \approx 0.069/a_s$, where we again refer to the appendix 3.B for the detailed numerical formulae. While at short distances ($D \lesssim D_C$) the classical Coulomb energy contribution is visible, at large distances ($D \gg D_C$) the ground state energy is dominated by the linear confining potential generated from quantum fluctuations. The first correction to the QED Hamiltonian due to the finite boson

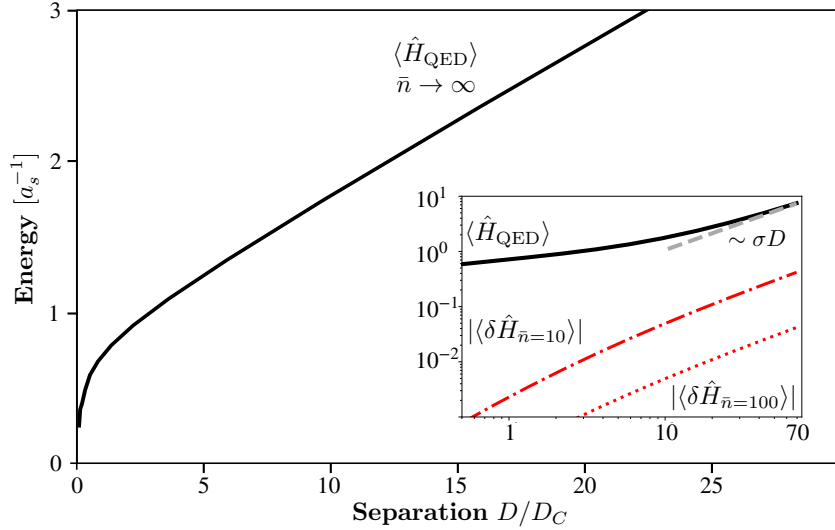


FIGURE 3.3: Confinement: Ground state energy $\langle \hat{H}_{\text{QED}} \rangle$ in presence of two external opposite charges at separation D . The linear confining potential dominates at large $D \gg D_C$. The inset shows the ground state energy on a logarithmic scale, as well as the leading finite \bar{n} corrections for $\bar{n} = 10$ (red dashed-dotted) and $\bar{n} = 100$ (red dotted). The dashed gray line is the leading analytic asymptotic result from Ref. [121], with string tension $\sigma = (\pi^2 - 4)\mu^2/(2\pi^3)$. (We have a factor 2 difference compared to Ref. [121]). Taken from [3].

number of the cold-atom realization (3.3) is given by

$$\begin{aligned} \delta \hat{H}_{\bar{n}} = & -\frac{1}{4\bar{n}a_s^2e^2} \sum_{\mathbf{n}} (\hat{\mathcal{E}}_{\mathbf{n},x} + \hat{\mathcal{E}}_{\mathbf{n},y} + \hat{\mathcal{E}}_{\mathbf{n}+\hat{x},y} + \hat{\mathcal{E}}_{\mathbf{n}+\hat{y},x} + 2) \\ & \times \cos(\hat{\phi}_{\mathbf{n},x} - \hat{\phi}_{\mathbf{n},y} + \hat{\phi}_{\mathbf{n}+\hat{x},y} - \hat{\phi}_{\mathbf{n}+\hat{y},x}), \end{aligned} \quad (3.5)$$

which, close to the continuum limit ($a_s \rightarrow 0$), reduces to

$$\delta \hat{H}_{\bar{n}} \rightarrow -(2\bar{n}a_s^2e^2)^{-1} \sum_{\mathbf{n}} \cos(\hat{\phi}_{\mathbf{n},x} - \hat{\phi}_{\mathbf{n},y} + \hat{\phi}_{\mathbf{n}+\hat{x},y} - \hat{\phi}_{\mathbf{n}+\hat{y},x}), \quad (3.6)$$

up to an irrelevant constant. With the identification $\hat{U}_{\mathbf{n},i} \approx \exp(i\hat{\phi}_{\mathbf{n},i})$ this term is of the same structure as the plaquette term in (3.1). Hence, at leading order, we obtain a correction to the string energy $\langle \delta \hat{H} \rangle_{\bar{n}} = -2\mu^2 D/(\pi^3 \bar{n})$, which smoothly goes to zero for large \bar{n} , see the inset of Fig. 3.3.

The second correction concerns the inter-species density interactions with strength δ . We find their contribution vanishes to linear order in δ within our perturbative analysis. This follows from the symmetry property of the ideal QED ground state (with external charges at $y = 0$) under the parity transformation $\mathcal{P}y = -y$: electric fields transform as vectors; they are antisymmetric along y -direction. While the leading ($\delta \rightarrow 0$) part of the Hamiltonian is invariant under this transformation, the linear δ -correction is antisymmetric and vanishes. We hence conclude that confinement persists against first-order corrections in our proposed implementation scheme.

3.3.2 Initial state preparation and observables

To observe confinement in our 2D quantum simulator we propose to prepare the system in its electric ground state in the limit $g^2 \rightarrow \infty$, corresponding to spatially separated species, i.e., $\lambda \rightarrow 0$. We assume that within each well of the optical lattice the atoms initially condense in the spin state $|1\rangle$ for both species. Then, electric field eigenstates are obtained by ramping up the coupling of the respective neighboring clouds to form the symmetric superpositions $|+\rangle^2$.

Introducing a pair of external charges $\pm Q$ requires single-site control over the atom number on a single-particle level. This allows to choose the initial state $|\psi\rangle$ as a product state of electric field eigenstates in accordance with the Gauss sectors $\hat{G}_{\mathbf{n}\pm} |\psi\rangle = \mp Q/e |\psi\rangle$ and $\hat{G}_{\mathbf{n}} |\psi\rangle = 0$ elsewhere.

The two species are slowly brought into spatial contact to adiabatically decrease the coupling g^2 , where $|\psi\rangle$ stays close to the instantaneous ground state under the Gauss constraint, see also 2. This adiabatic sweep, see e.g. Ref. [32], is possible in two-dimensional compact QED which does not exhibit a confinement-deconfinement transition as a function of the coupling [121, 122]. Since its spectrum is gapped for any value of g^2 , the adiabaticity condition can in principle be upheld deep into the weak coupling region. However, in order to reach weak couplings, long coherence times are required. Throughout this protocol, the flux tube can be observed as shown in Fig. 3.2 via the local expectation values $\langle \hat{\mathcal{E}}_{\mathbf{n},x} \rangle = \langle \hat{n}_{\mathbf{n},x} \rangle - \bar{n}$. The number expectation value $\langle \hat{n}_{\mathbf{n},x} \rangle$ therein is obtained as the total atom number in the corresponding underlying spin states $|0\rangle_{\mathbf{n}-\hat{y},B}$ and $|1\rangle_{\mathbf{n},B}$.

Having illustrated the physics of confinement for a quantum simulation experiment in this section, we turn to the real-time dynamics of gauge fields next. We focus on the case of a single plaquette, the physics of which will be discussed with an explicit experimental realization.

²Alternatively one can choose the antisymmetric state $|-\rangle$ for each species.

3.4 Experimental realization of a unit plaquette

In the previous section we have established confinement as an intriguing equilibrium phenomenon which could be accessed in cold-atom quantum simulators. In this section, we turn to the non-equilibrium dynamics of synthetic dynamical gauge fields, where we investigate an ultra-cold atomic mixture of ^{23}Na and ^7Li atoms. Such mixture experiments provide versatile platforms for quantum simulations of physical systems. Besides the simulation of artificial gauge fields, applications include for instance implementations of the Bose polaron problem [125, 126]. By using the spin-changing collisions [127] to couple the two atomic species, the experimental setup implements a scalable building block of the scheme outlined in the previous sections. While the present setup [52] was previously analyzed with respect to the dynamics of mean fields, we investigate the evolution of spin fluctuations across a wide range of non-equilibrium initial conditions in this section. Fluctuations can be crucial in out-of-equilibrium situations, such as instabilities [128], the build-up of structure far from equilibrium [88, 89, 129], or the fate of the “false vacuum” in tunneling decays toward equilibrium [130]. Here, cold-atom simulators promise unique insights into the dynamics of fluctuations in quantum many-body systems.

We identify different dynamical regimes of our system and characterize the evolution in terms of phenomena such as instabilities and the onset of thermalization. Depending on the initial spin imbalance of our mixture, we identify the three regimes: a long-lived metastable regime, an unstable region showing strong growth of fluctuations, and a fast relaxing regime approaching thermal equilibrium. We compare our data to theory by extending an earlier mean-field model [52] to incorporate the dynamics of fluctuations. Experimentally extracting the fluctuations allows us to reconstruct the effective potentials that characterize the various types of dynamics. Our approach enables a detailed characterization of the complex many-body states out-of-equilibrium in atomic mixture experiments.

3.4.1 Experimental setup and state preparation

The experiment is initiated by preparing an ultra-cold bosonic mixture of sodium (Na) and lithium (Li) atoms in a crossed optical dipole trap. After cooling and condensation, the sample consists of approximately $N_{\text{Na}} \approx 3 \times 10^5$ sodium and $N_{\text{Li}} \approx 3 \times 10^4$ lithium atoms in overlapping atomic clouds. The two species are prepared in their spin $F = 1$ manifolds, where the application of an external magnetic field ($B = 2.118(2)\text{G}$) leads to an energy splitting between three internal hyperfine states [120]. Suitably choosing such energy separations allows us to confine the atoms to their lowest lying states, $|F = 1, m_F = 0, 1\rangle$, for both species, see Fig. 3.4a.

Initially, the atoms are prepared in $m_F = 1$ corresponding to their single-particle ground state. To initialize the non-equilibrium dynamics, we follow the experimental sequence described in Ref. [52]. We transfer an average fraction $\bar{\eta}_{\text{Na}}$ of Na

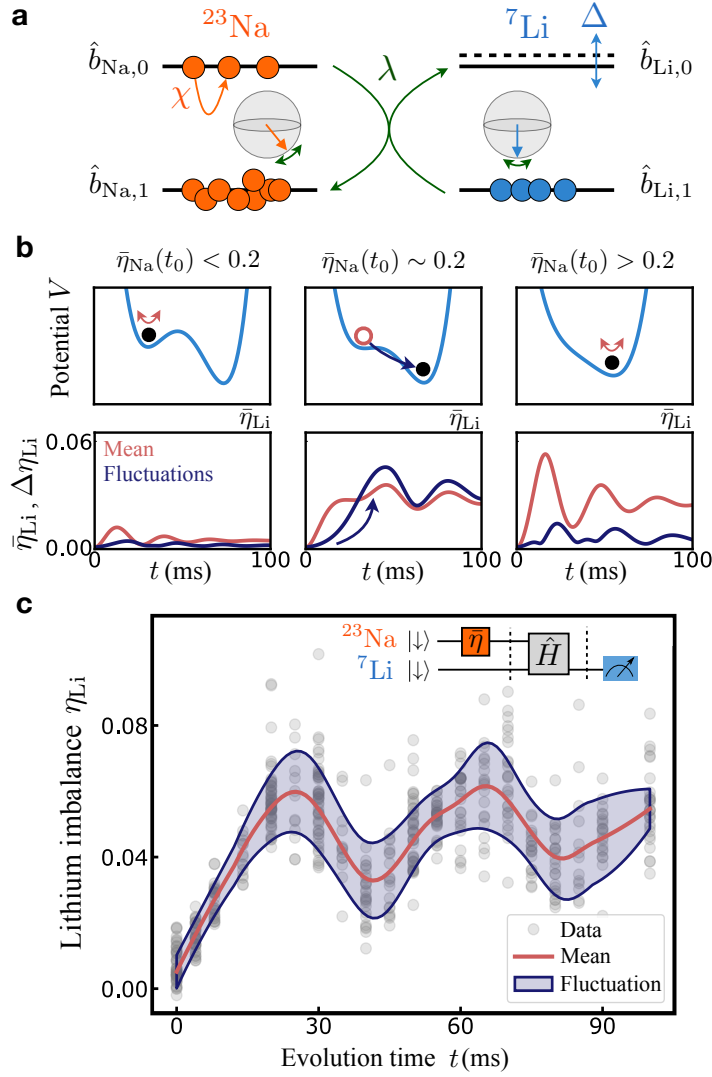


FIGURE 3.4: Dynamics of spin fluctuations induced by spin changing collisions: (a) The ultra-cold atomic mixture is coupled through spin-changing collisions between sodium and lithium atoms realizing effective spins degrees of freedom. (b) Varying initial conditions probe the mixture in three different regimes as illustrated with effective potentials: a meta-stable state, an instability with growth of fluctuations, and fast relaxation. Solid lines show numerical real-time calculations of our effective model (appendix 3.C.3). (c) The fluctuations of the data (shaded blue) around mean values (red) grow in time, where grey circles show single realizations of preparation, evolution and measurement (see inset). Solid lines are smoothed interpolations of data points. Figure taken from [7].

atoms to the energetically higher $m_F = 0$ state, thereby exciting the atoms out of equilibrium. To achieve this, the internal Na states are coupled with a highly tunable microwave setup, where a two-pulse sequence transfers the atoms through the intermediate state $|F = 2, m_F = 2\rangle$. While this provides an efficient passage for Na atoms, corresponding internal states of Li are kept out of resonance, and it remains polarized in $|F = 1, m_F = 1\rangle$ for all considered initial states at time $t_0 = 0$ ms. We prepare a wide range of Na initial states $\bar{\eta}_{\text{Na}}(t_0)$, which also sets the total (conserved)

magnetization for the dynamics and allows us to tune the effective system parameters to explore non-equilibrium physics in different regimes. The various types of non-equilibrium phenomena are illustrated in Fig. 3.4b, where the dynamics can be understood from effective potentials, which we reconstruct in the following.

3.4.2 Non-equilibrium dynamics

After state preparation, we let the system evolve for times of up to $t = 100\text{ms}$, during which the atoms exchange spin, resulting in oscillatory dynamics as shown in Fig. 3.4c. The spin dynamics is made possible through a precise control of the external magnetic field, such that spin states of Na and Li are kept in resonance during the evolution. To investigate the dynamics, we detect the resulting spin populations of lithium by performing state-selective time-of-flight (TOF) measurements (“Stern-Gerlach method” [52]). Here, atoms in different spin states are spatially separated with a magnetic field gradient before imaging, which gives access to the individual atom populations N_{Li,m_F} and hence the spin imbalance $\hat{\eta}_{\text{Li}} = \hat{N}_{\text{Li},0}/\hat{N}_{\text{Li}}$, where $\hat{N}_{\text{Li}} = \hat{N}_{\text{Li},0} + \hat{N}_{\text{Li},1}$, as shown in Fig. 3.4b. We repeat the experimental cycle up to 20 times per evolution time t to observe the fluctuating signal. From our measurements, we extract the mean values ($\bar{\eta}_{\text{Li}} = \langle \hat{\eta}_{\text{Li}} \rangle$) and second-order correlations ($\Delta\eta_{\text{Li}} = \sqrt{\langle \hat{\eta}_{\text{Li}} \hat{\eta}_{\text{Li}} \rangle - \langle \hat{\eta}_{\text{Li}} \rangle^2}$) in order to characterize the non-equilibrium dynamics³.

For the initial state with $\bar{\eta}_{\text{Na}} = 0.4$, the experimentally observed spin evolution is displayed in Fig. 3.5. As panel a shows, the signal of the mean Li imbalance $\bar{\eta}_{\text{Li}}$ rises rapidly initially, and it is strongly damped toward a steady state at late times. Furthermore, we investigate the data beyond mean populations by considering the dynamics of corresponding imbalance fluctuations ($\Delta\bar{\eta}_{\text{Li}}$), see panel b. Fluctuations, being small initially, build up quickly during the first 30ms, and they approach an approximately constant value of $\Delta\eta_{\text{Li}} \approx 0.01$ at later times.

3.4.3 Effective spin model

To diagnose relevant processes and access the effective potential landscape of the many-body problem, we compare our measurements to numerical real-time calculations. In the experiment, the atoms are localized in a deep harmonic trap. Hence, we describe the coupled system of sodium ($a = \text{Na}$) and lithium ($a = \text{Li}$) with single spatial modes for each magnetic sub-state $m_F = 0, 1$, where the bosonic creation (annihilation) operators $\hat{b}_{a,i}^\dagger$ ($\hat{b}_{a,i}$) fulfill commutation relations $[\hat{b}_{a,i}, \hat{b}_{b,j}^\dagger] = \delta_{ij}\delta_{ab}$. In view of the atoms’ SU(2) symmetry, we introduce collective spin operators using the Schwinger boson representation, i.e., $\hat{L}_{a,+} = \hat{b}_{a,0}^\dagger \hat{b}_{a,1}$, $\hat{L}_{a,-} = \hat{b}_{a,0} \hat{b}_{a,1}^\dagger$, and $\hat{L}_{a,z} = (\hat{b}_{a,0}^\dagger \hat{b}_{a,0} - \hat{b}_{a,1}^\dagger \hat{b}_{a,1})/2$. The evolution of the atoms is modelled by the Hamiltonian (see section 3.C.1 for derivational details)

$$\hat{H} = \chi \hat{L}_{\text{Na},z}^2 + \Delta \hat{L}_{\text{Li},z} + \lambda (\hat{L}_{\text{Na},+} \hat{L}_{\text{Li},-} + h.c.), \quad (3.7)$$

³Definitions of imbalances for Na are analogous.

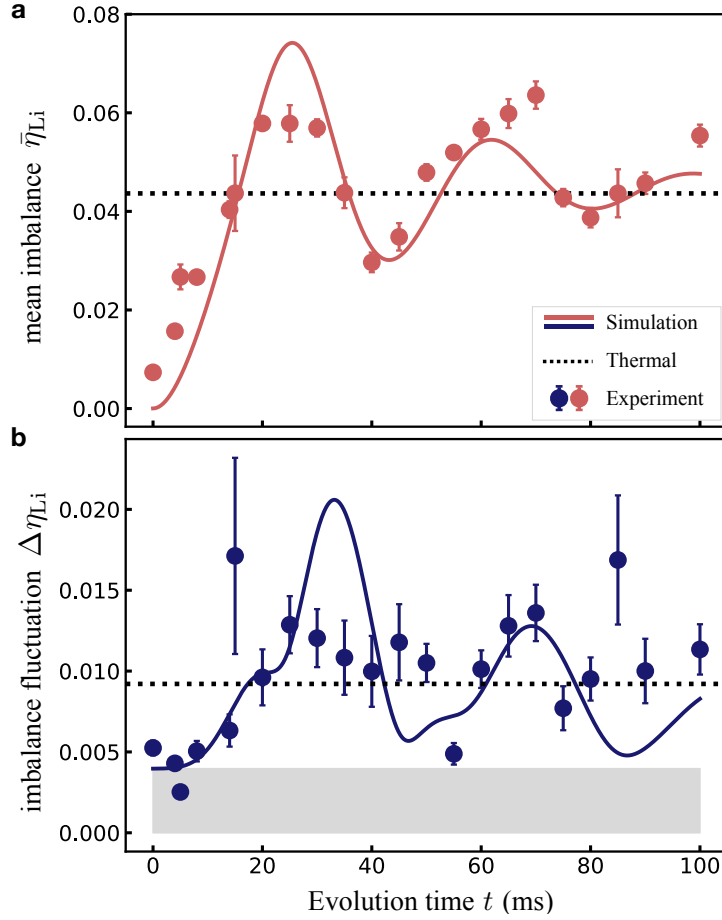


FIGURE 3.5: Time evolution of mean and fluctuations: (a) We show the evolution of mean lithium spin transfer $\bar{\eta}_{Li}$ for evolution times $t \leq 100$ ms starting from a mean sodium imbalance of $\bar{\eta}_{Na} = 0.406$. The damped-oscillatory behaviour of the data (red circles) is well-described by our semi-classical calculation (solid line) which accommodates initial state fluctuations. (b) The two-point correlation data (blue circles) shows an initial growth of fluctuations (see Fig. 3.4c) and reaches an approximately constant value at later times. The late time data is in approximate agreement with a thermal calculation for a temperature $T = 630$ nK (dotted line). Error bars represent standard error on the mean. Our detection of spin fluctuations has a systematic offset of $0.0040(1)$ for $\Delta\eta_{Li}$ (grey shaded area), which we added to the numerical curve in panel b. Figure taken from [7].

where $h.c.$ denotes hermitian conjugation. The spin-changing dynamics is driven by the interaction coupling λ . The term Δ models the effective energy offset between magnetic sub-states, and χ characterizes intra and inter-species interaction strengths from atom collisions without changes in spin. Here, Δ depends only on the total numbers of Na and Li atoms and the total magnetization ($\hat{M} = \hat{L}_{Li,z} + \hat{L}_{Na,z}$). They are modelled as conserved quantities during the evolution, but depend on the details of the initial condition. Carefully choosing these conserved quantities hence enables the controlled investigation of our system in different parameter regimes. We consider a semi-classical (truncated Wigner [131]) approximation to describe the large condensates realized in the experiment. The effective spin degrees

of freedom are simulated with classical evolution equations, and quantum effects are implemented as the Gaussian initial state fluctuations of the initial coherent spin states. Furthermore, we average over initial atom number fluctuations, which vary for different realizations by about 10% for both Na and Li. The initial state fluctuations and the model parameters are detailed in the sections 3.C.2 and 3.C.3.

In addition to the coherent spin dynamics, the spatial excitations of the atomic cloud are expected to interact with spin degrees of freedom and exchange energy. To account for such an effect in our model, we include a friction term for the spin as given by a Landau-Lifshitz-Gilbert-type damping [132] $\partial_t \mathbf{L}_{\text{Li}} = \{\mathbf{L}_{\text{Li}}, H\} - \gamma(L_{\text{Li},z} \mathbf{L}_{\text{Li}} - \mathbf{L}_{\text{Li}}^2 \mathbf{e}_z)$, where \mathbf{L}_{Li} is the three-component lithium spin, \mathbf{e}_z is the unit vector in z direction, and $\{\mathbf{L}_{\text{Li}}, H\}$ represents the (undamped) classical evolution equations via Poisson brackets. Here, we choose a damping rate of $\gamma = 1.8 \times 10^{-3} \text{Hz}$, and furthermore adjust the sodium spin accordingly to conserve the system's total magnetization, see 3.C.3. With this friction term, we observe a fast damping at long times, see Fig. 3.5.

To characterize the dynamics observed in the present experiment, we compare our data with thermal equilibrium. To this end, we define a canonical ensemble by the partition sum $Z = \text{Tr}[\hat{P}_M \exp(-\beta \hat{H})]$, where \hat{P}_M projects the system to a fixed magnetization which is set by the initial state $\langle \psi_0 | \hat{M} | \psi_0 \rangle$. Furthermore, $\beta = 1/(k_B T)$ sets the (inverse) temperature of the system, where k_B is the Boltzmann constant. In Fig. 3.5 we compare our results to a thermal ensemble with the temperature of the condensate $T = 630(20) \text{nK}$ as obtained by extracting the atoms' momentum distributions with TOF-measurements [109]. At late times, both mean value and fluctuations of the Li imbalance oscillate around these thermal estimates.

3.4.4 Probing the non-equilibrium regimes

To explore the dynamics in different parameter regimes, we consider the system evolution for different initial states in the following. In Fig. 3.6 we show the Li imbalance after 30ms evolution time for a range of Na initial states. We observe a pronounced resonance shape in the mean imbalance value, with a sharp transition around $\bar{\eta}_{\text{Na}} \approx 0.2$, as illustrated in panel b. On the left side of the transition, $\bar{\eta}_{\text{Na}} < 0.2$, the Li imbalance stays small. On the other hand, it decays on the right side of the resonance for larger values of $\bar{\eta}_{\text{Na}}$. The transition is accompanied with a sharp peak in the fluctuations $\Delta\eta_{\text{Li}}$, as displayed in panel c. This peak indicates an enhanced sensitivity of the dynamics, leading to a fast growth of fluctuations in the data. The data is in good agreement with the results from our semi-classical numerical calculations, as shown in Fig. 3.6, and our calculations recover the essential features of the spin-changing dynamics.

As illustrated for $\bar{\eta}_{\text{Na}} = 0.4$ in Fig. 3.5, data taken as early as 30ms may already provide valuable insight for the approximate late-time evolution of the system. In fact, for the given initial conditions, the experimental data in Fig. 3.6 shows an excellent agreement with late-time numerical results at $t = 150 \text{ms}$. To characterize our

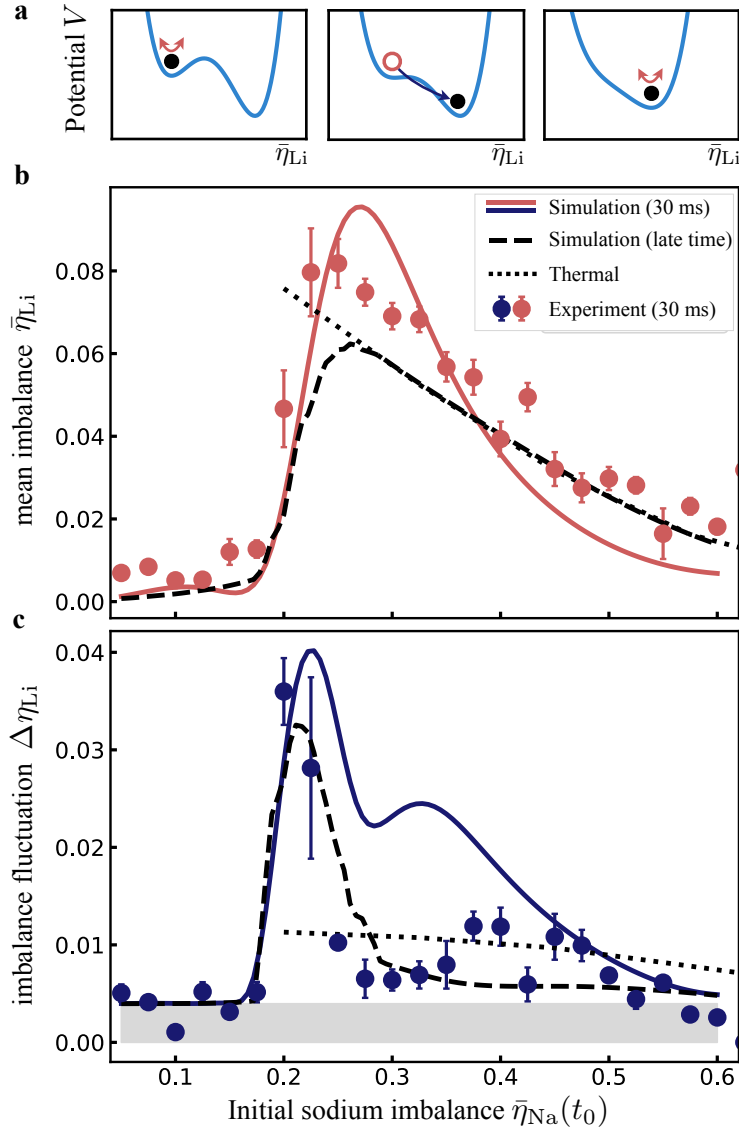


FIGURE 3.6: Non-equilibrium regimes: (a) We indicate the different dynamical regimes with sketches of the potential landscape (see main text). (b) After 30ms evolution time, the mean lithium imbalance $\bar{\eta}_{Li}$ reveals a sharp resonance behavior for changing initial conditions set by $\bar{\eta}_{Na}$. (c) The fluctuation signal shows a large peak around $\bar{\eta}_{Li} \sim 0.2$, indicating an instability regime characterized by the fast growth of fluctuations. We find an overall good agreement with numerical real-time calculations at 30ms (solid colored) and a late time calculation at 150 ms (dashed), indicating the robustness of our results. On the right-hand side of the transition we find good agreement with a (classical) thermal ensemble at temperature 630(20)nK (dotted). The shaded area in (c) indicates the fluctuation offset from detection noise, which we add to the numerical curve in panel c. Figure taken from [7].

system in the regime $\bar{\eta}_{Na} > 0.2$, we compare the data to corresponding predictions from the thermal ensemble, finding an overall good agreement on the right-hand side of the resonance shape, where the agreement is especially precise on the mean imbalance of Li. We thus observe indications for an onset of thermalization in our system. Conversely, on the left-hand side of the transition the spin-changing

dynamics is strongly suppressed, and thermalization dynamics is not initiated on observable time scales. In our theoretical modelling, this suppression extends to evolution times beyond 150ms, indicating a long-lived metastable state.

These qualitative features of the system dynamics may be illustrated in terms of an evolution within effective potentials for mean fields. For fixed conserved charges, the classical evolution of the Li imbalance, as relevant for the early time dynamics, may be written as a second-order differential equation $\partial_t^2 \bar{\eta}_{\text{Li}} = -\partial V(\bar{\eta}_{\text{Li}})/\partial \bar{\eta}_{\text{Li}}$ with a quartic potential V [110], see Section 3.C.5. In Fig. 3.6 we show three configurations of the potential for different values of the total magnetization as set by the initial state of Na. For small initial Na imbalances $\bar{\eta}_{\text{Na}} < 0.2$ the system is constrained to small Li imbalances, as indicated by a second, local minimum in the effective potential. Conversely, for larger $\bar{\eta}_{\text{Na}} > 0.2$, the system evolution is governed by oscillations around a single global minimum which approximately corresponds to the thermal mean value. These regimes are separated by a sharp transition at $\bar{\eta}_{\text{Na}} \sim 0.2$, where the system dynamics becomes unstable with respect to the second minimum. Corresponding mean and fluctuation values are expected to rapidly rise to similar magnitudes, as confirmed by the data in Fig. 3.6.

3.4.5 Identification with single-plaquette gauge theory

The model Eq. (3.7) may be identified with a single-plaquette realization of an atomic synthetic gauge theory, similar to the cold-atom Hamiltonian Eq. (3.2) proposed earlier in this chapter (see Section 3.2.2). By using the conservation laws of the dynamics and employing the original bosonic operators, Eq. (3.7) is equivalent to the following Hamiltonian,

$$\begin{aligned} \hat{H} = & \tilde{\chi}(\hat{N}_{\mathbf{n}_0,x}^2 + \hat{N}_{\mathbf{n}_0+\hat{x},y}^2 + \hat{N}_{\mathbf{n}_0+\hat{y},x}^2 + \hat{N}_{\mathbf{n}_0,y}^2) \\ & + \mu(\hat{N}_{\mathbf{n}_0,x} - \hat{N}_{\mathbf{n}_0+\hat{y},x} - \hat{N}_{\mathbf{n}_0,y} - \hat{N}_{\mathbf{n}_0+\hat{x},y}) \\ & - \lambda(\hat{b}_{\mathbf{n}_0,x}\hat{b}_{\mathbf{n}_0+\hat{x},y}\hat{b}_{\mathbf{n}_0+\hat{y},x}^\dagger\hat{b}_{\mathbf{n}_0,y}^\dagger + h.c.), \end{aligned} \quad (3.8)$$

where \mathbf{n}_0 marks the base position of the plaquette, see Fig. 3.7. We identified the indices for Na as $m_F = 0 \rightarrow \mathbf{n}_0$, $m_F = 1 \rightarrow \mathbf{n}_0 + \hat{y}$, and correspondingly for Li, as $m_F = 1 \rightarrow \mathbf{n}_0$, $m_F = 0 \rightarrow \mathbf{n}_0 + \hat{x}$. Here, Na plays the role of gauge fields in x direction and Li correspondingly represents the gauge fields along y direction, and the parameters $\tilde{\chi}$, and μ may be straightforwardly derived from the model Eq. (3.7). The Hamiltonian is invariant under the gauge transformations

$$\hat{b}_{\mathbf{n},i} \rightarrow e^{i\sum_{\mathbf{m}} \alpha_{\mathbf{m}} \hat{G}_{\mathbf{m}}} \hat{b}_{\mathbf{n},i} e^{-i\sum_{\mathbf{m}} \alpha_{\mathbf{m}} \hat{G}_{\mathbf{m}}}, \quad (3.9)$$

with arbitrary phases $\alpha_{\mathbf{m}}$, and Gauss operators

$$\hat{G}_{\mathbf{n}} = \hat{N}_{\mathbf{n}_0,x} + \hat{N}_{\mathbf{n}_0,y} - \hat{N}_{\mathbf{n}_0-\hat{x},x} - \hat{N}_{\mathbf{n}_0-\hat{y},y} - Q_{\mathbf{n}}. \quad (3.10)$$

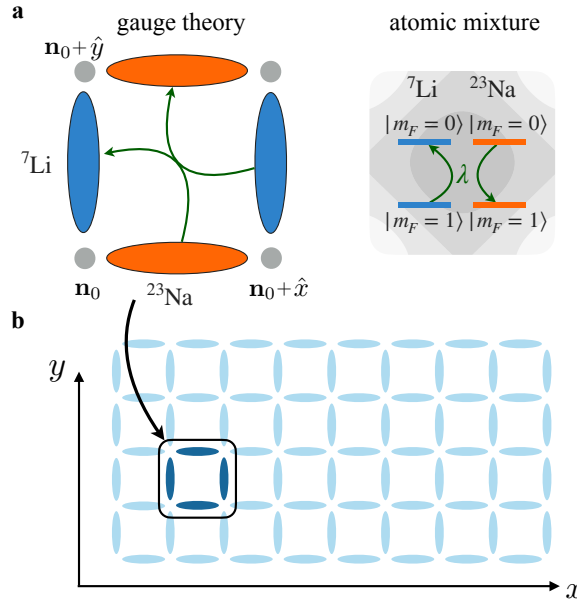


FIGURE 3.7: Identification of the mixture with a single-plaquette gauge theory: (a) The gauge links of a single plaquette may be identified with the magnetic sub-states of the mixture experiment. (b) The system can be scaled up to a gauge field theory by coupling multiple unit cells, following the scheme outlined in section 3.2.2.

Here, we included the classical charges $Q_{\mathbf{n}}$, and employed fixed boundary conditions where all fields outside of the plaquette \mathbf{n}_0 are set to zero. In the experiment, gauge invariance of the evolution corresponds to the conservation of total atom numbers and magnetization.

In contrast to Eq. 3.2, the Hamiltonian includes an additional single-particle energy offset $\sim \mu$. In the experimental realization, we required a non-zero value of μ owing to the large occupation difference in the initial spin states and in order to realize gauge-invariant dynamics on observable time scales. To approach the Hamiltonian for QED on the single plaquette, we consider initial states with $\langle \hat{b}_{\mathbf{n},i}^\dagger \hat{b}_{\mathbf{n},z} \rangle \approx \bar{n} \gg 1$, which translates to the condition $\langle \hat{L}_{a,i} \rangle \approx 0$, for $|\mathbf{L}_a| \gg 1$. Such initial states can be prepared experimentally, for instance with additional microwave pulses. For such initial conditions, one may tune the experimental parameters, for instance the external magnetic field, to set $\mu = 0$. The instability phenomenon discussed in the previous section translates to the continuous variable gauge fields of QED. Specifically, it can be observed through exponential growth of fluctuations in time, where the dynamics of QED gauge fields is obtained for large values of \bar{n} , as detailed in the appendix 3.C.6.

In this section, we have explored the non-equilibrium dynamics of gauge fields with mean values and second order correlations. In the following, we consider a different route, where we investigate the non-equilibrium dynamics of a \mathbb{Z}_2 lattice gauge theory through the entanglement spectrum.

3.5 Non-equilibrium entanglement spectrum of a gauge theory

In the previous sections, we considered the time-evolution of mean-values and second-order correlation functions to investigate the dynamics of cold-atom gauge theories. In this section, the non-equilibrium dynamics of gauge fields is investigated through their entanglement structure [133, 134].

Entanglement describes the non-local quantum correlations of microscopic particles [135], and thus may serve to characterize their interactions in space and time. While the spread of information in quantum many-body systems is often described with entanglement entropies between (bipartite) sub-systems [26], the reduced density matrix encodes the complete entanglement structure [133]. Here, we focus on the entanglement structure of a \mathbb{Z}_2 lattice gauge theory [54, 59] in two spatial dimensions. The complex evolution of the gauge fields is found to undergo a series of regimes, which we characterize by the non-equilibrium entanglement spectrum: level repulsion at earliest times, self-similar evolution at intermediate times and eventually relaxation [136].

3.5.1 Model and Hamiltonian

The lattice gauge theory is formulated on a two-dimensional spatial lattice labeled by sites $\mathbf{n} = (n_x, n_y)$, and the gauge fields are situated on the links (\mathbf{n}, x) and (\mathbf{n}, y) along x and y directions of the lattice. Their dynamics is governed by the Hamiltonian

$$\hat{H} = - \sum_{\mathbf{n}} \hat{\sigma}_{\mathbf{n},x}^z \hat{\sigma}_{\mathbf{n}+\hat{x},y}^z \hat{\sigma}_{\mathbf{n}+\hat{y},x}^z \hat{\sigma}_{\mathbf{n},y}^z - \epsilon \sum_{\mathbf{n},i} \hat{\sigma}_{\mathbf{n},i}^x, \quad (3.11)$$

where $\hat{\sigma}_{\mathbf{n},i}^j$ are Pauli- j operators on links (\mathbf{n}, i) which fulfill the commutation relations $[\hat{\sigma}_{\mathbf{n},i}^j, \hat{\sigma}_{\mathbf{n}',i'}^k] = i\epsilon_{jkl} \hat{\sigma}_{\mathbf{n},i}^l \delta_{\mathbf{nn}'} \delta_{ii'}$. Here, the first term represents the magnetic field interactions, while the term $\sim \epsilon$ is the electric energy.

Analogous to the previously considered U(1) gauge fields, gauge invariance in the evolution of the system is expressed in this model as the condition $[\hat{H}, \hat{G}_{\mathbf{n}}] = 0$, where

$$\hat{G}_{\mathbf{n}} = \hat{\sigma}_{\mathbf{n},x}^x \hat{\sigma}_{\mathbf{n}-\hat{x},x}^x \hat{\sigma}_{\mathbf{n}-\hat{y},y}^x \hat{\sigma}_{\mathbf{n},y}^x \quad (3.12)$$

are the \mathbb{Z}_2 Gauss operators. Physical states fulfill the condition $\hat{G}_{\mathbf{n}} |\psi\rangle = |\psi\rangle$, which, once enforced for the initial state, continues to hold due to the gauge invariance of the evolution.

To investigate the entanglement properties of this gauge theory, we employ a dual description, which we illustrate here for an infinite system following Refs. [137,

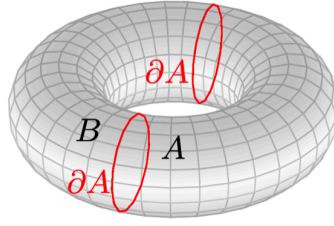


FIGURE 3.8: Two-dimensional lattice geometry theory: The \mathbb{Z}_2 lattice gauge theory is studied on a two dimensional torus, with entanglement cuts along ∂A , separating the system into subsystems A and B . Figure taken from [5].

138]. One defines a second set of operators

$$\hat{\mu}_{\mathbf{n}}^z = \hat{\sigma}_{\mathbf{n},x}^z \hat{\sigma}_{\mathbf{n}+\hat{x},y}^z \hat{\sigma}_{\mathbf{n}+\hat{y},x}^z \hat{\sigma}_{\mathbf{n},y}^z, \quad (3.13a)$$

$$\hat{\mu}_{\mathbf{n}}^x = \prod_{j \geq 0} \hat{\sigma}_{\mathbf{n}-j\hat{y},x}^x, \quad (3.13b)$$

where $\hat{\mu}_{\mathbf{n}}^x$ and $\hat{\mu}_{\mathbf{n}}^z$ fulfill the commutation relations $\{\hat{\mu}_{\mathbf{n}}^x, \hat{\mu}_{\mathbf{n}}^z\} = 0$, and $[\hat{\mu}_{\mathbf{n}}^x, \hat{\mu}_{\mathbf{m}}^z] = 0$ for $\mathbf{m} \neq \mathbf{n}$. Explicit computation shows that the dual operators are manifestly gauge invariant, and their implementation results in a simplified dual Hamiltonian, which involves only products of up to two operators, i.e.,

$$\begin{aligned} \hat{H} &= - \sum_{\mathbf{n}} \hat{\mu}_{\mathbf{n}}^z - \epsilon \sum_{\mathbf{n},i} \hat{\mu}_{\mathbf{n}-i}^x \hat{\mu}_{\mathbf{n}}^x \\ &\equiv \hat{B} + \hat{H}_{E,x} + \hat{H}_{E,y}, \end{aligned} \quad (3.14)$$

where we used that $\hat{\mu}_{\mathbf{n}}^x \hat{\mu}_{\mathbf{n}-\hat{y}}^x = \hat{\sigma}_{\mathbf{n},x}^x$, and, by employing Gauss law for the infinite system, $\hat{\mu}_{\mathbf{n}}^x \hat{\mu}_{\mathbf{n}-\hat{x}}^x = \hat{\sigma}_{\mathbf{n},y}^x$. Furthermore, we defined electric energies $\hat{H}_{E,i}$ and the magnetic energy \hat{H}_B . In Ref. [5] we present a dual description with virtual boundaries, where the Hamiltonian involves corresponding boundary terms, which arise from the string of operators in Eq. (3.13b) and enter the definitions of energies.

3.5.2 Non-equilibrium dynamics and approach to equilibrium

We consider numerical real-time calculation using exact diagonalization [107]. The non-equilibrium dynamics of the \mathbb{Z}_2 gauge fields is studied on the two-dimensional lattice with periodic boundary conditions, which results in the torus configuration shown in Fig. 3.8. The lattice is separated into two sub-systems A and B along the “entanglement cuts” ∂A . Here we distinguish between local observables, such as the mean energies in the electric and magnetic sectors of the theory, and the entanglement properties of the system. We define the entanglement Hamiltonian

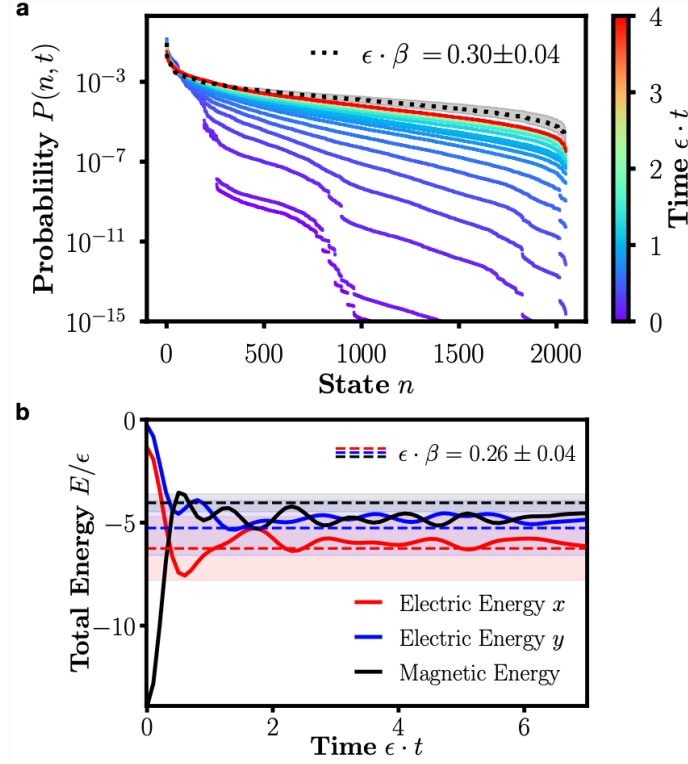


FIGURE 3.9: **Non-equilibrium dynamics of the \mathbb{Z}_2 lattice gauge theory:** (a) The non-equilibrium dynamics of the entanglement spectrum approaches thermal equilibrium. (b) The time-dependent expectation values of magnetic and electric field energies relax after the quench, approaching approximate thermal expectation values at late times. Figure taken from [5].

\hat{H}_{ent} as

$$\hat{\rho}_A = \text{Tr}_B(\hat{\rho}) = \sum_{n=1}^{\chi} P_n |\psi_A^n\rangle \langle \psi_A^n| \equiv e^{-\hat{H}_{\text{ent}}}. \quad (3.15)$$

Here, $\hat{\rho}$ is the time-dependent density operator on the entire system, and $\hat{\rho}_A$ its reduced density operator on sub-system A . We used a Schmidt decomposition into an orthogonal set of states $|\psi_A^n\rangle$ living in A , where n counts the dimensions of the reduced density operator up to the Schmidt rank χ . The spectrum of the entanglement Hamiltonian is also encoded in the Schmidt coefficients $P_n = e^{-\xi_n}$, which are the central objects of this section. For $\chi = 1$ the system is in a product state with respect to the bi-partition A/B , while the state is entangled in the cases where $\chi > 1$. Starting from systems with small Schmidt rank, one generally expects χ to grow during the initial stages of the dynamics which entangles both sub-systems.

To probe the non-equilibrium dynamics quantitatively, we consider a quench of the coupling parameter ϵ . We start from a randomly chosen eigenstate $|\psi_0\rangle$ of the spectrum for $\epsilon = 0.1$ but subsequently evolve the system with $\epsilon = 1$. During the evolution, the $\xi(t)$ are time-dependent parameters which encode the quantum-chaotic evolution of the system. In Fig. 3.9 we show the entanglement spectrum as a function of the state index n for a system with size $(n_x^A + n_x^B) \times n_y = (3 + 5) \times 3$. One

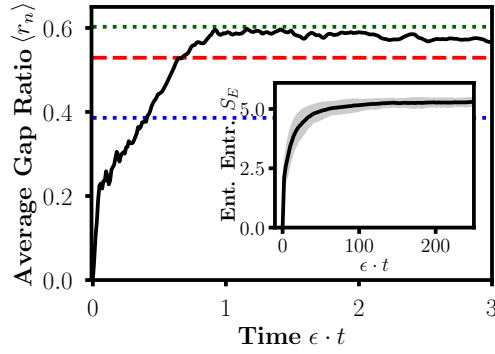


FIGURE 3.10: Evolution of gap ratio: The non-equilibrium dynamics of the average gap ratio of the entanglement spectrum approaches the expected value for a Gaussian unitary ensemble (green dotted) compared to the values of Gaussian orthogonal (dashed) and Poisson ensembles (blue dotted). The inset shows the corresponding von-Neumann entanglement entropy, which saturates on much longer time-scales. Figure adapted from [108].

observes the Schmidt rank χ to be maximized rapidly during the early evolution $t < 1/\epsilon$. For later times $1 < t/\epsilon < 4$, the evolution of the probabilities slows down and approaches a constant distribution. The Schmidt spectrum is compared to a thermal canonical ensemble, which is computed from the approximate thermal state $\hat{\rho}_\beta = e^{-\beta \hat{H}_A} / \text{Tr}(e^{-\beta \hat{H}_A})$, where we neglect the inter-system coupling between sub-systems A and B for simplicity. The corresponding entanglement spectrum of the thermal state is shown for the temperature $\beta = (0.30 \pm 0.04)\epsilon^{-1}$, which has been extracted by matching the thermal entropy with the (saturated) entanglement entropy of the evolution after $t = 4/\epsilon$ [5]. One finds that the general shape of the thermal distribution is approached, even for the small system sizes considered in the numerical calculation.

Relaxation is furthermore observed in the local correlations of the system on similar time scales. Panel b shows the non-equilibrium evolution of the mean electric energies along direction i , $\langle \hat{H}_{E,i} \rangle$ as well as the magnetic field energy $\langle \hat{H}_B \rangle$, where both quantities have been adapted to the system with size $((n_x^A + n_x^B) \times n_y = (3 + 3) \times 3)$. After the quench, the energy is rapidly re-distributed between electric and magnetic sectors of the theory. For times $t > 2/\epsilon$ the system approximately equilibrates, where it approaches a thermal state with temperature $\beta = (0.26 \pm 0.04)\epsilon^{-1}$.

We subsequently probe the dynamics of the gauge fields for a second quench, where the initial state is chosen as a random eigenstate of the Hamiltonian with $\epsilon \rightarrow \infty$. In this limit, eigenstates of the Hamiltonian are also eigenstates of the single-body electric field operators, thus being entirely unentangled, and $\chi = 1$ initially. The dynamics rapidly entangles the sub-systems A and B , thus again maximizing the Schmidt rank χ . The early stages of the entanglement dynamics are shown in Fig. 3.10, where we display the evolution of the average gap ratio of the

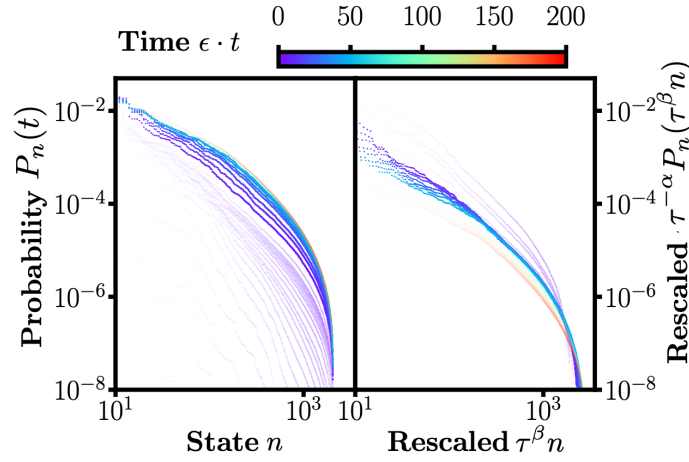


FIGURE 3.11: Self-similar dynamics: The entanglement spectrum undergoes a regime of self-similar dynamics (left), where curves at different times collapse for suitable scaling exponents (right, and main text), and suitably chosen $\tau = \epsilon(t - t_0)$, where $\epsilon t_0 = 1.8 \pm 0.2$. Figure adapted from [108].

entanglement spectrum, i.e.,

$$r_n = \frac{\min(\delta_n, \delta_{n-1})}{\max(\delta_n, \delta_{n-1})}, \quad (3.16)$$

where $\delta_n = \xi_n - \xi_{n-1}$ is the spacing of neighboring spectrum levels, which are resolved into symmetry sectors with respect to the center of the algebra of field operators in sub-system A [5]. The gap ratio exhibits level repulsion in agreement with a Gaussian unitary ensemble on earliest time scales $t \sim 1/\epsilon$ [139]. Conversely, the corresponding entanglement entropy $\text{Tr}_A[\hat{\rho}_A \ln(\hat{\rho}_A)]$ indicates equilibration for much longer times $t \sim 200/\epsilon$ [140].

In Fig. 3.11 we investigate the time-dependent Schmidt coefficients during this saturation dynamics. At late times, the Schmidt spectrum again approaches an approximately constant (equilibrium) distribution. In-between, however, for evolution times $2/\epsilon \lesssim t \lesssim 100/\epsilon$, the system undergoes a self-similar regime, where curves at different times collapse onto each other when rescaled with exponents $\alpha = 0.8 \pm 0.1$ and $\beta = 0.0 \pm 0.1$. Similar cases of self-similar dynamics are often discussed in the context of classical turbulence for distribution functions [69, 141].

3.6 Summary

In this chapter, we proposed a scalable implementation scheme to realize cold-atom gauge fields in two spatial dimensions. The challenge was to engineer the notoriously difficult magnetic field interactions, which we proposed to implement via spin-changing collisions in an ultra-cold atomic mixture.

Our scheme was applied in two different regimes. First, we considered the non-perturbative physics of confinement for the vacuum state of the gauge field theory, where we demonstrated the stability of the phenomenon against small imperfections of the implementation. Secondly, we considered the non-equilibrium dynamics of the gauge fields for a single plaquette, which we investigated experimentally in an ultra-cold mixture. Here, we characterized the gauge field dynamics in terms of various non-equilibrium phenomena such as instabilities or the onset of thermalization, which was enabled through the experimental extraction of fluctuations beyond standard mean-field observables [23, 24, 142, 143].

Finally, we explored a different route to gauge field thermalization, by computing the non-equilibrium time-evolution of the entanglement spectrum for a \mathbb{Z}_2 lattice gauge theory across bipartite entanglement cuts. The approach illustrated the relaxation of the system, which subsequently approached corresponding quantities computed from thermal density matrices. During quantum dynamics of the system undergoes an intermediate regime where the entanglement spectrum exhibits signatures of universal scaling, which is often associated with classical wave turbulence [69, 141].

3.A Detailed derivation of cold-atom Hamiltonian

In the following we briefly outline the derivation of the effective Hamiltonian (3.2). We consider two species A/B of spin-1 Bose gases with field operators $\hat{\psi}_{s=A/B,m}$. For each species, we restrict the dynamics to two hyperfine states $m = 0, 1$ by detuning the $m = -1$ state using a magnetic field \mathcal{B} . To engineer the electric and magnetic terms of the gauge theory, we introduce suitable energy separations and initial conditions to suppress unwanted processes, and couple neighboring plaquettes with laser-assisted tunneling, see Fig. 3.1.

A mixture of ultra-cold spinor Bose gases is described by the free and interaction Hamiltonians [120]

$$\hat{H}_0 = \int d^3\mathbf{x} \left[\hat{\psi}_{s,m}^\dagger \left(-\frac{\nabla^2}{2M_s} \delta_{mm'} + V_{s,mm'}(\mathbf{x}, t) \right) \hat{\psi}_{s,m'} \right] \quad (3.17a)$$

$$\hat{H}_{\text{int}} = \int d^3\mathbf{x} \left[c_0^{ss'} : \hat{n}_s \hat{n}_{s'} : + c_1^{ss'} : \hat{F}_s^a \hat{F}_{s'}^a : \right], \quad (3.17b)$$

where summation over repeated indices is implied. The potential terms are summarized in $V_{s,mm'}(x, t)$, M_s denotes the atomic mass of species s and the colon represents normal ordering. The density and spin operators in the interaction terms are given by $\hat{n}_s = \hat{\psi}_{s,m}^\dagger \hat{\psi}_{s,m}$ and $\hat{F}_s^a = \hat{\psi}_{s,m}^\dagger \mathbf{f}_{m,m'}^a \hat{\psi}_{s,m'}$, respectively. Here the $\mathbf{f}_{m,m'}^a$ denote the spin-1 matrices and $c_0^{ss'}$, $c_1^{ss'}$ are the coupling constants for the density- and spin interactions. In a deep optical lattice, we expand the field operators in terms of localized basis functions $\Phi_{\mathbf{n}}^s(x)$ as $\hat{\psi}_{s,m}(x) = \sum_{\mathbf{n}} \Phi_{\mathbf{n}}^s(x) \hat{a}_{\mathbf{n},m}$.

3.A.1 Quadratic terms

For the quadratic terms Eq. (3.17a) we hence only keep on-site or nearest neighbor couplings. The time-independent part takes the the form

$$\begin{aligned} \hat{H}_0 = & \sum_{\mathbf{n}} \left(\epsilon_{A,m,\mathbf{n}} \hat{a}_{\mathbf{n},m}^\dagger \hat{a}_{\mathbf{n},m} + \epsilon_{B,m,\mathbf{n}} \hat{b}_{\mathbf{n},m}^\dagger \hat{b}_{\mathbf{n},m} \right) \\ & + \sum_{\mathbf{n}, i=x,y} \left(J^A \hat{a}_{\mathbf{n},m}^\dagger \hat{a}_{\mathbf{n}+\hat{i},m} + J^B \hat{b}_{\mathbf{n},m}^\dagger \hat{b}_{\mathbf{n}+\hat{i},m} + h.c. \right), \end{aligned} \quad (3.18)$$

where we ignored irrelevant zero-point energies. The tunneling elements $J^{A/B}$ are equal in each direction and for both species. Direct tunneling is suppressed by a linear potential in $\epsilon_{s,m,\mathbf{n}} = E_{s,m}(\mathcal{B}) + \Delta_x^s n_x + \Delta_y^s n_y$, including the Zeeman energies $E_{s,m}(\mathcal{B})$. The laser-assisted tunneling introduces time-dependent terms, where we only keep the transitions which are driven resonantly

$$\hat{H}_{0,\text{drive}} = \sum_{\mathbf{n}} \left(\Omega_x e^{i\omega_x t + i\varphi_x} \hat{a}_{\mathbf{n},0}^\dagger \hat{a}_{\mathbf{n}+\hat{x},1} + \Omega_y e^{i\omega_y t + i\varphi_y} \hat{d}_{\mathbf{n},0}^\dagger \hat{d}_{\mathbf{n}+\hat{y},1} + h.c. \right), \quad (3.19)$$

with respective amplitudes Ω_i , phases φ_i and frequencies ω_i . Here, the Ω_i depend on the nearest-neighbor overlap and the intensity of the coupling lasers. In the next

step, we switch to the rotating frame

$$\hat{H}_0 \rightarrow \hat{H}'_0 = i(\partial_t \hat{U}(t)) \hat{U}^\dagger(t) + \hat{U}(t) \hat{H}_0 \hat{U}^\dagger(t), \quad (3.20)$$

by performing the unitary transformation $\hat{U}(t) = \exp(i\hat{T}t)$, with

$$\begin{aligned} \hat{T} = \sum_{\mathbf{n}} & \left(n_y (\Delta_y^A - E_{Z,A}(\mathcal{B})) (\hat{a}_{\mathbf{n},0}^\dagger \hat{a}_{\mathbf{n},0} + \hat{a}_{\mathbf{n},1}^\dagger \hat{a}_{\mathbf{n},1}) \right. \\ & \left. + n_x (\Delta_x^B - E_{Z,B}(\mathcal{B})) (\hat{b}_{\mathbf{n},0}^\dagger \hat{b}_{\mathbf{n},0} + \hat{b}_{\mathbf{n},1}^\dagger \hat{b}_{\mathbf{n},1}) \right). \end{aligned} \quad (3.21)$$

Here we defined the Zeeman splitting $E_{Z,s}(\mathcal{B}) = E_{s,1}(\mathcal{B}) - E_{s,0}(\mathcal{B})$. The transformed quadratic Hamiltonian is given by

$$\begin{aligned} \hat{H}'_0 = \sum_{\mathbf{n},m} & \left(\tilde{\epsilon}_{A,m,\mathbf{n}} \hat{a}_{\mathbf{n},m}^\dagger \hat{a}_{\mathbf{n},m} + \Omega_x e^{i\omega_x t + i\varphi_x} e^{-i\alpha_A t} \hat{a}_{\mathbf{n},0}^\dagger \hat{a}_{\mathbf{n}+\hat{y},1} + h.c. \right. \\ & \left. + \tilde{\epsilon}_{B,m,\mathbf{n}} \hat{b}_{\mathbf{n},m}^\dagger \hat{b}_{\mathbf{n},m} + \Omega_y e^{i\omega_y t + i\varphi_y} e^{-i\alpha_B t} \hat{b}_{\mathbf{n},0}^\dagger \hat{b}_{\mathbf{n}+\hat{x},1} + h.c. \right), \end{aligned} \quad (3.22)$$

with the shorthand notations for the phase $\alpha_A = \Delta_y^A - E_{Z,A}(\mathcal{B})$, $\alpha_B = \Delta_x^B - E_{Z,B}(\mathcal{B})$ and the transformed single-particle energies $\tilde{\epsilon}_{A,m,\mathbf{n}} = E_{A,m}(\mathcal{B}) + E_{Z,A}(\mathcal{B})n_y + \Delta_x^A n_x$, and $\tilde{\epsilon}_{B,m,\mathbf{n}} = E_{B,m}(\mathcal{B}) + \Delta_y^B n_y + E_{Z,B}(\mathcal{B})n_x$. On resonance, $\omega_x = \alpha_A$ and $\omega_y = \alpha_B$, and dropping the fast rotating terms (rotating wave approximation) we get

$$\begin{aligned} \hat{H}'_0 = \sum_{\mathbf{n}} & \left(\tilde{\epsilon}_{A,1,\mathbf{n}} (\hat{a}_{\mathbf{n},1}^\dagger \hat{a}_{\mathbf{n},1} + \hat{a}_{\mathbf{n}+\hat{y},0}^\dagger \hat{a}_{\mathbf{n}+\hat{y},0}) + \tilde{\epsilon}_{B,1,\mathbf{n}} (\hat{b}_{\mathbf{n},1}^\dagger \hat{b}_{\mathbf{n},1} + \hat{b}_{\mathbf{n}+\hat{x},0}^\dagger \hat{b}_{\mathbf{n}+\hat{x},0}) \right. \\ & \left. + \left(\tilde{\Omega}_x e^{i\tilde{\varphi}_x} \hat{a}_{\mathbf{n},0}^\dagger \hat{a}_{\mathbf{n}+\hat{y},1} + \tilde{\Omega}_y e^{i\tilde{\varphi}_y} \hat{b}_{\mathbf{n},0}^\dagger \hat{b}_{\mathbf{n}+\hat{x},1} + h.c. \right) \right). \end{aligned} \quad (3.23)$$

Here, we absorbed the phase of Ω_i into $\tilde{\varphi}_i$ to obtain real amplitudes $\tilde{\Omega}_i$. The Hamiltonian \hat{H}'_0 is diagonal in the $|\pm\rangle$ -basis, defined by

$$\hat{a}_{\mathbf{n},\pm} = \frac{\hat{a}_{\mathbf{n}-\hat{y},0} \pm \exp(i\tilde{\varphi}_x) \hat{a}_{\mathbf{n},1}}{\sqrt{2}}, \quad (3.24a)$$

$$\hat{b}_{\mathbf{n},\pm} = \frac{\hat{b}_{\mathbf{n}-\hat{x},0} \pm \exp(i\tilde{\varphi}_y) \hat{b}_{\mathbf{n},1}}{\sqrt{2}}. \quad (3.24b)$$

Up to an irrelevant constant it reads

$$\hat{H}'_0 = \sum_{\mathbf{n},\pm} \left[\left(\tilde{\epsilon}_{A,1,\mathbf{n}} \pm \tilde{\Omega}_x \right) \hat{a}_{\mathbf{n},\pm}^\dagger \hat{a}_{\mathbf{n},\pm} + \left(\tilde{\epsilon}_{B,1,\mathbf{n}} \pm \tilde{\Omega}_y \right) \hat{b}_{\mathbf{n},\pm}^\dagger \hat{b}_{\mathbf{n},\pm} \right], \quad (3.25)$$

where we sum over the $|+\rangle$ - and $|-\rangle$ -states. In our proposal we neglect the $|-\rangle$ -states since for proper initialization, i.e., starting with zero occupation in the $|-\rangle$ -states, they stay unpopulated. The detuning of the magnetic field interactions is set by the difference of the Zeeman splitting for both species. The interaction can be made resonant by tuning the magnetic field. On resonance, \hat{H}'_0 is constant throughout the dynamics and decouples.

3.A.2 Scattering terms

Next, we focus on the scattering terms, which then become the gauge-invariant magnetic and electric field energy terms in the Hamiltonian (3.2). In the m -basis, the inter-species spin-changing collisions (SCC) are represented by

$$\hat{H}_{\text{SCC}} = \sum_{\mathbf{n}} (X_{\text{SCC}} a_{\mathbf{n},0}^\dagger a_{\mathbf{n},1} b_{\mathbf{n},1}^\dagger b_{\mathbf{n},0} + h.c.). \quad (3.26)$$

Note that the SCC-term is not affected by the resonant driving but remains time-independent. Writing this in the new basis, and dropping the contributions from the $|-\rangle$ -states, we get

$$\hat{H}_{\text{SCC}} = \frac{X_{\text{SCC}}}{4} \sum_{\mathbf{n}} (e^{i(\tilde{\varphi}_y - \tilde{\varphi}_x)} \hat{a}_{\mathbf{n}+\hat{y},+}^\dagger \hat{a}_{\mathbf{n},+} \hat{b}_{\mathbf{n},+}^\dagger \hat{b}_{\mathbf{n}+\hat{x},+} + h.c.). \quad (3.27)$$

With the definitions $\hat{b}_{\mathbf{n},+} \rightarrow \hat{b}_{\mathbf{n},y}$ and $\hat{a}_{\mathbf{n},+} \rightarrow \hat{b}_{\mathbf{n},x}$ we obtain the magnetic field energy term in Eq. (3.2). The sign of the interaction λ is chosen positive, by phase-locking the driving lasers. The same-species density interactions within one hyperfine state take the form (illustrated for species A)

$$\begin{aligned} \hat{H}_{m=0}^{A-A} &= X_{0000}^{A-A} \sum_{\mathbf{n}} a_{\mathbf{n},0}^\dagger a_{\mathbf{n},0}^\dagger a_{\mathbf{n},0} a_{\mathbf{n},0} \\ &= \frac{X_{0000}^{A-A}}{4} \sum_{\mathbf{n}} b_{\mathbf{n},x}^\dagger b_{\mathbf{n},x}^\dagger b_{\mathbf{n},x} b_{\mathbf{n},x}, \end{aligned} \quad (3.28a)$$

$$\begin{aligned} \hat{H}_{m=1}^{A-A} &= X_{1111}^{A-A} \sum_{\mathbf{n}} a_{\mathbf{n},1}^\dagger a_{\mathbf{n},1}^\dagger a_{\mathbf{n},1} a_{\mathbf{n},1} \\ &= \frac{X_{1111}^{A-A}}{4} \sum_{\mathbf{n}} b_{\mathbf{n},x}^\dagger b_{\mathbf{n},x}^\dagger b_{\mathbf{n},x} b_{\mathbf{n},x}, \end{aligned} \quad (3.28b)$$

where we used an index shift in the first line. The density interactions between the two hyperfine states of the same species read

$$\begin{aligned} \hat{H}_{m=0,1}^{A-A} &= X_{0110}^{A-A} \sum_{\mathbf{n}} a_{\mathbf{n},0}^\dagger a_{\mathbf{n},1}^\dagger a_{\mathbf{n},1} a_{\mathbf{n},0} \\ &= \frac{X_{0110}^{A-A}}{4} \sum_{\mathbf{n}} b_{\mathbf{n}+\hat{y},x}^\dagger b_{\mathbf{n},x}^\dagger b_{\mathbf{n},x} b_{\mathbf{n}+\hat{y},x} \\ &= \frac{X_{0110}^{A-A}}{4} \sum_{\mathbf{n}} b_{\mathbf{n},x}^\dagger b_{\mathbf{n},x}^\dagger b_{\mathbf{n},x} b_{\mathbf{n},x} + \mathcal{O}(a_s). \end{aligned} \quad (3.29)$$

Together, these terms yield the first term of Eq. (3.2). The remaining inter-species density interactions are given by

$$\begin{aligned} \hat{H}^{A-B} &= \sum_{\mathbf{n}} (X_{0000}^{A-B} \hat{a}_{\mathbf{n},0}^\dagger \hat{a}_{\mathbf{n},0} \hat{b}_{\mathbf{n},0}^\dagger \hat{b}_{\mathbf{n},0} + X_{0110}^{A-B} \hat{a}_{\mathbf{n},0}^\dagger \hat{a}_{\mathbf{n},0} \hat{b}_{\mathbf{n},1}^\dagger \hat{b}_{\mathbf{n},1} \\ &\quad + X_{0110}^{A-B} \hat{a}_{\mathbf{n},1}^\dagger \hat{a}_{\mathbf{n},1} \hat{b}_{\mathbf{n},0}^\dagger \hat{b}_{\mathbf{n},0} + X_{1111}^{A-B} \hat{a}_{\mathbf{n},1}^\dagger \hat{a}_{\mathbf{n},1} \hat{b}_{\mathbf{n},1}^\dagger \hat{b}_{\mathbf{n},1}). \end{aligned} \quad (3.30)$$

For the coupling constants of the scattering terms we consider same species (U^{s-s}) and inter-species (U^{A-B}) overlap integrals

$$U^{s-s} = \int d^3x |\Phi_{\mathbf{n}}^s(x)|^4, \quad (3.31a)$$

$$U^{A-B} = \int d^3x |\Phi_{\mathbf{n}}^A(x)|^2 |\Phi_{\mathbf{n}}^B(x)|^2. \quad (3.31b)$$

The same-species scattering constants are given by (see also Ref. [118])

$$X_{0000}^{s-s} = U^{s-s} \frac{g_0^{s-s} + 2g_2^{s-s}}{3}, \quad X_{1111}^{s-s} = U^{s-s} g_2^{s-s}, \quad X_{0110}^{s-s} = 2U^{s-s} g_2^{s-s}, \quad (3.32)$$

where $g_i^{s-s'} = 2\pi\hbar^2 a_i^{s-s'} / \mu_{s-s'}$ is linked to the corresponding scattering length $a_i^{s-s'}$ between atoms of species s and s' . Here, $\mu_{s-s'}$ denotes the reduced mass and \hbar is the reduced Planck constant. Assuming approximately equal interaction strengths for both species, we identify $\chi = U^{s-s}(g_0^{s-s} + 11g_2^{s-s})/3$ which is typically positive [120]. Regarding the inter-species density interactions one finds

$$X_{0000}^{A-B} = U^{A-B} \frac{g_0^{A-B} + 2g_2^{A-B}}{3}, \quad X_{1111}^{A-B} = U^{A-B} g_2^{A-B}, \quad X_{0110}^{A-B} = U^{A-B} \frac{g_1^{A-B} + g_2^{A-B}}{2}. \quad (3.33)$$

We identify $\delta = X^{A-B}$, where we assume $X^{A-B} = X_{0000}^{A-B} \approx X_{1111}^{A-B} \approx X_{0110}^{A-B}$, i.e., approximately equal scattering lengths as for the sodium-lithium mixture of Ref. [52]. This yields the second line of Eq. (3.2) in the main text. While this assumption allows for a compact form of the unwanted inter-species density interactions, our results do not depend on it. In the main text we assumed $\delta > 0$ motivated by the scattering lengths for the sodium-lithium mixture, see Ref. [52]. However, the sign of δ does not enter our calculations at leading order. At last, the coupling of the spin-changing collisions is given by $X_{\text{SCC}} = U^{A-B}(g_2^{A-B} - g_1^{A-B})/2$.

3.B Flux fields and potential

To calculate the expectation values of electric fields and the Hamiltonian in this section, we introduce and employ the methods presented in Ref. [121].

We separate the electric field into a classical (longitudinal “ L ”) Coulomb field \mathbf{E}^L and a fluctuating (transversal “ T ”) ‘quantum field’ $\hat{\mathbf{E}}^T$. The Coulomb field is derived from the classical potential $\phi_{\mathbf{n}}$ governed by Poisson’s equation $\nabla^2 \phi_{\mathbf{n}} = \rho_{\mathbf{n}}$, where ∇^2 is the (symmetric) lattice Laplacian and $\rho_{\mathbf{n}}$ denotes the external charges. The expression for the energy presented in Fig. 3.3 is the sum of the resulting classical Coulomb energy and a quantum correction originating from fluctuations of $\hat{\mathbf{E}}^T$. This correction of the field energy is given by a string-string and a string-Coulomb contribution. In the following, we derive the formulae used to compute the numerical results presented in the main chapter. We furthermore give approximate analytical results for gauge fields and string tension in the limit of large separation D and infinite volume, closely following Ref. [121] throughout this section.

We consider a two dimensional square lattice with $n_x = 0, \dots, N - 1$ and $n_y = 0, \dots, N - 1$, with N even. We define a Fourier transformation of a field $\phi_{\mathbf{n}}$, and its inverse, as

$$\tilde{\phi}_{\mathbf{k}} = \frac{1}{V} \sum_{n_x, n_y} e^{i \frac{2\pi}{N} \mathbf{k} \mathbf{n}} \phi_{\mathbf{n}} \quad (3.34a)$$

$$\phi_{\mathbf{n}} = \sum_{k_x, k_y} e^{-i \frac{2\pi}{N} \mathbf{k} \mathbf{n}} \tilde{\phi}_{\mathbf{k}}. \quad (3.34b)$$

The physical momenta are given by $\mathbf{K} = \frac{2\pi}{Na_s} \mathbf{k}$, and $\mathbf{k} \mathbf{n} = k_x n_x + k_y n_y$ denotes the scalar product. The integer momenta are summed over $k_x = -\frac{N}{2}, \dots, \frac{N}{2} - 1$ and $k_y = -\frac{N}{2}, \dots, \frac{N}{2} - 1$. In the following we will drop the tilde on the Fourier transformed quantities. The volume is given by $V = N^2 a_s^2$. For the remainder of this section we will set the lattice spacing to unity, i.e., $a_s = 1$.

To perform explicit calculations Ref. [121] uses a dual formulation of the lattice gauge theory. Analogous to the classical potential one defines a quantum “potential” for the fluctuating electric field

$$\hat{L}_{\mathbf{n}} \equiv \sum_{m_y = -\infty}^{n_y} \hat{\mathbf{E}}_{\mathbf{m}, x}^T, \quad (3.35)$$

such that the electric field operator is given by the lattice curl $\hat{\mathbf{E}}_{\mathbf{n}}^T = \nabla \times \hat{L}_{\mathbf{n}}$

$$\hat{E}_{\mathbf{n}, x} = -(\phi_{\mathbf{n}+\hat{x}} - \phi_{\mathbf{n}}) + (\hat{L}_{\mathbf{n}} - \hat{L}_{\mathbf{n}-\hat{y}}) \quad (3.36a)$$

$$\hat{E}_{\mathbf{n}, y} = -(\phi_{\mathbf{n}+\hat{y}} - \phi_{\mathbf{n}}) - (\hat{L}_{\mathbf{n}} - \hat{L}_{\mathbf{n}-\hat{x}}) \quad (3.36b)$$

Similarly, the conjugate variable to \hat{L} is given by the lattice curl of the vector potential, i.e., the magnetic field $\hat{B}_{\mathbf{n}} = \nabla \times \hat{\mathbf{A}}_{\mathbf{n}}$. Specifically, we have

$$\hat{B}_{\mathbf{n}} \equiv \hat{A}_{\mathbf{n},x} + \hat{A}_{\mathbf{n}+\hat{x},y} - \hat{A}_{\mathbf{n}+\hat{y},x} - \hat{A}_{\mathbf{n},y}, \quad (3.37)$$

where the vector potential is the exponent of the link operator, i.e., $\hat{U}_{\mathbf{n},i} = \exp(ie\hat{A}_{\mathbf{n},i})$. The field operators fulfill the commutation relations

$$[\hat{L}_{\mathbf{n}}, \hat{B}_{\mathbf{m}}] = i\delta_{\mathbf{n},\mathbf{m}}. \quad (3.38)$$

With this, a dual Hamiltonian may be formulated in terms of gauge-invariant conjugate operators

$$\hat{H} = \frac{1}{2} \sum_{\mathbf{n}} (\mathbf{E}_{\mathbf{n}}^L)^2 + \frac{1}{2} \sum_{\mathbf{n},i} (\hat{L}_{\mathbf{n}+\hat{i}} - \hat{L}_{\mathbf{n}})^2 - \frac{1}{e^2} \sum_{\mathbf{n}} (1 - \cos(e\hat{B}_{\mathbf{n}}^2)), \quad (3.39)$$

where \hat{B} is a periodic angular variable. Focusing on the weak coupling regime, $e^2 \ll 1$, the Hamiltonian is approximately quadratic, and we consider the trial wave function

$$\psi(B) = \prod_{\mathbf{n}} \left(\sum_{n_{\mathbf{n}}=-\infty}^{\infty} \right) e^{2\pi i \sum_{\mathbf{m}} \epsilon_{\mathbf{m}} n_{\mathbf{m}}} \psi_0(B_{\mathbf{n}} - 2\pi n_{\mathbf{n}}), \quad (3.40)$$

with phases $2\pi\epsilon$ determined by the configuration of external charges. The summation over $2\pi n_{\mathbf{n}}$ accounts for the periodicity of the magnetic fields, and

$$\psi_0(B_{\mathbf{m}}) = e^{-\frac{1}{2e^2} \sum_{\mathbf{n}\mathbf{m}} B_{\mathbf{n}} G_{\mathbf{n}\mathbf{m}} B_{\mathbf{m}}} \delta\left(\sum_{\mathbf{n}} B_{\mathbf{n}}\right), \quad (3.41)$$

where the δ -distribution fixes the boundary condition and G is the equal-time propagator of the system, see also Chapter 4. Minimization of the ground state energy yields a propagator including the mass gap μ (see Eq. (3.4)) which acts as an infrared regulator for fluctuations and eventually yields confinement. For the specific case of two opposite external charges, we subsequently get the expressions for flux fields and ground state energies outlined in the following.

3.B.1 String-string contribution to the ground state energy

We compute the string-string contribution, following Eq. (4.46) of Ref. [121], by

$$\delta\langle \hat{H} \rangle_{s-s} = \frac{\pi^2 - 4}{2\pi^2 g^2} \mu^4 \sum_{\mathbf{n},\mathbf{m},i} E_{\mathbf{n},i}^{\text{st}} I_{\mathbf{n}\mathbf{m}} E_{\mathbf{m},i}^{\text{st}}, \quad (3.42)$$

with interaction kernel

$$I_{nm} = \frac{1}{V} \sum_{\mathbf{k}} e^{i\frac{2\pi}{N}\mathbf{k}(\mathbf{n}-\mathbf{m})} \frac{1}{(\sqrt{4 - 2 \cos(\frac{2\pi}{N}k_x) - 2 \cos(\frac{2\pi}{N}k_y) + \frac{\mu^2}{g^2}})^2}, \quad (3.43)$$

corresponding to Eq. (4.47) of Ref. [121], and translated to our notation of momenta. The integral kernel involves the propagator including the mass scale μ set by the quantum fluctuations of the system. The string fields are given by

$$E_{\mathbf{n},x}^{\text{st}} = \begin{cases} 1 & n_x \in [-\frac{D}{2}, \frac{D}{2} - 1] \text{ and } n_y = 0 \\ 0 & \text{else} \end{cases}, \quad E_{\mathbf{n},y}^{\text{st}} = 0, \quad (3.44)$$

which 'connect' the classical charges at positions $n_{x,+} = -D/2$ and $n_{x,-} = D/2$. Using this, we obtain the expression

$$\begin{aligned} \delta\langle\hat{H}\rangle_{s-s} &= \frac{\pi^2 - 4}{2\pi^2 g^2} \mu^4 \sum_{n_x, m_x = -\frac{D}{2}}^{\frac{D}{2}-1} \frac{1}{V} \sum_{\mathbf{k}} e^{i\frac{2\pi}{N}k_x(n_x - m_x)} \\ &\times \frac{1}{(\sqrt{4 - 2 \cos(\frac{2\pi}{N}k_x) - 2 \cos(\frac{2\pi}{N}k_y) + \frac{\mu^2}{g^2}})^2}. \end{aligned} \quad (3.45)$$

Let us first calculate the spatial sums

$$\sum_{n_x = -D/2}^{D/2-1} e^{i\frac{2\pi}{N}k_x n_x} = e^{-i\frac{2\pi}{N}k_x \frac{D}{2}} \frac{1 - e^{i\frac{2\pi}{N}k_x D}}{1 - e^{i\frac{2\pi}{N}k_x}} = \frac{\sin(\frac{2\pi}{N} \frac{k_x}{2} D) e^{-i\frac{2\pi}{N} \frac{k_x}{2} D}}{\sin(\frac{2\pi}{N} \frac{k_x}{2})}, \quad (3.46a)$$

$$\sum_{m_x = -D/2}^{D/2-1} e^{-i\frac{2\pi}{N}k_x m_x} = e^{i\frac{2\pi}{N}k_x \frac{D}{2}} \frac{1 - e^{-i\frac{2\pi}{N}k_x D}}{1 - e^{-i\frac{2\pi}{N}k_x}} = \frac{\sin(\frac{2\pi}{N} \frac{k_x}{2} D) e^{i\frac{2\pi}{N} \frac{k_x}{2} D}}{\sin(\frac{2\pi}{N} \frac{k_x}{2})}. \quad (3.46b)$$

Plugging this into the above expression yields

$$\delta\langle\hat{H}\rangle_{s-s} = \frac{\pi^2 - 4}{2\pi^2 g^2} \mu^4 \frac{1}{V} \sum_{\mathbf{k}} \frac{\sin(\frac{2\pi}{N} \frac{k_x}{2} D)^2}{\sin(\frac{2\pi}{N} \frac{k_x}{2})^2} \frac{1}{(\sqrt{4 - 2 \cos(\frac{2\pi}{N}k_x) - 2 \cos(\frac{2\pi}{N}k_y) + \frac{\mu^2}{g^2}})^2}. \quad (3.47)$$

This is the formula we implement for our numerical results presented in Fig. 3.3. To make analytical progress, let us go to infinite volume and large separations, and employ the replacement

$$\frac{1}{V} \sum_{\mathbf{k}} f\left(\frac{2\pi}{Na_s}\mathbf{k}\right) \rightarrow \frac{1}{(2\pi)^2} \int_{-\pi}^{\pi} d^2k f(k), \quad (3.48)$$

where k is a two-dimensional momentum vector. At large separations, the sine factor $\sin(\pi k_x D/N)$ in Eq. (3.47) is rapidly oscillating and confinement is dominated

by infrared modes. We hence consider the approximation(s)

$$\cos(k_i) \rightarrow 1 - \frac{k_i^2}{2}, \quad (3.49a)$$

$$\sin(k_i) \rightarrow k_i, \quad (3.49b)$$

$$\frac{1}{(2\pi)^2} \int_{-\pi}^{\pi} d^2k f(k) \rightarrow \frac{1}{(2\pi)^2} \int_{-\infty}^{\infty} d^2k f(k). \quad (3.49c)$$

With this, we obtain

$$\delta\langle\hat{H}\rangle_{s-s} \approx \frac{\pi^2 - 4}{2\pi^2 g^2} \mu^4 \int_{-\pi}^{\pi} \frac{d^2k}{(2\pi)^2} \frac{\sin\left(\frac{k_x}{2}D\right)^2}{k_x^2} \frac{4}{\left(\sqrt{k_x^2 + k_y^2 + \frac{\mu^2}{g^2}}\right)^2}, \quad (3.50)$$

where we kept the integration boundaries at $\pm\pi$ for now. This expression is identical to the first line of Eq. (4.48) in Ref. [121] up to a factor of 2 in the argument of the sine function and an overall factor π^2 . To compute the string tension, we differentiate with respect to the distance D

$$\begin{aligned} \lim_{D \rightarrow \infty} \frac{\partial}{\partial D} \delta\langle\hat{H}\rangle_{s-s} &\approx \lim_{D \rightarrow \infty} \frac{\pi^2 - 4}{2\pi^2 g^2} \mu^4 \int_{-\infty}^{\infty} \frac{d^2k}{(2\pi)^2} \frac{\sin(k_x D) \frac{k_x}{2}}{k_x^2} \frac{4}{\left(\sqrt{k_x^2 + k_y^2 + \frac{\mu^2}{g^2}}\right)^2} \\ &\approx \frac{\pi^2 - 4}{2\pi^2 g^2} \mu^4 \int_{-\infty}^{\infty} \frac{d^2k}{(2\pi)^2} \frac{\pi \delta(k_x)}{2} \frac{4}{\left(\sqrt{k_x^2 + k_y^2 + \frac{\mu^2}{g^2}}\right)^2} \\ &= \frac{\pi^2 - 4}{2\pi^2 g^2} \mu^4 \frac{1}{2\pi} \int_{-\infty}^{\infty} dk_y \frac{1}{\left(\sqrt{k_y^2 + \frac{\mu^2}{g^2}}\right)^2} \\ &= \frac{\pi^2 - 4}{2\pi^2 g^2} \frac{1}{2\pi} \mu^4 \frac{2g^2}{\mu^2} \\ &= \frac{\pi^2 - 4}{2\pi^3} \mu^2. \end{aligned} \quad (3.51)$$

Indeed, the mass scale μ acts as an infrared regulator which yields a finite string tension, in other words confinement. In the second line we approximated the infrared behavior of the integrand with the identification

$$\lim_{D \rightarrow \infty} \frac{\sin(Dk_x)}{k_x} \rightarrow \pi \delta(k_x). \quad (3.52)$$

Our result for the string-string energy at large separation is

$$\delta\langle H \rangle_{s-s} = \sigma D \quad , \quad \sigma = \frac{\pi^2 - 4}{2\pi^3} \mu^2, \quad (3.53)$$

up to sub-leading corrections, and σ is the string tension. Our result is by a factor 2 larger than the result of Ref. [121] in the last line of its Eq. (4.48).

3.B.2 Coulomb interaction

Coulomb potential

The classical potential ϕ is given by Poisson's equation

$$\nabla^2 \phi_{\mathbf{n}} = \rho_{\mathbf{n}} . \quad (3.54)$$

Note that this definition differs by a **minus** sign with respect to [121], which becomes important when calculating the string-Coulomb interaction. On the lattice, the equation reads

$$\phi_{\mathbf{n}+\hat{x}} + \phi_{\mathbf{n}-\hat{x}} + \phi_{\mathbf{n}+\hat{y}} + \phi_{\mathbf{n}-\hat{y}} - 4\phi_{\mathbf{n}} = (\delta_{n_x, -D/2} - \delta_{n_x, D/2})\delta_{n_y, 0} . \quad (3.55)$$

For periodic boundary conditions we get the following expression in Fourier space

$$\begin{aligned} V &= \phi_{\mathbf{k}} \left[\exp\left(-\frac{2\pi i}{N}k_x\right) + \exp\left(\frac{2\pi i}{N}k_x\right) + \exp\left(-\frac{2\pi i}{N}k_y\right) + \exp\left(\frac{2\pi i}{N}k_y\right) - 4 \right] \\ &= \exp\left(-\frac{i\pi D}{N}k_x\right) - \exp\left(\frac{i\pi D}{N}k_x\right) . \end{aligned} \quad (3.56)$$

Using the boundary condition $\phi_{q=0} = 0$, it can be inverted to yield

$$\phi_{\mathbf{k}} = \frac{1}{V} \frac{-2i \sin\left(\frac{\pi D k_x}{N}\right)}{2 \cos\left(\frac{2\pi}{N}k_x\right) + 2 \cos\left(\frac{2\pi}{N}k_y\right) - 4} = \frac{1}{V} \frac{2i \sin\left(\frac{2\pi}{N}\frac{Dk_x}{2}\right)}{4 - 2 \cos\left(\frac{2\pi}{N}k_x\right) - 2 \cos\left(\frac{2\pi}{N}k_y\right)} . \quad (3.57)$$

Transforming back to real space gives

$$\phi_{\mathbf{n}} = \frac{1}{V} \sum_{\mathbf{k} \neq 0} e^{-i\frac{2\pi}{N}\mathbf{k}\mathbf{n}} \frac{2i \sin\left(\frac{2\pi}{N}\frac{Dk_x}{2}\right)}{4 - 2 \cos\left(\frac{2\pi}{N}k_x\right) - 2 \cos\left(\frac{2\pi}{N}k_y\right)} , \quad (3.58)$$

where we do not sum over $\mathbf{k} = 0$ due to the choice of boundary condition.

Coulomb fields

The Coulomb electric fields are defined as

$$E_{\mathbf{n},x}^L = \phi_{\mathbf{n}} - \phi_{\mathbf{n}+\hat{x}} , \quad (3.59a)$$

$$E_{\mathbf{n},y}^L = \phi_{\mathbf{n}} - \phi_{\mathbf{n}+\hat{y}} . \quad (3.59b)$$

Plugging in the expression (3.58) yields

$$E_{\mathbf{n},x}^L = \frac{1}{V} \sum_{\mathbf{k} \neq 0} \left(1 - e^{-i\frac{2\pi}{N}k_x}\right) e^{-i\frac{2\pi}{N}\mathbf{k}\mathbf{n}} \frac{2i \sin\left(\frac{2\pi}{N}\frac{Dk_x}{2}\right)}{4 - 2 \cos\left(\frac{2\pi}{N}k_x\right) - 2 \cos\left(\frac{2\pi}{N}k_y\right)} , \quad (3.60a)$$

$$E_{\mathbf{n},y}^L = \frac{1}{V} \sum_{\mathbf{k} \neq 0} \left(1 - e^{-i\frac{2\pi}{N}k_y}\right) e^{-i\frac{2\pi}{N}\mathbf{k}\mathbf{n}} \frac{2i \sin\left(\frac{2\pi}{N}\frac{Dk_x}{2}\right)}{4 - 2 \cos\left(\frac{2\pi}{N}k_x\right) - 2 \cos\left(\frac{2\pi}{N}k_y\right)} . \quad (3.60b)$$

These are the numerical expressions we compute for the data shown in the lower panel of Fig. 3.2.

Coulomb energy

The classical Coulomb energy is defined as

$$H_{\text{Coul.}} = \frac{g^2}{2} \sum_{\mathbf{n}} ((E_{\mathbf{n},x}^L)^2 + (E_{\mathbf{n},y}^L)^2) . \quad (3.61)$$

Consider first the x -part

$$\begin{aligned} H_{\text{Coul.}}^x &= \frac{g^2}{2} \sum_{\mathbf{n}} (E_{\mathbf{n},x}^L)^2 \\ &= \frac{g^2}{2} \frac{1}{V^2} \sum_{\mathbf{n}} \sum_{\mathbf{k} \neq 0} \sum_{\mathbf{k}' \neq 0} \left(1 - e^{-i\frac{2\pi}{N}k_x}\right) \left(1 - e^{-i\frac{2\pi}{N}k'_x}\right) e^{-i\frac{2\pi}{N}(\mathbf{kn} + \mathbf{k}'\mathbf{n})} \\ &\quad \times \frac{2i \sin\left(\frac{2\pi}{N}\frac{Dk_x}{2}\right)}{4 - 2 \cos\left(\frac{2\pi}{N}k_x\right) - 2 \cos\left(\frac{2\pi}{N}k_y\right)} \frac{2i \sin\left(\frac{2\pi}{N}\frac{Dk'_x}{2}\right)}{4 - 2 \cos\left(\frac{2\pi}{N}k'_x\right) - 2 \cos\left(\frac{2\pi}{N}k'_y\right)} \\ &= \frac{g^2}{2} \frac{1}{V} \sum_{\mathbf{k} \neq 0} \left(1 - e^{-i\frac{2\pi}{N}k_x}\right) \left(1 - e^{i\frac{2\pi}{N}k_x}\right) \frac{4 \sin\left(\frac{2\pi}{N}\frac{Dk_x}{2}\right)^2}{\left(4 - 2 \cos\left(\frac{2\pi}{N}k_x\right) - 2 \cos\left(\frac{2\pi}{N}k_y\right)\right)^2} \\ &= \frac{g^2}{2} \frac{1}{V} \sum_{\mathbf{k} \neq 0} \left(2 - 2 \cos\left(\frac{2\pi}{N}k_x\right)\right) \frac{4 \sin\left(\frac{2\pi}{N}\frac{Dk_x}{2}\right)^2}{\left(4 - 2 \cos\left(\frac{2\pi}{N}k_x\right) - 2 \cos\left(\frac{2\pi}{N}k_y\right)\right)^2} . \quad (3.62) \end{aligned}$$

Similarly, we get for the y -part

$$\begin{aligned} H_{\text{Coul.}}^y &= \frac{g^2}{2} \sum_{\mathbf{n}} (E_{\mathbf{n},y}^L)^2 \\ &= \frac{g^2}{2} \frac{1}{V^2} \sum_{\mathbf{n}} \sum_{\mathbf{k} \neq 0} \sum_{\mathbf{k}' \neq 0} \left(1 - e^{-i\frac{2\pi}{N}k_y}\right) \left(1 - e^{-i\frac{2\pi}{N}k'_y}\right) e^{-i\frac{2\pi}{N}(\mathbf{kn} + \mathbf{k}'\mathbf{n})} \\ &\quad \times \frac{2i \sin\left(\frac{2\pi}{N}\frac{Dk_x}{2}\right)}{4 - 2 \cos\left(\frac{2\pi}{N}k_x\right) - 2 \cos\left(\frac{2\pi}{N}k_y\right)} \frac{2i \sin\left(\frac{2\pi}{N}\frac{Dk'_x}{2}\right)}{4 - 2 \cos\left(\frac{2\pi}{N}k'_x\right) - 2 \cos\left(\frac{2\pi}{N}k'_y\right)} \\ &= \frac{g^2}{2} \frac{1}{V} \sum_{\mathbf{k} \neq 0} \left(1 - e^{-i\frac{2\pi}{N}k_y}\right) \left(1 - e^{i\frac{2\pi}{N}k_y}\right) \frac{4 \sin\left(\frac{2\pi}{N}\frac{Dk_x}{2}\right)^2}{\left(4 - 2 \cos\left(\frac{2\pi}{N}k_x\right) - 2 \cos\left(\frac{2\pi}{N}k_y\right)\right)^2} \\ &= \frac{g^2}{2} \frac{1}{V} \sum_{\mathbf{k} \neq 0} \left(2 - 2 \cos\left(\frac{2\pi}{N}k_y\right)\right) \frac{4 \sin\left(\frac{2\pi}{N}\frac{Dk_x}{2}\right)^2}{\left(4 - 2 \cos\left(\frac{2\pi}{N}k_x\right) - 2 \cos\left(\frac{2\pi}{N}k_y\right)\right)^2} . \quad (3.63) \end{aligned}$$

These are the formulae we implement numerically as contributions to the ground state energy shown in Fig. 3.3.

3.B.3 String-Coulomb contribution to the ground state energy

We also include the string-Coulomb contribution, starting from Eq. (4.46) of Ref. [121]. It reads

$$\delta\langle\hat{H}\rangle_{s-c} = \frac{\pi^2 - 4}{2\pi^2 g^2} \mu^4 \sum_{\mathbf{n}, \mathbf{m}, i} E_{\mathbf{n}, i}^L I_{\mathbf{n}\mathbf{m}} E_{\mathbf{m}, i}^{\text{st}}, \quad (3.64)$$

which needs to be **subtracted** from $\delta\langle\hat{H}\rangle_{s-s}$. Again, only electric fields in x -direction enter and one finds

$$\delta\langle\hat{H}\rangle_{s-c} = \frac{\pi^2 - 4}{2\pi^2 g^2} \mu^4 \sum_{\mathbf{n}, \mathbf{m}} \frac{1}{V} \sum_{\mathbf{k} \neq 0} \frac{2i \sin\left(\frac{2\pi}{N} \frac{Dk_x}{2}\right) \left(1 - e^{-i\frac{2\pi}{N} k_x}\right) e^{-i\frac{2\pi}{N} \mathbf{k}\mathbf{n}}}{4 - 2 \cos\left(\frac{2\pi}{N} k_x\right) - 2 \cos\left(\frac{2\pi}{N} k_y\right)} I_{\mathbf{n}\mathbf{m}} E_{\mathbf{m}, x}^{\text{st}}. \quad (3.65)$$

To simplify things, let us first consider

$$\begin{aligned} \frac{1}{V} \sum_{\mathbf{n}, \mathbf{m}, \mathbf{k}'} e^{-i\frac{2\pi}{N} \mathbf{k}\mathbf{n}} e^{i\frac{2\pi}{N} \mathbf{k}'(\mathbf{n}-\mathbf{m})} E_{\mathbf{m}, x}^{\text{st}} &= \frac{1}{V} \sum_{\mathbf{n}, \mathbf{k}'} \sum_{m_x = -N/2}^{N/2-1} e^{-i\frac{2\pi}{N} \mathbf{k}\mathbf{n}} e^{i\frac{2\pi}{N} \mathbf{k}'(\mathbf{n}-m_x)} \\ &= \frac{1}{V} \sum_{\mathbf{k}', \mathbf{n}} e^{-i\frac{2\pi}{N} \mathbf{k}\mathbf{n}} e^{i\frac{2\pi}{N} \mathbf{k}'\mathbf{n}} \frac{\sin\left(\frac{2\pi}{N} \frac{k'_x}{2} D\right) e^{i\frac{2\pi}{N} \frac{k'_x}{2}}}{\sin\left(\frac{2\pi}{N} \frac{k'_x}{2}\right)} \\ &= \frac{\sin\left(\frac{2\pi}{N} \frac{k_x}{2} D\right) e^{i\frac{2\pi}{N} \frac{k_x}{2}}}{\sin\left(\frac{2\pi}{N} \frac{k_x}{2}\right)}. \end{aligned} \quad (3.66)$$

In summary, we get

$$\begin{aligned} \delta\langle\hat{H}\rangle_{s-c} &= \frac{\pi^2 - 4}{2\pi^2 g^2} \mu^4 \frac{1}{V} \sum_{\mathbf{k} \neq 0} \frac{(2i)^2 \sin\left(\frac{2\pi}{N} \frac{Dk_x}{2}\right)^2}{4 - 2 \cos\left(\frac{2\pi}{N} k_x\right) - 2 \cos\left(\frac{2\pi}{N} k_y\right)} \\ &\quad \times \frac{1}{\left(\sqrt{4 - 2 \cos\left(\frac{2\pi}{N} k_x\right) - 2 \cos\left(\frac{2\pi}{N} k_y\right) + \frac{\mu^2}{g^2}}\right)^2}. \end{aligned} \quad (3.67)$$

This is the formula we compute numerically to obtain the string-Coulomb interaction for the ground state energy in Fig. 3.3. Again, to make analytic progress we employ the usual approximations and limits to obtain the string-Coulomb interaction energy

$$\delta\langle\hat{H}\rangle_{s-c} = \frac{\pi^2 - 4}{2\pi^2 g^2} \mu^4 \int_{-\pi}^{\pi} \frac{d^2 k}{(2\pi)^2} \frac{(2i)^2 \sin\left(\frac{Dk_x}{2}\right)^2}{k_x^2 + k_y^2} \frac{1}{\left(\sqrt{k_x^2 + k_y^2 + \frac{\mu^2}{g^2}}\right)^2}. \quad (3.68)$$

Differentiation with respect to the distance D yields

$$\begin{aligned} \lim_{D \rightarrow \infty} \frac{\partial}{\partial D} \delta \langle \hat{H} \rangle_{s-c} &= \lim_{D \rightarrow \infty} \frac{\pi^2 - 4}{2\pi^2 g^2} \mu^4 \int_{-\pi}^{\pi} \frac{d^2 k}{(2\pi)^2} \frac{(2i)^2 \sin(Dk_x) \frac{k_x}{2}}{k_x^2 + k_y^2} \frac{1}{(\sqrt{k_x^2 + k_y^2 + \frac{\mu^2}{g^2}})^2} \\ &= \frac{\pi^2 - 4}{2\pi^2 g^2} \mu^4 \int_{-\pi}^{\pi} \frac{d^2 k}{(2\pi)^2} \frac{(2i)^2 \pi \delta(k_x) \frac{k_x}{2}}{k_x^2 + k_y^2} \frac{1}{(\sqrt{k_x^2 + k_y^2 + \frac{\mu^2}{g^2}})^2} = 0. \end{aligned} \quad (3.69)$$

Hence, we conclude that the string-Coulomb energy scales sub-linearly and becomes unimportant for large distances, in accordance with the conclusions of Ref. [121] and our numerical findings in Fig. 3.3.

3.B.4 Flux fields

We furthermore use the variational approach [121] as outlined above to derive the electric field expectation value via the "quantum potential" and to compute the flux string displayed in Fig. 3.2. We get

$$\begin{aligned} \langle \hat{L}_{\mathbf{n}} \rangle &= -\frac{\mu^2}{g^2} \frac{2i}{V} \sum_{\mathbf{k} \neq 0} e^{i \frac{2\pi}{N} \mathbf{k} (\mathbf{n} - \frac{\hat{x}}{2} - \frac{\hat{y}}{2})} \frac{\sin(\frac{2\pi}{N} \frac{k_x D}{2})}{\sin(\frac{2\pi}{N} \frac{k_x}{2})} \\ &\times \frac{\sin(\frac{2\pi}{N} \frac{k_y}{2}) \sin(\frac{2\pi}{N} \frac{k_x D}{2})}{4 - 2 \cos(\frac{2\pi}{N} k_x) - 2 \cos(\frac{2\pi}{N} k_y)} \frac{1}{\sqrt{4 - 2 \cos(\frac{2\pi}{N} k_x) - 2 \cos(\frac{2\pi}{N} k_y) + \frac{\mu^2}{g^2}}}. \end{aligned} \quad (3.70)$$

The electric field expectation values are given by $\langle \hat{E}_{\mathbf{n},y} \rangle = \phi_{\mathbf{n}} - \phi_{\mathbf{n}+\hat{y}} + \langle \hat{L}_{\mathbf{n}-\hat{x}} \rangle - \langle \hat{L}_{\mathbf{n}} \rangle$ and $\langle \hat{E}_{\mathbf{n},x} \rangle = \phi_{\mathbf{n}} - \phi_{\mathbf{n}+\hat{x}} + \langle \hat{L}_{\mathbf{n}} \rangle - \langle \hat{L}_{\mathbf{n}-\hat{y}} \rangle$. Using the previous approximations, the x -field at the center of the string can be expressed as

$$\begin{aligned} \langle \hat{E}_{x,\mathbf{n}} \rangle &\approx \frac{\mu^2}{g^2} \frac{4}{(2\pi)^2} \int_{-\pi}^{\pi} d^2 k \frac{\frac{k_y^2}{4} \sin(\frac{k_x}{2} D) e^{-i \frac{k_x}{2}} e^{-ik_y}}{\frac{k_x}{2} (k_x^2 + k_y^2) (\sqrt{k_x^2 + k_y^2 + \frac{\mu^2}{g^2}})} \\ &\approx \frac{\mu^2}{g^2} \frac{4}{(2\pi)^2} \int_{-\pi}^{\pi} d^2 k \frac{\frac{k_y^2}{2} \pi \delta(k_x) e^{-i \frac{k_x}{2}} e^{-ik_y}}{(k_x^2 + k_y^2) (\sqrt{k_x^2 + k_y^2 + \frac{\mu^2}{g^2}})} \\ &\approx \frac{\mu^2}{g^2} \frac{2\pi}{(2\pi)^2} \int_{-\pi}^{\pi} dk_y \frac{k_y^2 \cos(k_y)}{k_y^2 (\sqrt{k_y^2 + \frac{\mu^2}{g^2}})} \\ &\approx \frac{\mu^2}{g^2} \frac{2\pi}{(2\pi)^2} \int_{-\pi}^{\pi} dk_y \frac{1}{(\sqrt{k_y^2 + \frac{\mu^2}{g^2}})}, \end{aligned} \quad (3.71)$$

for spatial coordinates $|x| = |n_x|a_s \ll D$, $y = n_y a_s = 0$ and for $D \rightarrow \infty$. From this, we conclude the result for the field strength of the flux field stated in the main text

$$\langle \hat{E}_{x,\mathbf{n}} \rangle = \frac{\mu^2}{g^2} \frac{4\pi}{(2\pi)^2} \log \left(\frac{\frac{\mu^2}{g^2} + \pi}{\frac{\mu^2}{g^2}} \right) \approx \frac{\mu^2}{\pi g^2} \log \left(\frac{\pi g^2}{\mu^2} \right). \quad (3.72)$$

The corresponding expression for $\langle \hat{E}_{y,\mathbf{n}} \rangle$ vanishes in this limit.

3.C Details on the theoretical modelling of the experiment

3.C.1 Model Hamiltonian

In this section, we motivate the choice of Hamiltonian (3.7) through the microscopic theory of $F = 1$ spinor Bose gases [120], see also Ref. [52] and Section 3.A. We consider the microscopic Hamiltonian

$$H_0 = \sum_{m_F} \int d^3x \left[\hat{\psi}_{x,m_F}^\dagger \left(-\frac{\nabla^2}{2m} - \mu + V_{m_F}(x) \right) \hat{\psi}_{x,m_F} + : c_0 \hat{n}_x^2 + c_1 \hat{\mathbf{F}}_x^2 : \right], \quad (3.73)$$

with atomic mass m , chemical potential μ , and scattering constants c_0, c_1 for local interactions of density $\hat{n}_x = \sum_{m_F} \hat{\psi}_{x,m_F}^\dagger \hat{\psi}_{x,m_F}$ and spin $\hat{\mathbf{F}}_x = \sum_{m_F, m'_F} \hat{\psi}_{x,m_F}^\dagger \mathbf{f}_{m_F m'_F} \hat{\psi}_{x,m'_F}$. Here, $\hat{\psi}_{x,m_F} = \hat{\psi}_{m_F}(x)$ are the bosonic field operators for hyperfine states $m_F = -1, 0, 1$ with commutation relations $[\hat{\psi}_{x,m_F}, \hat{\psi}_{y,m'_F}^\dagger] = \delta_{m_F m'_F} \delta(x - y)$, where $\mathbf{f} = (f^x, f^y, f^z)$ are the spin-1 matrices, and the colon represents normal ordering of operators.

The atomic mixture combines two such Bose gases: Na and Li. They are coupled through an interaction Hamiltonian

$$\hat{H}_{\text{int}} = c_0^{\text{NaLi}} \hat{n}_x^{\text{Na}} \hat{n}_x^{\text{Li}} + c_1^{\text{NaLi}} \hat{\mathbf{F}}_x^{\text{Na}} \cdot \hat{\mathbf{F}}_x^{\text{Li}}, \quad (3.74)$$

such that the total Hamiltonian reads

$$\hat{H}_{\text{NaLi}} = \hat{H}_{\text{Na},0} + \hat{H}_{\text{Li},0} + \hat{H}_{\text{int}}. \quad (3.75)$$

In the experiment the atoms are strongly confined in a crossed optical dipole trap, i.e., they are tightly bound by optical potentials to suppress spatial dynamics in the gas. The system may effectively be described by a model with a single spatial mode for each magnetic substate. Detuning the $m_F = -1$ subspace from the dynamics, the free quadratic part of the resulting effective Hamiltonian reads

$$\hat{H}_{\text{NaLi},0} = \sum_{a,m_F=0,1} \epsilon_{a,m_F} \hat{b}_{a,m_F}^\dagger \hat{b}_{a,m_F}, \quad (3.76)$$

where m_F sums are restricted to 0 and 1 in the following. The single-particle energies ϵ_{a,m_F} are set by the trapping frequencies, external fields, fluctuations of spatial modes and we absorb further terms which arise from reordering the interaction operators. For fixed total atom numbers and magnetization, it may be expressed in a rotating frame as

$$\hat{H}_{\text{NaLi},0} = \frac{\tilde{\Delta}}{2} \sum_{m_F} (-1)^{m_F} \hat{b}_{\text{Li},m_F}^\dagger \hat{b}_{\text{Li},m_F} = \tilde{\Delta} \hat{L}_{\text{Li},z}. \quad (3.77)$$

In this approximation, the interaction Hamiltonian is given by

$$\begin{aligned} \hat{H}_{\text{int}} = & \sum_{a,m_F} \chi_{a,m_F} \hat{N}_{a,m_F}^2 + \chi_{\text{NaLi}} (\hat{N}_{\text{Na},0} - \hat{N}_{\text{Na},1}) (\hat{N}_{\text{Li},0} - \hat{N}_{\text{Li},1}) \\ & + \lambda \left(\hat{b}_{\text{Na},0}^\dagger \hat{b}_{\text{Li},1}^\dagger \hat{b}_{\text{Na},1} \hat{b}_{\text{Li},0} + h.c. \right), \end{aligned} \quad (3.78)$$

and all other combinations of operators have been absorbed into single-particle couplings. The effective interaction constants involve experimental details such as the scattering lengths, the atomic masses, magnetic fields and the spatial overlap of the condensates. We simplify the expression by using

$$\begin{aligned} \chi_{a,m_F} \hat{N}_{a,m_F}^2 &= \chi_{a,m_F} \left(\frac{\hat{M}_a}{2} + (-1)^{m_F} \hat{L}_{a,z} \right)^2 \\ &= \chi_{a,m_F} \left(\frac{\hat{N}_a^2}{4} + \hat{L}_{a,z}^2 + (-1)^{m_F} \hat{N}_a \hat{L}_{a,z} \right). \end{aligned} \quad (3.79)$$

By collecting all terms, assuming conservation of total atom numbers and magnetization during the dynamics, and dropping irrelevant constants, we may write the Hamiltonian as in Eq. (3.7) with the identifications

$$\begin{aligned} \Delta &= \tilde{\Delta} + 4\chi_{\text{NaLi}} \hat{M} + 2\hat{M}(\chi_{\text{Li},0} + \chi_{\text{Li},1}) + (\chi_{\text{Li},0} - \chi_{\text{Li},1}) \hat{N}_{\text{Li}} - (\chi_{\text{Na},0} - \chi_{\text{Na},1}) \hat{N}_{\text{Na}}, \\ \chi &= \chi_{\text{Na},0} + \chi_{\text{Na},1} + \chi_{\text{Li},0} + \chi_{\text{Li},1} - 4\chi_{\text{NaLi}}. \end{aligned} \quad (3.80)$$

For the chosen initial states, the magnetization is set by $\hat{L}_{\text{Na},z}(t_0) - \hat{N}_{\text{Li}}/2$. Neglecting fluctuations of the Li atom number in the model parameters, $N_{\text{Li}} = \langle \hat{N}_{\text{Li}} \rangle$ is absorbed into the parameters, and we get

$$\Delta = \Delta_0 + 2\Delta_L \hat{L}_{\text{Na},z}(t_0) + \Delta_N \hat{N}_{\text{Na}}, \quad (3.81)$$

where, specifically, we defined

$$\Delta_L = 2\chi_{\text{NaLi}} + (\chi_{\text{Li},0} + \chi_{\text{Li},1}), \quad (3.82a)$$

$$\Delta_0 = \tilde{\Delta} - \Delta_L N_{\text{Li}}, \quad (3.82b)$$

$$\Delta_N = \chi_{\text{Na},1} - \chi_{\text{Na},0}. \quad (3.82c)$$

In our numerical calculations we consider Δ including fluctuations of $\hat{L}_{\text{Na},z}(t_0)$, and \hat{N}_{Na} in the initial state as given in (3.81)

3.C.2 Model parameters

In this section, we determine the coupling parameters entering our model in the Hamiltonian given by Eq. (3.7). To achieve this, we post-select the experimental data to analyze the dependence of model parameters on the number of Na atoms in the atomic cloud. We assume that the atom number of Na has a relatively bigger

impact on the parameters compared to Li, as it is significantly higher, and hence we only consider atom number fluctuations of Na in this section. We focus our analysis on the data-set used in Fig. 3.6.

For the considered data set we measured the atom number of Na at $t = 30\text{ms}$ as $N_{\text{Na}} = (376.5 \pm 20.4) \times 10^3$, where the atom number fluctuation $\sigma = 20.4 \times 10^3$ is the standard deviation of the distribution of all experimental realizations. We split the data set into six “bands” of different mean atom numbers but fixed width set by $\sigma/2$, and selectively extract the lithium imbalance values η_{Li} . We then fit numerical calculations to the data to extract parameters for the different total atom numbers.

We extract the atom number dependence of parameters by fitting the data to a mean-field calculation of our model. As shown in Fig. 3.5, the observed Li imbalance at evolution time $t = 30\text{ms}$ is an estimate for stationary states at late times. Using this reasoning, we extract an estimate for our model parameters by fitting the data to the numerical calculation at $t = 150\text{ms}$ with a damping rate $\gamma = 2.2 \times 10^{-3}\text{Hz}$. For example, two such fits corresponding to the mean atom numbers $\bar{N}_{\text{Na}} = 397 \times 10^3$ and $\bar{N}_{\text{Na}} = 346 \times 10^3$ are shown in Fig. 3.12a. Matching the resonance requires a fine-tuning of χ and Δ . In Fig. 3.12 we show parameter sets obtained from these fits. Panel b indicates that χ and Δ_L are approximately equal on the percentage level. Further, both the ratio Δ_L/χ as well as the rate of the spin-changing collisions only weakly depend on the Na atom number \bar{N}_{Na} in the considered range, while χ and Δ_L show a stronger dependence. From the procedure explained above, we obtain $\lambda/2\pi = 2.038 \times 10^{-5}\text{Hz}$, $\chi/2\pi = 0.0092\text{Hz}$, $\Delta_L/2\pi = 0.00941\text{Hz}$, $\Delta_N/2\pi = -1.298 \times 10^{-4}\text{Hz}$ and $\Delta_0/2\pi = 43.30\text{Hz}$, by fitting the values in Fig. 3.12 with our model parameters. The similar values $\Delta_L \approx \chi$ as well as the relatively smaller $\Delta_N \ll \chi$ suggest that the dynamics of density interactions are dominated by the Li scattering constants $\chi_{\text{Li,mF}}$.

We use these parameters as a starting point to match both the mean and fluctuation data for both Fig. 3.5 and Fig. 3.6, and obtain $\lambda/2\pi = 1.8 \times 10^5\text{Hz}$, $\chi/2\pi = 0.00943\text{Hz}$, $\Delta_L/2\pi = 0.00961\text{Hz}$, $\Delta_0/2\pi = -73.81\text{Hz}$, $\Delta_N/2\pi = 2.108 \times 10^{-4}\text{Hz}$, and $\gamma = 1.8 \times 10^{-3}\text{Hz}$.

3.C.3 Numerical evolution

In our numerical real-time calculations we compute the classical evolution equations for an ensemble of initial states. The ensemble is characterized by Gaussian distributions of total atom numbers and magnetization. For the distribution of atom numbers we use the respectively measured mean values and standard deviations as $N_{\text{Na}} = (313.2 \pm 18.3) \times 10^3$, $N_{\text{Li}} = (34.6 \pm 3.2) \times 10^3$ for Fig. 3.5, and $N_{\text{Na}} = (376.5 \pm 20.4) \times 10^3$, $N_{\text{Li}} = (29.0 \pm 2.3) \times 10^3$ for Fig. 3.6. Further, we first consider the atoms in their respective $|F = 1, m_F = 1\rangle$ state as also prepared in the experiments. Here, we take into account the (Gaussian) quantum fluctuations via

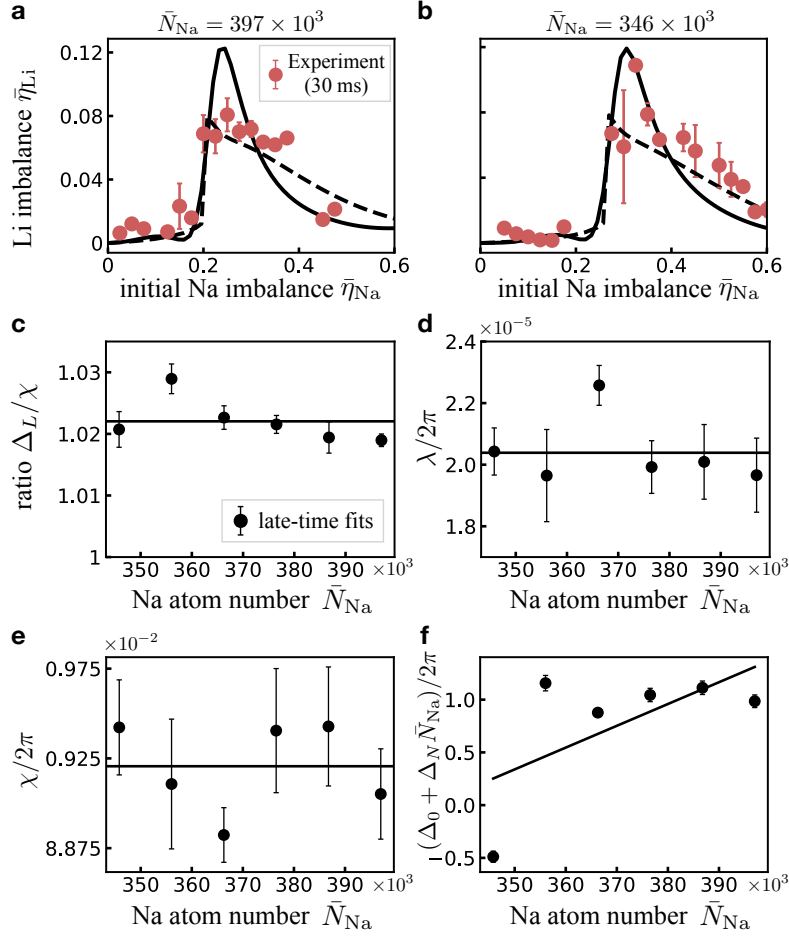


FIGURE 3.12: Model parameters: (a, b) We fit the data with the simulation result for $t = 150$ ms (dashed) for two different mean Na atom numbers \bar{N}_{Na} (as a comparison we also show the numerical result for $t = 30$ ms (solid)). (c-f) The parameters we obtain from fitting six different mean atom numbers are fitted to the model parameters. Figure taken from [7].

the following distributions of the (classical) boson variables

$$\langle b_{a,i} \rangle = \langle b_{a,i}^* \rangle = 0 \quad , \quad \langle b_{a,i}^* b_{a,i} \rangle = \tilde{N}_{a,i} + \frac{1}{2}, \quad (3.83)$$

where $\tilde{N}_{a,i}$ are given by $\tilde{N}_{Na,1} = N_{Na}$, $\tilde{N}_{Li,1} = N_{Li}$, and $\tilde{N}_{Na,0} = N_{Li,0} = 0$, with N_a being the total atom numbers in each realization for the two species. Subsequently, we simulate the initial state preparation with the (classical) Hamiltonian

$$H_{\text{prep}} = -i\Omega(b_{Na,0}^* b_{Na,1} - c.c.), \quad (3.84)$$

where *c.c.* denotes complex conjugation. To prepare the initial state, we apply the Hamiltonian H_{prep} for a time duration of $t_{\text{prep}}/\hbar = 2\pi\bar{\eta}_{Na}(t_0)/\Omega$.

For the curves shown in Fig. 3.5 and Fig. 3.6, we average the dynamics over 100 realizations of the above procedure. During the simulation of the system evolution,

we evolve the coupled spins with their classical equations of motion given by

$$\partial_t L_{\text{Li},x} = 2\lambda L_{\text{Li},z} L_{\text{Na},y} + \gamma L_{\text{Li},x} L_{\text{Na},z}, \quad (3.85a)$$

$$\partial_t L_{\text{Li},y} = -2\lambda L_{\text{Li},z} L_{\text{Na},x} + \gamma L_{\text{Li},y} L_{\text{Na},z}, \quad (3.85b)$$

$$\partial_t L_{\text{Li},z} = 2\lambda(L_{\text{Li},y} L_{\text{Na},x} - L_{\text{Li},x} L_{\text{Na},y}) - \gamma(L_{\text{Li},x}^2 + L_{\text{Li},y}^2), \quad (3.85c)$$

$$\partial_t L_{\text{Na},x} = (-2\chi L_{\text{Na},z} + \Delta) L_{\text{Na},y} + 2\lambda L_{\text{Na},z} L_{\text{Li},y} - \gamma L_{\text{Li},x} L_{\text{Li},z}, \quad (3.85d)$$

$$\partial_t L_{\text{Na},y} = (2\chi L_{\text{Na},z} - \Delta) L_{\text{Na},x} - 2\lambda L_{\text{Na},z} L_{\text{Li},x} - \gamma L_{\text{Li},y} L_{\text{Li},z}, \quad (3.85e)$$

$$\partial_t L_{\text{Na},z} = 2\lambda(L_{\text{Na},x} L_{\text{Li},x} - L_{\text{Li},y} L_{\text{Na},x}) + \gamma(L_{\text{Li},x}^2 + L_{\text{Li},y}^2), \quad (3.85f)$$

including the coherent evolution and the phenomenological damping with rate γ . Here, we transformed the equations into a rotating frame to reduce numerical cost.

The sketches of the dynamics of mean imbalance and fluctuations in Fig. 3.4 were plotted for the same parameters but with mean value and standard deviation of total atom numbers taken from the data of Fig. 3.6. The initial Na imbalance values are $\bar{\eta}_{\text{Na}}(t_0) = 0.15, 0.2, 0.5$ from left to right.

3.C.4 Thermal ensemble

We compare the data against a thermal ensemble with temperature $T = 630(20)\text{nK}$, as extracted from TOF-measurements [144]. Specifically, we compute observables $\hat{\mathcal{O}}$ in the canonical ensemble as

$$\langle \hat{\mathcal{O}} \rangle = \frac{1}{Z} \text{Tr} \left(\hat{\mathcal{O}} \hat{P}_M e^{-\beta \hat{H}} \right), \quad (3.86)$$

where $Z = \text{Tr} \left(\hat{P}_M \exp(-\beta \hat{H}) \right)$ is the canonical partition sum. Here, we focus on the gauge-invariant ensemble with fixed total magnetization \hat{M} . As our system evolves at high energies, we consider the classical thermal limit in the following, which is valid for high temperatures. We compute the classical partition function as

$$Z_{cl} = \left[\prod_{a,m_F} \int db_{a,m_F} db_{a,m_F}^* \right] e^{-\beta H(\{b_{a,m_F}\})}, \quad (3.87)$$

where H is the Wigner-Weyl transform of the system Hamiltonian \hat{H}_{NaLi} [142]. For fixed total atom numbers and magnetization, we consider the following Hamiltonian in the classical limit

$$H = \chi L_{\text{Na},z}^2 + \Delta L_{\text{Li},z} + 2\lambda(L_{\text{Na},x} L_{\text{Li},x} + L_{\text{Na},y} L_{\text{Li},y}), \quad (3.88)$$

where $L_{a,\pm} = L_{a,x} \pm iL_{a,y}$. The integral can be transformed to the coordinates

$$Z_{cl} = \mathcal{N} \int ds d\phi e^{-\beta H(s,\phi)}, \quad (3.89)$$

where \mathcal{N} is an (unimportant) normalization, and s, ϕ are the two remaining degrees of freedom of the classical system after using the conservation of magnetization, particle number and integrating out irrelevant absolute phases. Physically, ϕ represents the relative azimuthal angle between both spins and $s = 2\eta_{\text{Li}} - 1$ is the normalized z component of lithium. In this representation, the Hamiltonian is given by

$$H(s, \phi) = \chi \ell_{\text{Li}}^2 s^2 + (\Delta - 2M\chi) \ell_{\text{Li}} s + 2\lambda \ell_{\text{Li}} \ell_{\text{Na}} \sqrt{1 - s^2} \sqrt{1 - \frac{(M - \ell_{\text{Li}} s)^2}{\ell_{\text{Na}}^2}} \cos(\phi), \quad (3.90)$$

where we defined the spin lengths $\ell_a = N_a/2$. To derive Eq. (3.90), we used

$$L_{a,x} = \sqrt{N_{a,0} N_{a,1}} \cos(\phi_a), \quad (3.91a)$$

$$L_{a,y} = \sqrt{N_{a,0} N_{a,1}} \sin(\phi_a), \quad (3.91b)$$

$$L_{a,z} = \frac{N_{a,0} - N_{a,1}}{2}, \quad (3.91c)$$

where ϕ_a are the relative phases between the magnetic substates for each species. We then set $s_a = (N_{a,0} - N_{a,1})/(N_{a,0} + N_{a,1})$, and used

$$N_{0,a} N_{1,a} = \left(\frac{N_a}{2} + L_{z,a} \right) \left(\frac{N_a}{2} - L_{z,a} \right) \quad (3.92)$$

$$= \left(\frac{N_a}{2} \right)^2 - L_{z,a}^2 \quad (3.93)$$

$$= \ell_a^2 (1 - s_a^2), \quad (3.94)$$

which allowed us to rewrite the interaction term as

$$\begin{aligned} & L_{\text{Na},x} L_{\text{Li},x} + L_{\text{Na},y} L_{\text{Li},y} \\ &= \ell_{\text{Li}} \ell_{\text{Na}} \sqrt{1 - s_{\text{Na}}^2} \sqrt{1 - s_{\text{Li}}^2} \times (\cos(\phi_{\text{Na}}) \cos(\phi_{\text{Li}}) + \sin(\phi_{\text{Na}}) \sin(\phi_{\text{Li}})) \\ &= \ell_{\text{Li}} \ell_{\text{Na}} \sqrt{1 - s_{\text{Na}}^2} \sqrt{1 - s^2} \cos(\phi_{\text{Na}} - \phi_{\text{Li}}). \end{aligned} \quad (3.95)$$

Eq. (3.90) is obtained by further using $M = \ell_{\text{Li}} s + \ell_{\text{Na}} s_{\text{Na}}$ and defining the relative phase $\phi = \phi_{\text{Na}} - \phi_{\text{Li}}$ while integrating out the absolute phase $\phi_{\text{Na}} + \phi_{\text{Li}}$.

Observables are subsequently obtained by numerical integration of the partition sum. For instance, for the expectation value of the lithium z -spin, we get

$$\langle L_{\text{Li},z} \rangle = \int ds d\phi \ell_{\text{Li}} s e^{-\beta H(s, \phi)}, \quad (3.96)$$

and its fluctuations are computed as

$$\langle L_{\text{Li},z}^2 \rangle = \int ds d\phi \ell_{\text{Li}}^2 s^2 e^{-\beta H(s, \phi)}. \quad (3.97)$$

In the main text we show connected moments, which are defined as the corresponding variance

$$\sigma_{L_{Li,z}}^2 = \langle L_{Li,z}^2 \rangle - \langle L_{Li,z} \rangle^2. \quad (3.98)$$

Besides the thermal fluctuations represented by this partition sum, we average the results over 20 realizations of Gaussian atom number fluctuations for Na and Li with $N_{Na} = (313.2 \pm 18.3) \times 10^3$, $N_{Li} = (34.6 \pm 3.2) \times 10^3$ for Fig. 3.5 and $N_{Na} = (376.5 \pm 20.4) \times 10^3$, $N_{Li} = (29.0 \pm 2.3) \times 10^3$ for Fig. 3.6, where the values are mean and standard deviation of the measured overall atom number distributions. In our numerical evaluation of corresponding integrals for mean values and fluctuations of the ensemble, we discretize the integration domain from $\phi \in [0, 2\pi)$ in 60 evenly spaced intervals and similarly for $s \in [-1, s_{\max})$ in 150 intervals, where we chose a cutoff $s_{\max} = 0.4$. We checked the insensitivity of our results to these choices by varying the cutoff and the number of intervals.

3.C.5 Effective potentials

In this section we give a more detailed explanation of the effective potentials for mean fields as shown in the main text, see also [110]. Starting from the model Hamiltonian, the coherent evolution equation relevant for early times are given by the classical equations of motion $\partial_t \mathbf{L}_{Li} = \{H, \mathbf{L}_{Li}\}$, where $\{\cdot, \cdot\}$ denote the fundamental Poisson brackets with $\{L_{a,i}, L_{b,j}\} = \epsilon_{ijk} \delta_{ab} L_{a,k}$. Using the conservation of energy (H), magnetization (M), and total atom numbers (N_{Na}, N_{Li}) the evolution may be expressed as

$$\partial_t^2 L_{Li,z} = -\frac{\partial V(L_{Li,z})}{\partial L_{Li,z}}, \quad (3.99)$$

where V is a quartic potential $V(x) = \sum_{i=1}^4 c_i x^i / i$ and the coefficients c_i are given by

$$c_1 = (2\chi M - \Delta)(H - \chi M^2) - \lambda^2 M N_{Li}, \quad (3.100a)$$

$$c_2 = (2\chi M - \Delta)^2 + 2\chi(\chi M^2 - H) + \lambda^2(N_{Na}^2 + N_{Li}^2 - 4M^2), \quad (3.100b)$$

$$c_3 = -3\chi(2\chi M - \Delta) + 12\lambda^2 M, \quad (3.100c)$$

$$c_4 = 2\chi^2 - 8\lambda^2. \quad (3.100d)$$

Straightforward rescaling with the total atom number of Li yields the equations in the main text. In Fig. 3.13 we show the normalized potentials $V(x)/|V(-1)|$ for the imbalance values $\bar{\eta}_{Na}(t_0) = 0.15, 0.2, 0.5$. In Fig. 3.4 these potentials are drawn (from left to right) with arbitrary units on the y-axis.

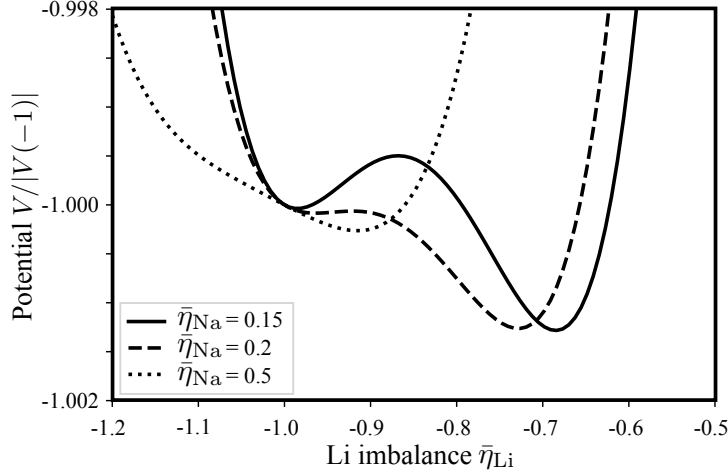


FIGURE 3.13: Effective mean-field potentials: We show the effective mean-field potential for $\bar{\eta}_{Li}$ for the values $\bar{\eta}_{Na}(t_0) = 0.15, 0.2,$ and 0.5 . Figure taken from [7].

3.C.6 Identification with QED and gauge field instability

In this section, we numerically investigate the real-time dynamics of a quantum simulator in the minimal case of a unit plaquette of the QED field theory. We demonstrate the phenomenon of a non-equilibrium instability for this model, and illustrate how the quantum simulator would approach the QED result with increasing atom number. As an experimental signature, we discuss growth rates of the electric field evolution for mean field and two-point functions. We furthermore comment on the identification of observables in the quantum simulator. The four-mode system is illustrated in Fig. 3.14.

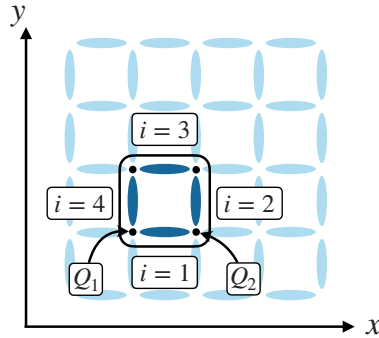


FIGURE 3.14: Single plaquette of the lattice gauge theory: We establish the non-perturbative dynamics of electromagnetic fields for the simplest case of a single plaquette.

The Hamiltonian for this unit building block of the two dimensional lattice field theory reads

$$\hat{H} = \frac{g^2}{2} \sum_{i=1}^4 \hat{E}_i^2 - \frac{1}{2g^2} \left(\hat{U}_1 \hat{U}_2 \hat{U}_3^\dagger \hat{U}_4^\dagger + h.c. \right), \quad (3.101)$$

where the (dimensionless) operators fulfill the gauge field commutation relations $[\hat{E}_i, \hat{U}_j] = \hat{U}_j \delta_{ij}^4$. For the four links of the model there are four associated Gauss operators

$$\hat{G}_1 = \hat{E}_1 + \hat{E}_4 - Q_1, \quad (3.102a)$$

$$\hat{G}_2 = \hat{E}_2 - \hat{E}_1 - Q_2, \quad (3.102b)$$

$$\hat{G}_3 = -\hat{E}_2 - \hat{E}_3 - Q_3, \quad (3.102c)$$

$$\hat{G}_4 = \hat{E}_3 - \hat{E}_4 - Q_4, \quad (3.102d)$$

with classical charges which we choose to be zero here, $Q_i = 0$. To simulate the real-time dynamics of the gauge fields we compute the operator evolution equations via the Heisenberg equation $i\partial_t \hat{O} = [\hat{O}, \hat{H}]$, see the following section 3.C.7 for details. We first solve the dynamics in a classical mean-field approximation which is expected to hold for small couplings and large occupations or mean fields⁵. The non-equilibrium evolution starts from the initial conditions

$$\langle \hat{E}_1(t_0) \rangle = E_0, \quad (3.103a)$$

$$\langle \hat{E}_2(t_0) \rangle = -E_0, \quad (3.103b)$$

$$\langle \hat{E}_3(t_0) \rangle = E_0, \quad (3.103c)$$

$$\langle \hat{E}_4(t_0) \rangle = -E_0, \quad (3.103d)$$

$$\langle \hat{B}(t_0) \rangle = -\pi, \quad (3.103e)$$

with $E_0 = 4$ and at first we neglect initial (co-)variances. Here, we introduced the magnetic field variable of the present system, $\hat{B} = \hat{\phi}_1 + \hat{\phi}_2 - \hat{\phi}_3 - \hat{\phi}_4$. It is the single physical combination of the gauge field potentials $\hat{\phi}_i$ (where $\hat{U}_i = \exp[i\hat{\phi}_i]$), which is a direct consequence of gauge-invariance.

The resulting evolution of the electric field at link $i = 1$, as well as the magnetic field are shown in Fig. 3.15 for the coupling value $g^2 = 0.01$. The initial dynamics is characterized by an exponential growth of the electric field value, which is followed by periodic oscillations. Conversely, the magnetic field increases monotonically, with branch cuts whenever it reaches the value $\langle \hat{B} \rangle = \pi$. The instability can be understood as a “rolling down” of the mean field variable, which initially evolves in the negatively curved region of a one-dimensional periodic potential. To derive the growth rate in the linear growth regime, we apply the duality, which we outline in the appendix 3.B for the field theory, to the single plaquette [121]. We define the operator $\hat{L} = (\hat{E}_1 + \hat{E}_2 - \hat{E}_3 - \hat{E}_4)/4$ which fulfills the commutation relations $[\hat{L}, \hat{B}] = i$, i.e., the electric field potential \hat{L} is conjugate to the magnetic field \hat{B} . Using the Gauss operators for the charge-neutral sector ($Q_i = 0$) we identify the electric field operators as $\hat{E}_1 = \hat{E}_2 = -\hat{E}_3 = -\hat{E}_4$, such that the dual Hamiltonian

⁴Compared to 3.1, we made the Hamiltonian dimensionless by multiplying with the length scale a_s .

⁵The applicability is justified since the system quickly evolves toward large mean field values.

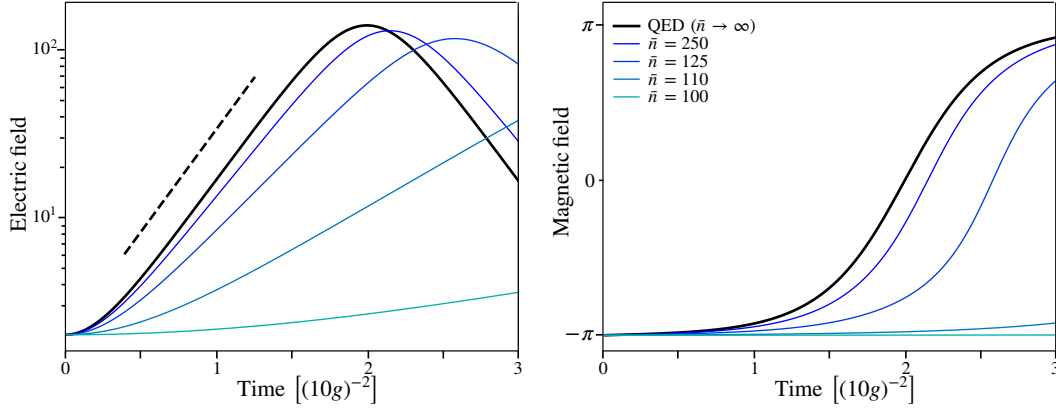


FIGURE 3.15: Gauge field instability in a single plaquette: We compare the classical evolution of QED gauge fields and ultra-cold atoms for different values of atom number offsets \bar{n} . The exponential growth is indicated by the dashed line.

reads

$$\hat{H} = 2g^2 \hat{L}^2 - \frac{1}{g^2} \cos(\hat{B}). \quad (3.104)$$

The corresponding operator evolution equations are given by

$$\partial_t \hat{B} = -4g^2 \hat{L} \quad , \quad \partial_t \hat{L} = -\frac{1}{g^2} \sin(\hat{B}), \quad (3.105)$$

and they encode the non-linear evolution of the gauge fields. At early times, where $\langle \hat{B} \rangle \approx -\pi$, we may expand $\sin(\hat{B}) \approx \hat{B} + \pi$ and thus approximate Eq. (3.105) with linear evolution equations which are exact at the classical level, i.e.,

$$\partial_t^2 B = 4(B + \pi). \quad (3.106)$$

Solutions are given by

$$B(t) \propto A_1 e^{\gamma t} + A_2 e^{-\gamma t} + 2\pi A_3 t^2, \quad L(t) = -\frac{\partial_t B(t)}{4g^2}, \quad (3.107)$$

where $B = \langle \hat{B} \rangle$, and $L = \langle \hat{L} \rangle$ denote the gauge field mean values, the constants A_i are fixed by the initial conditions, and $\gamma^2 = 4$. The growing mode quickly dominates, and thus leads to the exponential growth observed in Fig. 3.15, until higher-order terms become relevant and the linearization breaks down.

The proposed cold-atom Hamiltonian for the single plaquette (c.f. Eq. (3.2) with $\delta = 0$ for simplicity) is given by

$$\hat{H} = \frac{\chi}{2} \sum_{i=1}^4 \hat{b}_i^\dagger \hat{b}_i^\dagger \hat{b}_i \hat{b}_i - \lambda \left(\hat{b}_1^\dagger \hat{b}_2^\dagger \hat{b}_3 \hat{b}_4 + h.c. \right), \quad (3.108)$$

with coupling constants χ, λ representing density self-interactions and spin-changing

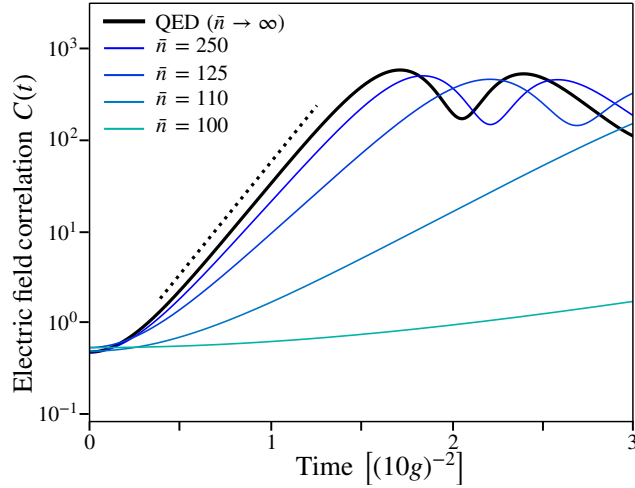


FIGURE 3.16: Growth of mean field and fluctuations: We compare the classical-statistical evolution of mean electric fields $\langle \hat{E}(t) \rangle$ and correlations $\langle \hat{E}^2(t) \rangle - \langle \hat{E}(t) \rangle^2$ for QED and ultra-cold atoms with different values of atom number offsets \bar{n} . The dotted line indicates twice the growth with rate compared to Fig. 3.15.

collisions of the atoms respectively. To approximate QED, we identify the couplings as $\chi = g^2$ and $\lambda = 1/(\bar{n}^2 g^2)$.

As outlined in Chapter 1, we expect the atoms' dynamics to converge to QED for sufficiently large $\bar{n} \gg 1$, thus working in the limit of Bose-Einstein condensates rather than individual atoms. This allows us to investigate the convergence toward continuous variable gauge fields (as realized in QED) for the above non-equilibrium dynamics. We employ the corresponding classical limit for the atomic condensates, where annihilation and creation operators are effectively replaced with complex numbers, see the next Section 3.C.7 for the detailed classical evolution equations. The atoms are initiated with mean atom number $b_i^* b_i = \bar{n}$ and a relative phase $\phi_1 + \phi_2 - \phi_3 - \phi_4 = \pm\pi$. By choosing these initial conditions, the atoms are effectively quenched out-of-equilibrium, thus initiating their dynamics. We show the subsequent dynamics in Fig. 3.15 for various values of \bar{n} . The controlled approach to the QED evolution, as specified by Eq. (3.101), is demonstrated in the limit $\bar{n} \rightarrow \infty$. Here, we defined the electric field in the quantum simulator as $\hat{\mathcal{E}} = \hat{b}_i^\dagger \hat{b}_i - \hat{n}$ as outlined in Chapter 1. Conversely, the magnetic field represents the relative phases of the condensates. Both quantities are accessible with current technology [23].

To go beyond the mean-field dynamics and investigate the evolution of correlation functions, we employ a classical-statistical approach next [131, 145, 146]. Here, we consider the same classical evolution equations but average the dynamics over Gaussian initial conditions to account for quantum fluctuations. In analogy with vacuum initial conditions in field theories, where initial fluctuations are described by the “quantum 1/2”, we choose the initial conditions as $\langle \hat{L}^2 \rangle = 1/2$, for the gauge fields and correspondingly $(1/2)\langle \{\hat{b}_i^\dagger, \hat{b}_i\} \rangle = \bar{n} + 1/2$ for the ultra-cold condensates. In Fig. 3.16 we show the classical-statistical evolution of the two-point function of

the electric field

$$C(t) = \langle \hat{E}(t)^2 \rangle - \langle \hat{E}(t) \rangle^2, \quad (3.109)$$

where we compare the ultra-cold condensates for several values of \bar{n} with QED. We find the two-point function to exhibit exponential growth at early times with twice the growth rate, i.e., $C(t) \propto \exp(2\gamma t)$.

Gauge field theory

The instability extends to the gauge field theory, as described by the Hamiltonian Eq. (3.1). In its dual form (see Eq. (3.39)), and for fixed external charges, it may be written as

$$\hat{H} = \frac{g^2}{2} \sum_{\mathbf{n}, i} (\hat{L}_{\mathbf{n}+i} - \hat{L}_{\mathbf{n}})^2 - \frac{1}{g^2} \sum_{\mathbf{n}} (1 - \cos(\hat{B}_{\mathbf{n}}^2)). \quad (3.110)$$

For the initial condition of a homogeneous magnetic field with $\langle \hat{B}_{\mathbf{n}} \rangle \approx \pi$ and weak coupling, we may approximately write for early times

$$\hat{H} = \frac{g^2}{2} \sum_{\mathbf{n}, i} (\hat{L}_{\mathbf{n}+i} - \hat{L}_{\mathbf{n}})^2 - \frac{1}{2g^2} \sum_{\mathbf{n}} \hat{B}_{\mathbf{n}}^2, \quad (3.111)$$

where we dropped an irrelevant constant. Rewriting the expression in Fourier space yields

$$\hat{H} = 2g^2 \sum_{\mathbf{q}, i} \sin^2(2q_i) \hat{L}_{\mathbf{q}}^2 - \frac{1}{2g^2} \sum_{\mathbf{q}} \hat{B}_{\mathbf{q}}^2. \quad (3.112)$$

The resulting Hamiltonian describes a collection of Fourier modes \mathbf{q} , each following the same evolution equations as the previously considered single plaquette degrees of freedom, but with momentum dependent growth rate, i.e.,

$$\gamma_{\mathbf{q}} \propto \left| \sqrt{\sin^2(2q_x) + \sin^2(2q_y)} \right|. \quad (3.113)$$

3.C.7 Evolution equations of gauge fields

In this section, we give further details on the numerical calculations presented in the previous Section 3.C.6.

Evolution equations

The numerical calculations are performed in the classical-statistical approximation [131, 145, 147]. For the case of small couplings and highly occupied one- or two-point functions, the dynamics is well-described by the following procedure: We compute the dynamics with classical (mean-field) evolution equations and average

a series of simulation runs over an ensemble of initial conditions specified by the quantum two-point functions of an initial Gaussian density matrix.

The operator evolution equations for the four-mode single plaquette dynamics are given by the Heisenberg operator equation $i\partial_t\hat{\mathcal{O}} = [\hat{\mathcal{O}}, \hat{H}]$, with Hamiltonian (3.101),

$$i\partial_t\hat{E}_1 = -\frac{1}{2g^2}(\hat{U}_1\hat{U}_2\hat{U}_3^\dagger\hat{U}_4^\dagger - \hat{U}_1^\dagger\hat{U}_2^\dagger\hat{U}_3\hat{U}_4), \quad (3.114a)$$

$$i\partial_t\hat{E}_2 = -\frac{1}{2g^2}(\hat{U}_1\hat{U}_2\hat{U}_3^\dagger\hat{U}_4^\dagger - \hat{U}_1^\dagger\hat{U}_2^\dagger\hat{U}_3\hat{U}_4), \quad (3.114b)$$

$$i\partial_t\hat{E}_3 = +\frac{1}{2g^2}(\hat{U}_1\hat{U}_2\hat{U}_3^\dagger\hat{U}_4^\dagger - \hat{U}_1^\dagger\hat{U}_2^\dagger\hat{U}_3\hat{U}_4), \quad (3.114c)$$

$$i\partial_t\hat{E}_4 = +\frac{1}{2g^2}(\hat{U}_1\hat{U}_2\hat{U}_3^\dagger\hat{U}_4^\dagger - \hat{U}_1^\dagger\hat{U}_2^\dagger\hat{U}_3\hat{U}_4), \quad (3.114d)$$

$$i\partial_t\hat{U}_1 = -\frac{g^2}{2}\{\hat{E}_1, \hat{U}_1\}, \quad (3.114e)$$

$$i\partial_t\hat{U}_2 = -\frac{g^2}{2}\{\hat{E}_2, \hat{U}_2\}, \quad (3.114f)$$

$$i\partial_t\hat{U}_3 = -\frac{g^2}{2}\{\hat{E}_3, \hat{U}_3\}, \quad (3.114g)$$

$$i\partial_t\hat{U}_4 = -\frac{g^2}{2}\{\hat{E}_4, \hat{U}_4\}, \quad (3.114h)$$

where $\{\cdot, \cdot\}$ denotes the anti-commutator. In the classical-statistical approximation the operator valued fields are "replaced" with classical variables and the anti-commutators become $\{\hat{E}_i, \hat{U}_i\} \rightarrow 2E_iU_i$.

The corresponding evolution equations of the ultra-cold atoms described by the Hamiltonian (3.108) are given by

$$i\partial_t\hat{b}_1 = \chi(\hat{b}_1^\dagger\hat{b}_1 - \bar{n})\hat{b}_1 - \lambda\hat{b}_3\hat{b}_2^\dagger\hat{b}_4, \quad (3.115a)$$

$$i\partial_t\hat{b}_2 = \chi(\hat{b}_2^\dagger\hat{b}_2 - \bar{n})\hat{b}_2 - \lambda\hat{b}_1^\dagger\hat{b}_3\hat{b}_4, \quad (3.115b)$$

$$i\partial_t\hat{b}_3 = \chi(\hat{b}_3^\dagger\hat{b}_3 - \bar{n})\hat{b}_3 - \lambda\hat{b}_1\hat{b}_4^\dagger\hat{b}_2, \quad (3.115c)$$

$$i\partial_t\hat{b}_4 = \chi(\hat{b}_4^\dagger\hat{b}_4 - \bar{n})\hat{b}_4 - \lambda\hat{b}_1\hat{b}_3^\dagger\hat{b}_2, \quad (3.115d)$$

where we switched to a rotating frame to reduce the amount of required evolution steps and thus save computational costs. For the classical-statistical approximation, we again replace observables with their mean values after symmetrically ordering the expression [131]. We get

$$i\partial_t b_1 = \chi(b_1^*b_1 - (\bar{n} + 1))b_1 - \lambda b_3 b_2^* b_4, \quad (3.116a)$$

$$i\partial_t b_2 = \chi(b_2^*b_2 - (\bar{n} + 1))b_2 - \lambda b_1^* b_3 b_4, \quad (3.116b)$$

$$i\partial_t b_3 = \chi(b_3^*b_3 - (\bar{n} + 1))b_3 - \lambda b_1 b_4^* b_2, \quad (3.116c)$$

$$i\partial_t b_4 = \chi(b_4^*b_4 - (\bar{n} + 1))b_4 - \lambda b_1 b_3^* b_2, \quad (3.116d)$$

We solve the dynamics using a numerical Runge-Kutta scheme with relative tolerance 10^{-8} .

Initial conditions

To employ the classical-statistical approximation, we consider an average over Gaussian initial state distributions involving one-point and connected two-point functions. In analogy with vacuum initial conditions in QED we set the initial two-point functions to

$$\langle L \rangle = 0, \quad (3.117a)$$

$$\langle L^2 \rangle = \frac{1}{2}. \quad (3.117b)$$

Correspondingly, for the ultra-cold condensates we choose the set-up

$$\langle b_i \rangle = 0, \quad (3.118a)$$

$$\langle b_i^* b_i \rangle = \bar{n} + \frac{1}{2}. \quad (3.118b)$$

to represent the quantum initial conditions. While these initial conditions lead to an average over different external charge sectors for the ultra-cold atoms, this detail can be addressed with an appropriate initial state preparation using Fock states, rather than coherent states. Also, the influence of this aspect on the dynamics quickly becomes negligible once fluctuations become large during the instability dynamics.

Chapter 4

Equal-time approach to quantum field dynamics

The contents of this chapter have been published in the following article:

- R. Ott, T. V. Zache, and J. Berges, “Equal-time approach to real-time dynamics of quantum fields”, arXiv preprint arXiv:2204.06463 (2022), see [6].

I performed the analytical calculations, and prepared the main text and figures in collaboration with the co-authors.

Large parts of the text as well as figures are taken from this publication. Parts of the calculations were previously presented in the doctoral thesis of T. V. Zache [110].

4.1 Motivation and Overview

Ultra-cold atom measurements are typically done at snapshots in time with the important ability to extract equal-time correlations to high orders [23, 24]. Equal-time correlations are highly suitable for the description of non-equilibrium systems, similar in spirit – but not limited to – kinetic descriptions in terms of single-time distributions. However, in contrast to these time-local approaches the conventional formulation of non-equilibrium quantum field theory is based on the closed-time-path contour [148–150] involving multiple-time correlations, which are difficult to access experimentally. In particular, standard derivations of effective kinetic descriptions from quantum field theory start from non-local equations in time which become time-local only after a series of approximations [146, 151].

In this chapter we derive effective kinetic theories for an ultra-cold Bose gas starting from an equal-time formulation of quantum field theory [142, 143, 152]. The central quantity is the time-dependent quantum effective action Γ_t , which contains the same information as the density operator at time t , but is expressed in terms of equal-time correlations. From the functional evolution equation for Γ_t [152] we derive evolution equations for equal-time vertices, which may be directly extracted from quantum simulation results as pioneered in Refs. [142, 143]. Here we demonstrate that the two- and four-point correlation functions at equal times

contain the complete information for the derivation of effective kinetic equations for time-dependent distribution functions $f_p(t)$

$$\begin{aligned} \partial_t f_p(t) = & \int_{q,r,s} |T_{pqrs}(t)|^2 ((f_p(t) + 1)(f_q(t) + 1)f_r(t)f_s(t) \\ & - f_p(t)f_q(t)(f_r(t) + 1)(f_s(t) + 1)), \end{aligned} \quad (4.1)$$

which shows characteristic “gain” and “loss” terms describing (in this case) $2 \leftrightarrow 2$ scattering into and out of the momentum mode p with matrix element $|T_{pqrs}(t)|^2$.

We first compute the dynamics of the Bose gas using a perturbative expansion in the small interaction strength $g \ll 1$ in section 4.4, where (4.1) reduces to the Boltzmann equation describing a dilute medium with occupancy $f_p \ll \mathcal{O}(1/g)$ such that particles stream freely in between individual scatterings. In this simplest case one finds from the (irreducible part) of the equal-time four-point function a time- and momentum-independent matrix element $|T_{pqrs}(t)|^2 = g^2/2(2\pi)^3 \delta(p + q - r - s)(2\pi)\delta(\Delta\omega_{pqrs})$, where $\Delta\omega_{pqrs} = \omega_p + \omega_q - \omega_r - \omega_s$ is the single-particle energy difference of in- and out-going particles. Therefore, one recovers that the scattering rate is given by the asymptotic T-matrix elements $|T_{pqrs}|^2$ in vacuum in this case.

In section 4.5 a non-perturbative approximation scheme is considered, where we employ an expansion in the number of field components N . At next-to-leading order in the large- N expansion we again recover an effective kinetic equation of the form (4.1), however, in this case with a time- and momentum-dependent $|T_{pqrs}(t)|^2$. We demonstrate that the latter is also fully determined by the irreducible part of the equal-time four-point function, which implements a geometric series resummation of the distribution $f_p(t)$ itself such that one obtains a closed equation for the time evolution. The importance of the large- N kinetic theory is that it can describe also strongly correlated systems with non-perturbatively high occupancies [153].

While these results establish a direct link between equal-time correlations and typical observables underlying effective kinetic theories, the exact quantum evolution equations we derive from the equal-time effective action are not limited to kinetic theory approximations. In section 4.6 we discuss an experimental protocol of how the exact equations could be established in quantum simulations with ultra-cold atom platforms, extending the procedures of Refs. [142, 143] to the Bose fields appearing in the defining Hamiltonian.

4.2 Correlations in a Bose gas

In our computations, we consider an N -component non-relativistic scalar field theory with Hamiltonian

$$\hat{H} = \int_x \left[\frac{\nabla \hat{\Psi}_x^\dagger \nabla \hat{\Psi}_x}{2m} - \mu \hat{\Psi}_x^\dagger \hat{\Psi}_x + \frac{g}{4N} : (\hat{\Psi}_x^\dagger \hat{\Psi}_x)^2 : \right]. \quad (4.2)$$

Here $\hat{\Psi}_x = (\hat{\psi}_{x,1}, \dots, \hat{\psi}_{x,N})$ is the N -component field operator at spatial position x , g is the scattering constant, m denotes the mass of the atoms, μ represents the chemical potential and the colons indicate normal ordering of operators. The field operators fulfill canonical commutation relations $[\hat{\psi}_{x,i}, \hat{\psi}_{y,j}^\dagger] = \delta(x-y)\delta_{ij}$, where we employ natural units with setting $\hbar = 1$. Here and in the following, we use shorthand notations for integrals over spatial coordinates $\int_x = \int_{-\infty}^{\infty} d^3x$ and momenta $\int_k = \int_{-\infty}^{\infty} d^3k/(2\pi)^3$. We focus on three spatial dimensions where Eq. (4.2) may be considered as a low-energy effective theory for ultra-cold Bose gases with a $U(N)$ symmetry.

We define a generating functional for equal-time correlations as [152]

$$Z_t[\mathbf{J}^{(*)}] = \text{Tr} \left(\hat{\rho}_t e^{\int_x (\hat{\Psi}_x^\dagger \mathbf{J}_x + \mathbf{J}_x^* \hat{\Psi}_x)} \right), \quad (4.3)$$

where $\hat{\rho}_t$ denotes the time-dependent density operator and $\mathbf{J}_x^{(*)} = (J_{x,1}^{(*)}, \dots, J_{x,N}^{(*)})$ are the N -component source fields. The generating functional contains the same information as the t -dependent density operator and fully describes the underlying quantum system at time t . With this representation the system is completely characterized by its set of equal-time correlations and its evolution is determined by the Hamiltonian of the theory. Repeated differentiation with respect to the sources, and evaluation for vanishing sources, yields symmetrically ordered correlation functions

$$G_{\alpha_1 \dots \alpha_j, \alpha_{j+1} \dots \alpha_n}^{(n)}(t) = \frac{1}{Z_t[\mathbf{J}^{(*)}]} \frac{\delta}{\delta J_{\alpha_1}^*} \dots \frac{\delta}{\delta J_{\alpha_j}^*} \frac{\delta}{\delta J_{\alpha_{j+1}}} \dots \frac{\delta}{\delta J_{\alpha_n}} Z_t[\mathbf{J}^{(*)}] \Big|_{\mathbf{J}, \mathbf{J}^* = 0}, \quad (4.4)$$

where we abbreviated the spatial and component indices as α_i , e.g. $\alpha_1 = (x_1, i_1)$. According to (4.4) we associate fields $\hat{\psi}$ with the indices to the left (here $\alpha_1 \dots \alpha_j$), and conjugate fields $\hat{\psi}^\dagger$ with the rightmost indices ($\alpha_{j+1} \dots \alpha_n$). Throughout this chapter we consider the case of $U(N)$ invariant correlations in the non-relativistic theory. By choosing a $U(N)$ invariant initial state the symmetry is preserved for the dynamics with Hamiltonian (4.2). As a consequence, all non-vanishing correlation functions involve an equal number of field and conjugate field operators. Specifically, this yields one type of two-point function which is given by

$$G_{\alpha_1, \alpha_2}^{(2)}(t) = \frac{1}{2} \langle \{ \hat{\psi}_{x_1, i_1}, \hat{\psi}_{x_2, i_2}^\dagger \} \rangle_t, \quad (4.5)$$

$$G^{\mathbf{c},(6)} = \begin{array}{c} \uparrow \\ \uparrow \\ \bullet \\ \downarrow \\ \downarrow \end{array} + \begin{array}{c} \uparrow \\ \uparrow \\ \bullet \\ \leftarrow \bullet \leftarrow \bullet \\ \downarrow \\ \downarrow \end{array} + \text{perm.}$$

FIGURE 4.1: Connected correlation functions from irreducible building blocks: We show the diagrammatic contributions to the 1PI connected six-point function ($G^{\mathbf{c},(6)}$). The first term involves a 1PI six-vertex, the second is assembled from two four-vertices. Field indices and permutations of external legs are implied and the number of in- and outgoing arrows is conserved due to $U(N)$ invariance. For details, see also appendix 4.B. Figure taken from [6].

where $\{\cdot, \cdot\}$ denotes the anti-commutator of operators, and the expectation value is given by the trace with respect to the density operator at time t .

In general, we distinguish between connected and disconnected correlation functions. Connected correlation functions (superscript “c”) are obtained by differentiating with respect to the equal-time Schwinger functional $W_t = \log(Z_t)$,

$$G_{\alpha_1 \dots \alpha_j, \alpha_{j+1} \dots \alpha_n}^{\mathbf{c},(n)}(t) = \frac{\delta}{\delta J_{\alpha_1}^*} \dots \frac{\delta}{\delta J_{\alpha_j}^*} \frac{\delta}{\delta J_{\alpha_{j+1}}} \dots \frac{\delta}{\delta J_{\alpha_n}} W_t[\mathbf{J}^{(*)}] \Big|_{\mathbf{J}, \mathbf{J}^* = 0}. \quad (4.6)$$

At order $2n$, they contain information about correlations of n bodies. Conversely, n -th order *disconnected* correlation functions are given by sums of all combinations of *connected* correlations involving in total $n/2$ bodies. For example, for $n = 4$ one gets (for the $U(N)$ -invariant case)

$$G_{\alpha_1 \alpha_2, \alpha_3 \alpha_4}^{(4)} = G_{\alpha_1 \alpha_2, \alpha_3 \alpha_4}^{\mathbf{c},(4)} + G_{\alpha_1, \alpha_3}^{\mathbf{c},(2)} G_{\alpha_2, \alpha_4}^{\mathbf{c},(2)} + G_{\alpha_1, \alpha_4}^{\mathbf{c},(2)} G_{\alpha_2, \alpha_3}^{\mathbf{c},(2)}, \quad (4.7)$$

and for $n = 2$ we have $G_{\alpha_1, \alpha_2}^{\mathbf{c},(2)} = G_{\alpha_1, \alpha_2}^{(2)}$ since the one-point function vanishes.

4.3 Equal-time 1PI effective action

In this section, we introduce the equal-time effective action and the corresponding time-dependent vertices, which are the irreducible building blocks of all connected equal-time correlation functions. The equal-time one-particle irreducible (1PI) effective action [142, 143, 152], analogous to the free energy, is defined as the Legendre transform

$$\Gamma_t[\Psi^{(*)}] = -W_t[\mathbf{J}^{(*)}] + \int_x \left(\Psi_x^\dagger \mathbf{J}_x + \mathbf{J}_x^* \Psi_x \right), \quad (4.8)$$

with field-dependent sources $\mathbf{J}(\Psi)$, $\mathbf{J}^*(\Psi^*)$, and $\Psi_x^{(*)}(\mathbf{J}^{(*)}) = \langle \hat{\Psi}_x^{(\dagger)} \rangle_J$, where the expectation value is defined with respect to the trace in Eq. (4.3) in the presence of sources. The effective action can be expanded in terms of the fields as

$$\Gamma_t[\Psi^{(*)}] = \sum_{n=2}^{\infty} \Gamma_{x_1 \dots x_n, i_1 \dots, i_n}^{(n)}(t) \times \psi_{x_1, i_1}^* \dots \psi_{x_n, i_n}, \quad (4.9)$$

with 1PI equal-time vertices that are obtained by differentiation as

$$\Gamma_{x_1 \dots x_n, i_1 \dots, i_n}^{(n)}(t) = \left. \frac{\delta^n \Gamma_t}{\delta \psi_{x_1, i_1}^* \dots \delta \psi_{x_n, i_n}} \right|_{\Psi^*, \Psi=0}. \quad (4.10)$$

These 1PI vertices are the irreducible building blocks for connected correlation functions. Specifically, this means that any equal-time connected correlation function is a combination of equal-time vertices and two-point functions. Important relations of correlation functions and effective vertices can be obtained by the definitions of the Schwinger functional and effective action, in combination with the chain rule for derivatives with respect to fields and sources. As an example, one finds for the two-point functions the relation $G_{\alpha_1 \alpha_2}^{\mathbf{c},(2)} = (\Gamma^{(2)})_{\alpha_1 \alpha_2}^{-1}$, and for four-point functions

$$G_{\alpha_1 \alpha_2, \alpha_3 \alpha_4}^{\mathbf{c},(4)} = -G_{\alpha_1 \alpha'_1}^{\mathbf{c},(2)} G_{\alpha_2 \alpha'_2}^{\mathbf{c},(2)} G_{\alpha_3 \alpha'_3}^{\mathbf{c},(2)} G_{\alpha_4 \alpha'_4}^{\mathbf{c},(2)} \Gamma_{\alpha'_1 \alpha'_2 \alpha'_3 \alpha'_4}^{(4)}. \quad (4.11)$$

Here, every index α'_i of the four-vertex is contracted with an equal-time two-point function also carrying a corresponding external index α_i . To illustrate this relation

graphically, we introduce the following notation

$$G_{\alpha_1\alpha_2}^{\mathbf{c},(2)} \equiv \text{---}\leftarrow\text{---} , \quad (4.12)$$

$$\Gamma_{\alpha_1\alpha_2}^{(2)} = \left(G_{\alpha_1\alpha_2}^{\mathbf{c},(2)}\right)^{-1} \equiv \text{---}\leftarrow\text{---} , \quad (4.13)$$

$$\Gamma_{\alpha_1\dots\alpha_n}^{(n)} \equiv \text{---}\leftarrow\text{---} , \quad (4.14)$$

where each ending line represents an index α , and 1PI vertices are amputated (red bars). Lines can furthermore meet at bare vertices, which in the evolution equations arise in combination with either one or three inverse two-point functions attached to them, as we will establish shortly.

In general, diagrams are assembled by connecting lines with vertices, which is accompanied by integration and summation over vertex positions and component indices as summarized by α . Importantly, the arrow indicates the flow of particles, such that all diagrams should conserve the arrows along the attached lines. While this diagrammatic language is very similar to perturbation theory in conventional quantum field theory, the equal-time correlation functions here depend on spatial coordinates and an overall time argument, rather than a set of spacetime coordinates, and no time-integrals appear.

Assuming spatial translation invariance, it will be beneficial to transform these objects and their evolution equations to Fourier space, where two-point functions and vertices are assigned momentum variables. Overall, momentum variables are assigned in a momentum conserving manner, i.e., a δ -distribution $(2\pi)^3\delta(p_1 + p_2 - p_3 - p_4)$ is implied at each vertex with ingoing momenta p_1, p_2 and outgoing ones p_3, p_4 . While connected four-point correlations originate from the four-vertex, all connected n -point correlations with $n > 4$ are built from sums over different diagrams involving vertices $\Gamma^{(4)}, \dots, \Gamma^{(n)}$. For example, the diagrams corresponding to the connected six-point function are displayed in Fig. 4.1. To clarify the diagrammatic rules, explicit formulae for diagrams are given in appendix 4.B.

In the following, we first consider $N = 1$. The straightforward generalization to the N component field theory will become important later for non-perturbative approximations based on an expansion in powers of $1/N$.

The effective action obeys an exact flow equation [152], which for the current model reads (see 4.A for derivational details),

$$\begin{aligned}
i\partial_t\Gamma_t = & \int_x \left(\frac{\delta\Gamma_t}{\delta\psi_x} \left(\frac{\nabla^2}{2m} + \mu \right) \psi_x - \frac{\delta\Gamma_t}{\delta\psi_x^*} \left(\frac{\nabla^2}{2m} + \mu \right) \psi_x^* \right. \\
& + \frac{g/2}{Z_t[J^{(*)}]} \frac{\delta^3 Z_t[J^{(*)}]}{(\delta J_x)^2 \delta J_x^*} \frac{\delta\Gamma_t}{\delta\psi_x^*} - \frac{g/2}{Z_t[J^{(*)}]} \frac{\delta^3 Z_t[J^{(*)}]}{\delta J_x (\delta J_x^*)^2} \frac{\delta\Gamma_t}{\delta\psi_x} \\
& \left. - \frac{g}{8} \psi_x^* \frac{\delta\Gamma_t}{\delta\psi_x} \frac{\delta\Gamma_t}{\delta\psi_x^*} \frac{\delta\Gamma_t}{\delta\psi_x^*} + \frac{g}{8} \frac{\delta\Gamma_t}{\delta\psi_x} \frac{\delta\Gamma_t}{\delta\psi_x} \frac{\delta\Gamma_t}{\delta\psi_x^*} \psi_x \right), \quad (4.15)
\end{aligned}$$

where $J^{(*)} = J^{(*)}[\psi^{(*)}]$, such that the effective action is a functional of the fields $\psi^{(*)}$ [110]. Similar to the von-Neumann equation for the density operator, the evolution equation of the equal-time effective action is time-local. This is different from functional approaches involving unequal-time effective actions, where the system's history enters at each step of the evolution. The first two lines of Eq. (4.15) represent the terms also present in the classical-statistical theory, while the third line represents genuine quantum corrections. The term $\sim \delta^3 Z_t[J^{(*)}]/((\delta J_x)^2 \delta J_x^*)$ corresponds to a symmetrized third-order correlation function which may be written in terms of the effective action. To this end, we split it into connected and disconnected correlations

$$\langle \hat{\psi}_x^\dagger \hat{\psi}_x^\dagger \hat{\psi}_x \rangle_{\text{sym}} = \langle \hat{\psi}_x^\dagger \hat{\psi}_x^\dagger \hat{\psi}_x \rangle_{\text{sym}}^{\text{c}} + 2G_{xx}^{\text{c},(2)} \psi_x^* + \langle \hat{\psi}_x^\dagger \hat{\psi}_x^\dagger \rangle_{\text{sym}}^{\text{c}} \psi_x + (\psi_x^*)^2 \psi_x, \quad (4.16)$$

where ‘‘sym’’ implies the symmetrization over all operator orderings. We furthermore have $G_{xx}^{\text{c},(2)} = (\Gamma^{(2)})_{xx}^{-1}$ and $\langle \hat{\psi}_x^\dagger \hat{\psi}_x^\dagger \hat{\psi}_x \rangle_{\text{sym}}^{\text{c}} = -(\Gamma^{(2)})_{xy_1}^{-1} (\Gamma^{(2)})_{xy_2}^{-1} (\Gamma^{(2)})_{y_3x}^{-1} \Gamma_{y_1y_2y_3}^{(3)}$. Since odd orders of correlations vanish in the absence of a mean field ($\psi^{(*)}[J^{(*)} = 0] = 0$), these contributions only contribute in the presence of further field derivatives.

Differentiation with respect to the fields $\psi^{(*)}$ yields the evolution equations for the inverse propagators and vertices. After applying the derivatives $\delta^2/\delta\psi_x^* \delta\psi_y$, and evaluating the resulting expression for $\psi^{(*)}[J^{(*)} = 0] = 0$, we get

$$\begin{aligned}
i\partial_t\Gamma_{xy}^{(2)} = & \left(\frac{\nabla_y^2}{2m} - \frac{\nabla_x^2}{2m} + g(\Gamma_{xx}^{(2)})^{-1} - g(\Gamma_{yy}^{(2)})^{-1} \right) \Gamma_{xy}^{(2)} \\
& + \frac{g}{2} \int_{\mathbf{y}} \Gamma_{xy_4}^{(2)} (\Gamma_{y_4y_1}^{(2)})^{-1} (\Gamma_{y_4y_2}^{(2)})^{-1} (\Gamma_{y_3y_4}^{(2)})^{-1} \Gamma_{y_1y_2y_3y}^{(4)} \\
& - \frac{g}{2} \int_{\mathbf{y}} \Gamma_{xy_3y_1y_2}^{(4)} (\Gamma_{y_1y_4}^{(2)})^{-1} (\Gamma_{y_2y_4}^{(2)})^{-1} (\Gamma_{y_4y_3}^{(2)})^{-1} \Gamma_{y_4y}^{(2)}, \quad (4.17)
\end{aligned}$$

where \mathbf{y} refers to the set of integration variables y_1, \dots, y_4 . For translationally invariant systems we switch to Fourier space, where the expression simplifies to

$$i\partial_t\Gamma_p^{(2)} = -\frac{g}{2} \int_{q,r,s} \Gamma_p^{(2)} (\Gamma_q^{(2)})^{-1} (\Gamma_r^{(2)})^{-1} (\Gamma_s^{(2)})^{-1} (\Gamma_{pqrs}^{(4)} - \Gamma_{rspq}^{(4)}). \quad (4.18)$$

Here, we used the definition $\Gamma_p^{(2)}(2\pi)^3 \delta(p - q) = \int_{xy} \exp(ipx - iqy) \Gamma_{xy}^{(2)}$, see also

corresponding expressions in section 4.B. Similarly, the four-vertices $\Gamma_{pqrs}^{(4)}$ carry a momentum conserving delta distribution $(2\pi)^3\delta(p+q-r-s)$ which will be implied throughout the rest of this work. From now on, we furthermore abbreviate $G_p^{c,(2)} = G_p$ and $\Gamma_p^{(2)} = \Gamma_p$. The evolution equation (4.18) has a characteristic two-loop structure reminiscent of scattering diagrams in quantum field theory [146]. We note that at this stage the evolution equation is exact, such that knowledge of the four-vertex allows one to compute the exact solution for the inverse two-point functions.

For the four-vertex, we analogously obtain

$$i\partial_t\Gamma_{pqrs}^{(4)} = \Delta\omega_{pqrs}\Gamma_{pqrs}^{(4)} + V_{pqrs}(\Gamma^{(2)}) - \mathcal{M}_{pqrs}(\Gamma). \quad (4.19)$$

The result consists of three different contributions: The first term corresponds to the free evolution, and it is obtained by applying the four field-derivatives to the terms in the first line of Eq. (4.15). Corresponding terms will appear at all orders in the hierarchy of evolution equations and they lead to phase rotations with the single particle energies, $\Delta\omega_{pqrs} = \omega_p + \omega_q - \omega_r - \omega_s$, with $\omega_p = p^2/2m - \mu$. The second term is the “bare” vertex function

$$V_{pqrs} = V_{pqrs}^C + V_{pqrs}^Q, \quad (4.20)$$

which consists of a classical scattering vertex

$$\begin{aligned} V_{pqrs}^C &= -g(\Gamma_p + \Gamma_q - \Gamma_r - \Gamma_s) \\ &\equiv \text{[diagram: four external lines meeting at a central vertex, with two solid lines and two dashed lines, and red arrows on the solid lines]} + \text{perm.}, \end{aligned} \quad (4.21)$$

as well as a quantum contribution

$$\begin{aligned} V_{pqrs}^Q &= \frac{g}{4}(\Gamma_p\Gamma_q(\Gamma_r + \Gamma_s) - \Gamma_r\Gamma_s(\Gamma_p + \Gamma_q)) \\ &\equiv \text{[diagram: four external lines meeting at a central vertex, with two solid lines and two dashed lines, and red arrows on the solid lines]} + \text{perm.}, \end{aligned} \quad (4.22)$$

where solid lines are amputated, i.e., corresponding two-point functions are removed. Quantum scattering involves additional factors of inverse two-point functions, such that classical scattering dominates for large occupancies. We furthermore obtain higher-loop contributions $\mathcal{M}_{pqrs}(\Gamma)$, which contain interaction vertices up to sixth order $\Gamma^{(n\leq 6)}$, see Fig. 4.2. They originate from derivatives acting on the second line of Eq. (4.15), as detailed in appendix 4.B.2, and here we focus on the translation invariant system. The set of diagrams couples the evolution of four-point interactions with six-point correlations as well as non-linear combinations of four-vertices to realize the complex dynamics of the Bose fields. Corresponding higher-order evolution equations for $\Gamma^{(n\geq 6)}$ follow from analogous differentiations of Eq. (4.15).

$$\mathcal{M}(\Gamma^{(4)}, \Gamma^{(6)}) =$$

FIGURE 4.2: Loop-contributions to the evolution equation of $\Gamma^{(4)}$: We show the relevant combinations of two-point functions with 1PI four- and six-vertices for the evolution of four-vertices in a translation invariant system. Note that all external propagators (solid lines) are amputated and permutations of legs are implied. For the underlying analytical expressions, see 4.B.2. Figure taken from [6].

The vertex (4.20) already carries the “gain minus loss” structure characteristic for effective descriptions in terms of kinetic equations. To also make contact with kinetic descriptions, we derive the evolution equation for two-point functions from Eq. (4.18)

$$\begin{aligned} \partial_t G_p &= -G_p(\partial_t \Gamma_p)G_p \\ &= iG_p \left[\text{diagram 1} - \text{diagram 2} \right] G_p \\ &= \int_{q,r,s} g \text{Im}(\Gamma_{pqrs}^{(4)}) G_p G_q G_r G_s. \end{aligned} \quad (4.23)$$

Here, the imaginary part originates from the structure $\sim \Gamma_{pqrs}^{(4)} - \Gamma_{rspq}^{(4)}$ in Eq. (4.18) and the identity $(\Gamma_{pqrs}^{(4)})^* = \Gamma_{rspq}^{(4)}$.

In the following, we discuss different approximation schemes to compute the effective vertices entering the evolution of two-point functions. We start by a perturbative expansion valid for dilute, weakly coupled gases, and proceed with an expansion in the number of field components to describe the non-perturbative dynamics of highly-occupied Bose fields.

4.4 Perturbative expansion

The evolution equations derived in the previous section constitute an infinite hierarchy of equations at higher orders of the vertices. The four-vertex is coupled to the six-vertex which will depend on the eight-vertex, etc. In practice, solving this set of equations requires us to truncate the hierarchy, for instance at a certain order of the vertices. In this section, we consider a perturbative expansion in powers of the coupling constant g .

To achieve this, we address Eq. (4.19) by first transforming to a rotating frame $\tilde{\Gamma}_{pqrs}^{(4)}(t) = \exp(i\Delta\omega_{pqrs}t)\Gamma_{pqrs}^{(4)}(t)$, such that

$$i\partial_t\tilde{\Gamma}_{pqrs}^{(4)} = e^{i\Delta\omega_{pqrs}t} \left(V_{pqrs}(\Gamma^{(2)}) - \mathcal{M}_{pqrs}(\Gamma) \right). \quad (4.24)$$

This equation may be integrated on both sides to yield our analog of a Bethe-Salpeter equation

$$i\Gamma_{pqrs}^{(4)} = \int_{t_0}^t dt' e^{i\Delta\omega_{pqrs}(t'-t)} \left(V_{pqrs}(\Gamma_{t'}^{(2)}) - \mathcal{M}_{pqrs}(\Gamma_{t'}) \right), \quad (4.25)$$

where we assumed the initial condition $\Gamma_{pqrs}^{(4)}(t_0) = 0$ for all momenta p, q, r, s . This amounts to starting the evolution from Gaussian initial conditions which is typical for kinetic descriptions.

4.4.1 Leading order

At $\mathcal{O}(g^2)$ we focus on the bare vertex and neglect all higher-order terms \mathcal{M} . One can show that this represents a self-consistent power counting, as $\Gamma^{(4)}$ is sourced by bare vertex terms of order $\mathcal{O}(g)$ and hence $\mathcal{M} = \mathcal{O}(g^2)$. The contribution of loop diagrams to the evolution of two-point functions will be of order $\mathcal{O}(g^3)$. We get

$$i\Gamma_{pqrs}^{(4)}(t) = \int_{t_0}^t dt' e^{i\Delta\omega_{pqrs}(t'-t)} V_{pqrs}(t'). \quad (4.26)$$

In the following, we focus on the late-time regime where the evolution of the two-point functions is slow compared to the fast-rotating phase factor $\sim \exp(i\Delta\omega_{pqrs}(t' - t))$. Hence, we set $t_0 \rightarrow -\infty$ and the evaluation of the integral yields

$$\begin{aligned} i\Gamma_{pqrs}^{(4)}(t) &= \int_{-\infty}^t dt' e^{i\Delta\omega_{pqrs}(t'-t)} V_{pqrs}(t') \\ &= \int_{-\infty}^{\infty} dt' \theta(t - t') e^{i\Delta\omega_{pqrs}(t'-t)} V_{pqrs}(t'). \end{aligned} \quad (4.27)$$

Unless stated otherwise, integration boundaries are taken as $\pm\infty$ henceforth. Here, we employ an integral representation of the Heaviside function

$$\theta(x) = \int \frac{d\omega}{2\pi} e^{-i\omega x} \frac{i}{\omega + i\epsilon}, \quad (4.28)$$

evaluated in the limit $\epsilon \rightarrow 0^+$. Specifically, we get

$$\Gamma_{pqrs}^{(4)}(t) = \int \frac{dt' d\omega}{2\pi} \frac{1}{\omega + i\epsilon} e^{i(\Delta\omega_{pqrs} + \omega)(t' - t)} V_{pqrs}(t') \quad (4.29)$$

Using a Taylor expansion of the time-dependent bare vertex with respect to the coordinate t ,

$$V_{pqrs}(t') = e^{(t' - t)\partial_s} V_{pqrs}(s) \Big|_{s=t}, \quad (4.30)$$

yields the expression

$$\Gamma_{pqrs}^{(4)}(t) = \int \frac{d\omega}{2\pi} \frac{1}{\omega + i\epsilon} e^{-i\partial_\omega \partial_s} V_{pqrs}(s) \Big|_{s=t} \int dt' e^{i(\Delta\omega_{pqrs} + \omega)(t' - t)}. \quad (4.31)$$

From the integral in the second line we obtain a Dirac δ -distribution, i.e.,

$$\Gamma_{pqrs}^{(4)}(t) = \int \frac{d\omega}{2\pi} \frac{1}{\omega + i\epsilon} e^{-i\partial_\omega \partial_l} V_{pqrs}(l) \Big|_{l=t} \delta(\Delta\omega_{pqrs} + \omega). \quad (4.32)$$

This expression can be integrated by parts and rewritten in terms of a derivative with respect to ϵ , which subsequently is evaluated in the limit $\epsilon \rightarrow 0$,

$$\Gamma_{pqrs}^{(4)}(t) = e^{\partial_\epsilon \partial_l} \left(\frac{V_{pqrs}(l)}{-\Delta\omega_{pqrs} + i\epsilon} \right) \Big|_{l=t, \epsilon \rightarrow 0}. \quad (4.33)$$

At sufficiently late times we expect time derivatives of distribution functions to be small. This follows from the assumption that distribution functions evolve slowly at long times [151]. Specifically, higher-order terms in the expansion of the exponential function include terms as $\partial_l G_p(l) = \mathcal{O}(g^2)$, which are again higher-order in the interaction constant. At order $\mathcal{O}(g^2)$, we approximate $\exp(\partial_\epsilon \partial_l) \rightarrow 1$ and get

$$\Gamma_{pqrs}^{(4)}(t) = \frac{V_{pqrs}(t)}{-\Delta\omega_{pqrs} + i\epsilon} \equiv \text{Diagram} \quad (4.34)$$

Here, we defined a new Feynman rule representation for the solution of $\Gamma^{(4)}$ at leading order, which includes the frequency factors. Corresponding factors will appear at every subsequent coupling order as discussed next.

4.4.2 Next-to-leading order (NLO)

Analogous to the leading-order result (4.34), one may systematically derive higher-order contributions. To compute $\Gamma^{(4)}$ at order $\mathcal{O}(g^2)$, we consider the following loop diagrams in its evolution equation

$$\mathcal{M}_{pqrs}(\Gamma^{(4)}) = \text{[Diagram 1]} + \text{[Diagram 2]} + \text{perm.} + \mathcal{O}(g^3), \quad (4.35)$$

where the four-vertices on the right-hand side are expanded to leading-order $\mathcal{O}(g)$.

To illustrate the computation of next-to-leading order contributions to the solution of $\Gamma^{(4)}$, we focus on the first diagram in Eq. (4.35) next. Explicitly, we get

$$\text{[Diagram 1]} = g\Gamma_q \int_{k'} G_{k'} G_{k''} \Gamma_{pk'k''s}^{(4)} \Big|_t, \quad (4.36)$$

where all ingredients are evaluated at time t and we introduced the shorthand notation $k'' = p - s + k'$ to abbreviate the loop momentum variable. The diagram's contribution to the solution for $\Gamma^{(4)}$ reads

$$\Gamma_{pqrs}^{(4)}(t) \supset g \int_{t_0}^t dt' e^{i\Delta\omega_{pqrs}(t-t')} \Gamma_q(t') \int_{k'} G_{k'}(t') G_{k''}(t') \Gamma_{pk'k''s}^{(4)}(t'). \quad (4.37)$$

To compute $\Gamma^{(4)}$ at order $\mathcal{O}(g^2)$ on the left-hand side, we approximate $\Gamma^{(4)}$ at order $\mathcal{O}(g)$, as given in Eq. (4.26), on the right-hand side of Eq. (4.37). We obtain

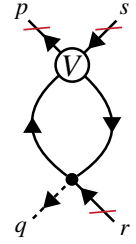
$$\Gamma_{pqrs}^{(4)} \supset \int \frac{dt' d\omega dt'' d\omega'}{(2\pi)^2} \Gamma_q(t') \int_{k'} G_{k'}(t') G_{k''}(t') \times \frac{e^{i(\Delta\omega_{pqrs} + \omega)(t'-t)}}{\omega + i\epsilon} \frac{e^{i(\Delta\omega_{pk'k''s} + \omega')(t''-t')}}{\omega' + i\epsilon'} V_{pk'k''s}(t''), \quad (4.38)$$

where we again have set $t_0 \rightarrow -\infty$ and used the integral representation of the heaviside function. Next, we rewrite the expression in analogy to the steps performed in Eqs. (4.30)-(4.33) to arrive for the right-hand side of q. (4.38) at

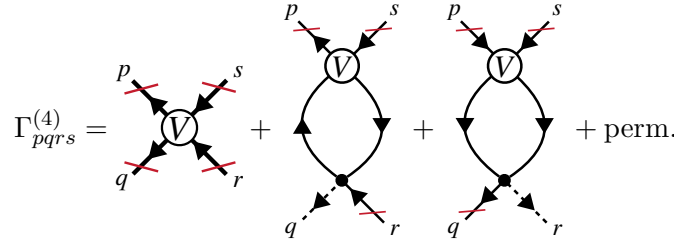
$$e^{(\partial_{\epsilon'} - \partial_{\epsilon})\partial_{t'}} e^{\partial_{\epsilon}\partial_t} \left(\frac{\Gamma_q(l) \int_{k'} G_{k'}(l) G_{k''}(l)}{\Delta\omega_{pqrs} - i\epsilon} \frac{V_{pk'k''s}(l')}{\Delta\omega_{pk'k''s} - i\epsilon'} \right) \Big|_{l=l'=t, \epsilon'=\epsilon \rightarrow 0}. \quad (4.39)$$

At order $\mathcal{O}(g^2)$, we again approximate the exponential operators by unity. Similar

to Eq. (4.34), we identify this result after time integration with a diagrammatic expression

$$\Gamma_{pqrs}^{(4)} \supset \frac{\Gamma_q \int_{k'} G_{k'} G_{k''}}{\Delta\omega_{pqrs} - i\epsilon} \frac{V_{pk'k''s}}{\Delta\omega_{pk'k''s} - i\epsilon} \equiv \text{Diagram}, \quad (4.40)$$


where all quantities are evaluated at time t . It is important to keep track of the frequency factors. In the present case, there is one factor $1/(-\Delta\omega_{pk'k''s} + i\epsilon)$ which comes with the vertex “V” and another factor $1/(-\Delta\omega_{pqrs} + i\epsilon)$ carrying the external momentum labels of the left-hand side’s vertex $\Gamma_{pqrs}^{(4)}$. At order $\mathcal{O}(g^2)$ we then write the solution for the time-dependent four-vertex diagrammatically as

$$\Gamma_{pqrs}^{(4)} = \text{Diagram 1} + \text{Diagram 2} + \text{Diagram 3} + \text{perm.} \quad (4.41)$$


In general, frequency factors enter the calculation for each “insertion” of $\Gamma^{(4)}$ as demonstrated for the present order in Eqs. (4.37) and (4.38).

4.4.3 Boltzmann equation

To derive the late-time evolution equation for the two-point functions at leading order ($\partial_t G_p = \mathcal{O}(g^2)$), we consider the imaginary part of the corresponding solution of the four-vertex

$$\text{Im} \left(\Gamma_{pqrs}^{(4)}(t) \right) = -\pi \delta(\Delta\omega_{pqrs}) V_{pqrs}(t). \quad (4.42)$$

Here, the imaginary part is a crucial ingredient to obtain the energy conservation of the particles which stream freely in-between collisions. Plugging this result into Eq. (4.23), one finds

$$\begin{aligned} \partial_t f_p &= \frac{g^2}{2} \int_{q,r,s} (2\pi)^3 \delta(p+q-r-s) (2\pi) \delta(\Delta\omega_{pqrs}) \\ &\quad \times ((f_p+1)(f_q+1)f_r f_s - f_p f_q (f_r+1)(f_s+1)), \end{aligned} \quad (4.43)$$

which is the well-known Boltzmann equation for weakly correlated non-relativistic systems. Here, we defined a distribution function as

$$G_p = f_p + 1/2 \quad (4.44)$$

corresponding to $f_p = \langle \hat{\psi}_p^\dagger \hat{\psi}_p \rangle$, with $\hat{\psi}_p$ being the Fourier transformed field operator. Using this, one finds

$$V_{pqrs} G_p G_q G_r G_s = g[f_p f_q (f_r + 1)(f_s + 1) - (f_p + 1)(f_q + 1) f_r f_s], \quad (4.45)$$

which yields the result (4.43). It contains a characteristic “gain minus loss” structure and has a momentum independent scattering rate $g^2/2$, such that we get the matrix element $|T_{pqrs}|^2 = g^2/2(2\pi)^3 \delta(p + q - r - s)(2\pi) \delta(\Delta\omega_{pqrs})$. The equation describes a dilute medium with occupancy $f_p \sim \mathcal{O}(1)$ for weak coupling at sufficiently late times, where leading-order perturbation theory is expected to be valid. In the following section we derive the corresponding scattering rate for a non-perturbative setting which allows to also access the regime of over-occupied Bose fields.

4.5 Non-perturbative large- N expansion

While the previous section dealt with a perturbative expansion of equal-time vertices, we consider a non-perturbative expansion for large numbers of field components next [154, 155]. Starting from the corresponding flow equation, the expansion will allow us to sum an infinite number of scattering interactions as shown below. This yields important corrections to the equal-time effective vertices, which can drastically alter the dynamics of Bose fields in strongly correlated regimes.

The large- N counting scheme is detailed in appendix 4.B.3. We use in the following that for suitable initial conditions, for instance Gaussian states, equal-time vertices obey [156]

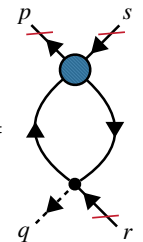
$$\Gamma^{(n)} = \mathcal{O}\left(\frac{1}{N^{\frac{n-2}{2}}}\right), \quad n > 2. \quad (4.46)$$

Specifically, for Gaussian initial states, where $\Gamma^{(n>2)}(t_0) = 0$, the evolution of $\Gamma^{(4)}$ is sourced by the bare vertex (see Eq. (4.2)) at order $\mathcal{O}(1/N)$. Vertices $\Gamma^{(n>4)}$ subsequently build up at corresponding higher orders through combinations of bare vertices and $\Gamma^{(4)}$ according to Eq. (4.46). Then, loop diagrams as displayed in Fig. 4.2 also contribute to the evolution of $\Gamma^{(4)}$ at order $\mathcal{O}(1/N)$ at most, where every vertex comes with a factor of $1/N$ and factors of N originate from summation over field components in closed loops. To determine the contribution of equal-time vertices to the evolution equation at order $1/N$, we focus on the case, with external field indices $i_1 = i_4$ and $i_2 = i_3$.

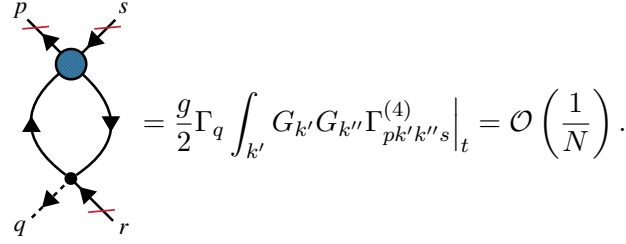
In the following, to keep the notation in the main text simple, we use the $U(N)$ symmetry to diagonalize the two-point function in field space as $G_{\alpha_1, \alpha_2}^{(2)} \rightarrow G_{x_1, x_2}^{(2)} \delta_{i_1, i_2}$. Subsequently, we may explicitly sum over the field components, and we will omit the field index i in our notation. The bare vertex is given by

$$V_{pqrs} = -\frac{g}{2N}(\Gamma_p^{(2)} + \Gamma_q^{(2)} - \Gamma_r^{(2)} - \Gamma_s^{(2)}) + \frac{g}{8N}(\Gamma_p^{(2)}\Gamma_q^{(2)}(\Gamma_r^{(2)} + \Gamma_s^{(2)}) - \Gamma_r^{(2)}\Gamma_s^{(2)}(\Gamma_p^{(2)} + \Gamma_q^{(2)})), \quad (4.47)$$

and using the expansion to order $\mathcal{O}(1/N)$, the evolution equation for $\Gamma^{(4)}$ involves no more than propagators and four-vertices, i.e.,

$$\mathcal{M}_{pqrs}(\Gamma^{(4)}) = \text{Diagram} + \text{perm.} + \mathcal{O}\left(\frac{1}{N^2}\right), \quad (4.48)$$


where



$$= \frac{g}{2} \Gamma_q \int_{k'} G_{k'} G_{k''} \Gamma_{pk'k''s}^{(4)} \Big|_t = \mathcal{O}\left(\frac{1}{N}\right). \quad (4.49)$$

The shown diagram involves two factors of $1/N$ for the bare vertex and for $\Gamma^{(4)}$, as well as a factor of N representing the different field components which “run” in the loop (cf. appendix 4.B.3). The corresponding evolution equation thus evolves $\Gamma^{(4)}$ again at order $1/N$, and it can formally be integrated to yield

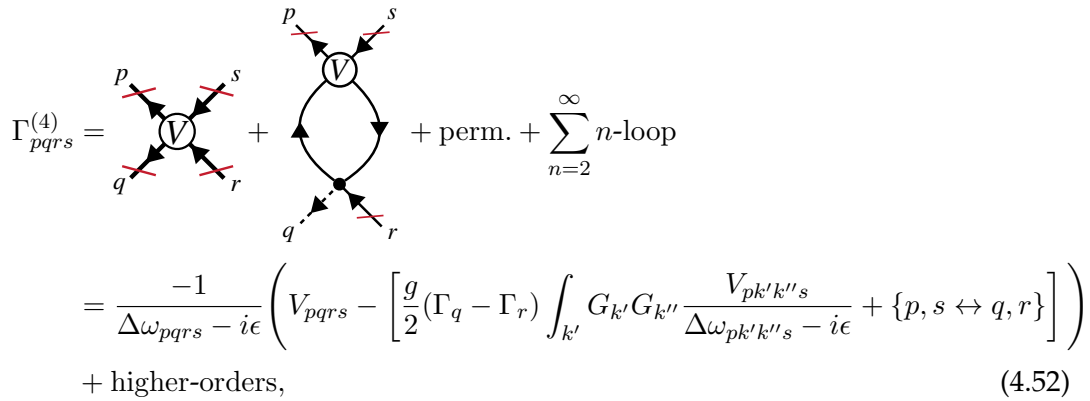
$$i\Gamma_{pqrs}^{(4)}(t) = \int_{t_0}^t dt' e^{i\Delta\omega_{pqrs}(t'-t)} (V_{pqrs}(t') - \mathcal{M}_{pqrs}(t')), \quad (4.50)$$

which by employing analogous approximations as in the previous section becomes

$$\Gamma_{pqrs}^{(4)}(t) = \frac{-1}{\Delta\omega_{pqrs} - i\epsilon} \left(V_{pqrs}(t) + \left[\frac{g}{2} (\Gamma_q - \Gamma_r) \right. \right. \\ \left. \left. \times \int_{k'} G_{k'} G_{k''} \Gamma_{pk'k''s}^{(4)}(t) + \{p, s \leftrightarrow q, r\} \right] \right), \quad (4.51)$$

where we sum over a second term with permuted external legs. For $i_1 = i_4$ and $i_2 = i_3$ at order $1/N$, only combined permutations of p, s with q, r appear. At this stage, Eq. (4.51) is analogous to Eq. (4.37), but we keep $\Gamma^{(4)}$ consistently at order $1/N$ here. Eq. (4.51) can be solved by iteration in terms of an infinite set of loop diagrams. In the following we first illustrate the iterative computation to two-loop order, while we subsequently calculate the full evolution of distribution functions at order $1/N$.

The vertex is diagrammatically given by



$$\Gamma_{pqrs}^{(4)} = \text{tree-level } V + \text{one-loop diagram} + \text{perm.} + \sum_{n=2}^{\infty} n\text{-loop} \\ = \frac{-1}{\Delta\omega_{pqrs} - i\epsilon} \left(V_{pqrs} - \left[\frac{g}{2} (\Gamma_q - \Gamma_r) \int_{k'} G_{k'} G_{k''} \frac{V_{pk'k''s}}{\Delta\omega_{pk'k''s} - i\epsilon} + \{p, s \leftrightarrow q, r\} \right] \right) \\ + \text{higher-orders}, \quad (4.52)$$

where frequency factors are assigned analogous to Eq. (4.40). The corresponding two-loop expression is given by summing the following diagrams

$$2\text{-loop} = \begin{array}{c} \begin{array}{ccc} \begin{array}{c} p \quad s \\ \diagdown \quad / \\ \text{V} \\ \diagup \quad \diagdown \\ \text{---} \\ \diagdown \quad / \\ \text{---} \\ \diagup \quad \diagdown \\ q \quad r \end{array} & + & \begin{array}{c} p \quad s \\ \diagdown \quad / \\ \text{V} \\ \diagup \quad \diagdown \\ \text{---} \\ \diagdown \quad / \\ \text{---} \\ \diagup \quad \diagdown \\ q \quad r \end{array} & + & \begin{array}{c} p \quad s \\ \diagdown \quad / \\ \text{---} \\ \diagdown \quad / \\ \text{---} \\ \text{V} \\ \diagup \quad \diagdown \\ \text{---} \\ \diagdown \quad / \\ \text{---} \\ \diagup \quad \diagdown \\ q \quad r \end{array} \end{array} + \text{perm.}, \quad (4.53)$$

where summation over permutations of external lines is implied. The first diagram corresponds to the equation

$$\begin{array}{c} p \quad s \\ \diagdown \quad / \\ \text{V} \\ \diagup \quad \diagdown \\ \text{---} \\ \diagdown \quad / \\ \text{---} \\ \diagup \quad \diagdown \\ q \quad r \end{array} \equiv \left(\frac{g}{2}\right)^2 \int_{k', q'} \frac{-\Gamma_r}{\Delta\omega_{pqr s} - i\epsilon} \frac{G_{k'}}{\Delta\omega_{pk'k'' s} - i\epsilon} \frac{G_{q'} G_{q''} V_{pq'q'' s}}{\Delta\omega_{pq'q'' s} - i\epsilon}, \quad (4.54)$$

where the two-point function at momentum k'' is amputated by the inverse propagator represented by the dashed line. The first frequency factor $1/(-\Delta\omega_{pqr s} + i\epsilon)$ originates from the external lines, the second factor carries the momentum labels of lines connecting to the upper loop, i.e., p, k', k'' , and s . The last insertion is given by the bare vertex, which comes with a frequency factor carrying the same momentum labels, $1/(-\Delta\omega_{pq'q'' s} + i\epsilon)$. Analogously, the last diagram is obtained as

$$\begin{array}{c} p \quad s \\ \diagdown \quad / \\ \text{---} \\ \diagdown \quad / \\ \text{---} \\ \text{V} \\ \diagup \quad \diagdown \\ \text{---} \\ \diagdown \quad / \\ \text{---} \\ \diagup \quad \diagdown \\ q \quad r \end{array} \equiv \left(\frac{g}{2}\right)^2 \int_{q', k'} \frac{-\Gamma_r \Gamma_s}{\Delta\omega_{pqr s} - i\epsilon} \frac{G_{k'} G_{k''}}{\Delta\omega_{pk'k'' s} - i\epsilon} \frac{G_{q'} G_{q''} V_{k'q''q'k''}}{\Delta\omega_{k'q''q'k''} - i\epsilon}. \quad (4.55)$$

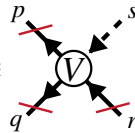
Again, the result is augmented with frequency factors for each iteration step, which carry in-going and out-going momentum labels according to the momenta of the internal four-vertex which is iterated. Here, the last insertion of the bare vertex is internal, i.e., the corresponding frequency factor carries internal momenta only. In general, one needs to keep track of the ‘‘history’’ of insertions for the correct assignment of labels.

At this point, we distinguish different cases originating from the various possibilities of forming diagrams at order $1/N$. In the following, we sort contributions according to the number of external inverse two-point functions attached to the

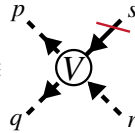
diagram. To this end, we will name the set of loop diagrams leading to an odd number of external inverse propagators Γ^A , while the loop diagrams with an even number are represented by Γ^B . Thus, Γ^A represents important corrections to the bare classical and quantum vertices, while Γ^B yields a new type of vertex which is not present in the perturbative theory. The summation of both contributions will yield a Boltzmann equation for a strongly correlated Bose system with momentum- and medium-dependent scattering rate. We note that the series of diagrams at order $1/N$ is reminiscent of the diagrams employed in Ref. [157], where (unequal-time) propagators are similarly sorted by their quantum (dashed) and classical (solid) external lines.

4.5.1 Vertex Γ^A

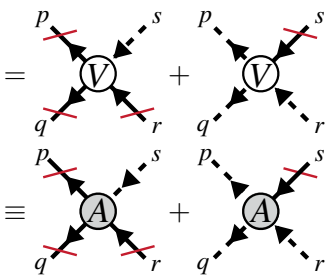
At first, we consider the terms with an odd number of external propagators. To distinguish the diagrams with respect to their configuration of external legs we introduce the vertices

$$\frac{V_{pqrs}^C}{-\Delta\omega_{pqrs} + i\epsilon} \equiv \text{Diagram (V)} + \text{perm.}, \quad (4.56)$$


and

$$\frac{V_{pqrs}^Q}{-\Delta\omega_{pqrs} + i\epsilon} \equiv \text{Diagram (V)} + \text{perm.}, \quad (4.57)$$


see also the definition of Eq. (4.34). The expression Γ^A is given by the sum of the bare vertices (4.56) and (4.57) with all n -loop diagrams $\Gamma^{A,n}$ involving an odd number of external $\Gamma^{(2)}$, i.e.,

$$\begin{aligned} \Gamma_{pqrs}^A(t) &= \text{Diagram (V)} + \text{Diagram (V)} + \text{perm.} + \sum_{n=1}^{\infty} \Gamma_{pqrs}^{A,n}(t) \\ &\equiv \text{Diagram (A)} + \text{Diagram (A)} + \text{perm.}, \end{aligned} \quad (4.58)$$


where the symbol “A” comprises all diagrams with according configuration of external legs. For a particular configuration, Eq. (4.51) reads diagrammatically

The diagrammatic equation (4.59) shows a vertex labeled 'A' with four external legs (p, s, q, r) on the left. This is equal to a vertex labeled 'V' with the same external legs, plus two diagrams. Each of the two diagrams consists of a loop with two vertices, one labeled 'A' and one unlabeled, connected by dashed lines. The external legs p, s, q, r are attached to the vertices in a specific configuration.

$$\text{Diagram A} = \text{Diagram V} + \text{Diagram 1} + \text{Diagram 2} \quad (4.59)$$

Iterating this equation for example to one-loop order, we obtain

The diagrammatic equation (4.60) shows two diagrams, each consisting of a loop with two vertices, one labeled 'V' and one unlabeled, connected by dashed lines. The external legs p, s, q, r are attached to the vertices. This is equal to a frequency integral expression.

$$\text{Diagram 1} + \text{Diagram 2} = -\frac{1}{N} \frac{\Gamma_r}{\Delta\omega_{pqrs} - i\epsilon} \Pi_{ps}, \quad (4.60)$$

including the usual frequency factors. Here, we also defined a one-loop self-energy function as

$$\Pi_{ps}(t) = \frac{g}{2} \int_{k'} \frac{G_{k'}(t) - G_{k''}(t)}{\Delta\omega_{pk'k''s} - i\epsilon}, \quad (4.61)$$

where we sum over both possibilities of amputating an internal loop propagator. Using the series $\sum_{n \geq 0} (-\Pi_{ps})^n = 1/(1 + \Pi_{ps})$, the sum over all loop orders reads

$$\Gamma_{pqrs}^A = -\frac{V_{pqrs}}{\Delta\omega_{pqrs} - i\epsilon} \times \frac{1}{1 + \Pi_{ps}} + \{p, s \leftrightarrow q, r\}, \quad (4.62)$$

where we introduced the notation

$$V_{pqrs}/g = -\frac{1}{2N} (\Gamma_q - \Gamma_r) \left(1 - \frac{1}{4} \Gamma_p \Gamma_s\right), \quad (4.63)$$

$$V_{pqr\bar{s}}/g = -\frac{1}{2N} (\Gamma_p - \Gamma_s) \left(1 - \frac{1}{4} \Gamma_q \Gamma_r\right), \quad (4.64)$$

i.e., $V_{pqrs} = V_{pqrs} + V_{pqr\bar{s}}$.

The vertex Γ^A has a similar structure as the bare vertex defined in Eq. (4.34), including a correction arising from the non-perturbative resummation of the infinite series of diagrams presented in this section. Indeed, the bare vertex V emerges from Eq. (4.62) in the perturbative expansion at leading order, where $\Pi = \mathcal{O}(g)$ and hence $1/(1 + \Pi) \rightarrow 1 + \mathcal{O}(g)$.

The relevant contribution to the evolution equation (4.23) is the imaginary part of the four-vertices. Here, we get

$$\begin{aligned} \text{Im}(\Gamma_{pqrs}^A) &= -\pi\delta(\Delta\omega_{pqrs})\text{Re}\left(\frac{V_{pqrs}}{1+\Pi_{ps}}\right) - \mathcal{P}\left[\frac{1}{\Delta\omega_{pqrs}-i\epsilon}\right]\text{Im}\left(\frac{V_{pqrs}}{1+\Pi_{ps}}\right) \\ &\quad + \{p, s \leftrightarrow q, r\}, \end{aligned} \quad (4.65)$$

where \mathcal{P} denotes the Cauchy principal value. Using the identities $\text{Im}(1/(1+\Pi)) = -\text{Im}(\Pi)/|1+\Pi|^2$, and $\text{Re}(1/(1+\Pi)) = (1+\text{Re}(\Pi))/|1+\Pi|^2$, and the definition of an effective coupling and vertex

$$g_{ps}^{\text{eff}} = \frac{g}{|1+\Pi_{ps}|^2}, \quad V_{pqrs}^{\text{eff}} = \frac{V_{pqrs}}{|1+\Pi_{ps}|^2}, \quad (4.66)$$

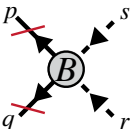
we find

$$\begin{aligned} \text{Im}(\Gamma_{pqrs}^A) &= -\pi\delta(\Delta\omega_{pqrs})V_{pqrs}^{\text{eff}}(1+\mathcal{P}(\Pi_{ps})) \\ &\quad + \mathcal{P}\left[\frac{1}{\Delta\omega_{pqrs}-i\epsilon}\right]\left[V_{pqrs}^{\text{eff}}\text{Im}(\Pi_{ps}) + \{p, s \leftrightarrow q, r\}\right]. \end{aligned} \quad (4.67)$$

In the first line, we used that $\text{Re}(\Pi_{qr}) = \text{Re}(\Pi_{ps})$ under the conditions of energy and momentum conservation, represented by $\delta(\Delta\omega_{pqrs})\delta(p+q-r-s)$, see appendix 4.C.3. We thus find an on-shell contribution $\sim \delta(\Delta\omega_{pqrs})$ as well as off-shell terms involving the principle value $\mathcal{P}(1/(\Delta\omega_{pqrs}-i\epsilon))$. All terms include the effective coupling g^{eff} , which leads to a suppression of the effective interaction of modes if the gas is highly occupied toward lower momenta [141]. In this regime, the denominator is dominated by the large distribution function in the one-loop self-energy Π [153]. Our findings are in qualitative agreement with results obtained from Ref. [143], where such an infrared suppression was observed experimentally.

4.5.2 Vertex Γ^B

Next, we consider the diagrams with an even number of external inverse propagators and (amputated) propagators. We may similarly sort terms by their number of loops

$$\Gamma_{pqrs}^B(t) = \sum_{n=1}^{\infty} \Gamma_{pqrs}^{B,n}(t) \equiv \text{Diagram B} + \text{perm.}, \quad (4.68)$$


however, no bare vertices appear in this case, and we define the diagram “B” according to the configuration of the two external $\Gamma^{(2)}$. In terms of bare vertices, we get the

series

Diagrammatic equation (4.69) showing the resummation of a vertex B into a series of diagrams with vertices V and higher-order loops. The left side is a vertex B with external legs p, q, r, s . The right side is a sum of diagrams: a vertex V with external legs p, q, r, s , followed by a series of diagrams with two V vertices connected by internal lines, and higher-order loops. The diagrams are summed over permutations of external legs $\{p, s \leftrightarrow q, r\}$.

$$+ \{p, s \leftrightarrow q, r\} + \text{higher-order loops.} \quad (4.69)$$

For any loop order, this equation may equivalently be written in the form

Diagrammatic equation (4.70) showing the resummation of a vertex B into a series of diagrams with vertices A and B and higher-order loops. The left side is a vertex B with external legs p, q, r, s . The right side is a sum of diagrams: a vertex A with external legs p, q, r, s , followed by a series of diagrams with two A vertices connected by internal lines, and higher-order loops. The diagrams are summed over permutations of external legs $\{p, s \leftrightarrow q, r\}$.

$$+ \{p, s \leftrightarrow q, r\} + \text{higher-order loops.} \quad (4.70)$$

Explicitly, for a general configuration of external legs, we obtain the integral equation

$$\begin{aligned} \Gamma_{pqrs}^B &= \frac{1}{N} \left(\frac{g}{2}\right)^2 \frac{(\Gamma_p - \Gamma_s)(\Gamma_q - \Gamma_r)}{-\Delta\omega_{pqrs} + i\epsilon} \\ &\times \int_{k'} \left(-\frac{G_{k'} G_{k''} - \frac{1}{4}}{\Delta\omega_{k'psk''} - i\epsilon} \frac{1}{1 + \Pi_{k'k''}} - \frac{G_{k'} G_{k''} - \frac{1}{4}}{\Delta\omega_{k''qrk'} - i\epsilon} \frac{1}{1 + \Pi_{k''k'}} \right) \\ &+ \frac{g}{2} \frac{\Gamma_r - \Gamma_q}{-\Delta\omega_{pqrs} + i\epsilon} \int_{k'} G_{k'} G_{k''} \Gamma_{pk'k''s}^B + \frac{g}{2} \frac{\Gamma_s - \Gamma_p}{-\Delta\omega_{pqrs} + i\epsilon} \int_{k'} G_{k'} G_{k''} \Gamma_{k''qrk'}^B, \end{aligned} \quad (4.71)$$

where we used the solution for Γ^A , Eq. (4.62). In the following, we focus on the imaginary part of Eq. (4.71), as $\text{Im}(\Gamma^B)$ is the relevant quantity to determine the evolution of two-point functions in the Bose system. In appendix 4.C, we demonstrate that this equation is solved by the ansatz

$$\begin{aligned} \text{Im}(\Gamma_{pqrs}^B) &= \mathcal{P} \left[\frac{(\Gamma_p - \Gamma_s)(\Gamma_q - \Gamma_r)}{-\Delta\omega_{pqrs} + i\epsilon} \right] \times \\ &\left(\frac{gg_{ps}^{\text{eff}}}{4N} \int_{k'} \pi \delta(\Delta\omega_{pk'k''s}) \left(G_{k'} G_{k''} - \frac{1}{4} \right) + \{p, s \leftrightarrow q, r\} \right). \end{aligned} \quad (4.72)$$

Again, we find that each term contains the medium-augmented non-perturbative interaction vertex g^{eff} through the resummation of diagrams.

4.5.3 Non-perturbative Boltzmann equation

In this section we assemble the results for the resummed effective vertices to derive the evolution equation for two-point functions. Starting from Eq. (4.23), one gets

$$\begin{aligned}\partial_t G_p &= \int_{q,r,s} g \text{Im}(\Gamma_{pqrs}^{(4)}) G_p G_q G_r G_s \\ &= \int_{q,r,s} g \text{Im}(\Gamma_{pqrs}^A + \Gamma_{pqrs}^B) G_p G_q G_r G_s,\end{aligned}\quad (4.73)$$

where momentum conservation, represented by $\delta(p + q - r - s)$, is implied. The full vertex solution is the sum over all configurations of external legs and hence we add Γ^A and Γ^B . Plugging in Eqs. (4.67) and (4.72) we obtain by direct computation (appendix 4.C.2)

$$\partial_t G_p = - \int_{q,r,s} \pi \delta(\Delta\omega_{pqrs}) V_{pqrs}^{\text{eff}} G_p G_q G_r G_s, \quad (4.74)$$

which is equivalent to the previous perturbative Boltzmann equation except for the replacement $V \rightarrow V^{\text{eff}}$, i.e.,

$$\begin{aligned}\partial_t f_p &= \int_{q,r,s} \frac{g g_{ps}^{\text{eff}}}{4N} (2\pi)^3 \delta(p + q - r - s) (2\pi) \delta(\Delta\omega_{pqrs}) \\ &\quad \times ((f_p + 1)(f_q + 1) f_r f_s - f_p f_q (f_r + 1)(f_s + 1)).\end{aligned}\quad (4.75)$$

Accordingly, the matrix element of the kinetic equation is given by $|T_{pqrs}|^2 = g g_{ps}^{\text{eff}} / (4N) (2\pi)^3 \delta(p+q-r-s) (2\pi) \delta(\Delta\omega_{pqrs})$, which receives the momentum-dependent correction $1/|1 + \Pi_{ps}|^2$ compared to the perturbative case. This momentum dependence dominates the non-perturbative evolution with large occupations where $\Pi \gg 1$, with drastic consequences for dynamical phenomena such as turbulence and far-from-equilibrium universality [88, 141, 158].

4.6 Measurement protocol

The above coupling and large- N expansion results establish a direct link between equal-time correlations and standard observables for effective kinetic theories and corresponding hydrodynamic descriptions. However, the quantum evolution equations we derive in section 4.3 from the equal-time effective action are exact and not limited to kinetic theory approximations. For instance, the exact time evolution equation (4.18) relates the time derivative of $\Gamma^{(2)}$ – encoding distribution information – to the effective interaction $\Gamma^{(4)}$ and convolutions with the distributions. It would be a tremendous progress for quantum many-body physics to be able to extract the exact quantum evolution equation for strongly correlated systems from quantum simulation measurements of $\Gamma^{(2)}$ and $\Gamma^{(4)}$ for relevant times. This would provide important insights into the long-standing problem of finding suitable approximations of the time evolution equations also for strongly coupled systems and their range of validity.

In this section we devise an efficient scheme to measure equal-time effective vertices, in particular $\Gamma^{(2)}$ and $\Gamma^{(4)}$, in cold-atom quantum simulators. This discussion extends the procedures of Refs. [142, 143] to the underlying Bose fields appearing in the defining Hamiltonian. Often, such experiments are limited to extracting equal-time density correlations. A common strategy is to let the system evolve to time t and illuminate with light to obtain a snapshot at this instant of time. Subsequently, density correlations are extracted by averaging over many repetitions of this procedure.

To relate the experiment with theory it is especially beneficial to express effective descriptions of the system in such equal-time quantities. We hence provide a protocol to extract the relevant two- and four-point correlation functions via density measurements. 1PI equal-time vertices are extracted according to Eq. (4.11), i.e., by “amputating” the external legs. This is most efficiently performed in Fourier space, where amputation refers to dividing out the corresponding two-point functions. While we illustrate our scheme for the case of a single-component gas, it is more general and can similarly be applied to multi-component systems.

The desired quantities are the symmetrized two- and four-point correlation functions of the fields, i.e., $\langle \{\hat{\psi}_x^\dagger, \hat{\psi}_y\} \rangle$ and $\langle \hat{\psi}_x^\dagger \hat{\psi}_v^\dagger \hat{\psi}_y \hat{\psi}_w \rangle_{\text{sym}}$. While we specify the symmetrically ordered correlation functions here, all other operator orderings are equivalent and they are related through the equal-time commutation relations. For simplicity, we focus here on the observables

$$\mathcal{O}_1 = \langle \hat{\mathcal{O}}_1 \rangle = \langle \hat{\psi}_x^\dagger \hat{\psi}_y \rangle, \quad (4.76a)$$

$$\mathcal{O}_2 = \langle \hat{\mathcal{O}}_2 \rangle = \langle \hat{\psi}_x^\dagger \hat{\psi}_v^\dagger \hat{\psi}_y \hat{\psi}_w \rangle. \quad (4.76b)$$

The central idea is to couple the atoms at the respective positions to ancilla degrees of freedom to create effective three-state systems, for instance in a Λ -type configuration, see Fig. 4.3. Raman beams or microwave pulses can transfer population among the

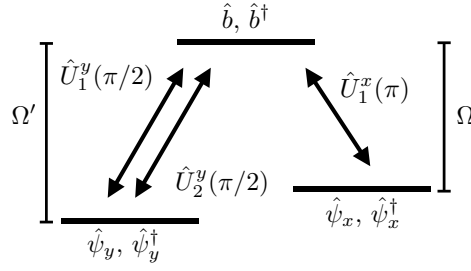


FIGURE 4.3: Schematics of the measurement scheme: We construct an effective Λ -type level scheme and propose to introduce rotations between the states with Raman transitions or microwave coupling with strengths Ω, Ω' . Figure taken from [6].

three states or manipulate their relative phases. Achieving this requires addressing the bosonic fields position-selectively, e.g. by locally adjusting the chemical potential μ .

We start by transferring the population from position x to the ancilla. Afterwards we couple position y to the ancilla, therefore effectively coupling positions x and y . Density measurements of ancilla and the spatial mode at y will then give rise to $\langle \mathcal{O}_1 \rangle$. Here we use that these manipulations can be performed on much shorter time-scales compared to the system evolution, such that the information about the quantum state is effectively frozen during the measurement procedure. We outline this procedure in detail next.

We describe the ancilla degree of freedom “b” with bosonic operators \hat{b}, \hat{b}^\dagger . The microwave interaction of the ancilla with a bosonic mode $\hat{\psi}_x, \hat{\psi}_x^\dagger$ is described by the two unitary operators

$$\hat{U}_1^x(\varphi) = e^{i\varphi(\hat{b}^\dagger \hat{\psi}_x + \hat{\psi}_x^\dagger \hat{b})}, \quad (4.77a)$$

$$\hat{U}_2^x(\varphi) = e^{\varphi(\hat{b}^\dagger \hat{\psi}_x - \hat{\psi}_x^\dagger \hat{b})}. \quad (4.77b)$$

In a Schwinger boson representation, see also 1, these operators may locally be interpreted as rotations of the collective spin on a Bloch sphere. Using bosonic commutation relations, we obtain the transformations of the operators

$$\hat{\psi}_x \rightarrow \hat{U}_1^x(\varphi) \hat{\psi}_x (\hat{U}_1^x(\varphi))^\dagger = \cos(\varphi) \hat{\psi}_x + i \sin(\varphi) \hat{b}, \quad (4.78a)$$

$$\hat{\psi}_x \rightarrow \hat{U}_2^x(\varphi) \hat{\psi}_x (\hat{U}_2^x(\varphi))^\dagger = \cos(\varphi) \hat{\psi}_x + \sin(\varphi) \hat{b}. \quad (4.78b)$$

We first couple the ancilla to the atoms at position x with $\hat{U}_1^x(\pi)$. Secondly, we couple position y to the ancilla with $\hat{U}_1^y(\pi/2)$. A subsequent density measurement yields

$$\begin{aligned} \langle \hat{b}^\dagger \hat{b} \rangle_1 &= \langle \psi(t) | \hat{U}_1^y(\pi/2) \hat{U}_1^x(\pi) \hat{b}^\dagger \hat{b} \hat{U}_1^{x,\dagger}(\pi) \hat{U}_1^{y,\dagger}(\pi/2) | \psi(t) \rangle \\ &= \frac{1}{2} (\langle \hat{\psi}_x^\dagger \hat{\psi}_x \rangle + \langle \hat{\psi}_y^\dagger \hat{\psi}_y \rangle) - \text{Im}(\mathcal{O}_1), \end{aligned} \quad (4.79)$$

where $|\psi(t)\rangle$ is the time-dependent Schrödinger quantum state, and $\langle\hat{\psi}_x^\dagger\hat{\psi}_x\rangle$ is the local mean number density at time t , which can be accessed in a separate measurement. Measuring the density at position y after the rotation \hat{U}_1 similarly yields

$$\begin{aligned}\langle\hat{\psi}_y^\dagger\hat{\psi}_y\rangle_1 &= \langle\psi(t)|\hat{U}_1^y(\pi/2)\hat{\psi}_y^\dagger\hat{\psi}_y\hat{U}_1^{y,\dagger}(\pi/2)|\psi(t)\rangle \\ &= \frac{1}{2}(\langle\hat{\psi}_x^\dagger\hat{\psi}_x\rangle + \langle\hat{\psi}_y^\dagger\hat{\psi}_y\rangle) + \text{Im}(\mathcal{O}_1),\end{aligned}\quad (4.80)$$

such that we obtain $\text{Im}(\mathcal{O}_1)$ by subtracting the two measurements. In order to measure the corresponding real part in separate realizations of the experiment, we perform the same series of unitary operations with \hat{U}_2 replacing the second operator. We get

$$\begin{aligned}\langle\hat{b}^\dagger\hat{b}\rangle_2 &= \langle\psi(t)|\hat{U}_2^y(\pi/2)\hat{U}_1^x(\pi)\hat{b}^\dagger\hat{b}\hat{U}_1^{x,\dagger}(\pi)\hat{U}_2^{y,\dagger}(\pi/2)|\psi(t)\rangle \\ &= \frac{1}{2}(\langle\hat{\psi}_x^\dagger\hat{\psi}_x\rangle + \langle\hat{\psi}_y^\dagger\hat{\psi}_y\rangle) + \text{Re}(\mathcal{O}_1),\end{aligned}\quad (4.81)$$

and for position y one finds

$$\begin{aligned}\langle\hat{\psi}_y^\dagger\hat{\psi}_y\rangle_2 &= \langle\psi(t)|\hat{U}_2^y(\pi/2)\hat{\psi}_y^\dagger\hat{\psi}_y\hat{U}_2^{y,\dagger}(\pi/2)|\psi(t)\rangle \\ &= \frac{1}{2}(\langle\hat{\psi}_x^\dagger\hat{\psi}_x\rangle + \langle\hat{\psi}_y^\dagger\hat{\psi}_y\rangle) - \text{Re}(\mathcal{O}_1).\end{aligned}\quad (4.82)$$

The difference yields the real part $\text{Re}(\mathcal{O}_1)$, which subsequently allows to reconstruct the observable \mathcal{O}_1 by combining real and imaginary part. In the Schwinger boson representation real and imaginary parts of \mathcal{O}_1 correspond to spin projections in x and y direction, respectively. Our scheme thus effectively employs appropriate spin rotations to rotate the information to the z component which can be accessed with density measurements.

Similarly, one can access the observable \mathcal{O}_2 by adding a second ancilla mode “d” with bosonic operators \hat{d}, \hat{d}^\dagger and measuring density correlations between both ancillas. Here, we focus on the situation where all four positions x, v, y, w are different, assuming those cases with equal positions to become irrelevant in the thermodynamic limit of a large-scale quantum system described by quantum field theory. We assign ancilla b to positions x, y and ancilla d to positions v, w and subsequently perform the same operations on both sets of modes individually. Appropriate density correlation measurements of both ancillas give the four combinations

$$\left\langle \left\{ \text{Re}(\hat{\mathcal{O}}_1(x, y)), \text{Re}(\hat{\mathcal{O}}_1(v, w)) \right\} \right\rangle, \quad (4.83a)$$

$$\left\langle \left\{ \text{Re}(\hat{\mathcal{O}}_1(x, y)), \text{Im}(\hat{\mathcal{O}}_1(v, w)) \right\} \right\rangle, \quad (4.83b)$$

$$\left\langle \left\{ \text{Im}(\hat{\mathcal{O}}_1(x, y)), \text{Re}(\hat{\mathcal{O}}_1(v, w)) \right\} \right\rangle, \quad (4.83c)$$

$$\left\langle \left\{ \text{Im}(\hat{\mathcal{O}}_1(x, y)), \text{Im}(\hat{\mathcal{O}}_1(v, w)) \right\} \right\rangle, \quad (4.83d)$$

where $\{\cdot, \cdot\}$ is the anti-commutator. These contributions can be combined with

the equal-time commutation relations and two-point functions \mathcal{O}_1 to compute the observable \mathcal{O}_2 .

4.7 Summary

In this chapter, we outlined an equal-time approach to the dynamics of quantum fields out of equilibrium. Starting from the equal-time quantum effective action, we derived effective kinetic equations in two regimes: First we considered a dilute, perturbative system governed by two-to-two scattering. Secondly, we extended our analysis to the case of non-perturbatively large occupancies of the gas, which results in important vertex corrections to the scattering rates.

Our results open up new avenues in non-equilibrium quantum field theory. While our calculations are performed for a non-relativistic Bose gas, the approach is general and can also be applied to systems with fermions, relativistic field theories, and in particular gauge theories where the time-local formulation can provide important advantages in finding approximations consistent with local gauge symmetries. Moreover, the textbook (“unequal-time”) approach to non-equilibrium quantum field theory employing a closed-time path yields *ab initio* evolution equations that are non-local in time, such that late times are difficult to reach and the derivation of efficient time-local descriptions require additional approximations.

Most importantly, our approach matches experimental capabilities of quantum simulators such as employing ultra-cold quantum gases. These platforms offer the unique opportunity to extract the irreducible correlations directly from experiments in the many-body regime described by quantum fields. Our results demonstrate that the extraction of lower equal-time correlations, such as the two- and four-point functions, involve already all the ingredients to obtain effective kinetic descriptions from first principles. Strikingly, the approach also offers the perspective of determining the exact evolution equations from quantum simulations. This can provide essential insights into the long-standing problem of finding non-perturbative approximations for strongly coupled systems.

4.A Derivation of flow equation

In this section, we demonstrate the derivation of an exact flow equation for equal-time correlation functions for the example of a single component, non-relativistic, complex Bose field, see [110, 152]. The derivation can be straightforwardly extended to the case of the $U(N)$ symmetric N component case considered in the main text.

4.A.1 Details on the effective action

We start from the equal-time generating functional

$$Z_t[J, J^*] = \text{Tr} \left(\hat{\rho}_t e^{\int_x (\hat{\psi}_x^\dagger J_x + J_x^* \hat{\psi}_x)} \right). \quad (4.84)$$

with sources J and J^* . This definition yields a generating functional for *symmetrically* ordered correlation functions. Correlation functions are obtained by functional differentiation, as we demonstrate for the example of a two-point function here. First, we note the commutation relations

$$\left[\hat{\psi}_x, \hat{\psi}_y^\dagger \right] = \delta_{xy}, \quad (4.85)$$

as well as the Baker-Campbell-Hausdorff formula,

$$\begin{aligned} e^{\int_x (\hat{\psi}_x^\dagger J_x + J_x^* \hat{\psi}_x)} &= e^{\int_x \hat{\psi}_x^\dagger J_x} e^{\int_x J_x^* \hat{\psi}_x} e^{-\frac{1}{2} \int_x J_x J_y^* [\hat{\psi}_x^\dagger, \hat{\psi}_y]} \\ &= e^{\int_x \hat{\psi}_x^\dagger J_x} e^{\int_x J_x^* \hat{\psi}_x} e^{\frac{1}{2} \int_x J_x^* J_x}. \end{aligned} \quad (4.86)$$

Using this, one finds

$$\begin{aligned} \frac{\delta^2}{\delta J_x \delta J_y^*} Z_t \Big|_{J, J^*=0} &= \frac{\delta^2}{\delta J_x \delta J_y^*} \text{Tr} \left(\hat{\rho}_t e^{\int_x \hat{\psi}_x^\dagger J_x} e^{\int_x J_x^* \hat{\psi}_x} e^{\frac{1}{2} \int_x J_x^* J_x} \right) \Big|_{J, J^*=0} \\ &= \frac{\delta}{\delta J_x} \text{Tr} \left(\hat{\rho}_t e^{\int_x \hat{\psi}_x^\dagger J_x} \left(\hat{\psi}_y + \frac{1}{2} J_y \right) e^{\int_x J_x^* \hat{\psi}_x} e^{\frac{1}{2} \int_x J_x^* J_x} \right) \Big|_{J, J^*=0} \\ &= \text{Tr} \left(\hat{\rho}_t \left[\hat{\psi}_x^\dagger \hat{\psi}_y + \frac{1}{2} \delta_{xy} \right] \right) \\ &= \text{Tr} \left(\hat{\rho}_t \left[\hat{\psi}_x^\dagger \hat{\psi}_y + \frac{1}{2} [\hat{\psi}_y, \hat{\psi}_x^\dagger] \right] \right) \\ &= \frac{1}{2} \text{Tr} \left(\hat{\rho}_t \left[\hat{\psi}_y \hat{\psi}_x^\dagger + \hat{\psi}_x^\dagger \hat{\psi}_y \right] \right). \end{aligned} \quad (4.87)$$

The equal-time effective action is defined as

$$\begin{aligned} \Gamma_t[\psi, \psi^*] &= -\log(Z_t[J, J^*]) + \int_x (\psi_x^* J_x + J_x^* \psi_x) \\ &\equiv -W_t[J(\psi), J^*(\psi^*)] + \int_x (\psi_x^* J_x + J_x^* \psi_x), \end{aligned} \quad (4.88)$$

where we shorten the notation as $J(\psi) = J(\psi, \psi^*)$. We implicitly defined the Schwinger functional $W_t = \log(Z_t)$, which is the generating functional for *connected*

correlation functions, i.e.,

$$G^{c,(3)}(x, y, w) = \frac{\delta^3 W_t}{\delta J_x^* \delta J_y^* \delta J_w} \quad (4.89a)$$

$$G^{c,(4)}(x, y, w, z) = \frac{\delta^4 W_t}{\delta J_x^* \delta J_y^* \delta J_w \delta J_z} . \quad (4.89b)$$

Here, we picked one representative each, where in principle all combinations of n field derivatives yield a correlation function of n th order. However, when evaluating the expressions for absent external sources, we focus on the U(1)-invariant case where the only surviving correlations are those with equal numbers of fields and conjugate fields.

Field expectation values and sources are related by

$$\psi_x(J) = \frac{\delta W_t}{\delta J_x^*} = \text{Tr} \left(\hat{\rho}_t e^{\int_x \hat{\psi}_x^\dagger J_x} \left[\hat{\psi}_x + \frac{J_x}{2} \right] e^{\int_x J_x^* \hat{\psi}_x} e^{\frac{1}{2} \int_x J_x^* J_x} \right), \quad (4.90a)$$

$$\psi_x^*(J^*) = \frac{\delta W_t}{\delta J_x} = \text{Tr} \left(\hat{\rho}_t e^{\int_x \hat{\psi}_x^\dagger J_x} \left[\hat{\psi}_x^\dagger + \frac{J_x^*}{2} \right] e^{\int_x J_x^* \hat{\psi}_x} e^{\frac{1}{2} \int_x J_x^* J_x} \right), \quad (4.90b)$$

$$\frac{\delta \Gamma_t}{\delta \psi_x} = J_x^*, \quad (4.90c)$$

$$\frac{\delta \Gamma_t}{\delta \psi_x^*} = J_x, \quad (4.90d)$$

where the last two lines follow directly from the definition of the effective action

$$\begin{aligned} \frac{\delta \Gamma_t}{\delta \psi_x} &= \int_y \left(-\frac{\delta J_y}{\delta \psi_x} \frac{\delta W_t}{\delta J_y} + \frac{\delta J_y}{\delta \psi_x} \psi_y^* \right) + \int_y \left(-\frac{\delta J_y^*}{\delta \psi_x} \frac{\delta W_t}{\delta J_y^*} + \frac{\delta J_y^*}{\delta \psi_x} \psi_y \right) + J_x^* \\ &= J_x . \end{aligned} \quad (4.91)$$

We may generalize these relations to obtain the connection between correlation functions and derivatives of the effective action, so-called *vertices*. We consider the following expression

$$\Gamma_{yx}^{(2)} \equiv \frac{\delta^2}{\delta \psi_y^* \delta \psi_x} \Gamma_t[\psi, \psi^*] = \frac{\delta J_x^*}{\delta \psi_y^*}, \quad (4.92)$$

which we use to obtain

$$\delta_{xz} = \int_y \frac{\delta J_x^*}{\delta \psi_y^*} \frac{\delta \psi_y^*}{\delta J_z^*} = \int_y \frac{\delta^2 \Gamma_t}{\delta \psi_y^* \delta \psi_x} \frac{\delta^2 W_t}{\delta J_z^* \delta J_y} = G_{zy}^{c,(2)} \Gamma_{yx}^{(2)}. \quad (4.93)$$

Hence, the second derivative of the effective action is the inverse connected two-point function. Using the following identity for an arbitrary (invertible) matrix $M(\lambda)$

$$M \partial_\lambda M^{-1} = \partial_\lambda \underbrace{[MM^{-1}]}_{=1} - [\partial_\lambda M] M^{-1} = -[\partial_\lambda M] M^{-1}, \quad (4.94)$$

we get

$$\begin{aligned}
\frac{\delta}{\delta\psi_z} G_{xy}^{\mathbf{c},(2)} &= \frac{\delta}{\delta\psi_z} \left[\Gamma^{(2)} \right]_{xy}^{-1} \\
&= -G_{xy_1}^{\mathbf{c},(2)} \frac{\delta}{\delta\psi_z} \left[\Gamma^{(2)} \right]_{y_1 y_2} G_{y_2 y}^{\mathbf{c},(2)} \\
&= -G_{zy_3}^{\mathbf{c},(2)} G_{xy_1}^{\mathbf{c},(2)} \Gamma_{y_1, y_2 y_3}^{(3)} G_{y_2 y}^{\mathbf{c},(2)}, \tag{4.95}
\end{aligned}$$

where the comma in $\Gamma_{y_1, y_2 y_3}^{(3)}$ separates the indices for derivations with respect to ψ^* from those associated with ψ -derivatives. Higher-order correlations are obtained accordingly, where each (connected) correlation function may be translated to a corresponding combination of two-point functions (propagators) and vertices.

4.A.2 Flow equation

Here, we consider a non-relativistic Bose gas with Hamiltonian

$$\hat{H} = \int_x \left[\frac{\nabla \hat{\psi}_x^\dagger \nabla \hat{\psi}_x}{2m} - \mu \hat{\psi}_x^\dagger \hat{\psi}_x + \frac{g}{2} \hat{\psi}_x^\dagger \hat{\psi}_x^\dagger \hat{\psi}_x \hat{\psi}_x \right]. \tag{4.96}$$

Its dynamics is determined by the von-Neumann equation

$$i\partial_t \hat{\rho}_t = \left[\hat{H}, \hat{\rho}_t \right], \tag{4.97}$$

for the time-dependent (Schrödinger) density operator $\hat{\rho}_t$. Using this, we may derive an evolution equation for the equal-time effective action with fixed external fields

$$\begin{aligned}
i\partial_t \Gamma_t &= -i\partial_t \log(Z_t) \\
&= -\frac{1}{Z_t} \text{Tr} \left(i\partial_t \hat{\rho}_t e^{\int_x (\hat{\psi}_x^\dagger J_x + J_x^* \hat{\psi}_x)} \right) \\
&= -\frac{1}{Z_t} \text{Tr} \left(\left[\hat{H}, \hat{\rho}_t \right] e^{\int_x (\hat{\psi}_x^\dagger J_x + J_x^* \hat{\psi}_x)} \right) \\
&= \frac{1}{Z_t} \text{Tr} \left(\hat{\rho}_t \left[\hat{H}, e^{\int_x (\hat{\psi}_x^\dagger J_x + J_x^* \hat{\psi}_x)} \right] \right), \tag{4.98}
\end{aligned}$$

and we used the cyclicity of the trace in the last step. The right-hand side of the evolution equation is evaluated by explicit computation of the commutators and by subsequently re-expressing field correlations in terms of propagators and effective vertices. To compute the commutators, we consider

$$\begin{aligned}
\left[\hat{H}, e^{\int_x (\hat{\psi}_x^\dagger J_x + J_x^* \hat{\psi}_x)} \right] &= \left[\hat{H}, e^{\int_x \hat{\psi}_x^\dagger J_x} e^{\int_x J_x^* \hat{\psi}_x} e^{\frac{1}{2} \int_x J_x^* J_x} \right] \\
&= \left[\hat{H}, e^{\int_x \hat{\psi}_x^\dagger J_x} e^{\int_x J_x^* \hat{\psi}_x} \right] e^{\frac{1}{2} \int_x J_x^* J_x}, \tag{4.99}
\end{aligned}$$

as well as the commutators

$$[\hat{\psi}, e^{\hat{\psi}^\dagger J}] = J e^{\hat{\psi}^\dagger J}, \quad (4.100a)$$

$$[(\hat{\psi})^2, e^{\hat{\psi}^\dagger J}] = \{\hat{\psi}, J e^{\hat{\psi}^\dagger J}\} = e^{\hat{\psi}^\dagger J} J (2\hat{\psi} + J), \quad (4.100b)$$

$$[\hat{\psi}^\dagger, e^{J^* \hat{\psi}}] = -J^* e^{J^* \hat{\psi}}, \quad (4.100c)$$

$$[(\hat{\psi}^\dagger)^2, e^{J^* \hat{\psi}}] = -J^* (2\hat{\psi}^\dagger + J^*) e^{J^* \hat{\psi}}, \quad (4.100d)$$

which we illustrated here for a single bosonic mode. We get

$$\begin{aligned} & \left[\hat{H}, e^{\int_x (\hat{\psi}_x^\dagger J_x + J_x^* \hat{\psi}_x)} \right] = \left[\hat{H}, e^{\int_x \hat{\psi}_x^\dagger J_x} e^{\int_x J_x^* \hat{\psi}_x} \right] e^{\frac{1}{2} \int_x J_x^* J_x} \\ &= e^{\frac{1}{2} \int_x J_x^* J_x} \left[\int_x \left(\frac{\nabla \hat{\psi}_x^\dagger \nabla \hat{\psi}_x}{2m} - \mu \hat{\psi}_x^\dagger \hat{\psi}_x + \frac{g}{2} \hat{\psi}_x^\dagger \hat{\psi}_x^\dagger \hat{\psi}_x \hat{\psi}_x \right), e^{\int_x \hat{\psi}_x^\dagger J_x} e^{\int_x J_x^* \hat{\psi}_x} \right] \\ &= e^{\frac{1}{2} \int_x J_x^* J_x} e^{\int_x \hat{\psi}_x^\dagger J_x} \left[\int_x \left(\frac{\nabla \hat{\psi}_x^\dagger \nabla \hat{\psi}_x}{2m} - \mu \hat{\psi}_x^\dagger \hat{\psi}_x + \frac{g}{2} \hat{\psi}_x^\dagger \hat{\psi}_x^\dagger \hat{\psi}_x \hat{\psi}_x \right), e^{\int_x J_x^* \hat{\psi}_x} \right] \\ &+ e^{\frac{1}{2} \int_x J_x^* J_x} \left[\int_x \left(\frac{\nabla \hat{\psi}_x^\dagger \nabla \hat{\psi}_x}{2m} - \mu \hat{\psi}_x^\dagger \hat{\psi}_x + \frac{g}{2} \hat{\psi}_x^\dagger \hat{\psi}_x^\dagger \hat{\psi}_x \hat{\psi}_x \right), e^{\int_x \hat{\psi}_x^\dagger J_x} \right] e^{\int_x J_x^* \hat{\psi}_x} \\ &= e^{\frac{1}{2} \int_x J_x^* J_x} e^{\int_x \hat{\psi}_x^\dagger J_x} e^{\int_x J_x^* \hat{\psi}_x} \int_x \left(\frac{J_x^* \nabla^2 \hat{\psi}_x}{2m} + \mu J_x^* \hat{\psi}_x - \frac{g}{2} J_x^* (2\hat{\psi}_x^\dagger - J_x^*) \hat{\psi}_x \hat{\psi}_x \right) \\ &- c.c., \end{aligned} \quad (4.101)$$

where we used an integration by parts and *c.c.* abbreviates complex conjugation. Further simplifications yield

$$\begin{aligned} &= e^{\int_x \frac{J_x^* J_x}{2}} e^{\int_x \hat{\psi}_x^\dagger J_x} e^{\int_x J_x^* \hat{\psi}_x} \int_x \left(\frac{J_x^* \nabla^2 \hat{\psi}_x}{2m} + \mu J_x^* \hat{\psi}_x - \frac{g}{2} J_x^* (2\hat{\psi}_x^\dagger - J_x^*) \hat{\psi}_x^2 \right) \\ &= e^{\int_x \frac{J_x^* J_x}{2}} e^{\int_x \hat{\psi}_x^\dagger J_x} \int_x \left(\frac{J_x^* \nabla^2 \hat{\psi}_x}{2m} + \mu J_x^* \hat{\psi}_x - \frac{g}{2} J_x^* (2\hat{\psi}_x^\dagger + J_x^*) \hat{\psi}_x^2 \right) e^{\int_x J_x^* \hat{\psi}_x} \\ &= \int_x \left(\frac{J_x^* \nabla^2 \left(\frac{\delta}{\delta J_x^*} - \frac{J_x}{2} \right)}{2m} + \mu J_x^* \left(\frac{\delta}{\delta J_x^*} - \frac{J_x}{2} \right) \right. \\ &\quad \left. - g J_x^* \frac{\delta}{\delta J_x} \left(\frac{\delta}{\delta J_x^*} - \frac{J_x}{2} \right)^2 \right) e^{\int_x \frac{J_x^* J_x}{2}} e^{\int_x \hat{\psi}_x^\dagger J_x} e^{\int_x J_x^* \hat{\psi}_x} \end{aligned} \quad (4.102)$$

where we normal ordered the expressions to replace field operators by their respective derivatives and source fields. Source derivatives are interpreted as acting on the exponential functions only.

Combining the various expressions, one gets

$$\begin{aligned}
 i\partial_t\Gamma_t = & \int_x \left[\frac{\delta\Gamma_t}{\delta\psi_x} \left(\frac{\nabla^2}{2m} + \mu \right) \psi_x - \psi_x^* \left(\frac{\nabla^2}{2m} + \mu \right) \frac{\delta\Gamma_t}{\delta\psi_x^*} + gG_{xxx}^{\psi^*\psi^*\psi} \frac{\delta\Gamma_t}{\delta\psi_x^*} - g \frac{\delta\Gamma_t}{\delta\psi_x} G_{xxx}^{\psi^*\psi\psi} \right] \\
 & + \int_x \left(\frac{g}{4} \frac{\delta\Gamma_t}{\delta\psi_x} \frac{\delta\Gamma_t}{\delta\psi_x} \frac{\delta\Gamma_t}{\delta\psi_x^*} \psi_x - \frac{g}{4} \psi_x^* \frac{\delta\Gamma_t}{\delta\psi_x} \frac{\delta\Gamma_t}{\delta\psi_x^*} \frac{\delta\Gamma_t}{\delta\psi_x^*} \right), \tag{4.103}
 \end{aligned}$$

see the corresponding result in Eq. (4.15).

4.B Diagrammatic rules and examples

In this section, we give further details on the diagrammatic language employed in the main chapter.

4.B.1 Examples

To illustrate the diagrammatic rules Eqs. (4.12)-(4.14), we give the full expression for the exemplary diagrams of Fig. 4.1 for the example of $N = 1$. The first diagram represents the connected four-point function (Eq. (4.11)), which is obtained as

$$\begin{aligned}
G_{x_1 x_2 x_3 x_4}^{\mathbf{c},(4)} &= \frac{\delta}{\delta J_{x_1}^*} \frac{\delta}{\delta J_{x_2}^*} \frac{\delta}{\delta J_{x_3}} \frac{\delta}{\delta J_{x_4}} W_t[J^{(*)}] \Big|_{J, J^*=0} \\
&= - \int_{\mathbf{y}} \frac{\delta \psi_{y_1}}{\delta J_{x_1}^*} \frac{\delta \psi_{y_2}}{\delta J_{x_2}^*} \frac{\delta \psi_{y_3}}{\delta J_{x_3}} \frac{\delta \psi_{y_4}}{\delta J_{x_4}} \Gamma_{y_1 y_2 y_3 y_4}^{(4)} \\
&= - \int_{\mathbf{y}} \frac{\delta W_t}{\delta J_{x_1}^* \delta J_{y_1}} \frac{\delta W_t}{\delta J_{x_2}^* \delta J_{y_2}} \frac{\delta W_t}{\delta J_{y_3}^* \delta J_{x_3}} \frac{\delta W_t}{\delta J_{y_4}^* \delta J_{x_4}} \Gamma_{y_1 y_2 y_3 y_4}^{(4)} \\
&= - \int_{\mathbf{y}} G_{x_1 y_1}^{\mathbf{c},(2)} G_{x_2 y_2}^{\mathbf{c},(2)} G_{y_3 x_3}^{\mathbf{c},(2)} G_{y_4 x_4}^{\mathbf{c},(2)} \Gamma_{y_1 y_2 y_3 y_4}^{(4)}, \tag{4.104}
\end{aligned}$$

where we used the definitions for n -point functions and the effective action, the U(1) symmetry, and \mathbf{y} refers to position variables y_1, \dots, y_4 . Going to Fourier space $G_{xy}^{\mathbf{c},(2)} = \int_p G_p^{\mathbf{c},(2)} \exp(ip(x-y))$, we get

$$G_{x_1 x_2 x_3 x_4}^{\mathbf{c},(4)} = - \int_{\mathbf{p}} G_{p_1}^{\mathbf{c},(2)} G_{p_2}^{\mathbf{c},(2)} G_{p_3}^{\mathbf{c},(2)} G_{p_4}^{\mathbf{c},(2)} e^{ip_1 x_1 + ip_2 x_2} e^{-ip_3 x_3 - ip_4 x_4} \Gamma_{p_1 p_2 p_3 p_4}^{(4)}, \tag{4.105a}$$

such that

$$G_{p_1 p_2 p_3 p_4}^{\mathbf{c},(4)} = - G_{p_1}^{\mathbf{c},(2)} G_{p_2}^{\mathbf{c},(2)} G_{p_3}^{\mathbf{c},(2)} G_{p_4}^{\mathbf{c},(2)} \Gamma_{p_1 p_2 p_3 p_4}^{(4)}. \tag{4.105b}$$

Here we used

$$\Gamma_{p_1 p_2 p_3 p_4}^{(4)} = \int_{\mathbf{y}} e^{-ip_1 y_1 - ip_2 y_2} e^{ip_3 y_3 + ip_4 y_4} \Gamma_{y_1 y_2 y_3 y_4}^{(4)}, \tag{4.105c}$$

$$G_{p_1 p_2 p_3 p_4}^{\mathbf{c},(4)} = \int_{\mathbf{x}} e^{-ip_1 x_1 - ip_2 x_2} e^{ip_3 x_3 + ip_4 x_4} G_{x_1 x_2 x_3 x_4}^{\mathbf{c},(4)}. \tag{4.105d}$$

Using the translation invariance in real-space one finds that $\Gamma_{x_1 x_2 x_3 x_4}^{(4)}$ is independent of the sum of its arguments $x_1 + x_2 + x_3 + x_4$ such that the integration over this component results in a momentum conserving factor $\delta(p_1 + p_2 - p_3 - p_4)$ in Fourier space.

The second and third diagrams are given accordingly by

$$\begin{aligned}
G_{p_1 \dots p_6}^{\mathbf{c},(6)} &= -G_{p_1}^{\mathbf{c},(2)} G_{p_2}^{\mathbf{c},(2)} G_{p_3}^{\mathbf{c},(2)} G_{p_4}^{\mathbf{c},(2)} G_{p_5}^{\mathbf{c},(2)} G_{p_6}^{\mathbf{c},(2)} \times \Gamma_{p_1 \dots p_6}^{(6)} \\
&+ \int_q G_{p_1}^{\mathbf{c},(2)} G_{p_2}^{\mathbf{c},(2)} G_{p_3}^{\mathbf{c},(2)} \Gamma_{p_1 p_2 p_3 q}^{(4)} G_q^{\mathbf{c},(2)} \Gamma_{q p_4 p_5 p_6}^{(4)} G_{p_4}^{\mathbf{c},(2)} G_{p_5}^{\mathbf{c},(2)} G_{p_6}^{\mathbf{c},(2)} \\
&+ \text{permutations.}
\end{aligned} \tag{4.106}$$

4.B.2 Loop expressions

The loop diagrams which involve the scattering of two and three particles are summarized in the function \mathcal{M} , and diagrammatically displayed in Fig. 4.2 for $N = 1$. In this section, we derive the analytic expressions which underlie the individual diagrams contributing to the evolution of $\Gamma^{(4)}$. The loop expressions originate from field-derivatives acting on the second line of Eq. (4.15), where we focus on one representative of each type of diagram (without listing complex conjugates or trivial permutations). Also, the integration over internal indices will be implied throughout this section. We consider

$$\frac{1}{Z_t[J^{(*)}]} \frac{\delta^3 Z_t[J^{(*)}]}{(\delta J_x)^2 \delta J_x^*} \frac{\delta \Gamma_t}{\delta \psi_x^*} = G_{xx,x}^{(3)} \frac{\delta \Gamma_t}{\delta \psi_x^*}, \tag{4.107}$$

where $G_{xx,x}^{(3)} = \langle (\hat{\psi}_x^\dagger)^2 \hat{\psi}_x \rangle_{J, \text{sym}}$ is non-zero in the presence of a source J . The expression may be split into its connected components and is subsequently differentiated with respect to the four external fields:

- **First**, one gets

$$\frac{\delta}{\delta \psi_{x_1}} \frac{\delta}{\delta \psi_{x_2}} \frac{\delta}{\delta \psi_{x_3}^*} \frac{\delta}{\delta \psi_{x_4}^*} \left[\psi_x^* \psi_x^* \psi_x \frac{\delta \Gamma_t}{\delta \psi_x^*} \right] \supset \delta_{x_1 x_4} \delta_{x_2 x_4} \delta_{x_3 x_4} \Gamma_{x_1 x_4}^{(2)} \rightarrow \text{diagram}, \tag{4.108a}$$


representing the bare classical scattering vertex.

- **Secondly**, one finds terms of the kind

$$\frac{\delta}{\delta \psi_{x_1}} \frac{\delta}{\delta \psi_{x_2}} \frac{\delta}{\delta \psi_{x_3}^*} \frac{\delta}{\delta \psi_{x_4}^*} \left[\psi_x^* G_{xx}^{\mathbf{c},(2)} \frac{\delta \Gamma_t}{\delta \psi_x^*} \right], \tag{4.109}$$

$$\frac{\delta}{\delta \psi_{x_1}} \frac{\delta}{\delta \psi_{x_2}} \frac{\delta}{\delta \psi_{x_3}^*} \frac{\delta}{\delta \psi_{x_4}^*} \left[\psi_x \tilde{G}_{xx}^{\mathbf{c},(2)} \frac{\delta \Gamma_t}{\delta \psi_x^*} \right], \tag{4.110}$$

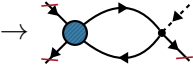
with $\tilde{G}_{xx}^{\mathbf{c},(2)} = \langle (\hat{\psi}_x^*)^2 \rangle_J$. Applying all derivatives in (4.109) to the first and the last factor in the bracket, we get the first diagram of \mathcal{M}

$$\frac{\delta}{\delta\psi_{x_1}} \frac{\delta}{\delta\psi_{x_2}} \frac{\delta}{\delta\psi_{x_3}^*} \frac{\delta}{\delta\psi_{x_4}^*} \left[\psi_x^* G_{xx}^{\mathbf{c},(2)} \frac{\delta\Gamma_t}{\delta\psi_x^*} \right] \supset -G_{x_1x_1}^{\mathbf{c},(2)} \Gamma_{x_1x_2x_3x_4}^{(4)} \rightarrow \text{Diagram (4.111)}$$


(4.111)

For translation invariant systems this diagram cancels against its permutations. The analogous expression (4.110) vanishes as $\tilde{G}_{xx}^{\mathbf{c},(2)} = 0$ when setting $J = 0$. When acting two derivatives on the two-point function in (4.109), we get

$$\frac{\delta}{\delta\psi_{x_1}} \frac{\delta}{\delta\psi_{x_2}} \frac{\delta}{\delta\psi_{x_3}^*} \frac{\delta}{\delta\psi_{x_4}^*} \left[\psi_x^* G_{xx}^{\mathbf{c},(2)} \frac{\delta\Gamma_t}{\delta\psi_x^*} \right] \supset -\Gamma_{x_1y_1y_2x_4}^{(4)} G_{x_3y_1}^{\mathbf{c},(2)} G_{y_2x_3}^{\mathbf{c},(2)} \Gamma_{x_3x_2}^{(2)}$$

$$\rightarrow \text{Diagram (4.112)}$$


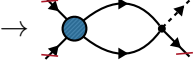
(4.112)

by using that

$$\frac{\delta}{\delta\psi_{x_1}} \frac{\delta}{\delta\psi_{x_2}^*} G_{xz}^{\mathbf{c},(2)} \Big|_{\psi^{(*)}=0} = -\Gamma_{x_1y_1y_2x_2}^{(4)} G_{x_3y_1}^{\mathbf{c},(2)} G_{y_2x_3}^{\mathbf{c},(2)}, \quad (4.113)$$

where contributions involving the three-vertex vanish due to U(1) invariance. Similarly, an analogous contribution arises from (4.109)

$$\frac{\delta}{\delta\psi_{x_1}} \frac{\delta}{\delta\psi_{x_2}} \frac{\delta}{\delta\psi_{x_3}^*} \frac{\delta}{\delta\psi_{x_4}^*} \left[\psi_x^* G_{xx}^{\mathbf{c},(2)} \frac{\delta\Gamma_t}{\delta\psi_x^*} \right] \supset -\Gamma_{x_1y_1y_2x_4}^{(4)} G_{x_3y_1}^{\mathbf{c},(2)} G_{y_2x_3}^{\mathbf{c},(2)} \Gamma_{x_3x_2}^{(2)}$$

$$\rightarrow \text{Diagram (4.114)}$$


(4.114)

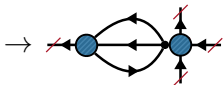
- **Third**, we consider

$$\frac{\delta}{\delta\psi_{x_1}} \frac{\delta}{\delta\psi_{x_2}} \frac{\delta}{\delta\psi_{x_3}^*} \frac{\delta}{\delta\psi_{x_4}^*} \left[G_{xx,x}^{\mathbf{c},(3)} \frac{\delta\Gamma_t}{\delta\psi_x^*} \right] \quad (4.115)$$

By U(1) symmetry, the only surviving contributions are obtained by applying an odd number of derivatives to each factor inside the brackets.

For one derivative acting on the three-point function, we use that

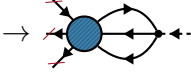
$$\frac{\delta}{\delta\psi_{x_4}^*} G_{xx,x}^{\mathbf{c},(3)} \Big|_{\psi^{(*)}=0} = -\Gamma_{x_4z_1z_2z_3}^{(4)} G_{xz_1}^{\mathbf{c},(2)} G_{z_2x}^{\mathbf{c},(2)} G_{z_3x}^{\mathbf{c},(2)},$$

$$\rightarrow \text{Diagram (4.116)}$$


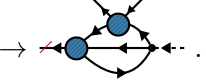
(4.116)

which yields the diagram in combination with the other derivatives acting on the second factor to yield $\Gamma_{xx_3x_1x_2}^{(4)}$.

In the case where three derivatives act on the three-point function, we get terms of the kind

$$\frac{\delta}{\delta\psi_{x_2}} \frac{\delta}{\delta\psi_{x_3}^*} \frac{\delta}{\delta\psi_{x_4}^*} G_{xx,x}^{c,(3)} \Big|_{\psi^{(*)}=0} \rightarrow -\Gamma_{x_3x_4z_1x_2z_2z_3}^{(6)} G_{xz_1}^{c,(2)} G_{z_2x}^{c,(2)} G_{z_3x}^{c,(2)}$$

(4.117)

where we again augmented the result with the second factor, here $\Gamma_{xx_1}^{(2)}$, or alternatively

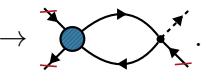
$$\begin{aligned} \frac{\delta}{\delta\psi_{x_2}} \frac{\delta}{\delta\psi_{x_3}^*} \frac{\delta}{\delta\psi_{x_4}^*} G_{xx,x}^{c,(3)} \Big|_{\psi^{(*)}=0} &= \frac{\delta}{\delta\psi_{x_2}} \frac{\delta}{\delta\psi_{x_3}^*} \left[-\Gamma_{x_4z_1z_2z_3}^{(4)} G_{xz_1}^{c,(2)} G_{z_2x}^{c,(2)} G_{z_3x}^{c,(2)} \right] \\ &\supset -\Gamma_{x_4z_1z_2z_3}^{(4)} G_{xz_1}^{c,(2)} G_{z_2x}^{c,(2)} \frac{\delta}{\delta\psi_{x_2}} \frac{\delta}{\delta\psi_{x_3}^*} \left[G_{z_3x}^{c,(2)} \right] \\ &= \Gamma_{x_4z_1z_2z_3}^{(4)} G_{xz_1}^{c,(2)} G_{z_2x}^{c,(2)} \Gamma_{x_3y_1y_2x_2}^{(4)} G_{z_3y_1}^{c,(2)} G_{y_2x}^{c,(2)}, \end{aligned}$$

(4.118)

including again $\Gamma_{xx_1}^{(2)}$.

Analogously, we give the expression for the computation of the conjugate of the diagram shown in Eq. (4.112). This diagram will be especially important for the computation of observables in the $1/N$ expansion of the effective action. It originates from the term

$$-\frac{1}{Z_t[J^{(*)}]} \frac{\delta^3 Z_t[J^{(*)}]}{(\delta J_x^*)^2 \delta J_x} \frac{\delta \Gamma_t}{\delta \psi_x} = -G_{x,xx}^{(3)} \frac{\delta \Gamma_t}{\delta \psi_x}, \quad (4.119)$$

where $G_{x,xx}^{(3)} = 1/2 \langle \{\hat{\psi}_x^\dagger, \hat{\psi}_x^2\} \rangle_J$. Again applying the external derivatives, we get

$$-\frac{\delta}{\delta\psi_{x_1}} \frac{\delta}{\delta\psi_{x_2}} \frac{\delta}{\delta\psi_{x_3}^*} \frac{\delta}{\delta\psi_{x_4}^*} \left[\psi_x G_{xx}^{c,(2)} \frac{\delta \Gamma_t}{\delta \psi_x} \right] \supset -\Gamma_{x_1y_1y_2x_4}^{(4)} G_{x_2y_1}^{c,(2)} G_{y_2x_2}^{c,(2)} \Gamma_{x_2x_3}^{(2)}$$

(4.120)

4.B.3 $1/N$ counting of diagrams

In this section, we briefly review the counting of powers of N in loop diagrams. While the Hamiltonian is invariant under a global $U(N)$ symmetry, there are N

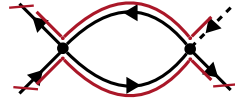
$U(1)$ subgroups which imply the conservation of particle number for the individual components i . Since we diagonalized the two-point function in field space, i.e., $G_{\alpha_1\alpha_2}^{c,(2)} = G_{x_1x_2}^{c,(2)}\delta_{i_1i_2}$, lines carrying a certain field index are never interrupted throughout a diagram. For the effective vertices, we get

$$\Gamma_{\alpha_1\dots\alpha_4}^{(4)} \propto \delta_{i_1i_3}\delta_{i_2i_4} + \text{perm.}, \quad (4.121a)$$


$$\Gamma_{\alpha_1\dots\alpha_6}^{(6)} \propto \delta_{i_1i_4}\delta_{i_2i_5}\delta_{i_3i_6} + \text{perm.}, \quad (4.121b)$$

and analogously for all higher-order vertices.

Depending on field indices and orientation of vertices, we can differentiate between different contributions, illustrated here for the example of a one-loop diagram



$$= \mathcal{O}(1/N^2), \quad (4.122a)$$



$$= \mathcal{O}(1/N^2) \times \mathcal{O}(N), \quad (4.122b)$$

where red lines follow field components through the diagrams. The factor of $1/N^2$ originates from the two bare vertices, which come with a factor of $1/N$ each. The additional factor of N in the second diagram originates from the summation over all possible intermediate particles within the loop. In general, each such closed loop of field indices yields a factor of N . Using this and assuming Eq. (4.46), we get the following power counting for the diagrams shown in Fig. 4.2 (where we always pick the representative with the largest power of N). Subleading diagrams of Fig. 4.2 are

the following

$$\begin{array}{c} \text{Diagram 1} \end{array} = \mathcal{O}(1/N^2), \quad (4.123a)$$

$$\begin{array}{c} \text{Diagram 2} \end{array} = \mathcal{O}(1/N^3) \times N = \mathcal{O}(1/N^2), \quad (4.123b)$$

$$\begin{array}{c} \text{Diagram 3} \end{array} = \mathcal{O}(1/N^3) \times N = \mathcal{O}(1/N^2), \quad (4.123c)$$

$$\begin{array}{c} \text{Diagram 4} \end{array} = \mathcal{O}(1/N^3) \times N = \mathcal{O}(1/N^2). \quad (4.123d)$$

The dominant contribution at order $1/N$ is given by

$$\begin{array}{c} \text{Diagram 5} \end{array} = \mathcal{O}(1/N^2) \times N = \mathcal{O}(1/N). \quad (4.124)$$

Eventually, we can confirm self-consistently that all contributions lead to an evolution of the four-vertex at order $\mathcal{O}(1/N)$. As $\Gamma^{(4)}$ is initially sourced by the bare vertex at order $\mathcal{O}(1/N)$, it confirms our initial assumption Eq. (4.46). This line of argument can be applied to the entire hierarchy of equal-time vertices: $\Gamma^{(6)}$ is sourced by a combination of the bare vertex and $\Gamma^{(4)}$ (i.e., at order $\mathcal{O}(1/N^2)$) and the corresponding diagrams for its evolution remain at this order.

4.C Details on the non-perturbative Boltzmann equation

In this section, we give the analytical expressions to detail the derivation of the non-perturbative Boltzmann equation which was outlined in the main chapter.

4.C.1 Proof of expression (4.72)

Here, we explicitly demonstrate that the expression (4.72) is a solution to the imaginary part of Eq. 4.71. First, we make use of the defining property of Γ^B , to define

$$\Gamma_{pqrs}^B \equiv (\Gamma_p - \Gamma_s)(\Gamma_q - \Gamma_r)B_{pqrs}, \quad (4.125)$$

where we made the external inverse propagators explicit. With this, Eq. (4.72) becomes

$$\begin{aligned} B_{pqrs} = & \frac{g^2/(4N)}{-\Delta\omega_{pqrs} + i\epsilon} \int_{k'} \underbrace{\left(-\frac{G_{k'}G_{k''} - \frac{1}{4}}{\Delta\omega_{k'psk''} - i\epsilon} \frac{1}{1 + \Pi_{k'k''}} - \frac{G_{k'}G_{k''} - \frac{1}{4}}{\Delta\omega_{k''qrk'} - i\epsilon} \frac{1}{1 + \Pi_{k''k'}} \right)}_{(I)} \\ & - \underbrace{\frac{g/2}{-\Delta\omega_{pqrs} + i\epsilon} \int_{k'} (G_{k''} - G_{k'}) B_{pk'k''s}}_{(II)} - \underbrace{\frac{g/2}{-\Delta\omega_{pqrs} + i\epsilon} \int_{k'} (G_{k'} - G_{k''}) B_{k''qrk'}}_{(III)}, \end{aligned} \quad (4.126)$$

and our ansatz for the solution (4.72) is accordingly given by

$$\text{Im}(B_{pqrs}) = \mathcal{P} \left[\frac{gg_{ps}^{\text{eff}}/(4N)}{-\Delta\omega_{pqrs} + i\epsilon} \right] \int_{k'} \pi \delta(\Delta\omega_{pk'k''s}) \left(G_{k'}G_{k''} - \frac{1}{4} \right) + \{p, s \leftrightarrow q, r\}. \quad (4.127)$$

In the following, we will strip Eq. (4.126) into its individual parts and analyse terms separately.

First term: (I)

Considering the first term of Eq. (4.126), we use the symmetry relation (4.142) to get

$$\delta(\Delta\omega_{pqrs}) \int_{k'} \text{Re} \left(-\frac{G_{k'}G_{k''} - \frac{1}{4}}{\Delta\omega_{k'psk''} - i\epsilon} \frac{1}{1 + \Pi_{k'k''}} - \frac{G_{k'}G_{k''} - \frac{1}{4}}{\Delta\omega_{k''qrk'} - i\epsilon} \frac{1}{1 + \Pi_{k''k'}} \right) = 0. \quad (4.128)$$

Using this, the imaginary part of the first term in Eq. (4.126) is given by

$$\text{Im}(I) = \mathcal{P} \left(\frac{g^2/(4N)}{-\Delta\omega_{pqrs} + i\epsilon} \right) \text{Im} \left[\int_{k'} \frac{G_{k'}G_{k''} - \frac{1}{4}}{\Delta\omega_{k'psk''} - i\epsilon} \frac{1}{1 + \Pi_{k'k''}} + \{p, q \leftrightarrow r, s\} \right] \quad (4.129)$$

Next, we compute the second factor separately,

$$\begin{aligned} \int_{k'} \text{Im} \left(\frac{G_{k'} G_{k''} - \frac{1}{4}}{\Delta\omega_{k'psk''} - i\epsilon} \frac{1}{1 + \Pi_{k'k''}^*} \right) &= \int_{k'} \pi\delta(\Delta\omega_{k'psk''}) \left(G_{k'} G_{k''} - \frac{1}{4} \right) \frac{1 + \text{Re}(\Pi_{k'k''}^*)}{|1 + \Pi_{k'k''}^*|^2} \\ &+ \int_{k'} \text{Re} \left(\frac{G_{k'} G_{k''} - \frac{1}{4}}{\Delta\omega_{k'psk''} - i\epsilon} \right) \frac{\text{Im}(\Pi_{k'k''}^*)}{|1 + \Pi_{k'k''}^*|^2}, \end{aligned} \quad (4.130)$$

Second and third term: (II) and (III)

Similarly, for the second and third term of Eq. (4.126), which involves B itself, we have

$$\begin{aligned} \text{Im} \left[\frac{g/2}{-\Delta\omega_{pqr} + i\epsilon} \right] \int_{k'} (G_{k''} - G_{k'}) \text{Re} [B_{pk'k''s} - B_{k''qrk'}] \\ = -\pi \frac{g}{2} \delta(\Delta\omega_{pqr}) \int_{k'} (G_{k''} - G_{k'}) \text{Re} [B_{pk'k''s} - B_{pk'k''s}^*] \\ = 0, \end{aligned} \quad (4.131)$$

where we used the identity $B_{pk'k''s}^* = B_{sk''k'p}$, see section 4.C.3. As a consequence, we focus on the following combination of real and imaginary parts

$$\begin{aligned} -\frac{g}{2} \text{Re} \left[\frac{1}{-\Delta\omega_{pqr} + i\epsilon} \right] \int_{k'} (G_{k''} - G_{k'}) \text{Im}(B_{pk'k''s}) \\ = -\mathcal{P} \left[\frac{g/2}{-\Delta\omega_{pqr} + i\epsilon} \right] \int_{k'} (G_{k''} - G_{k'}) \text{Im}(B_{pk'k''s}). \end{aligned} \quad (4.132)$$

Next, we compute the second factor of this term by employing the definition of B , i.e., Eq (4.127)

$$\begin{aligned} \int_{k'} (G_{k''} - G_{k'}) \text{Im}(B_{pk'k''s}) &= \int_{q',k'} \left(G_{q'} G_{q''} - \frac{1}{4} \right) \\ &\times \left[\frac{gg_{ps}^{\text{eff}}}{4} \mathcal{P} \left[\frac{(G_{k''} - G_{k'})}{-\Delta\omega_{pk'k''s} + i\epsilon} \right] \pi\delta(\Delta\omega_{pq'q''s}) \right. \\ &+ \left. \frac{gg_{k'k''}^{\text{eff}}}{4} \mathcal{P} \left[\frac{(G_{k''} - G_{k'})}{-\Delta\omega_{pk'k''s} + i\epsilon} \right] \pi\delta(\Delta\omega_{k'q'q''k''}) \right] \\ &= \frac{gg_{ps}^{\text{eff}}}{4} \mathcal{P}(\Pi_{ps}) \int_{q'} \pi\delta(\Delta\omega_{pq'q''s}) \left(G_{q'} G_{q''} - \frac{1}{4} \right) \\ &\int_{q'} \frac{gg_{q'q''}^{\text{eff}}}{4} \mathcal{P} \left[\frac{G_{q'} G_{q''} - \frac{1}{4}}{-\Delta\omega_{pq'q''s} + i\epsilon} \right] \text{Im}(\Pi_{q''q'}). \end{aligned} \quad (4.133)$$

Putting all terms together, we observe

$$\begin{aligned}
& \text{Im(I)} + \text{Im(II)} + \text{Im(III)} \\
&= \mathcal{P} \left(\frac{g^2/(4N)}{-\Delta\omega_{pqrs} + i\epsilon} \right) \int_{k'} \pi \delta(\Delta\omega_{k'psk''}) \frac{G_{k'} G_{k''} - \frac{1}{4}}{|1 + \Pi_{k'k''}|^2} + \{p, s \leftrightarrow q, r\} \\
&= \mathcal{P} \left(\frac{g g_{ps}^{\text{eff}}/(4N)}{-\Delta\omega_{pqrs} + i\epsilon} \right) \int_{k'} \pi \delta(\Delta\omega_{k'psk''}) \left(G_{k'} G_{k''} - \frac{1}{4} \right) + \{p, s \leftrightarrow q, r\} \\
&= \text{Im}(B_{pqrs}), \tag{4.134}
\end{aligned}$$

which confirms that the ansatz Eq (4.127) solves the imaginary part of Eq. (4.126).

4.C.2 Non-perturbative Boltzmann equation

To derive the non-perturbative Boltzmann equation, we compute

$$\partial_t G_p = - \int_{q,r,s} g \text{Im}(\Gamma_{pqrs}^A + \Gamma_{pqrs}^B) G_p G_q G_r G_s. \tag{4.135}$$

To this end, we again split the expression into individual parts

$\text{Im}(\Gamma^A)$

We first consider the following term, see also (4.67),

$$\begin{aligned}
\int_{q'} \text{Im}(\Gamma_{pq'q''s}^A) G_{q'} G_{q''} &= - \int_{q'} \pi G_{q'} G_{q''} \delta(\Delta\omega_{pq'q''s}) V_{pq'q''s}^{\text{eff}} \\
&\quad - \int_{q'} \pi G_{q'} G_{q''} \delta(\Delta\omega_{pq'q''s}) V_{pq'q''s}^{\text{eff}} \mathcal{P}(\Pi_{ps}) \\
&\quad + \int_{q'} \mathcal{P} \left[\frac{G_{q'} G_{q''}}{\Delta\omega_{pq'q''s} - i\epsilon} \right] \left[V_{pq'q''s}^{\text{eff}} \text{Im}(\Pi_{ps}) \right. \\
&\quad \left. + \{p, s \leftrightarrow q', q''\} \right], \tag{4.136}
\end{aligned}$$

where we adapted the notation of Eqs. (4.63) and (4.64). Here, the second line is given by

$$\begin{aligned}
& - \int_{q'} \pi G_{q'} G_{q''} \delta(\Delta\omega_{pq'q''s}) V_{pq'q''s}^{\text{eff}} \mathcal{P}(\Pi_{ps}) \\
&= -(\Gamma_p - \Gamma_s) \frac{g_{ps}^{\text{eff}}}{2N} \mathcal{P}(\Pi_{ps}) \int_{q'} \pi \delta(\Delta\omega_{pq'q''s}) \left(G_{q'} G_{q''} - \frac{1}{4} \right) \\
&\quad + \frac{g_{ps}^{\text{eff}}}{2N} \mathcal{P}(\Pi_{ps}) \text{Im}(\Pi_{ps}) \left(1 - \frac{\Gamma_p \Gamma_s}{4} \right). \tag{4.137}
\end{aligned}$$

The third line can be rewritten to yield

$$\int_{q'} \mathcal{P} \left[\frac{G_{q'} G_{q''}}{\Delta\omega_{pq'q''s} - i\epsilon} \right] V_{pq'q''s}^{\text{eff}} \text{Im}(\Pi_{ps}) = -\frac{g_{ps}^{\text{eff}}}{2N} \mathcal{P}(\Pi_{ps}) \text{Im}(\Pi_{ps}) \left(1 - \frac{\Gamma_p \Gamma_s}{4} \right), \quad (4.138)$$

and similarly, we obtain for the fourth line

$$\begin{aligned} & \int_{q'} \mathcal{P} \left[\frac{G_{q'} G_{q''}}{\Delta\omega_{pq'q''s} - i\epsilon} \right] V_{q'psq''}^{\text{eff}} \frac{\text{Im}(\Pi_{q'q''})}{|1 + \Pi_{q'q''}|^2} \\ &= (\Gamma_p - \Gamma_s) \int_{q',k'} \frac{gg_{k'k''}^{\text{eff}}}{4N} \left(G_{q'} G_{q''} - \frac{1}{4} \right) \pi \delta(\Delta\omega_{q'k''k'q''}) \mathcal{P} \left[\frac{G_{k'} - G_{k''}}{\Delta\omega_{pk'k''s} - i\epsilon} \right]. \end{aligned} \quad (4.139)$$

$\text{Im}(\Gamma^B)$

The second term can be brought into the form

$$\begin{aligned} & \int_{q'} \text{Im}(\Gamma_{pq'q''s}^B) G_{q'} G_{q''} = -(\Gamma_p - \Gamma_s) \frac{g_{ps}^{\text{eff}}}{2N} \mathcal{P}(\Pi_{ps}) \int_{q'} \pi \delta(\Delta\omega_{pk'k''s}) \left(G_{k'} G_{k''} - \frac{1}{4} \right) \\ & - (\Gamma_p - \Gamma_s) \int_{q',k'} \frac{gg_{q'q''}^{\text{eff}}}{4N} \left(G_{k'} G_{k''} - \frac{1}{4} \right) \pi \delta(\Delta\omega_{q'k''k'q''}) \\ & \times \mathcal{P} \left[\frac{G_{q'} - G_{q''}}{\Delta\omega_{pq'q''s} - i\epsilon} \right]. \end{aligned} \quad (4.140)$$

In summary, all but one term cancel, and we get

$$\int_{q'} \text{Im}(\Gamma_{pq'q''s}^A + \Gamma_{pq'q''s}^B) G_{q'} G_{q''} = - \int_{q'} \pi G_{q'} G_{q''} \delta(\Delta\omega_{pq'q''s}) V_{pq'q''s}^{\text{eff}}, \quad (4.141)$$

which straightforwardly leads to Eq. (4.74).

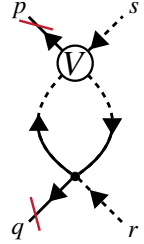
4.C.3 Symmetries under coordinate exchange

In our calculations we frequently use the symmetry of certain objects under the momentum exchange $p, s \leftrightarrow s, p$ (i.e., $p, s \leftrightarrow q, r$ in the presence of the momentum and energy conserving delta functions). For instance, we get for the one-loop self-energy function

$$\begin{aligned} \Pi_{sp} &= g \int_{k'} \frac{G_{k'} - G_{k'-(p-s)}}{\Delta\omega_{sk'(k'-(p-s))p} - i\epsilon} \\ &= g \int_{k'} \frac{G_{k'+(p-s)} - G_{k'}}{\Delta\omega_{s(k'+(p-s))k'p} - i\epsilon} \\ &= g \int_{k'} \frac{G_{k'} - G_{k'+(p-s)}}{\Delta\omega_{pk'(k'+(p-s))s} + i\epsilon} \\ &= \Pi_{ps}^*. \end{aligned} \quad (4.142)$$

Here, a crucial ingredient was the anti-symmetry of the numerator under the coordinate flip.

We employ similar arguments to demonstrate the relation $B_{pqrs}^* = B_{rspq}$ which we use to solve the non-perturbative evolution equation for $\text{Im}(\Gamma^B)$. First, we show the identity at the one-loop level, cf. Eq. (4.69). Using



$$\propto \frac{1}{N} \frac{\Gamma_r \Gamma_s}{\Delta\omega_{pqrs} - i\epsilon} \int_{k'} \frac{G_{k'} G_{k''} - \frac{1}{4}}{\Delta\omega_{pk'k''s} - i\epsilon}. \quad (4.143)$$

one gets

$$B_{pqrs} = \frac{-g^2/N}{\Delta\omega_{pqrs} - i\epsilon} \int_{k'} \frac{G_{k'} G_{k''} - \frac{1}{4}}{\Delta\omega_{pk'k''s} - i\epsilon} + \text{higher-order loops}. \quad (4.144)$$

In presence of the energy and momentum conserving δ -distributions $\delta(\Delta\omega_{pqrs})\delta(p + q - r - s)$, we find

$$\begin{aligned} \left[\frac{-g^2/N}{\Delta\omega_{pqrs} - i\epsilon} \int_{k'} \frac{G_{k'} G_{k''} - \frac{1}{4}}{\Delta\omega_{pk'k''s} - i\epsilon} \right]^* &= \frac{-g^2/N}{\Delta\omega_{pqrs} + i\epsilon} \int_{k'} \frac{G_{k'} G_{k''} - \frac{1}{4}}{\Delta\omega_{pk'k''s} + i\epsilon} \\ &= \frac{-g^2/N}{\Delta\omega_{rspq} - i\epsilon} \int_{k'} \frac{G_{k'} G_{k''} - \frac{1}{4}}{\Delta\omega_{k''spk'} - i\epsilon} \\ &= \frac{-g^2/N}{\Delta\omega_{rspq} - i\epsilon} \int_{k'} \frac{G_{k'} G_{k'+(p-s)} - \frac{1}{4}}{\Delta\omega_{(k'+(p-s))spk'} - i\epsilon} \\ &= \frac{-g^2/N}{\Delta\omega_{rspq} - i\epsilon} \int_{k'} \frac{G_{k'+(s-p)} G_{k'} - \frac{1}{4}}{\Delta\omega_{sk'(k'+(s-p))p} - i\epsilon} \\ &= \left[\frac{-g^2/N}{\Delta\omega_{pqrs} - i\epsilon} \int_{k'} \frac{G_{k'} G_{k''} - \frac{1}{4}}{\Delta\omega_{pk'k''s} - i\epsilon} \right]_{p,q \leftrightarrow r,s}. \end{aligned} \quad (4.145)$$

With this, the identity $B_{pqrs}^* = B_{rspq}$ is easily shown at the one-loop level. The generalization to any loop order, and thus the full expression B , follows in the same manner iteratively from Eq. (4.126), where it is respected in each term individually.

Chapter 5

Conclusion

This dissertation was devoted to the advance of quantum simulation techniques for the complex dynamics of quantum fields such as lattice gauge theories and Bose gases. We conclude by summarizing and discussing the central results, and by giving an outlook on future research.

5.1 Summary

The achievements of this thesis were presented in the following main chapters:

In *Chapter 2* we developed a quantum simulator to investigate a one-dimensional $U(1)$ lattice gauge theory with ultra-cold atoms and demonstrated its controlled operation. A strong motivation for the experiment was to demonstrate the scalability of our approach. The faithful implementation of gauge invariance was probed with experimentally accessible observables to anticipate the regime of large-scale quantum systems where numerical calculations become too costly to follow the detailed evolution in general. We highlighted the importance of gauge symmetry in the many-body dynamics, which lead the system to gauge invariant thermal ensembles different from corresponding simulations without the symmetry constraints. Our results demonstrate that large-scale quantum simulations of gauge theories are in immediate reach with current technology, and lay the foundation for further investigations into their emergent phenomena.

In *Chapter 3* we proposed a scalable scheme to realize $U(1)$ gauge fields with ultra-cold quantum gases in two dimensions. To illustrate our proposal, we studied how charge confinement could become accessible with ultra-cold atoms. To make optimal use of the underlying platform, we utilized the spin-changing collisions of the atoms and promoted their spin conservation to a (local) gauge symmetry. This strategy provides a reliable mechanism to enforce the gauge invariant dynamics, which extends to the case where individual unit-cells of our proposal are scaled-up with two dimensional optical lattices.

The single-plaquette realization of the two-dimensional gauge theory was subsequently investigated experimentally through fluctuations of the ultra-cold atoms. Our theoretical modelling of the experimental data enabled us to identify various

non-equilibrium phenomena. For a class of initial states, the system evolution allowed for a description of fast relaxation with signatures of equilibration at already early times. For a different regime of initial states, relaxation to equilibrium was suppressed on observable times, suggesting the existence of a long-lived metastable state. These regions of the parameter space were separated by an instability, which we diagnosed with the large fluctuations in the data, and our theoretical modelling was assisted by an interpretation of the observed data through mean-field potentials. At last, we explored a different approach by studying the non-equilibrium dynamics of \mathbb{Z}_2 gauge fields through the evolution of their entanglement spectra. The numerical results allowed us to distinguish different regimes from early level repulsion to late-time equilibration even for the small considered system sizes, thus setting the stage for applications with quantum simulators. The entanglement structure revealed an intermediate regime of self-similar evolution where probability is transported similar to particle or energy transport in wave turbulence [69, 141], as recently also considered experimentally with Bose gases [88–90].

In the last part, *Chapter 4*, we considered the far-from-equilibrium dynamics of Bose gases from the perspective of experimentally accessible equal-time correlations. We elaborated on a formulation of quantum field theory based on the equal-time effective action, which builds on such time-local correlation functions. The effective action obeys a functional evolution equation, which enables the derivation of exact evolution equations for two-point functions and interaction vertices. Extending earlier work, we derived kinetic theories in two regimes: the perturbative, weakly interacting gas and the highly occupied non-perturbative gas. The latter is dominated by important vertex corrections, which we computed analytically.

5.2 Outlook

An important step toward realistic applications of quantum simulation experiments is to further extend current platforms and the outlined theoretical and experimental techniques of realizing the gauge theories, e.g., to three-dimensional setups, continuous-variable gauge fields as realized in QED, and more complex, non-abelian gauge groups.

As a first step, the approach discussed in Chapter 2 should be extended to higher-spin representations of the quantum link formalism. While such models lie beyond the scope of this thesis, they seem possible with state-of-the-art technology. As demonstrated in Refs. [78, 79], extensions to spin-3 could already yield valuable insight into the continuum limit of QED, e.g. in the strong coupling regime.

Future work will also focus on the various phenomena which will be accessible in higher dimensional setups. In one spatial dimension, the gauge fields are heavily

restricted and even basic aspects such as the propagation of transversal gauge field modes are not present. Investigating the non-equilibrium dynamics of the gauge fields in higher-dimensional large-scale quantum simulators may provide valuable insight also for more complex, e.g. non-abelian, gauge theories.

Extending the presented single-plaquette realization with optical lattices would enable us, for example, to study the thermalization dynamics of higher-dimensional gauge fields in detail. The isolated, interacting field theory gives rise to investigations of strongly correlated regimes of gauge theories as relevant for the evolution of fields in heavy-ion collisions [14, 159]. Our results suggest that methods and some of the phenomenology observed in Section 3.4 extend to the two-dimensional lattice. As illustrated in Section 3.4, the far-from-equilibrium evolution often involves large fluctuations or high occupation numbers of gauge fields and is thus expected to require the many degrees of freedom provided by Bose-Einstein condensates [77].

By coupling fermions to the gauge fields, our approach would also give rise to studies of a series of strong-field aspects of continuum QED [160]. So far, this regime of QED has not extensively been addressed experimentally as the necessary field strengths of orders $\sim 10^{18}\text{V/m}$ are beyond the capabilities of current facilities [161, 162]. Target phenomena range from Schwinger pair production beyond one spatial dimension [145, 163] to quantum anomalies out of equilibrium [8, 164], and string breaking [165–167], which will also provide valuable insights for similar facets of QCD. While we transformed the fermion matter fields to corresponding interaction terms of hard-core bosons in Chapter 2, such an approach cannot be straightforwardly applied beyond a single dimension. Ultra-cold Fermi gases [168–170] offer a way forward, as they intrinsically carry the necessary quantum statistics for the realization of fermionic matter. Here, ultra-cold atoms hold a natural advantage over alternative platforms based on Rydberg atoms, trapped ions, or superconducting circuits.

Such Fermi gases are also natural extensions for the effective action approach presented in Chapter 4. Despite the illustration with scalar Bose fields, the concept of effective actions is more general and could also be applied to fermions, relativistic fields, or even more complex systems, for example, gauge theories. Such an extension may enable the detailed verification of symmetry constraints in the exact evolution equations of large-scale quantum simulators. Relevant ingredients for the complex field dynamics could be discovered experimentally, which might lead to valuable insights toward efficient descriptions of gauge theories in strongly-correlated regimes.

The work presented in Chapter 4 may also shed new light on non-equilibrium universality as recently observed in experiments [88–90]. Our equal-time computations

were partly motivated by the experiment [143], where effective vertices have been extracted during the far-from-equilibrium evolution of a spinor Bose gas. Our approach yields a qualitative basis to understand the strong suppression and universal dynamics measured for vertices in the highly-occupied infrared regime. Detailed comparisons of the 1PI vertices computed in Chapter 4 with measured vertices in terms of composite spin-1 operators is beyond the scope of this thesis, but lies within immediate reach.

Effective actions yield the characterization of quantum simulators via field correlations, however, as demonstrated in Section 3.5 of Chapter 3, non-equilibrium dynamics can also become accessible through entanglement spectra. Recent years have brought substantial progress in the development of experimental methods to extract suitable measures for entanglement [25, 26, 171–175]. Applications to quantum simulation would allow for a deeper understanding of the complex gauge field dynamics from the perspectives of both entanglement and field correlations.

In this context, it is crucial to also consider the vast possibilities offered by available platforms beyond analog quantum simulation. For instance, there has been great progress toward universal quantum computing schemes, as often discussed in the context of trapped ions or superconducting circuits [91, 176]. They offer precise control and great flexibility to engineer in principle arbitrary types quantum states and time evolution, yet, their scalability to large systems is challenging. In this context, large arrays of Rydberg atoms have been pioneered recently and their application to quantum simulation offers exciting new perspectives [55, 177, 178]. It seems essential for future quantum simulators to exploit the natural characteristics of the simulating platforms such as the underlying symmetry groups. An exciting direction is to combine aspects of different platforms to use their individual strengths and balance weaknesses. In this context, promising directions involve hybrid analog-digital simulation schemes [39], or quantum-classical optimization [56, 179], where large parts of the computational tasks are efficiently performed with classical machines. Research in these directions could open new ways toward the far-reaching goal of realizing quantum simulations of QCD and beyond.

List of figures

1.1	Analog vs. digital quantum simulations (schematics).	16
2.1	Quantum simulator for the gauge theory.	21
2.2	Gauss law in gauge theory and simulator.	22
2.3	Initial state preparation.	25
2.4	Schematic ground states in gauge theory and simulator.	26
2.5	Time-resolved transition of atoms.	27
2.6	Density correlation of atoms.	28
2.7	Local gauge invariance.	30
2.8	“Clean case” without defects.	31
2.9	“Gauge impurity” defect.	32
2.10	Effect of initial state defects	33
2.11	Final state distribution after the ramp.	34
2.12	Schematic non-equilibrium evolution toward steady states.	35
2.13	Non-equilibrium evolution of the matter density.	36
2.14	Controlled approach to gauge-theory dynamics.	37
2.15	Controlled approach to gauge-theory dynamics.	38
2.16	Thermalization dynamics with and without gauge-symmetry constraint.	39
2.17	Initial state preparation and schematics of thermalization.	40
2.18	Effective loss of initial-state information.	41
2.19	Perturbation theory of effective interactions.	43
2.20	Suppression of second-order tunneling with a tilt.	45
2.21	Extraction of the correlation length.	46
2.22	System size dependence of numerical calculations.	47
2.23	System size dependence of matter density for infinite temperature state.	50
3.1	Proposed implementation of the two-dimensional simulator.	54
3.2	Flux string between two opposite charges.	58
3.3	Confinement of charges.	59
3.4	Dynamics of spin fluctuations induced by spin changing collisions.	62
3.5	Time-evolving mean and fluctuations of the spin imbalance.	64
3.6	Different regimes of non-equilibrium evolution.	66
3.7	Identification of the mixture with a single-plaquette gauge theory.	68
3.8	Two-dimensional lattice geometry.	70
3.9	Non-equilibrium dynamics of the \mathbb{Z}_2 lattice gauge theory	71

3.10	Evolution of gap ratio.	72
3.11	Self-similar dynamics of the entanglement spectrum.	73
3.12	Effective spin model parameters.	92
3.13	Effective mean-field potentials.	96
3.14	Single plaquette of the lattice gauge theory.	96
3.15	Gauge field instability in a single plaquette.	98
3.16	Growth of mean field and fluctuations.	99
4.1	Connected correlation functions from irreducible building blocks. . .	106
4.2	Loop-contributions to the evolution equation of $\Gamma^{(4)}$	111
4.3	Schematics of the measurement scheme.	126

List of abbreviations

1D	One dimension/One-dimensional
1PI	One-particle irreducible
2D	Two dimensions/Two-dimensional
BEC	Bose-Einstein Condensate
BHM	Bose-Hubbard model
GI	Gauge impurity
IR	Infra-red
Li	Lithium (${}^7\text{Li}$)
MH	Matter hole
MI	Matter impurity
Na	Sodium (${}^{23}\text{Na}$)
QCD	Quantum chromodynamics
QCP	Quantum critical point
QED	Quantum electrodynamics
QLM	Quantum link model
SCC	Spin-changing collisions
UV	Ultra-violet

Bibliography

- ¹B. Yang, H. Sun, R. Ott, H.-Y. Wang, T. V. Zache, J. C. Halimeh, Z.-S. Yuan, P. Hauke, and J.-W. Pan, “Observation of gauge invariance in a 71-site bose–hubbard quantum simulator”, *Nature* **587**, 392–396 (2020) (cit. on pp. vii, 19, 25–30, 36, 46, 47).
- ²J. C. Halimeh, R. Ott, I. P. McCulloch, B. Yang, and P. Hauke, “Robustness of gauge-invariant dynamics against defects in ultracold-atom gauge theories”, *Physical Review Research* **2**, 033361 (2020) (cit. on pp. vii, 19, 31–34).
- ³R. Ott, T. V. Zache, F. Jendrzejewski, and J. Berges, “Scalable cold-atom quantum simulator for two-dimensional qed”, *Physical Review Letters* **127**, 130504 (2021) (cit. on pp. vii, 51, 54, 58, 59).
- ⁴Z.-Y. Zhou, G.-X. Su, J. C. Halimeh, R. Ott, H. Sun, P. Hauke, B. Yang, Z.-S. Yuan, J. Berges, and J.-W. Pan, “Thermalization dynamics of a gauge theory on a quantum simulator”, arXiv preprint arXiv:2107.13563 (2021) (cit. on pp. vii, 19, 21, 22, 35–41).
- ⁵N. Mueller, T. V. Zache, and R. Ott, “Thermalization of gauge theories from their entanglement spectrum”, arXiv preprint arXiv:2107.11416 (2021) (cit. on pp. vii, 51, 70–73).
- ⁶R. Ott, T. V. Zache, and J. Berges, “Equal-time approach to real-time dynamics of quantum fields”, arXiv preprint arXiv:2204.06463 (2022) (cit. on pp. vii, 103, 106, 111, 126).
- ⁷A. Hegde, R. Ott, A. Xia, V. Kasper, J. Berges, and F. Jendrzejewski, “Non-equilibrium dynamics of fluctuations in an ultra-cold atomic mixture”, arXiv preprint arXiv:2204.06456 (2022) (cit. on pp. vii, 51, 62, 64, 66, 92, 96).
- ⁸R. Ott, T. V. Zache, N. Mueller, and J. Berges, “Non-cancellation of the parity anomaly in the strong-field regime of qed₂₊₁”, *Physics Letters B*, 135459 (2020) (cit. on pp. vii, 149).
- ⁹S. Weinberg, *The quantum theory of fields*, Vol. 2 (Cambridge university press, 1995) (cit. on pp. 1, 2, 7).
- ¹⁰C. Gattringer and C. Lang, *Quantum chromodynamics on the lattice: an introductory presentation*, Vol. 788 (Springer Science & Business Media, 2009) (cit. on pp. 1, 10).
- ¹¹I. Montvay and G. Münster, *Quantum fields on a lattice* (Cambridge University Press, 1997) (cit. on pp. 1, 9, 10, 57).
- ¹²*European organization for nuclear research (cern)*, Accessed 2022-04-18 (cit. on p. 1).

- ¹³N. Cabibbo and G. Parisi, “Exponential hadronic spectrum and quark liberation”, *Physics Letters B* **59**, 67–69 (1975) (cit. on p. 1).
- ¹⁴J. Berges, M. P. Heller, A. Mazeliauskas, and R. Venugopalan, “Qcd thermalization: ab initio approaches and interdisciplinary connections”, *Reviews of Modern Physics* **93**, 035003 (2021) (cit. on pp. 1, 149).
- ¹⁵I. Bloch, J. Dalibard, and S. Nascimbene, “Quantum simulations with ultracold quantum gases”, *Nature Physics* **8**, 267–276 (2012) (cit. on p. 1).
- ¹⁶R. Blatt and C. F. Roos, “Quantum simulations with trapped ions”, *Nature Physics* **8**, 277–284 (2012) (cit. on p. 1).
- ¹⁷A. A. Houck, H. E. Türeci, and J. Koch, “On-chip quantum simulation with superconducting circuits”, *Nature Physics* **8**, 292–299 (2012) (cit. on p. 1).
- ¹⁸P. W. Anderson, “More is different: broken symmetry and the nature of the hierarchical structure of science.”, *Science* **177**, 393–396 (1972) (cit. on p. 1).
- ¹⁹M. Troyer and U.-J. Wiese, “Computational complexity and fundamental limitations to fermionic quantum monte carlo simulations”, *Physical review letters* **94**, 170201 (2005) (cit. on pp. 1, 16).
- ²⁰E. Loh Jr, J. Gubernatis, R. Scalettar, S. White, D. Scalapino, and R. Sugar, “Sign problem in the numerical simulation of many-electron systems”, *Physical Review B* **41**, 9301 (1990) (cit. on p. 1).
- ²¹J. Argüello-Luengo, A. González-Tudela, T. Shi, P. Zoller, and J. I. Cirac, “Analogue quantum chemistry simulation”, *Nature* **574**, 215–218 (2019) (cit. on p. 2).
- ²²U.-J. Wiese, “Towards quantum simulating qcd”, *Nuclear Physics A* **931**, 246–256 (2014) (cit. on p. 2).
- ²³T. Schweigler, V. Kasper, S. Erne, I. Mazets, B. Rauer, F. Cataldini, T. Langen, T. Gasenzer, J. Berges, and J. Schmiedmayer, “Experimental characterization of a quantum many-body system via higher-order correlations”, *Nature* **545**, 323–326 (2017) (cit. on pp. 2, 75, 99, 103).
- ²⁴M. Rispoli, A. Lukin, R. Schittko, S. Kim, M. E. Tai, J. Léonard, and M. Greiner, “Quantum critical behaviour at the many-body localization transition”, *Nature* **573**, 385–389 (2019) (cit. on pp. 2, 75, 103).
- ²⁵A. M. Kaufman, M. E. Tai, A. Lukin, M. Rispoli, R. Schittko, P. M. Preiss, and M. Greiner, “Quantum thermalization through entanglement in an isolated many-body system”, *Science* **353**, 794–800 (2016) (cit. on pp. 2, 150).
- ²⁶T. Brydges, A. Elben, P. Jurcevic, B. Vermersch, C. Maier, B. P. Lanyon, P. Zoller, R. Blatt, and C. F. Roos, “Probing rényi entanglement entropy via randomized measurements”, *Science* **364**, 260–263 (2019) (cit. on pp. 2, 69, 150).
- ²⁷K. G. Wilson, “Confinement of quarks”, *Physical review D* **10**, 2445 (1974) (cit. on pp. 2, 3).

- ²⁸U.-J. Wiese, “Ultracold quantum gases and lattice systems: quantum simulation of lattice gauge theories”, *Annalen der Physik* **525**, 777–796 (2013) (cit. on p. 2).
- ²⁹M. Aidelsburger, L. Barbiero, A. Bermudez, T. Chanda, A. Dauphin, D. González-Cuadra, P. R. Grzybowski, S. Hands, F. Jendrzejewski, J. Jünemann, et al., “Cold atoms meet lattice gauge theory”, *Philosophical Transactions of the Royal Society A* **380**, 20210064 (2022) (cit. on p. 2).
- ³⁰E. Zohar, J. I. Cirac, and B. Reznik, “Quantum simulations of gauge theories with ultracold atoms: local gauge invariance from angular-momentum conservation”, *Physical Review A* **88**, 023617 (2013) (cit. on pp. 2, 53).
- ³¹E. Zohar and B. Reznik, “Confinement and lattice quantum-electrodynamics electric flux tubes simulated with ultracold atoms”, *Physical review letters* **107**, 275301 (2011) (cit. on pp. 2, 14, 52, 53, 55).
- ³²E. Zohar, J. I. Cirac, and B. Reznik, “Simulating compact quantum electrodynamics with ultracold atoms: probing confinement and nonperturbative effects”, *Physical review letters* **109**, 125302 (2012) (cit. on pp. 2, 52, 60).
- ³³E. Zohar, J. I. Cirac, and B. Reznik, “Cold-atom quantum simulator for su (2) yang-mills lattice gauge theory”, *Physical review letters* **110**, 125304 (2013) (cit. on p. 2).
- ³⁴D. Yang, G. S. Giri, M. Johanning, C. Wunderlich, P. Zoller, and P. Hauke, “Analog quantum simulation of (1+ 1)-dimensional lattice qed with trapped ions”, *Physical Review A* **94**, 052321 (2016) (cit. on pp. 2, 14, 52, 55).
- ³⁵D Marcos, P. Widmer, E Rico, M Hafezi, P Rabl, U.-J. Wiese, and P Zoller, “Two-dimensional lattice gauge theories with superconducting quantum circuits”, *Annals of physics* **351**, 634–654 (2014) (cit. on pp. 2, 52).
- ³⁶K Stannigel, P Hauke, D Marcos, M Hafezi, S Diehl, M Dalmonte, and P Zoller, “Constrained dynamics via the zeno effect in quantum simulation: implementing non-abelian lattice gauge theories with cold atoms”, *Physical review letters* **112**, 120406 (2014) (cit. on p. 2).
- ³⁷D. González-Cuadra, E. Zohar, and J. I. Cirac, “Quantum simulation of the abelian-higgs lattice gauge theory with ultracold atoms”, *New Journal of Physics* **19**, 063038 (2017) (cit. on pp. 2, 52).
- ³⁸D. González-Cuadra, T. V. Zache, J. Carrasco, B. Kraus, and P. Zoller, “Hardware efficient quantum simulation of non-abelian gauge theories with qudits on rydberg platforms”, *arXiv preprint arXiv:2203.15541* (2022) (cit. on p. 2).
- ³⁹Z. Davoudi, N. M. Linke, and G. Pagano, “Toward simulating quantum field theories with controlled phonon-ion dynamics: a hybrid analog-digital approach”, *Physical Review Research* **3**, 043072 (2021) (cit. on pp. 2, 150).

- ⁴⁰Z. Davoudi, I. Raychowdhury, and A. Shaw, “Search for efficient formulations for hamiltonian simulation of non-abelian lattice gauge theories”, *Physical Review D* **104**, 074505 (2021) (cit. on p. 2).
- ⁴¹J. Bender, E. Zohar, A. Farace, and J. I. Cirac, “Digital quantum simulation of lattice gauge theories in three spatial dimensions”, *New Journal of Physics* **20**, 093001 (2018) (cit. on pp. 2, 52).
- ⁴²J. F. Haase, L. Dellantonio, A. Celi, D. Paulson, A. Kan, K. Jansen, and C. A. Muschik, “A resource efficient approach for quantum and classical simulations of gauge theories in particle physics”, arXiv preprint arXiv:2006.14160 (2020) (cit. on pp. 2, 52).
- ⁴³J. C. Halimeh and P. Hauke, “Reliability of lattice gauge theories”, *Physical Review Letters* **125**, 030503 (2020) (cit. on p. 2).
- ⁴⁴J. C. Halimeh, H. Lang, J. Mildenberger, Z. Jiang, and P. Hauke, “Gauge-symmetry protection using single-body terms”, *PRX Quantum* **2**, 040311 (2021) (cit. on p. 2).
- ⁴⁵V. Kasper, T. V. Zache, F. Jendrzejewski, M. Lewenstein, and E. Zohar, “Non-abelian gauge invariance from dynamical decoupling”, arXiv preprint arXiv:2012.08620 (2020) (cit. on p. 2).
- ⁴⁶D. Paulson, L. Dellantonio, J. F. Haase, A. Celi, A. Kan, A. Jena, C. Kokail, R. van Bijnen, K. Jansen, P. Zoller, et al., “Towards simulating 2d effects in lattice gauge theories on a quantum computer”, arXiv preprint arXiv:2008.09252 (2020) (cit. on pp. 2, 52).
- ⁴⁷B. Andrade, Z. Davoudi, T. Graß, M. Hafezi, G. Pagano, and A. Seif, “Engineering an effective three-spin hamiltonian in trapped-ion systems for applications in quantum simulation”, *Quantum Science and Technology* (2022) (cit. on p. 2).
- ⁴⁸C. Muschik, M. Heyl, E. Martinez, T. Monz, P. Schindler, B. Vogell, M. Dalmonte, P. Hauke, R. Blatt, and P. Zoller, “U (1) wilson lattice gauge theories in digital quantum simulators”, *New Journal of Physics* **19**, 103020 (2017) (cit. on pp. 2, 20).
- ⁴⁹L. Tagliacozzo, A. Celi, P. Orland, M. Mitchell, and M. Lewenstein, “Simulation of non-abelian gauge theories with optical lattices”, *Nature communications* **4**, 1–8 (2013) (cit. on p. 2).
- ⁵⁰A. Celi, B. Vermersch, O. Viyuela, H. Pichler, M. D. Lukin, and P. Zoller, “Emerging two-dimensional gauge theories in rydberg configurable arrays”, *Phys. Rev. X* **10**, 021057 (2020) (cit. on pp. 2, 52).
- ⁵¹E. A. Martinez, C. A. Muschik, P. Schindler, D. Nigg, A. Erhard, M. Heyl, P. Hauke, M. Dalmonte, T. Monz, P. Zoller, et al., “Real-time dynamics of lattice gauge theories with a few-qubit quantum computer”, *Nature* **534**, 516–519 (2016) (cit. on pp. 2, 20).

- ⁵²A. Mil, T. V. Zache, A. Hegde, A. Xia, R. P. Bhatt, M. K. Oberthaler, P. Hauke, J. Berges, and F. Jendrzejewski, “A scalable realization of local $U(1)$ gauge invariance in cold atomic mixtures”, *Science* **367**, 1128–1130 (2020) (cit. on pp. 2, 20, 51, 53, 61, 63, 79, 89).
- ⁵³F. Görg, K. Sandholzer, J. Minguzzi, R. Desbuquois, M. Messer, and T. Esslinger, “Realization of density-dependent Peierls phases to engineer quantized gauge fields coupled to ultracold matter”, *Nature Physics* **15**, 1161–1167 (2019) (cit. on pp. 2, 20).
- ⁵⁴C. Schweizer, F. Grusdt, M. Berngruber, L. Barbiero, E. Demler, N. Goldman, I. Bloch, and M. Aidelsburger, “Floquet approach to z_2 lattice gauge theories with ultracold atoms in optical lattices”, *Nature Physics* **15**, 1168–1173 (2019) (cit. on pp. 2, 20, 69).
- ⁵⁵H. Bernien, S. Schwartz, A. Keesling, H. Levine, A. Omran, H. Pichler, S. Choi, A. S. Zibrov, M. Endres, M. Greiner, et al., “Probing many-body dynamics on a 51-atom quantum simulator”, *Nature* **551**, 579–584 (2017) (cit. on pp. 2, 16, 40, 47, 150).
- ⁵⁶C. Kokail, C. Maier, R. van Bijnen, T. Brydges, M. K. Joshi, P. Jurcevic, C. A. Muschik, P. Silvi, R. Blatt, C. F. Roos, et al., “Self-verifying variational quantum simulation of lattice models”, *Nature* **569**, 355–360 (2019) (cit. on pp. 2, 20, 150).
- ⁵⁷N. Klco, E. F. Dumitrescu, A. J. McCaskey, T. D. Morris, R. C. Pooser, M. Sanz, E. Solano, P. Lougovski, and M. J. Savage, “Quantum-classical computation of Schwinger model dynamics using quantum computers”, *Physical Review A* **98**, 032331 (2018) (cit. on pp. 2, 20).
- ⁵⁸H.-N. Dai, B. Yang, A. Reingruber, H. Sun, X.-F. Xu, Y.-A. Chen, Z.-S. Yuan, and J.-W. Pan, “Four-body ring-exchange interactions and anyonic statistics within a minimal toric-code hamiltonian”, *Nature Physics* **13**, 1195–1200 (2017) (cit. on p. 2).
- ⁵⁹J. Milderberger, W. Mruczkiewicz, J. C. Halimeh, Z. Jiang, and P. Hauke, “Probing confinement in a z_2 lattice gauge theory on a quantum computer”, arXiv preprint arXiv:2203.08905 (2022) (cit. on pp. 2, 69).
- ⁶⁰Y. Y. Atas, J. Zhang, R. Lewis, A. Jahanpour, J. F. Haase, and C. A. Muschik, “ $SU(2)$ hadrons on a quantum computer via a variational approach”, *Nature communications* **12**, 1–11 (2021) (cit. on p. 2).
- ⁶¹P. Hauke, F. M. Cucchietti, L. Tagliacozzo, I. Deutsch, and M. Lewenstein, “Can one trust quantum simulators?”, *Reports on Progress in Physics* **75**, 082401 (2012) (cit. on p. 2).
- ⁶²J. I. Cirac and P. Zoller, “Goals and opportunities in quantum simulation”, *Nature physics* **8**, 264–266 (2012) (cit. on p. 2).
- ⁶³J. Berges, *Scaling up quantum simulations*, 2019 (cit. on p. 2).

- ⁶⁴T. V. Zache, F. Hebenstreit, F Jendrzejewski, M. Oberthaler, J Berges, and P Hauke, “Quantum simulation of lattice gauge theories using wilson fermions”, *Quantum science and technology* **3**, 034010 (2018) (cit. on pp. 2, 53).
- ⁶⁵E. Zohar, “Quantum simulation of lattice gauge theories in more than one space dimension—requirements, challenges and methods”, *Philosophical Transactions of the Royal Society A* **380**, 20210069 (2022) (cit. on p. 2).
- ⁶⁶S. Sachdev, *Quantum phase transitions* (Cambridge university press, 2011) (cit. on pp. 3, 16).
- ⁶⁷J. Berges and J. Cox, “Thermalization of quantum fields from time-reversal invariant evolution equations”, *Physics Letters B* **517**, 369–374 (2001) (cit. on pp. 3, 16, 35).
- ⁶⁸G. Felder, L. Kofman, and A. Linde, “Tachyonic instability and dynamics of spontaneous symmetry breaking”, *Physical Review D* **64**, 123517 (2001) (cit. on p. 3).
- ⁶⁹R. Micha and I. I. Tkachev, “Turbulent thermalization”, *Physical Review D* **70**, 043538 (2004) (cit. on pp. 3, 73, 75, 148).
- ⁷⁰K. Fujikawa, “Path-integral measure for gauge-invariant fermion theories”, *Physical Review Letters* **42**, 1195 (1979) (cit. on p. 9).
- ⁷¹H. J. Rothe, *Lattice gauge theories: an introduction* (World Scientific Publishing Company, 2012) (cit. on p. 10).
- ⁷²H. Nielsen and M. Ninomiya, “A no-go theorem for regularizing chiral fermions”, *Physics Letters B* **105**, 219–223 (1981) (cit. on p. 10).
- ⁷³L. Susskind, “Lattice fermions”, *Physical Review D* **16**, 3031 (1977) (cit. on pp. 10, 21).
- ⁷⁴M. Creutz, “Gauge fixing, the transfer matrix, and confinement on a lattice”, *Physical Review D* **15**, 1128 (1977) (cit. on p. 11).
- ⁷⁵J. Kogut and L. Susskind, “Hamiltonian formulation of wilson’s lattice gauge theories”, *Physical Review D* **11**, 395 (1975) (cit. on p. 12).
- ⁷⁶S. Elitzur, “Impossibility of spontaneously breaking local symmetries”, *Physical review d* **12**, 3978 (1975) (cit. on p. 12).
- ⁷⁷V. Kasper, F. Hebenstreit, M. K. Oberthaler, and J. Berges, “Schwinger pair production with ultracold atoms”, *Physics Letters B* **760**, 742–746 (2016) (cit. on pp. 14, 149).
- ⁷⁸J. C. Halimeh, M. Van Damme, T. V. Zache, D. Banerjee, and P. Hauke, “Achieving the quantum field theory limit in far-from-equilibrium quantum link models”, arXiv preprint arXiv:2112.04501 (2021) (cit. on pp. 14, 148).
- ⁷⁹T. V. Zache, M. Van Damme, J. C. Halimeh, P. Hauke, and D. Banerjee, “Achieving the continuum limit of quantum link lattice gauge theories on quantum devices”, arXiv preprint arXiv:2104.00025 (2021) (cit. on pp. 14, 40, 47, 48, 148).

- ⁸⁰K. Kasamatsu, I. Ichinose, and T. Matsui, “Atomic quantum simulation of the lattice gauge-higgs model: higgs couplings and emergence of exact local gauge symmetry”, *Physical review letters* **111**, 115303 (2013) (cit. on pp. 14, 52, 55).
- ⁸¹A. Polkovnikov, K. Sengupta, A. Silva, and M. Vengalattore, “Colloquium: nonequilibrium dynamics of closed interacting quantum systems”, *Reviews of Modern Physics* **83**, 863 (2011) (cit. on p. 16).
- ⁸²J. Eisert, M. Friesdorf, and C. Gogolin, “Quantum many-body systems out of equilibrium”, *Nature Physics* **11**, 124–130 (2015) (cit. on p. 16).
- ⁸³M. Rigol, V. Dunjko, and M. Olshanii, “Thermalization and its mechanism for generic isolated quantum systems”, *Nature* **452**, 854–858 (2008) (cit. on pp. 16, 35).
- ⁸⁴M. Serbyn, D. A. Abanin, and Z. Papić, “Quantum many-body scars and weak breaking of ergodicity”, *Nature Physics* **17**, 675–685 (2021) (cit. on p. 16).
- ⁸⁵C. J. Turner, A. A. Michailidis, D. A. Abanin, M. Serbyn, and Z. Papić, “Weak ergodicity breaking from quantum many-body scars”, *Nature Physics* **14**, 745–749 (2018) (cit. on pp. 16, 40, 47).
- ⁸⁶W. W. Ho, S. Choi, H. Pichler, and M. D. Lukin, “Periodic orbits, entanglement, and quantum many-body scars in constrained models: matrix product state approach”, *Physical review letters* **122**, 040603 (2019) (cit. on p. 16).
- ⁸⁷R. Nandkishore and D. A. Huse, “Many-body localization and thermalization in quantum statistical mechanics”, *Annu. Rev. Condens. Matter Phys.* **6**, 15–38 (2015) (cit. on p. 16).
- ⁸⁸M. Prüfer, P. Kunkel, H. Strobel, S. Lannig, D. Linnemann, C.-M. Schmied, J. Berges, T. Gasenzer, and M. K. Oberthaler, “Observation of universal dynamics in a spinor bose gas far from equilibrium”, *Nature* **563**, 217–220 (2018) (cit. on pp. 16, 61, 124, 148, 149).
- ⁸⁹S. Erne, R. Bücker, T. Gasenzer, J. Berges, and J. Schmiedmayer, “Universal dynamics in an isolated one-dimensional bose gas far from equilibrium”, *Nature* **563**, 225–229 (2018) (cit. on pp. 16, 61, 148, 149).
- ⁹⁰J. A. Glidden, C. Eigen, L. H. Dogra, T. A. Hilker, R. P. Smith, and Z. Hadzibabic, “Bidirectional dynamic scaling in an isolated bose gas far from equilibrium”, *Nature Physics* **17**, 457–461 (2021) (cit. on pp. 16, 148, 149).
- ⁹¹F. Arute, K. Arya, R. Babbush, D. Bacon, J. C. Bardin, R. Barends, R. Biswas, S. Boixo, F. G. Brandao, D. A. Buell, et al., “Quantum supremacy using a programmable superconducting processor”, *Nature* **574**, 505–510 (2019) (cit. on pp. 16, 150).
- ⁹²D. Jaksch, C. Bruder, J. I. Cirac, C. W. Gardiner, and P. Zoller, “Cold bosonic atoms in optical lattices”, *Physical Review Letters* **81**, 3108 (1998) (cit. on p. 17).
- ⁹³S. Coleman, “More about the massive schwinger model”, *Annals of Physics* **101**, 239–267 (1976) (cit. on pp. 20, 25).

- ⁹⁴S. Chandrasekharan and U.-J. Wiese, “Quantum link models: a discrete approach to gauge theories”, *Nuclear Physics B* **492**, 455–471 (1997) (cit. on p. 20).
- ⁹⁵A. Kale, J. H. Huhn, M. Xu, L. H. Kendrick, M. Lebrat, F. Grusdt, A. Bohrdt, and M. Greiner, “Schrieffer-wolff transformations for experiments: dynamically suppressing virtual doublon-hole excitations in a fermi-hubbard simulator”, arXiv preprint arXiv:2203.07366 (2022) (cit. on p. 23).
- ⁹⁶B. Yang, H. Sun, C.-J. Huang, H.-Y. Wang, Y. Deng, H.-N. Dai, Z.-S. Yuan, and J.-W. Pan, “Cooling and entangling ultracold atoms in optical lattices”, *Science* **369**, 550–553 (2020) (cit. on pp. 24, 31).
- ⁹⁷E. Rico, T. Pichler, M. Dalmonte, P. Zoller, and S. Montangero, “Tensor networks for lattice gauge theories and atomic quantum simulation”, *Physical Review Letters* **112**, 201601 (2014) (cit. on p. 25).
- ⁹⁸E. Altman, E. Demler, and M. D. Lukin, “Probing many-body states of ultracold atoms via noise correlations”, *Physical Review A* **70**, 013603 (2004) (cit. on p. 27).
- ⁹⁹S. Fölling, F. Gerbier, A. Widera, O. Mandel, T. Gericke, and I. Bloch, “Spatial quantum noise interferometry in expanding ultracold atom clouds”, *Nature* **434**, 481–484 (2005) (cit. on pp. 27, 28).
- ¹⁰⁰J. Simon, W. S. Bakr, R. Ma, M. E. Tai, P. M. Preiss, and M. Greiner, “Quantum simulation of antiferromagnetic spin chains in an optical lattice”, *Nature* **472**, 307–312 (2011) (cit. on p. 27).
- ¹⁰¹S. Fölling, “Quantum noise correlation experiments with ultracold atoms”, in *Quantum gas experiments: exploring many-body states* (World Scientific, 2015), pp. 145–177 (cit. on pp. 28, 29).
- ¹⁰²U. Schollwöck, “The density-matrix renormalization group in the age of matrix product states”, *Annals of physics* **326**, 96–192 (2011) (cit. on p. 36).
- ¹⁰³G. Aarts, G. F. Bonini, and C. Wetterich, “On thermalization in classical scalar field theory”, *Nuclear Physics B* **587**, 403–418 (2000) (cit. on p. 40).
- ¹⁰⁴F. M. Surace, P. P. Mazza, G. Giudici, A. Lerose, A. Gambassi, and M. Dalmonte, “Lattice gauge theories and string dynamics in rydberg atom quantum simulators”, *Physical Review X* **10**, 021041 (2020) (cit. on pp. 40, 47).
- ¹⁰⁵M. Lewenstein, A. Sanpera, V. Ahufinger, B. Damski, A. Sen, and U. Sen, “Ultra-cold atomic gases in optical lattices: mimicking condensed matter physics and beyond”, *Advances in Physics* **56**, 243–379 (2007) (cit. on p. 43).
- ¹⁰⁶S. Bravyi, D. P. DiVincenzo, and D. Loss, “Schrieffer–wolff transformation for quantum many-body systems”, *Annals of physics* **326**, 2793–2826 (2011) (cit. on p. 43).
- ¹⁰⁷P. Weinberg and M. Bukov, “Quspin: a python package for dynamics and exact diagonalisation of quantum many body systems. part ii: bosons, fermions and higher spins”, *SciPost Physics* **7**, 020 (2019) (cit. on pp. 47, 70).

- ¹⁰⁸N. Mueller, T. V. Zache, and R. Ott, “Quantum thermalization of gauge theories: chaos, turbulence and universality”, arXiv preprint arXiv:2111.01155 (2021) (cit. on pp. 51, 72, 73).
- ¹⁰⁹A. Mil, “Experimental realization of $u(1)$ gauge invariance in ultracold atomic mixtures”, Doctoral Thesis (2020) 10.11588/heidok.00028454 (cit. on pp. 51, 65).
- ¹¹⁰T. V. Zache, “Quantum simulation of high-energy physics with ultracold atoms”, Doctoral thesis (2020) 10.11588/heidok.00028536 (cit. on pp. 51, 67, 95, 103, 109, 130).
- ¹¹¹H.-N. Dai, B. Yang, A. Reingruber, H. Sun, X.-F. Xu, Y.-A. Chen, Z.-S. Yuan, and J.-W. Pan, “Four-body ring-exchange interactions and anyonic statistics within a minimal toric-code hamiltonian”, *Nature Physics* **13**, 1195–1200 (2017) (cit. on p. 52).
- ¹¹²N. Klco, M. J. Savage, and J. R. Stryker, “ $Su(2)$ non-abelian gauge field theory in one dimension on digital quantum computers”, *Physical Review D* **101**, 074512 (2020) (cit. on p. 52).
- ¹¹³A. Yamamoto, “Real-time simulation of $(2+1)$ -dimensional lattice gauge theory on qubits”, arXiv preprint arXiv:2008.11395 (2020) (cit. on p. 52).
- ¹¹⁴H. Büchler, M. Hermele, S. D. Huber, M. P. Fisher, and P. Zoller, “Atomic quantum simulator for lattice gauge theories and ring exchange models”, *Physical review letters* **95**, 040402 (2005) (cit. on p. 52).
- ¹¹⁵B. Paredes and I. Bloch, “Minimum instances of topological matter in an optical plaquette”, *Physical Review A* **77**, 023603 (2008) (cit. on p. 52).
- ¹¹⁶G. Brennen, G. Pupillo, E. Rico, T. Stace, and D. Vodola, “Loops and strings in a superconducting lattice gauge simulator”, *Physical review letters* **117**, 240504 (2016) (cit. on p. 52).
- ¹¹⁷L. Barbiero, C. Schweizer, M. Aidelsburger, E. Demler, N. Goldman, and F. Grusdt, “Coupling ultracold matter to dynamical gauge fields in optical lattices: from flux attachment to z_2 lattice gauge theories”, *Science advances* **5**, eaav7444 (2019) (cit. on p. 52).
- ¹¹⁸V. Kasper, F. Hebenstreit, F. Jendrzejewski, M. K. Oberthaler, and J. Berges, “Implementing quantum electrodynamics with ultracold atomic systems”, *New journal of physics* **19**, 023030 (2017) (cit. on pp. 53, 79).
- ¹¹⁹V. Kasper, G. Juzeliunas, M. Lewenstein, F. Jendrzejewski, and E. Zohar, “From the jaynes-cummings model to non-abelian gauge theories: a guided tour for the quantum engineer”, arXiv preprint arXiv:2006.01258 (2020) (cit. on p. 53).
- ¹²⁰D. M. Stamper-Kurn and M. Ueda, “Spinor bose gases: symmetries, magnetism, and quantum dynamics”, *Reviews of Modern Physics* **85**, 1191 (2013) (cit. on pp. 53, 61, 76, 79, 89).

- ¹²¹S. D. Drell, H. R. Quinn, B. Svetitsky, and M. Weinstein, “Quantum electrodynamics on a lattice: a hamiltonian variational approach to the physics of the weak-coupling region”, *Physical Review D* **19**, 619 (1979) (cit. on pp. 56, 57, 59, 60, 80–84, 86, 87, 97).
- ¹²²A. M. Polyakov, “Quark confinement and topology of gauge theories”, *Nuclear Physics B* **120**, 429–458 (1977) (cit. on pp. 57, 60).
- ¹²³B. Svetitsky, “Symmetry aspects of finite-temperature confinement transitions”, *Physics Reports* **132**, 1–53 (1986) (cit. on p. 57).
- ¹²⁴J. Bender, P. Emonts, E. Zohar, and J. I. Cirac, “Real-time dynamics in 2+ 1d compact qed using complex periodic gaussian states”, arXiv preprint arXiv:2006.10038 (2020) (cit. on p. 58).
- ¹²⁵M.-G. Hu, M. J. Van de Graaff, D. Kedar, J. P. Corson, E. A. Cornell, and D. S. Jin, “Bose polarons in the strongly interacting regime”, *Physical review letters* **117**, 055301 (2016) (cit. on p. 61).
- ¹²⁶N. B. Jørgensen, L. Wacker, K. T. Skalmstang, M. M. Parish, J. Levinsen, R. S. Christensen, G. M. Bruun, and J. J. Arlt, “Observation of attractive and repulsive polarons in a bose-einstein condensate”, *Physical review letters* **117**, 055302 (2016) (cit. on p. 61).
- ¹²⁷X. Li, B. Zhu, X. He, F. Wang, M. Guo, Z.-F. Xu, S. Zhang, and D. Wang, “Coherent heteronuclear spin dynamics in an ultracold spinor mixture”, *Phys. Rev. Lett.* **114**, 255301 (2015) (cit. on p. 61).
- ¹²⁸K. Wintersperger, M. Bukov, J. Näger, S. Lellouch, E. Demler, U. Schneider, I. Bloch, N. Goldman, and M. Aidelsburger, “Parametric instabilities of interacting bosons in periodically driven 1d optical lattices”, *Physical Review X* **10**, 011030 (2020) (cit. on p. 61).
- ¹²⁹N. Navon, A. L. Gaunt, R. P. Smith, and Z. Hadzibabic, “Critical dynamics of spontaneous symmetry breaking in a homogeneous bose gas”, *Science* **347**, 167–170 (2015) (cit. on p. 61).
- ¹³⁰S. Coleman, “Fate of the false vacuum: semiclassical theory”, *Physical Review D* **15**, 2929 (1977) (cit. on p. 61).
- ¹³¹A. Polkovnikov, “Quantum corrections to the dynamics of interacting bosons: beyond the truncated wigner approximation”, *Physical Review A* **68**, 053604 (2003) (cit. on pp. 64, 99–101).
- ¹³²J. L. García-Palacios and F. J. Lázaro, “Langevin-dynamics study of the dynamical properties of small magnetic particles”, *Physical Review B* **58**, 14937 (1998) (cit. on p. 65).
- ¹³³H. Li and F. D. M. Haldane, “Entanglement spectrum as a generalization of entanglement entropy: identification of topological order in non-abelian fractional quantum hall effect states”, *Physical review letters* **101**, 010504 (2008) (cit. on p. 69).

- ¹³⁴P. Buividovich and M. Polikarpov, “Entanglement entropy in gauge theories and the holographic principle for electric strings”, *Physics Letters B* **670**, 141–145 (2008) (cit. on p. 69).
- ¹³⁵A. Einstein, B. Podolsky, and N. Rosen, “Can quantum-mechanical description of physical reality be considered complete?”, *Physical review* **47**, 777 (1935) (cit. on p. 69).
- ¹³⁶P.-Y. Chang, X. Chen, S. Gopalakrishnan, and J. Pixley, “Evolution of entanglement spectra under generic quantum dynamics”, *Physical review letters* **123**, 190602 (2019) (cit. on p. 69).
- ¹³⁷F. J. Wegner, “Duality in generalized ising models and phase transitions without local order parameters”, *Journal of Mathematical Physics* **12**, 2259–2272 (1971) (cit. on p. 69).
- ¹³⁸D. Horn, M. Weinstein, and S. Yankielowicz, “Hamiltonian approach to $z(n)$ lattice gauge theories”, *Physical Review D* **19**, 3715 (1979) (cit. on p. 69).
- ¹³⁹L. D’Alessio, Y. Kafri, A. Polkovnikov, and M. Rigol, “From quantum chaos and eigenstate thermalization to statistical mechanics and thermodynamics”, *Advances in Physics* **65**, 239–362 (2016) (cit. on p. 73).
- ¹⁴⁰T. Rakovszky, S. Gopalakrishnan, S. Parameswaran, and F. Pollmann, “Signatures of information scrambling in the dynamics of the entanglement spectrum”, *Physical Review B* **100**, 125115 (2019) (cit. on p. 73).
- ¹⁴¹J. Berges, A. Rothkopf, and J. Schmidt, “Nonthermal fixed points: effective weak coupling for strongly correlated systems far from equilibrium”, *Physical review letters* **101**, 041603 (2008) (cit. on pp. 73, 75, 122, 124, 148).
- ¹⁴²T. V. Zache, T. Schweigler, S. Erne, J. Schmiedmayer, and J. Berges, “Extracting the field theory description of a quantum many-body system from experimental data”, *Phys. Rev. X* **10**, 011020 (2020) (cit. on pp. 75, 93, 103, 104, 107, 125).
- ¹⁴³M. Prüfer, T. V. Zache, P. Kunkel, S. Lannig, A. Bonnin, H. Strobel, J. Berges, and M. K. Oberthaler, “Experimental extraction of the quantum effective action for a non-equilibrium many-body system”, *Nature Physics* **16**, Publisher: Nature Publishing Group, 1012–1016 (2020) (cit. on pp. 75, 103, 104, 107, 122, 125, 150).
- ¹⁴⁴A. Mil, “Experimental realization of U(1) gauge invariance in ultracold atomic mixtures”, *Doctoral thesis* (2020) 10.11588/heidok.00028454 (cit. on p. 93).
- ¹⁴⁵V. Kasper, F. Hebenstreit, and J. Berges, “Fermion production from real-time lattice gauge theory in the classical-statistical regime”, *Physical Review D* **90**, 025016 (2014) (cit. on pp. 99, 100, 149).
- ¹⁴⁶J. Berges, “Introduction to nonequilibrium quantum field theory”, in *Aip conference proceedings*, Vol. 739, 1 (American Institute of Physics, 2004), pp. 3–62 (cit. on pp. 99, 103, 110).

- ¹⁴⁷J. Berges and T. Gasenzer, “Quantum versus classical statistical dynamics of an ultracold bose gas”, *Physical Review A* **76**, 033604 (2007) (cit. on p. 100).
- ¹⁴⁸J. Schwinger, “Brownian motion of a quantum oscillator”, *Journal of Mathematical Physics* **2**, 407–432 (1961) (cit. on p. 103).
- ¹⁴⁹L. V. Keldysh et al., “Diagram technique for nonequilibrium processes”, *Sov. Phys. JETP* **20**, 1018–1026 (1965) (cit. on p. 103).
- ¹⁵⁰L. P. Kadanoff and G. Baym, *Quantum statistical mechanics: green's function methods in equilibrium and nonequilibrium problems* (CRC Press, 2018) (cit. on p. 103).
- ¹⁵¹E. Lifschitz and L. Pitajewski, “Physical kinetics”, in *Textbook of theoretical physics*. **10** (1983) (cit. on pp. 103, 113).
- ¹⁵²C. Wetterich, “Time evolution of nonequilibrium effective action”, *Physical review letters* **78**, 3598 (1997) (cit. on pp. 103, 105, 107, 109, 130).
- ¹⁵³R Walz, K. Boguslavski, and J Berges, “Large-n kinetic theory for highly occupied systems”, *Physical Review D* **97**, 116011 (2018) (cit. on pp. 104, 122).
- ¹⁵⁴G. F. Bonini and C. Wetterich, “Time evolution of correlation functions and thermalization”, *Physical Review D* **60**, 105026 (1999) (cit. on p. 117).
- ¹⁵⁵G. Aarts, G. F. Bonini, and C. Wetterich, “Exact and truncated dynamics in nonequilibrium field theory”, *Physical Review D* **63**, 025012 (2000) (cit. on p. 117).
- ¹⁵⁶A. V. Ryzhov and L. G. Yaffe, “Large n quantum time evolution beyond leading order”, *Physical Review D* **62**, 125003 (2000) (cit. on p. 117).
- ¹⁵⁷J. Berges and G. Hoffmeister, “Nonthermal fixed points and the functional renormalization group”, *Nuclear Physics B* **813**, 383–407 (2009) (cit. on p. 120).
- ¹⁵⁸S. Bhattacharyya, J. F. Rodriguez-Nieva, and E. Demler, “Universal prethermal dynamics in heisenberg ferromagnets”, *Physical Review Letters* **125**, 230601 (2020) (cit. on p. 124).
- ¹⁵⁹F. Gelis, E. Iancu, J. Jalilian-Marian, and R. Venugopalan, “The color glass condensate”, *Annual Review of Nuclear and Particle Science* **60**, 463–489 (2010) (cit. on p. 149).
- ¹⁶⁰F. Sauter, “Über das verhalten eines elektrons im homogenen elektrischen feld nach der relativistischen theorie diracs”, *Zeitschrift für Physik* **69**, 742–764 (1931) (cit. on p. 149).
- ¹⁶¹*Extreme light infrastructure (eli)*, Accessed 2022-04-17 (cit. on p. 149).
- ¹⁶²D. Papadopoulos, J. Zou, C Le Blanc, G Chériaux, P. Georges, F Druon, G Menerat, P Ramirez, L Martin, A Fréneaux, et al., “The apollon 10 pw laser: experimental and theoretical investigation of the temporal characteristics”, *High Power Laser Science and Engineering* **4** (2016) (cit. on p. 149).
- ¹⁶³J. Schwinger, “On gauge invariance and vacuum polarization”, *Physical Review* **82**, 664 (1951) (cit. on p. 149).

- ¹⁶⁴N. Mueller, F. Hebenstreit, and J. Berges, “Anomaly-induced dynamical refringence in strong-field qed”, *Physical review letters* **117**, 061601 (2016) (cit. on p. 149).
- ¹⁶⁵F. Hebenstreit, J. Berges, and D. Gelfand, “Real-time dynamics of string breaking”, *Physical review letters* **111**, 201601 (2013) (cit. on p. 149).
- ¹⁶⁶T. Pichler, M. Dalmonte, E. Rico, P. Zoller, and S. Montangero, “Real-time dynamics in $u(1)$ lattice gauge theories with tensor networks”, *Physical Review X* **6**, 011023 (2016) (cit. on p. 149).
- ¹⁶⁷D. Banerjee, M Dalmonte, M Müller, E Rico, P Stebler, U.-J. Wiese, and P Zoller, “Atomic quantum simulation of dynamical gauge fields coupled to fermionic matter: from string breaking to evolution after a quench”, *Physical review letters* **109**, 175302 (2012) (cit. on p. 149).
- ¹⁶⁸S. Giorgini, L. P. Pitaevskii, and S. Stringari, “Theory of ultracold atomic fermi gases”, *Reviews of Modern Physics* **80**, 1215 (2008) (cit. on p. 149).
- ¹⁶⁹A. Mazurenko, C. S. Chiu, G. Ji, M. F. Parsons, M. Kanász-Nagy, R. Schmidt, F. Grusdt, E. Demler, D. Greif, and M. Greiner, “A cold-atom fermi–hubbard antiferromagnet”, *Nature* **545**, 462–466 (2017) (cit. on p. 149).
- ¹⁷⁰P. Murthy, I Boettcher, L Bayha, M Holzmann, D Kedar, M Neidig, M. Ries, A. Wenz, G Zürn, and S Jochim, “Observation of the berezinskii-kosterlitz-thouless phase transition in an ultracold fermi gas”, *Physical Review Letters* **115**, 010401 (2015) (cit. on p. 149).
- ¹⁷¹C. Kokail, B. Sundar, T. V. Zache, A. Elben, B. Vermersch, M. Dalmonte, R. van Bijnen, and P. Zoller, “Quantum variational learning of the entanglement hamiltonian”, *Physical review letters* **127**, 170501 (2021) (cit. on p. 150).
- ¹⁷²T. V. Zache, C. Kokail, B. Sundar, and P. Zoller, “Entanglement spectroscopy and probing the li-haldane conjecture in topological quantum matter”, *arXiv preprint arXiv:2110.03913* (2021) (cit. on p. 150).
- ¹⁷³A. Lukin, M. Rispoli, R. Schittko, M. E. Tai, A. M. Kaufman, S. Choi, V. Khemani, J. Léonard, and M. Greiner, “Probing entanglement in a many-body–localized system”, *Science* **364**, 256–260 (2019) (cit. on p. 150).
- ¹⁷⁴P. Kunkel, M. Prüfer, H. Strobel, D. Linnemann, A. Frölian, T. Gasenzer, M. Gärttner, and M. K. Oberthaler, “Spatially distributed multipartite entanglement enables epr steering of atomic clouds”, *Science* **360**, 413–416 (2018) (cit. on p. 150).
- ¹⁷⁵P. Kunkel, M. Prüfer, S. Lannig, R. Strohmaier, M. Gärttner, H. Strobel, and M. K. Oberthaler, “Detecting entanglement structure in continuous many-body quantum systems”, *Physical Review Letters* **128**, 020402 (2022) (cit. on p. 150).
- ¹⁷⁶J. Preskill, “Quantum computing in the nisq era and beyond”, *Quantum* **2**, 79 (2018) (cit. on p. 150).

- ¹⁷⁷S. Ebadi, T. T. Wang, H. Levine, A. Keesling, G. Semeghini, A. Omran, D. Bluvstein, R. Samajdar, H. Pichler, W. W. Ho, et al., “Quantum phases of matter on a 256-atom programmable quantum simulator”, *Nature* **595**, 227–232 (2021) (cit. on p. 150).
- ¹⁷⁸P. Scholl, M. Schuler, H. J. Williams, A. A. Eberharter, D. Barredo, K.-N. Schymik, V. Lienhard, L.-P. Henry, T. C. Lang, T. Lahaye, et al., “Quantum simulation of 2d antiferromagnets with hundreds of rydberg atoms”, *Nature* **595**, 233–238 (2021) (cit. on p. 150).
- ¹⁷⁹J. R. McClean, J. Romero, R. Babbush, and A. Aspuru-Guzik, “The theory of variational hybrid quantum-classical algorithms”, *New Journal of Physics* **18**, 023023 (2016) (cit. on p. 150).